Construction and Application of the Endstation for Controlled Molecular Experiments in Chemical Dynamics

Dissertation
zur Erlangung des Doktorgrades an der Fakultät für Mathematik, Informatik und Naturwissenschaften
Fachbereich Physik
der Universität Hamburg

vorgelegt von
Wuwei Jin

Hamburg
2026

Gutachter/innen der Dissertation:	Prof. Dr. Jochen Küpper Dr. Sebastian Trippel
Zusammensetzung der Prüfungskommission:	Prof. Dr. Jochen Küpper Dr. Sebastian Trippel Prof. Dr. Francesca Calegari Prof. Dr. Franz Kärtner Prof. Dr. Robin Santra
Vorsitzende/r der Prüfungskommission:	Prof. Dr. Robin Santra
Datum der Disputation:	22.05.2026
Vorsitzender des Fach-Promotionsausschusses PHYSIK:	Prof. Dr. Johannes Haller
Leiter des Fachbereichs PHYSIK:	Prof. Dr. Markus Drescher
Dekan der Fakultät MIN:	Prof. Dr.-Ing. Norbert Ritter

Eidesstattliche Versicherung / Declaration on oath

I hereby declare and affirm that this doctoral dissertation is my own work and that I have not used any aids and sources other than those indicated.

If electronic resources based on generative artificial intelligence (gAI) were used in the course of writing this dissertation, I confirm that my own work was the main and value-adding contribution and that complete documentation of all resources used is available in accordance with good scientific practice. I am responsible for any erroneous or distorted content, incorrect references, violations of data protection and copyright law or plagiarism that may have been generated by the gAI.

Hamburg, den 2026-05-26

Unterschrift:

Wuwei Jin

Abstract

Direct imaging chemical reactions with atomic-scale spatial resolution and femtosecond-to-attosecond temporal precision is long seeking goal to better understand molecular chemistry. This vision, called "molecular movie" is a direct step for understanding of molecule dynamics and reactivity during isomerization, bond breaking and reformation, and photocatalytic reactions. Its significance lies not only in elucidating the fundamental laws of molecular dynamics, but also in advancing our understanding of functional regulation in biological systems, atmospheric chemistry, and key reactions in interstellar environments. The requirements to achieve this goal is to establish experimental techniques that combine ultrahigh spatiotemporal resolution with highly sensitive detection of ions and electrons. Meanwhile, complex molecular systems often consist of multiple conformers and clusters, which frequently cause experimental signals to represent ensemble averages, thereby blurring the distinct dynamics of individual species. Therefore, development of experiment providing precisely described molecular ensemble and ability to probe these samples with high spatiotemporal resolution is crucial step towards the understanding the intrinsic nature of complex dynamical processes.

This thesis addresses these challenges with both experimental technique development and molecular system dynamics studies. First, a new experimental setup, an endstation named eCOMO, was successfully constructed, tested, and brought into operation. The system provides a purified molecular beam source integrated with a double-sided VMI spectrometer and high spatiotemporal-resolution Timepix3 cameras. In addition, a novel methodology was developed for precise evaluation of the VMI spectrometer resolution, enabling a systematic analysis of the origins and influencing factors of spatial and temporal resolution under diverse experimental conditions. Then, the apparatus was employed to perform a series of experimental investigations. In the case of OCS molecules, a UV-pump/IR-probe experiment revealed damped oscillation patterns for OCS^+ signal, with clear intensity dependence, thereby revealing a previously unobserved potential predissociation pathway in ultrafast ionization dynamics. Furthermore, using the pyrrole-water cluster samples, a combined soft x-ray-pump/IR-probe scheme enabled site-selective ionization of the nitrogen atom in pyrrole. Multi-channel analysis of the resulting processes revealed charge transfer, proton migration, and fragmentation pathways under solvation conditions, offering deeper insights into water-biomolecule interactions.

In summary, through the integration of instrument development, methodological innovation, and experimental studies on representative molecules and clusters, this thesis reveals and analyzes several novel phenomena related to molecular dynamics and solvation effects. The developed setups and obtained results provide a robust platform and valuable foundation for advancing the realization of the "molecular movie" vision and for future ultrafast dynamical studies in chemistry, biology, and broader interdisciplinary domains.

Zusammenfassung

Das direkte Abbilden chemischer Reaktionen mit atomarer räumlicher Auflösung und zeitlicher Präzision im Femtosekunden- bis Attosekundenbereich stellt ein zentrales, seit Langem verfolgtes Ziel dar, um die fundamentalen Prozesse der molekularen Chemie besser zu verstehen. Die Vision eines "molekularen Films" bildet eine wesentliche Voraussetzung für ein detailliertes Verständnis von Moleküldynamik und Reaktivität während Isomerisierungsprozessen, Bindungsbruch und -neubildung sowie photokatalytischer Reaktionen. Ihre Relevanz erstreckt sich über die Aufklärung grundlegender dynamischer Gesetze hinaus und trägt maßgeblich zum Verständnis funktioneller Regulationsmechanismen in biologischen Systemen, zur Atmosphärenchemie sowie zu zentralen Reaktionspfaden in interstellaren Umgebungen bei. Die Realisierung einer derart umfassenden Abbildung erfordert experimentelle Ansätze mit hoher räumlicher und zeitlicher Auflösung in Kombination mit äußerst empfindlichen Detektionsmethoden für Ionen und Elektronen. Gleichzeitig bestehen viele molekulare Systeme aus mehreren Konformeren oder Clustern, deren Beiträge in herkömmlichen Experimenten meist nur ensemblegemittelt zugänglich sind und somit artspezifische Dynamiken verschleiern können. Die Entwicklung experimenteller Methoden, die sowohl gut definierte molekulare Ensembles bereitstellen als auch deren Untersuchung mit hoher raumzeitlicher Präzision erlauben, ist daher ein entscheidender Schritt zum Verständnis komplexer intrinsischer Dynamiken.

Die vorliegende Dissertation begegnet diesen Herausforderungen durch die Entwicklung neuer experimenteller Techniken sowie durch detaillierte Untersuchungen der Dynamik ausgewählter molekularer Systeme. Zunächst wurde eine neue experimentelle Endstation, bezeichnet als eCOMO, erfolgreich konstruiert, charakterisiert und in den regulären Betrieb überführt. Das System kombiniert eine Molekularstrahlquelle mit einem zweiseitigen VMI-Spektrometer, einem MCP und einer Timepix3 Kamera, wodurch eine hohe räumliche und zeitliche Auflösung erreicht wird. Darüber hinaus wurde eine neuartige Methodik zur quantitativen Bewertung der VMI-Auflösung entwickelt, die eine systematische Analyse der zugrunde liegenden Beiträge und Einflussfaktoren unter variierenden experimentellen Bedingungen ermöglicht. Anschließend kam der Aufbau zur Untersuchung spezifischer Moleküle und Cluster zum Einsatz. Im Fall von OCS-Molekülen zeigte ein UV-Pump/IR-Probe-Experiment gedämpfte Schwingungen im OCS^+-Signal mit ausgeprägter Intensitätsabhängigkeit und zeigte damit einen bislang unbeobachteten potenziellen Prädissoziationskanal in der ultraschnellen Ionisationsdynamik. Zudem ermöglichte die Studie an Pyrrole-Wasser-Clustern mittels eines kombinierten Soft-X-ray-Pump/IR-Probe-Schemas eine selektive Ionisation des Stickstoffatoms im Pyrrole. Die Analyse der Folgedynamik zeigte Ladungsübertragungsprozesse, Protonentransfer sowie charakteristische Fragmentierungspfade unter Solvatisierungsbedingungen auf und liefert somit neue Einblicke in die Wechselwirkungen zwischen Wasser und Biomolekülen.

Zusammenfassend werden in dieser Arbeit durch die Verbindung instrumenteller

Weiterentwicklungen, methodischer Innovationen und exemplarischer experimenteller Studien mehrere bislang unbekannte Phänomene der Moleküldynamik und Solvatation aufgezeigt und analysiert. Die entwickelten experimentellen Plattformen sowie die gewonnenen Ergebnisse bilden eine robuste Grundlage für die weitere Annäherung an die Vision eines "molekularen Films" und eröffnen vielfältige Perspektiven für zukünftige ultraschnelle dynamische Untersuchungen in der Chemie, Biologie und angrenzenden interdisziplinären Forschungsbereichen.

Contents

1. Introduction

1.1. Motivation

Elucidating molecular structures and imaging photochemical processes, such as isomerization, catalytic reactions, protein folding and damage, and chemical bond dynamics, on the natural timescale of atomic motion has long been one of the most compelling goals in physical chemistry [1–5]. The significance of this pursuit lies not only in uncovering the fundamental principles of molecular dynamics but also in its broad relevance to understanding key reactions in biological systems, atmospheric phenomena, and interstellar environments [4, 6, 7]. Achieving this goal imposes stringent demands on experimental methodologies: ultrafast temporal resolution on the picosecond to attosecond scale must be combined with spatial sensitive structural probes [8–10]. To truly "captur" molecular snapshots, such techniques must resolve both the instantaneous kinetic information of atomic nuclei and the electron and simultaneously tracing nuclear and electronic motion. This real-time dissection of molecular motion is often evocatively described as a "molecular movie", akin to a film reel in which each frame reveals a decisive step in structural evolution.

The central focus of this thesis lies in chemical reaction dynamics, with particular emphasis on the interactions of atoms and molecules in the gas phase under the influence of intense laser fields. Broadly situated within the domain of atomic, molecular, and optical (AMO) physics, the primary objective is to probe the dynamical behavior of neutral atoms and molecules driven by laser pulses. As an inherently interdisciplinary field, AMO not only examines the composition, structure, and properties of matter but also tries to describe the mechanisms of intermolecular interactions [11–13]. Through the combined application of theoretical frameworks and experimental techniques, it aims to unravel the electronic structures of atoms and molecules, thereby deepening our understanding of the fundamental properties of matter and the processes governing chemical reactivity [4, 7, 14].

Over the past decades, the advancement of synchrotron and x-ray free-electron laser (XFEL) facilities has propelled the frontiers of molecular science and chemical physics. Representative large-scale installations include FLASH at DESY, the Linac Coherent Light Source (LCLS), the free-electron laser radiation for multidisciplinary investigations (FERMI), the SPring-8 Angstrom Compact free-electron Laser (SACLA), SwissFEL at the Paul Scherrer Institute, the European XFEL (EuXFEL), and the Shanghai Soft x-ray Free Electron Laser (SXFEL) [15, 15–22]. Owing to their brightness, ultrafast temporal resolution, and high coherence, these sources have not only enabled breakthrough discoveries in fundamental science but also greatly expanded the experimental landscape, opening new avenues to address previously inaccessible scientific questions [23–25]. In parallel, the increasing diversity of user-driven experimental requirements has posed new challenges for instrument design and implementation.

Velocity map imaging (VMI) [26] is a powerful high-resolution technique for probing molecular dynamics. By detecting the velocity distributions of ionic or electronic

fragments, VMI provides direct insight into the atomic-scale details of molecular transformations, revealing the mechanisms of bond formation and dissociation [27]. The subsequent molecular dynamics, whether induced by photon-driven photodissociation or by collisions with other molecules in scattering experiments [28], are encoded in the kinematic distributions of the detected fragments. These fragments exhibit well-defined, strictly constrained velocity distributions forming concentric spherical shells, commonly referred to as Newton spheres [29]. Through a carefully designed electrostatic lens system, the three-dimensional velocity distribution of charged particles is projected onto a position-sensitive two-dimensional detector in a manner that is largely independent of their initial ionization position. More specifically, the in-plane velocity components of the Newton sphere are mapped onto the same point on the detector [26]. VMI has been widely implemented at major research facilities and has yielded numerous high-resolution characterizations across a variety of experimental systems [30–40]. However, discussions concerning the methodology of VMI resolution remain ongoing, particularly regarding how resolution varies systematically under different experimental conditions and molecular systems. Many studies have sought to identify and theoretically derive the factors influencing resolution [30, 40–43]. These theoretical treatments often rely on simplified models with limited generality and practical applicability. Developing methodologies capable of quantitatively assessing the attainable resolution under specific experimental conditions is therefore essential for advancing both the precision and interpretability of VMI-based measurements.

1.2. Preparation of cold molecular beam of clusters

In chemistry textbooks, molecular structure is commonly defined in terms of atomic coordinates and bond orders, and visualized through representations such as ball-and-stick models or Lewis structures [44, 45]. In biology, an analogous structure-function relationship is equally crucial; for instance, the biological activity of a protein is often dictated by its specific folding pattern [46, 47]. In other words, structure determines function, and this structure fundamentally arises from the spatial distributions of electronic wavefunctions and nuclear distribution. Ultimately, the function itself emerges from the dynamical processes of these distributions.

In complex molecular systems, however, a single molecular formula often corresponds to multiple conformational isomers. Owing to differences in spatial geometry, these isomers exhibit markedly distinct physical and chemical properties when interacting with laser fields. Classic examples include enantiomers of chiral molecules, cis-trans and ortho-para isomers [48–50], all of which vividly illustrate the impact of structural variation on functional behavior. This subtle yet intricate structure-function coupling is particularly pronounced in biomolecules and molecular clusters. Under typical experimental conditions, conformational isomers can interconvert, resulting in samples that are inherently mixtures of multiple conformers [45, 51, 52]. In experiments driven by laser fields, the absence of molecular selectivity often leads to observed signals that represent incoherent superpositions of contributions from different conformers. To accurately characterize the properties of a single conformer, it is therefore essential to develop a technique to obtain highly purified, species-selective samples [45, 53, 54].

The presence of water is indispensable for the persistence of carbon-based life on Earth [55, 56]. As a fundamental component of the earth environment, water not only

provided the primordial platform for the emergence of life, but also serves as a critical medium driving biological evolution and the development of molecular complexity [55–57]. Owing to its role as the "universal solvent", water effectively dissolves ions and furnishes a flexible, dynamic reaction environment for the formation of essential biomolecular units such as amino acids and peptides [58–60]. Water constitutes nearly 70% of the cellular content, thereby exerting both structural and dynamical functions at molecular and cellular levels [61–63].

Within aqueous environments, hydrogen-bond networks are crucial for protein assembly, stability, and functional regulation [64, 65]. Interactions between solute and solvent are primarily mediated through van der Waals forces, electrostatics, and hydrogen bonding, all of which are significantly reinforced by solvent effects driven by water molecules [55, 56, 62]. Because hydrogen bonds in water are constantly breaking and reforming [62, 63], solvation processes not only determine the structural and functional organization of complex biological systems [66, 67], but also impart a highly dynamic character to molecular reaction [68–73].

This dynamic complexity often blurs the underlying mechanisms of interest: solvents may form stable complexes with reactants or products, thereby reshaping the energetic landscape of the reaction coordinate; simultaneously, rotational and vibrational modes of reactants may couple with solvent shells, adding further intricacy to mechanistic interpretation [74]. Water clusters exemplify this challenge: under solvated conditions, water commonly exists as dimers, trimers, or higher-order aggregates. The coexistence of these multiple cluster species results in experimental observables that represent superimposed contributions from several clusters, thereby complicating the interpretation of the measured data. Consequently, the distinctive reactivity of individual clusters is frequently masked. To resolve the physical and chemical properties of a single cluster, the generation of highly purified and species-selective cluster samples is a prerequisite [6, 7]. The microsolvation effect is challenging to study due to the inherent mix of the produced gas-phase aggregates [7, 62, 63, 75].

The development of experimental techniques capable of preparing and probing such highly specific molecular ensembles has thus emerged as a central frontier in molecular science. Gaining deeper insight into the structures, physicochemical properties, interconversion mechanisms, and environmental interactions of conformational isomers is of critical importance for unraveling the dynamics of complex molecular processes. At the same time, the molecular beam technique, as the method for probing gas-phase molecules and chemical processes, has a development history spanning more than a century and plays a pivotal role in elucidating the fundamental physicochemical properties of small molecules and enabling their precise manipulation [76–78]. The cold and highly purified gas-phase molecular beams have gradually emerged as ideal tools for exploring molecular dynamics, particularly within the domain of AMO. Correspondingly, the development of scalable and versatile endstation instrumentation tailored to the diverse requirements of multiple beamline facilities has become a central challenge at the interface of research and technology in this field [54, 79, 80].

1.3. Time-resolved photophysics dynamics

Imaging the quantum-mechanical properties of ultrafast photochemical reactions with decent spatiotemporal resolution has long stood at the forefront of contemporary

physical chemistry and molecular science [8, 81]. The advent of strong-field physics, driven by the generation and application of ultrashort laser pulses, has rendered the capture of such ultrafast dynamics feasible [82–84]. In particular, the rise of attosecond technology, through the production of sub-femtosecond laser pulses, has enabled real-time observation and control of electron dynamics [85, 86]. The application of attosecond pulses has not only deepened our understanding of fundamental processes such as Auger decay, autoionization, and photoionization, but has also allowed these phenomena to be directly observed on their corresponding timescales [19, 48, 87]. Experimentally, pump-probe techniques [88] have become the cornerstone of ultrafast spectroscopy. By employing pump and probe pulses, this method records the time evolution of physical observables: the pump pulse initiates the dynamics, while the probe pulse, with adjustable delay, captures transient changes. In the realm of attosecond physics, this technique imposes stringent requirements on pulse duration: true temporal resolution can only be achieved if the probe pulse is shorter than the process under investigation.

A representative case study is the time-resolved investigation of the ultraviolet photodissociation dynamics of carbonyl sulfide (OCS) molecules. OCS serves as a key benchmark system for investigating photodissociation dynamics. As an important natural source of sulfur in the atmosphere [89], OCS, as an asymmetric triatomic molecule, exhibits pronounced differences between the oxygen and sulfur atoms. These distinctions facilitate clear separation of symmetric and antisymmetric stretching vibrations, making OCS an ideal model system for studying molecular dynamics [90]. In an earlier work [91], OCS molecules were utilized to carry out the first time-resolved experimental insight into the transient electronic and fragments structures along the dissociation pathway, laying groundwork for representing molecular dissociation processes. However, owing to limitations in both temporal resolution and theoretical modeling, the rapid oscillations observed in CO^+ and S^+ fragments as the function of time delay experimentally lacked a definitive physical explanation. Refined investigations of the photodissociation of OCS, aimed at uncovering the physical mechanisms underlying the fast oscillations unresolved in previous experiments and thereby advancing the quantum-mechanical understanding of ultrafast molecular dynamics, are necessary.

The interactions between water and biomolecules are fundamental to life, as they directly govern a wide range of essential biological processes and phenomena. In particular, under the influence of high-energy ionizing radiation, the aqueous environment plays a decisive role in radiotherapy, cellular damage, radiation-induced effects, genetic mutations, self-repair, and even programmed cell death [57, 61, 62, 65, 92–102]. During such processes, water radiolysis generates reactive species including ions, radicals, and solvated electrons [103–105], which can further damage biomolecules through excitation or ionization pathways [99, 101, 102]. To disentangle the intrinsic differences between isolated and hydrated molecules in their photophysical behavior, gas-phase microsolvated biomolecular model systems have become state of the art research targets [45]. A prototypical example is the hydrogen-bonded complex of a biomolecular chromophore with a single water molecule, which provides a good testbed to probe the influence of hydration on molecular photophysics. The pyrrole-water dimer, where the water molecule forms a hydrogen bond at the N-H site of pyrrole [106], is such a good candidate. The pyrrole ring constitutes a fundamental building block of a variety of biologically important molecules, including tryptophan, vitamin B12, chlorophyll, and hemoglobin [107–109], and its photophysical properties

are sensitive to local hydration [61], making it a decent probe of water-biomolecule interactions [4, 15, 110, 111].

1.4. Outline of this thesis

The principal contributions of this thesis encompass two major aspects. First, the successful construction, commissioning, and characterization of a new experimental setup to be used as a endstation, together with the development of a novel methodology to characterize the resolution of a VMI spectrometer integrated into the platform. Second, the systematic investigation of the dynamics of strong-field-ionization imaging of molecules, using this new endstation and similar experimental setups.

The thesis is structured as follows: In Chapter 2, the fundamental concepts are introduced, including the technical details and underlying physical principles of the methods employed in this thesis. In Chapter 3, I present the technical details and parameters of the newly constructed endstation, with setup and commissioning data employed to characterize its overall performance. In Chapter 4, we analyze and characterize the origins and contributing factors of resolution in various dimensions of the VMI. We propose a new methodology to evaluate the VMI resolution under diverse experimental conditions. In Chapter 5, we investigate the strong-field ionization dynamics of OCS molecules in a UV-pump/IR-probe experiment. The results are discussed in detail, with particular emphasis on the laser intensity dependent damped oscillation motion patterns. In Chapter 6, we describe an experiment on the pyrrole-water clusters where near-infrared (NIR) excitation was followed by soft x-ray site-specific core-level ionization of the nitrogen atom from pyrrole. The subsequent photophysical properties were investigated through multi-channel analysis and characterization of the fragmentation. Finally, Chapter 7 summarizes the research presented in this thesis and offers an outlook on ongoing and prospective studies aimed at extending the work presented in this thesis.

2. Fundamental concepts

This chapter provides an overview of the fundamental concepts necessary to understand the experimental approaches and theoretical frameworks applied and developed in the investigation of molecular systems presented in this thesis. The discussion traces the sequential evolution of the target molecular beam, starting from its generation and purification, continuing with the physical mechanisms governing its interaction and ultrafast dynamics with the laser field, concepts of pump-probe experiments, and concluding with the final detection stage. Additional details on the concepts discussed in this chapter are available on standard textbooks [44, 112–116].

2.1. Generation of clusters and molecular beam

Within the framework of thermodynamics, the thermal motion of gas molecules is inherently continuous and random, and at the quantum level, it manifests in the population of discrete vibrational and rotational energy levels [117]. This results in a broad momentum distribution for particles at a given temperature and relative higher internal rotational and vibrational degrees of freedom. In this thesis, we introduce the supersonic molecular beam technique [113, 118, 119], which enable us to prepare the internally cold and isolated gas-phase molecules. Moreover, we extend this technique by application of the electrostatic deflector that provides us with a well-defined ensembles of selected particles.

The working principle of supersonic molecular beam relies on an isentropic adiabatic expansion process [44]. When gas expands from a high-pressure environment (0.1 - 100 bar) into a low-pressure (vacuum) region through a small orifice, inelastic collisions between the target molecules and the carrier gas effectively cool the internal degrees of freedom, namely rotational and vibrational modes [119–124]. In addition, adiabatic expansion converts transverse velocity components into longitudinal translational energy through intermolecular collisions, thereby producing a fast and relatively collimated molecular beam, i. e., the expanded beam exhibits a narrow angular divergence and a well-defined velocity distribution [123]. The mean translational velocity is influenced by the stagnation pressure and the properties of the carrier gas, while the velocity spread determines the translational temperature, which is typically a few kelvin [123]. Under such conditions, the rotational temperature of the molecules also reaches only a few kelvin, whereas the vibrational temperature remains significantly higher, on the order of tens of kelvin [119, 125]. The efficiency of the cooling process strongly depends on the specific type of molecules or clusters. Subsequently, the combination with a skimmer enables beam collimation, generating a well-defined molecular beam.

The role of low-energy collisions in supersonic expansions is of concern for achieving efficient cluster formation [122]. For instance in biomolecular clusters with water, the binding energies of hydrogen-bonded clusters are typically on the order of several hundred meV [124, 126]. Consequently, the formation of stable clusters requires low-energy three-body collisions, in which a third body carries away excess kinetic energy,

thereby stabilizing the cluster [112]. Under equilibrium conditions, the number of hydrogen-bonded complexes formed in a conventional gas reservoir remains relatively low, as the high internal energy of the molecules does not favor low energy collisions necessary for clustering. In contrast, during supersonic gas expansion, adiabatic cooling drastically lowers the gas temperature, and promotes cluster formation. Furthermore, the conditions for cluster formation can be controlled by adjusting the nozzle size, carrier gas, pre-cooling, and stagnation parameters (i. e., pressure and temperature) [44, 118, 124, 127].

Molecular beam technique have been widely applied in gas-phase studies of ultrafast ionization and dissociation dynamics in physical chemistry, as well as in molecular structure measurements in molecular physics [112–114, 128]. In this thesis, we employ the supersonic molecular beam technique in our apparatus [54, 79]. The experimental setup presented here has been applied to a variety of cluster systems, including water dimers [36], pyrrole–water clusters [54], and uracil–water clusters. The pulsed valves primarily used in this setup include the Even–Lavie valves [120, 121] and the Amsterdam Piezovalve [129]. The generation of internally cold molecular beams enables us to further employ the DC-Stark effect for the spatial separation of species-selected conformers [45].

2.2. Species selection and separation with the electrostatic deflector

In this section, we introduce how the electrostatic deflector, based on the DC-Stark effect [130], is employed to manipulate the trajectories of different molecules within the cold molecular beams described in the previous section, ultimately achieving spatial separation of not only conformers, but also clusters, etc. We begin by presenting the Stark effect and explaining how the rotational eigenstates of the molecules are modified in the presence of an external electric field. Finally, we describe the methodology for species selection using the electrostatic deflector. In this thesis, we employ the *b*-type electrostatic deflector [54, 79]. For further details on deflectors and calculations, please see [45, 131, 132].

2.2.1. Motion of polar molecules in static electric fields

Polar molecules, in which the centers of positive and negative charges are partially separated within the molecular framework, possess a permanent electric dipole moment [133]. The interaction between this dipole moment and an external electric field leads to an energy shift and hybridization of the wave-function [130]. This phenomenon is referred to as the Stark effect. The resulting shifting Stark energy is expressed in [45] as:

$$W = -\vec{\mu} \cdot \vec{\epsilon} = -\mu\epsilon \langle \cos\theta \rangle = -\mu_{\text{eff}}\epsilon. \tag{2.1}$$

Here, $\vec{\mu}$ denotes the permanent dipole moment, $\vec{\epsilon}$ represents the external electric field, and θ is the angle between their respective directions. The angular probability distribution and the corresponding expectation values $\langle \cos\theta \rangle$ are determined by the superposition of the molecular rotational wavefunctions [134]. Consequently, the effective dipole moment μ_{eff} along the field axis depends on both the quantum state and the strength of the electric field.

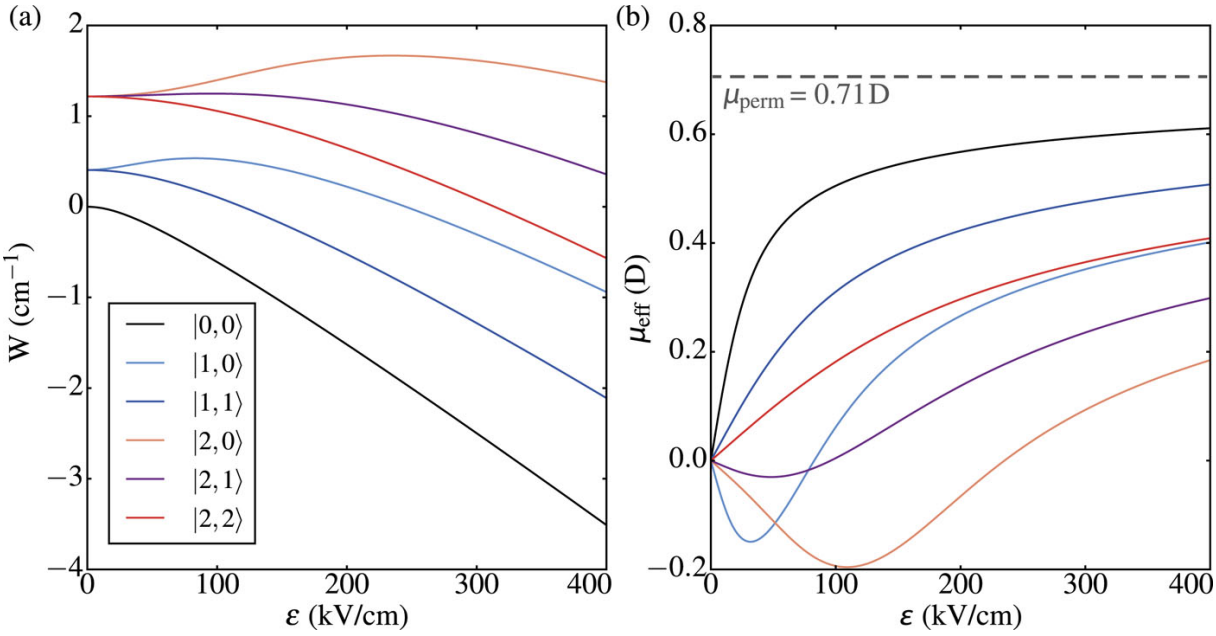

Figure 2.1.: (a) Stark energies (W) of the lowest-energy states of OCS in a static electric field for selected $|J, M\rangle$. (b) the corresponding effective dipole moments (μ_{eff}). The gray line depicts the strong-field limit of the permanent dipole moment. All data was calculated using CMIstark [131]. The image and calculation is taken from [132].

In field-free space, the different projections M of the angular momentum onto the laboratory axis are degenerate, and the sum over all M yields $\langle\cos\theta\rangle = 0$, indicating that the molecule has no space-fixed dipole moment [131]. The application of an external electric field lifts this degeneracy via the Stark effect and induces mixing of the rotational wavefunctions, resulting in $\langle\cos\theta\rangle \neq 0$. The system's energy becomes dependent on the external electric field strength. As a result, molecules experience a force in an inhomogeneous electric field [131].

To describe this theoretically at the quantum level, we separate the electronic and nuclear motions, as well as the rotational and vibrational motions, using the Born–Oppenheimer approximation together with the Eckart conditions [134–136]. For rigid, closed-shell molecules subjected to moderately strong electric fields, the Stark interaction can be treated exclusively within the rotational degrees of freedom [134]. The rotational wavefunctions serve as the bridge between the molecular and laboratory frames, linking the molecule-fixed permanent dipole moment $\vec{\mu}$ with the laboratory-frame effective dipole moment μ_{eff} [45]. Within this framework, the Hamiltonian for a polar molecule in an external field can be expressed as:

$$\mathbf{H} = \mathbf{H}_{\text{rot}} + \mathbf{H}_{\text{Stark}} = \mathbf{H}_{\text{rot}} - \vec{\mu} \cdot \vec{\epsilon} \tag{2.2}$$

where $\mathbf{H}_{\text{rot}}$ represents the field-free rotational Hamiltonian, and the second term denotes the Stark interaction. The effective dipole moment function is defined from (2.1) as:

$$\mu_{\text{eff}}(\epsilon) = -\frac{\partial W}{\partial \epsilon} \tag{2.3}$$

In Fig. 2.1 a, the Stark energy (W) is shown as a function of the electric field strength for the rotational states $J = 0 - 2$ of the molecule OCS. Among these, the lowest rotational state exhibits the most pronounced decrease in Stark energy as the electric field strength

increases. In Fig. 2.1 b, the corresponding effective dipole moment is presented, which can take either positive or negative values.Consequently, depending on the specific quantum state, the molecule can orient or anti-orient its dipole moment with respect to the electric field. According to the sign of the effective dipole moment, molecules in these states are either attracted toward regions of stronger field intensity (strong-field seeking states, positive values) or repelled toward weaker field regions (weak-field seeking states, negative values).

2.2.2. Electrostatic deflector

Since the Stark energy (W) depends on the electric field strength, and by applying the principle of minimal energy, molecules experience a force in an inhomogeneous electric field. Specifically, the force $\vec{F}$ acting on a molecule is given by the negative gradient of the Stark energy:

$$\vec{F} = -\vec{\nabla}W = \mu_{\text{eff}} \cdot \vec{\nabla}\epsilon \tag{2.4}$$

Here, $\vec{\nabla}\epsilon$ is the gradient of the electric field. Electrostatic deflectors employ forces arising from a molecule's effective dipole moment, which varies with its quantum state, to spatially separate molecular beams. Ideally, such a deflector would generate a constant deflection force in one direction while exerting zero force in the perpendicular direction. Maxwell's equations, however, forbid the realization of a true static field with this property. In practice, this configuration is approximated using a two-wire field [113] which creates a strong inhomogeneous electric gradient along one axis and negligible field variation along the orthogonal axis.

To generate an inhomogeneous electric field that exerts optimal forces for manipulating transverse motion, various electrode geometries have been devised. Fig. 2.2 illustrates two prototypical deflection field configurations, both based on the "two-wire" field concept [113].

Although the electrode shapes and electric potentials differ between the two designs, both geometries generate a strong field gradient along one axis (horizontal in Fig. 2.2) and remain nearly uniform along the perpendicular axis (vertical in Fig. 2.2) within the region suitable for molecular beam deflection.

As the species traverse this inhomogeneous electric field, they acquire different transverse velocities which is proportional to their effective-dipole-moment-to-mass ratios: μ_{eff}/m, hence enabling lateral spatial separation. Specifically, the deflector acts as a prism, dispersing molecular trajectories according to this ratio. Species with the highest μ_{eff}/m ratio undergo the greatest deflection and may be fully isolated from the molecular beam. This principle also enables the purification of a polar conformer in a mixture of different structural isomers [49]. The conformer exhibiting the maximum (minimum) ratio among all conformers is deflected most (least) strongly and can therefore be selectively separated and isolated [50]. Electrostatic deflectors have been successfully used for quantum-state selection [138], nuclear-spin isomers [50, 139, 140], conformers [49, 141, 142], and molecular clusters [36, 143–145].

To obtain particle ensembles consisting of only a small subset of quantum states, an effective approach is to employ an initially cold molecular beam, which suppresses internal (non-rigid) motions such as vibrations and rotations [143, 146]. As a result, only the lowest-energy rotational and vibrational states are significantly populated. These low-lying states carry minimal angular momentum and exhibit the largest effective

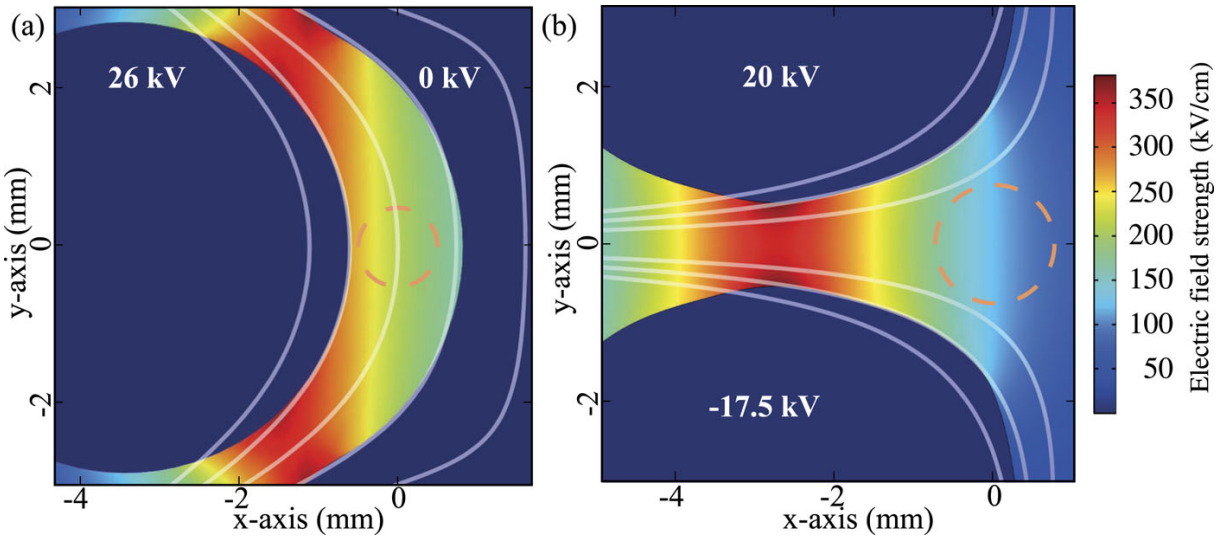

Figure 2.2.: Shape and electric field distributions of the (left) a-type and (right) b-type deflector geometries. The numerically calculated electric field strengths for the actual electrode configurations are represented by color coding, while the white lines indicate equipotential lines according to a_i/b_i coefficients for ϕ/ϕ_0 [137]. The dashed orange circles denote the positions and sizes of the molecular beam, marking the location of the incoming molecular beam pulse. In both geometries, molecules in strong-field-seeking states are deflected toward the left. The image is taken from [132].

dipole moments, μ_{eff}, among the populated states. Consequently, they display strong Stark interactions and respond most effectively to the applied electric field.

2.3. Molecules in ionizing fields

The purified molecular beam then interacts with the laser. In this thesis, the light-matter interaction primarily involves the ionization of molecules. The underlying ionization mechanisms strongly depend on multiple factors, such as the ionization energy, the electric field strength and the frequency of the external light field [34, 84]. Here, we focus on two specific cases: strong-field ionization and site-specific x-ray ionization.

2.3.1. Strong-field ionization

In the context of ionization, fields are termed strong when the strength of the external light field becomes comparable to the internal fields of matter and can no longer be treated as a small perturbation. Within this regime, the interaction of atoms and molecules with intense laser fields can be divided into three principal mechanisms: perturbative regime (10^{10}–10^{12} W/cm^2), Coulomb regime (10^{12}–10^{17} W/cm^2), and relativistic regime ($> 10^{17}$ W/cm^2) [147–149]. In the perturbative regime, the electric field strength of the laser is far weaker than the Coulomb field binding the electrons to the nucleus. Under these conditions, phenomena such as resonance between bound states and multi-photon ionization can occur, and higher-order perturbation theory remains valid [148]. As the intensity increases and the laser field strength approaches or exceeds the internal Coulomb field experienced by bound electrons, additional phenomenons can take place, marking a transition from multi-photon ionization towards tunneling ionization and

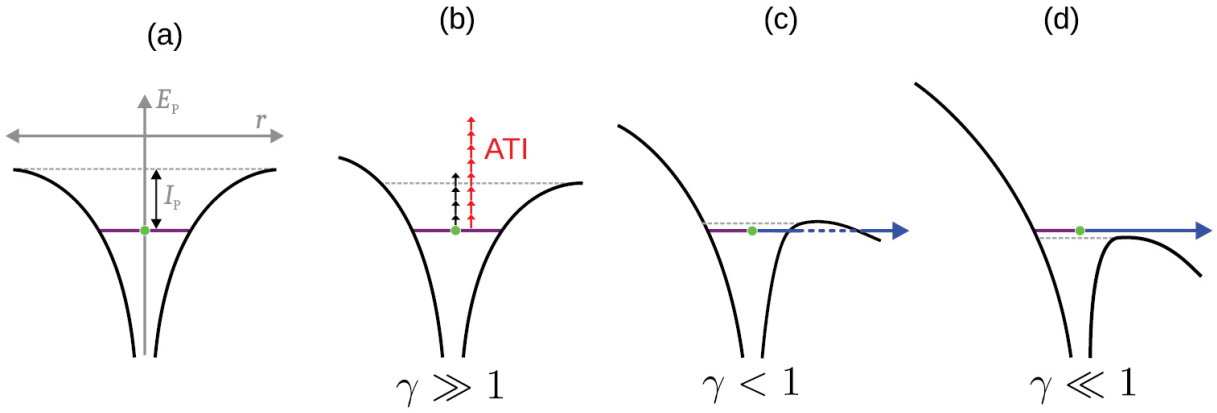

Figure 2.3.: The atomic Coulomb potentials under the influence of intense laser fields are shown for the (a) field free; (b) multi-photon ionization; (c) tunnel ionization, and (d) over-the-barrier ionization cases. Above-threshold ionization (ATI) is also presented (red vertical arrows) as compared to multi-photon ionization (black vertical arrows) in (b). Here, I_p is the ionization potential, and γ is the Keldysh parameter. Figure adapted from [151].

eventually to over-the-barrier ionization [149]. At higher intensities, the relativistic regime can occur. Here, valence electron ionization becomes progressively suppressed, and additional processes can occur such as inner-shell excitation and ionization, x-ray emission, and even nuclear excitation and reactions [150]. The work presented in this thesis primarily focuses on the perturbative and Coulomb regimes.

Fig. 2.3 illustrates light-induced ionization mechanisms in atoms. Keldysh was the first to classify atomic ionization in static electric fields using an adiabatic parameter(γ) [152–154], defined as [152]:

$$\gamma = \sqrt{\frac{I_p}{2U_p}} \tag{2.5}$$

Here, I_p denotes the ionization potential energy and U_p denotes the ponderomotive energy. In a laser field, in addition to translational motion, electrons undergo rapid oscillatory motion driven by the high-frequency electric field, often referred to as quiver motion. The ponderomotive energy means the cycle-averaged kinetic energy associated with this oscillation[155].

When $\gamma \gg 1$, as shown in Fig. 2.3 b, multi-photon ionization dominates. In this regime, multiple photons are absorbed simultaneously to overcome the ionization potential barrier [116, 148, 156], and the interaction between the laser field and the atom can be effectively treated using low-order perturbation theory. According to perturbation theory, the ionization probability w as the function of the laser intensity I as follows [148]:

$$w_n = \sigma_n I^n. \tag{2.6}$$

Here, σ_n represents the corresponding absorption cross section for the electronic transition and n denotes the number of photons. It is evident that multi-photon ionization exhibits pronounced nonlinear characteristics. When the number of absorbed photons exceeds the minimum required for ionization, an above-threshold ionization (ATI) process occurs [157]. In this case, the excess photons are absorbed by the released electron [156–158], resulting in the appearance of equally spaced ATI peaks in the photoelectron kinetic energy spectrum, with adjacent peaks separated by the energy of

a single photon. In addition to simple multi-photon ionization, resonance-enhanced multi-photon ionization (REMPI) typically involves a resonant single or multiple photon absorption to an electronically excited intermediate state followed by another photon which ionizes molecules. This technique is also widely employed to achieve quantum-state-specific ionization [159].

When $\gamma < 1$, as illustrated in Fig. 2.3 c, the potential energy of the laser electric field becomes comparable to the atomic binding potential and can no longer be neglected. The superposition of these two potentials leads to an asymmetric distortion of the atomic potential, lowering the barrier on one side. The electron can then quantum mechanically tunnel through this suppressed barrier into the continuum, resulting in ionization via the tunneling mechanism [149, 160]. After tunneling through the laser-field-suppressed barrier into the continuum, this free electron is subject to the oscillating laser electric field, undergoing successive acceleration, deceleration, and reacceleration. In some cases, the electron can be driven back to the parent ion and undergo recollision. This so-called three-step model [156] provides the theoretical foundation for explaining key phenomena in strong-field physics, including high-harmonic generation, non-sequential double ionization, and high-energy above-threshold ionization [161, 162].

As the laser intensity increases, the distorted potential barrier becomes progressively lower and narrower, thereby enhancing the probability of tunneling ionization. At sufficiently high field strengths, the molecular binding potential is severely distorted, and the electron escapes directly into the continuum. This process is referred to as over-the-barrier ionization [163], as depicted in Fig. 2.3 d.

Theoretical models describing the tunneling ionization process and the ionization rates of atomic-like systems are provided by the Ammosov, Delone and Krainov (ADK) model [164] and the Keldysh, Faisal and Reiss (KFR) theory [116, 152, 165], both commonly referred to as the strong-field approximation (SFA). The ADK model was later extended to incorporate molecular ionization effects, leading to the development of the MO-ADK (molecular ADK) model [166], which accounts for the symmetry and asymptotic behavior of molecular electronic wavefunctions. This framework also provides the necessary molecular-specific parameters for theoretical calculations [153].

The experiments presented in this thesis are conducted in the regime where $\gamma \approx 1$, in which neither the pure tunneling mechanism nor the pure multi-photon ionization mechanism fully applies. Considering the spatial focusing characteristics of the laser beam, the intensity distribution within the focal volume further adds complexity to the interaction. In summary, this intermediate regime is referred to as nonadiabatic ionization [116, 149], where the ionization process exhibits a hybrid character that combines features of both mechanisms.

The interaction of molecules with intense laser fields is not limited to single ionization but can also induce multiple ionization phenomena. For instance, charge resonance enhanced ionization (CREI) [167] occurs when laser-induced nuclear vibrations lead to variations in the internuclear separation. As the nuclei move toward a critical distance, the molecular ionization rate increases sharply, resulting in multiple ionization [167–170]. Multiple ionization can further lead to Coulomb explosion, a distinct molecular dissociation phenomenon. In this scenario, the Coulomb repulsion between the positively charged atomic cores increases dramatically, causing the molecule to rapidly fragment into multiple high-energy ionic fragments [171–173]. These processes are directly relevant in this thesis for analyzing the origins of detected particle fragments.

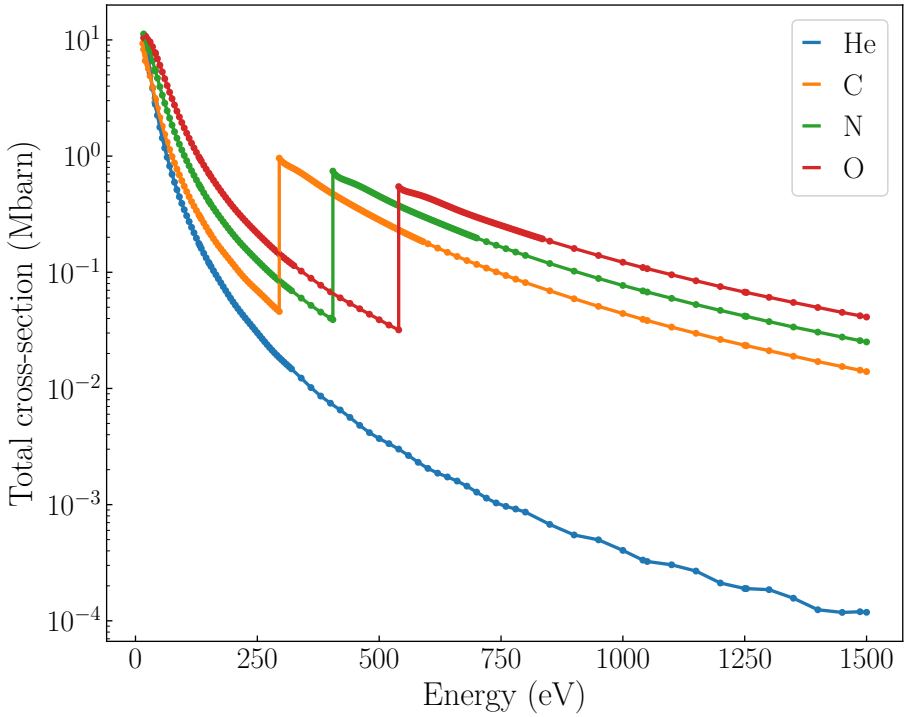

Figure 2.4.: x-ray absorption edges of He, C, N, and O atoms. A rapid increase in absorption occurs at the energy thresholds required to excite electrons from the inner 1s shells. The sharp absorption edges correspond to photon energies of approximately 284 eV for carbon, 401 eV for nitrogen, and 532 eV for oxygen. Helium is included as a reference, and the data are taken from [177].

2.3.2. Site-specific soft x-ray ionization

As a special case of single-photon ionization, the use of soft x-rays enables site-specific core-shell ionization of molecules, allowing highly localized and precise manipulation of molecular targets. The total x-ray absorption cross-section of an atom is determined by its electronic structure and the photon energy [174]. The general trend is that the total absorption cross-section approximately scales as Z^4, where Z is the atomic number [115]. As a function of photon energy, the absorption cross-section typically follows a smoothly decreasing function that is proportional to E^{-3}, where E is the photon energy [175]. For a given atom, the cross section decreases with increasing photon energy, except at the absorption edges [176], where the photon energy matches the binding energy of a core-shell (or valence-shell) electron and the absorption spectrum exhibits a sharp increase. This enhancement arises from the opening of a new absorption channel, in which the entire photon energy is used to overcome the ionization potential, resulting in core-shell (or valence-shell) ionization, where an electron is directly ejected from this unique shell into the continuum.

Fig. 2.4 shows the calculated total x-ray absorption cross sections for He, C, N, and O atoms, with the corresponding absorption edges indicating the ionization potentials of the 1s orbitals [177]. By selecting specific photon energies, for instance, 495 eV as employed in this thesis for the study of pyrrole-water clusters, the atomic absorption cross-sections of nitrogen and carbon exhibit a ratio of approximately 5:3 under these conditions. At this energy, the absorption cross-sections of nitrogen and carbon are significantly larger than that of oxygen. Owing to the strong element-specific dependence

of the x-ray absorption cross-section, tuning the photon energy thus provides an effective means for achieving localized ionization within a molecule [174].

Following x-ray ionization, the resulting core-ionized species are unstable and can undergo various relaxation processes. One such radiative relaxation process is fluorescence [176, 178], in which the vacancy in the inner shell is filled by an outer-shell electron, accompanied by the emission of a photon. Alternatively, the transition energy of an outer-shell electron filling the core vacancy can be transferred via Coulomb interaction to another electron, leading to its ejection as a non-radiative relaxation process is so called the Auger decay process [179, 180]. Beyond intramolecular relaxation, energy can also be transferred to a neighboring atom or molecule. In interatomic (or intermolecular) Coulombic decay (ICD) [181–183], the excess energy is released through the emission of a low-energy electron from a nearby site. In hydrogen-bonded systems, this energy can be transferred in the form of a proton along a hydrogen-bonding pathway, resulting in proton-transfer-mediated charge separation (PTMCS) [184–186]. Similarly, the vacancy may be filled through electron transfer from a neighboring particle, with the excess energy released by emitting an electron in the electron-transfer-mediated decay (ETMD) process [6, 182, 184].

These ultrafast dynamical processes are imprinted in momentum distribution, etc [22]. Therefore, we infer the complex reaction dynamics by measuring, e. g., the momentum and kinetic energy distributions, as well as other characteristic properties of the resulting ionic and electronic fragments. Through detailed analysis of these distributions, the underlying energy levels and geometric configurations can be deduced, enabling the reconstruction of the complete chemical dynamics [6, 187].

2.4. Concept of pump-probe experiment

Pump-probe spectroscopy based on ultrafast lasers is a powerful technique for investigating molecular ultrafast dynamics [188, 189]. It enables access to phenomena occurring on picosecond and even femtosecond timescales. The basic principle is as follows: the sample is first excited by a pump pulse, which excited the system into an unstable quantum state (or induces other modification). After a controllable temporal delay, a probe pulse is applied to further promote the excited state into a final state suitable for measurement. By monitoring the probe signal as a function of the pump–probe delay, one can obtain information on relaxation pathways of the excited states, or on other dynamical processes triggered by the pump pulse.

In most implementations, the pump and probe pulses originate from a common source, e. g. a mode-locked laser combined with a beam splitter, and their relative delay is controlled via an optical delay line. Variations in the delay are directly inferred from changes in path length of the delay line. By scanning the pump-probe delay, one can directly track the temporal evolution of quantum-state populations in real time.

A variety of detection schemes have been developed to study physical and chemical processes, employing photons ranging from the mid-infrared to the x-ray regime, or even electron pulses [190–192]. The studied processes span many dynamical phenomena of interest, including coherent vibrational excitation, ultrafast relaxation in electronic states, and dissociation dynamics driven by Coulomb explosion [7, 87, 104, 193, 194]. In Chapter 5 and Chapter 6, pump-probe techniques are employed to investigate the vibrational relaxation of ionized molecular states and the molecular dissociation

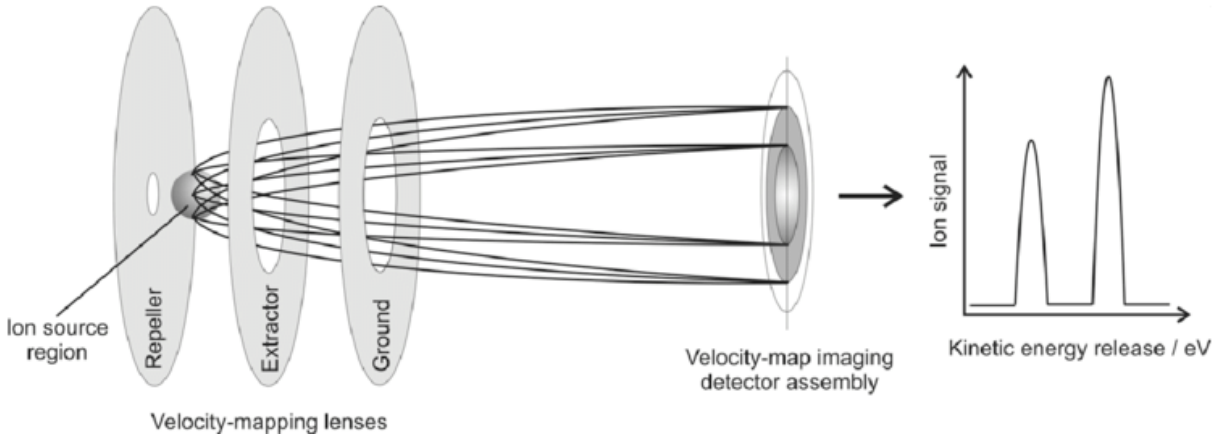

Figure 2.5.: A schematic diagram of the conventional velocity map imaging spectrometer (VMI) illustrates its composition, which includes a repeller electrode, an extractor electrode, and a ground plate. A position-sensitive detector is employed to record the arrival positions of charged particles. The electrostatic field generated by the VMI lens ensures that particles possessing identical initial transverse momentum are mapped to the same position on the $x - y$ plane of the detector. The image is taken from [197].

dynamics, including Coulomb explosion.

2.5. Velocity map imaging spectrometer

To access detailed information about the electrons and ionic fragments generated after ionization, an appropriate detection method is required. Imaging techniques for ions and electrons have found widespread application in visualizing the momentum vectors of charged particles. Among them, Velocity Map Imaging (VMI) provides an intuitive representation of the kinetic energy and angular distributions of ions and electrons, thereby enabling a deeper understanding of the underlying chemical dynamics governing these processes. This methodology has opened new avenues for a broad range of studies in molecular chemistry and physics, including photodissociation, particle collisions, chemical reactions, and ionization processes [195, 196].

The velocity map imaging technique (VMI), originally introduced by Eppink and Parker [198], represents a specialized variant of time-of-flight (ToF) mass spectrometry (MS) [199]. The conventional VMI geometry, illustrated in Fig. 2.5, consists of three electrodes: the repeller, the extractor, and the grounded plate. The electrostatic lens formed by this electrode configuration generates an electric field that maps ions with identical initial momentum which parallel to the detector onto the same position on a position-sensitive detector. Ions are generated in the interaction region, and are spatially defined between the repeller and extractor electrodes by a tightly focused laser beam. A specific set of voltages is applied to the repeller and extractor plates to create a gradient field in the extraction region. This setup will ensure that the impact position of a charged particle on the detector plane is, to first order, independent of its point of origin within the interaction region. The third electrode is typically grounded or maintained at the same potential as the flight tube, allowing ions to drift through a field-free region—commonly referred to as the drift tube—before reaching the detector. In simplified terms, the time-of-flight (ToF) of an ion to the detector is proportional

to $\sqrt{m/q}$, where m is the ion's mass and q its charge. Under ideal velocity mapping conditions, the radial position on the detector is given by:

$$R = M \cdot v_r \cdot t_{\text{tof}}, \tag{2.7}$$

where M is the image magnification factor, v_r is the initial transverse velocity of the ion, and t_{tof} is its flight time.

In this thesis, we employ a double-sided VMI configuration, in which ion and electron detectors are placed in opposite directions, and the same principle applies on the electron side. This setup enables the simultaneous recording of the kinetic energy and angular distributions of both ions and electrons, thereby providing a more comprehensive dataset for analyzing and elucidating the underlying chemical dynamics. The detailed methodology for calculating and improving the VMI resolution is discussed in Chapter 4. For further information on the fundamentals of VMI, refer to [198].

2.6. Time and position sensitive detectors system

For particles passing through the VMI spectrometer and reaching the detectors, we present a methodology for collecting, recording, and storing multiple types of information for each individual particle, thereby enabling comprehensive data acquisition for subsequent analysis and processing.

2.6.1. Timepix3 camera

When electrons and ions are accelerated through a time-of-flight mass spectrometer and reach detectors on opposite sides, they first strike on microchannel plates (MCPs) [201], which serve as highly effective signal amplifiers. The fundamental structure of an MCP is illustrated in Fig. 2.6 a. The glass substrate contains an array of microscopic holes, typically with diameters of several tens of micrometers, each inclined at a specific angle. The inner walls of these channels are coated to facilitate the emission of secondary electron. Fig. 2.6 b illustrates the electron signal amplification process. When an incoming particle enters a microchannel, it collides with the inner walls, generating secondary electrons. These secondary electrons undergo successive collisions, producing additional electrons in a cascading avalanche effect, ultimately amplifying the original signal by a factor of 10^3 to 10^4, significantly enhancing both detection efficiency and signal strength. This substantial amplification makes the MCP an essential component in high-sensitivity detection systems. To further increase the overall gain, multiple MCPs can be stacked in series, such as chevron type (2 plates) and z-stack type (3 plates).

After amplification by the MCP, the resulting electron avalanche strikes on a phosphor screen, where it is converted into visible light. The emitted signal is subsequently recorded by cameras. Traditional cameras, e. g., complementary metal–oxide–semiconductor (CMOS) or charge-coupled devices (CCDs) cameras [202, 203], lack the temporal resolution required to distinguish flight-time differences between ions of distinct mass-to-charge ratios, which typically span several hundred nanoseconds to a few microseconds. As a result, these cameras are inadequate for resolving velocity maps of ions with different m/q values. Furthermore, projecting the ions' velocity vectors onto the detector plane inherently compresses the three-dimensional momentum distribution—commonly referred to as a Newton sphere—into a two-dimensional image.

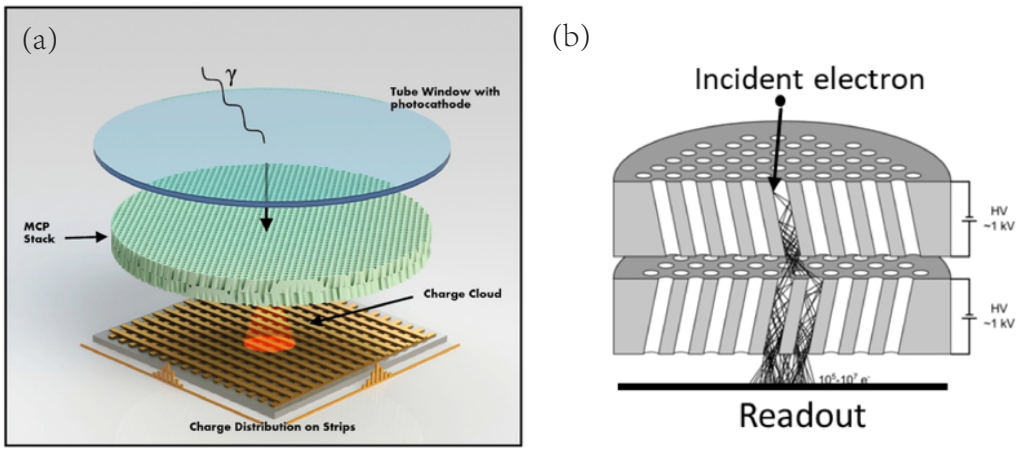

Figure 2.6.: (a) Schematic illustration of a detector equipped with a Microchannel Plate (MCP) amplifier, in which incoming particles (photons, ions, electrons) are first converted into electrons, subsequently amplified, and finally encoded using a dedicated readout system. (b) Operating principle of an MCP-based electron amplifier. Typically, two or more MCPs are stacked in series, with approximately 1000 V applied across each plate. When an incident ionizing particle strikes the wall of a microchannel, secondary electrons are emitted from the channel's coating. These electrons are accelerated along the channel, triggering an avalanche multiplication process that achieves a gain on the order of 10^6–10^7. The resulting electron cloud exiting the MCP stack can then be detected using various readout options, such as phosphor screens coupled to Timepix3 cameras in this thesis. The image is taken from [200, 201].

To recover the full three-dimensional momentum distribution, cylindrical symmetry is typically required for performing an inverse Abel transformation. This symmetry constraint significantly limits the scope and flexibility of experimental applications [204].

As an upgrading techique, the approach involves event-driven optical sensors with time-stamping capabilities used in this thesis is the Timepix3 camera [205]. This is an application specific integrated circuit (ASIC) hybrid pixel detector developed by the MediPix3 collaboration [206], which offers both time- and position-sensitive detection. The light signal flashes emitted from the fast phosphor screen are focused onto the camera sensor chip. The detector comprises a silicon photosensor (256×256 pixels, with a pixel size of 55 μm^2), attached to a Speedy PIxel Detector Readout (SPIDER) chip [207, 208], which enables precise temporal and spatial-resolved detection of light hits at MHz rates.

Each pixel operates as an independent fast digitizer, applying a predefined threshold. If the detected signal exceeds this threshold, the arrival time (ToA) and time-over-threshold (ToT) are recorded. The ToA indicates the time taken for the signal to cross the threshold, while the ToT corresponds to the duration that the signal remains above it. The ToA provides time-of-flight information, and the ToT reflects the signal amplitude. The Timepix3 camera achieves a nominal time resolution of 1.6 ns [8]. Compared to traditional method, a key advantage of this data-driven camera lies in its ability to handle multiple hits simultaneously, thus enabling measurements at significantly higher count rates. For more detailed information, refer to [205].

2.6.2. `Pymepix`

For the Timepix3 camera, the data pipeline and acquisition workflow are inherently complex and require considerable effort for proper operation. Typically, decoding scripts are necessary to correctly interpret raw data packets, and further data processing is often required, such as enhancing temporal resolution, correlating between triggers and event and time, centroiding events from raw pixel data. This multilayered process imposes a substantial burden on users before they can even begin visual inspection and analysis of the data stream.

To address these challenges, we employed the custom-developed software package `Pymepix` [209, 210] for data recording and processing with centroid algorithm for raw data, which significantly simplifies and streamlines the use of Timepix3 and the SPIDR readout system. `Pymepix` facilitates connection establishment with the Timepix3 device, initiation of data acquisition, real-time visualization of the acquisition process, and retrieval and plotting of pixel and timing information, as well as data recording. These functionalities are encapsulated within modular, black-box-style package that abstract away low-level complexities.

Moreover, `Pymepix` is designed to integrate seamlessly with interactive `Python` environments such as `IPython` and `Jupyter` Notebooks, thereby enhancing user accessibility and enabling more intuitive handling of streaming data. The adoption of this software framework greatly simplifies the entire workflow of ion and electron imaging experiments—from data acquisition and storage to retrieval and analysis. For more detailed information, please see [209, 210].

3. A versatile and transportable endstation for controlled molecule experiments[1]

3.1. Introduction

The advancement of synchrotron and x-ray free-electron laser (XFEL) radiation sources, such as those at DESY (FLASH), the linac coherent light source (LCLS), the free-electron laser radiation for multidisciplinary investigations (FERMI), the SPring-8 Angstrom compact free-electron laser (SACLA), the x-ray free-electron laser at the Paul Scherrer Institute (SwissFEL), the European x-ray free-electron laser (EuXFEL), and the Shanghai soft x-ray free-electron laser (SXFEL), substantially pushes the boundaries of existing research areas and breaks the ground for completely new fields [15–19, 211–219]. These sources generate ultrashort x-ray pulses spanning from tens of femtoseconds down to the attosecond range [220–222]. Furthermore, they provide a high peak brilliance, coherence and photon energies ranging from 5 to 250 keV [18, 223–230]. Table-top laser systems offer unique advantages in other areas: These sources include variable-wavelength optical-parametric-amplifier (OPA)-based systems [231, 232], high power lasers with repetition rates up to 1 MHz using optical parametric chirped-pulse amplification (OPCPA) [233, 234], and lasers with attosecond pulse durations [235, 236]. Each photon source has unique properties, functions, and parameters that make it suitable for different investigations, ranging from ultrafast studies of chemical reactions over bio-molecular dynamics to materials and life science [195, 237–241]. This progress led to particular needs on user-side applications, notably atomic-level-resolution molecular dynamics experiments based on ultra-cold molecular beam methods [17, 187, 214, 242–246].

Molecular beams are of significant importance in physical chemistry and molecular physics as they provide a unique opportunity to obtain fundamental insights into molecular photophysics and chemical processes [76–78, 247, 248]. Whereas substantial research was conducted on isolated small molecules and atoms, investigating more complex molecular systems with molecular-level insight is still restricted by many experimental challenges [45, 219, 249]. One of these challenges is to generate well-defined ensembles of the reactant particles. In this regard, many molecular beams usually contain mixtures of isolated molecules, various molecular clusters, or multiple isomers, e. g., of chiral molecules or large biomolecules. The ability to select a particular species plays a crucial role in gaining a deeper understanding of its importance in

[1] This chapter is based on the publication by Wuwei Jin, Hubertus Bromberger, Lanhai He, Melby Johny, Ivo S. Vinklárek, Karol Długołęcki, Andrey Samartsev, Francesca Calegari, Sebastian Trippel, and Jochen Küpper, "A versatile and transportable endstation for controlled molecule experiments", *Review of Scientific Instruments* **96**, 023305 (2025), DOI: 10.1063/5.0228913. My contributions to this work were setting up the setup, commissioning, maintenance and improvements to the setup, data analysis, and writing of the manuscript.

chemical behavior that also impacts a wide range of biological processes [6, 7, 48, 250]. To overcome this obstacle, the electrostatic deflector was developed to achieve spatial separation of different neutral species in ultra-cold ($T_{\mathrm{rot}} < 1$ K) molecular beams, ultimately obtaining pure particle ensembles [45, 49, 50, 141, 143, 251].

A second challenge is recording the molecular dynamics using experimentally accessible observables. The reaction microscope (REMI) technique, for example, provides complete, correlated, 3D velocity information of all particles detected in coincidence [219, 234, 252]. However, it is limited by low count-per-shot rates, which can lead to poor statistics. High-count-rate approaches such as velocity-map imaging (VMI) [198], provide a significant improvement in that respect. A significant drawback of VMI in high count rate conditions however is that one cannot rely on coincidence detection to extract, e. g., information about different electrons and ions coming from the same target molecule, although covariance mapping methods [253] can partially overcome this problem. Lastly, for VMIs, photoelectron-photoion coincidence (PEPICO) spectroscopy that is synchronizing VMI- and time-of-flight (TOF) information, is also challenging [254]. These issues so far limit access to the full kinematics of single reactions and, therefore, systematic studies of the underlying physical mechanisms.

This article provides a comprehensive overview of the newly established endstation for controlled molecule experiments (eCOMO). It addresses the aforementioned challenges of the current experimental research. eCOMO provides pure, cold, dense, and pulsed molecular beams of selected species using Even-Lavie valves [121] in combination with the electrostatic deflector [45]. The endstation is equipped with a double-sided VMI spectrometer combined with high spatio-temporal-resolution Timepix3 cameras combined with the software package PymePix [8, 209]. This event-driven approach enables us overcome the limitations of standard, frame-based, camera technology. It allows for quick and accurate reconstructing of the full 3D-momentum distribution of all created ions for advanced imaging experiments with high event rates [8, 200, 205, 255]. Moreover, this also meets the high-frequency data acquisition requirements of various light sources with high repetition rates mentioned earlier [8, 223].

To demonstrate the capabilities of the novel system, we present the results of its commissioning with an optical laser in our laboratory. We used the fragmentation of OCS after strong-field ionization as a benchmark to characterize the molecular beam, the electrostatic deflector, and the electron-and-ion-VMI spectrometer.

3.2. Apparatus description

3.2.1. Vacuum system

The vacuum setup, shown schematically in the upper left corner of Fig. 3.1, consists of four differentially pumped vacuum chambers housing the molecular beam source, the electrostatic *b*-type deflector [132], the double-sided VMI spectrometer, and the molecular beam dump. All chambers are mounted on rails to allow easy translation of the setup along the *z*-axis, which is parallel to the molecular beam propagation direction. The source chamber is pumped with two turbomolecular pumps (Pfeiffer Vacuum ATH2303 M), which results in a total pumping speed of ~3600 l/s for helium. The source chamber is equipped with two quick-access DN250 CF doors (Pfeiffer Vacuum 420KTU250), enabling easy sample replacement in the Even-Lavie valve sample container [121]. Furthermore, the source chamber is separated from the deflector

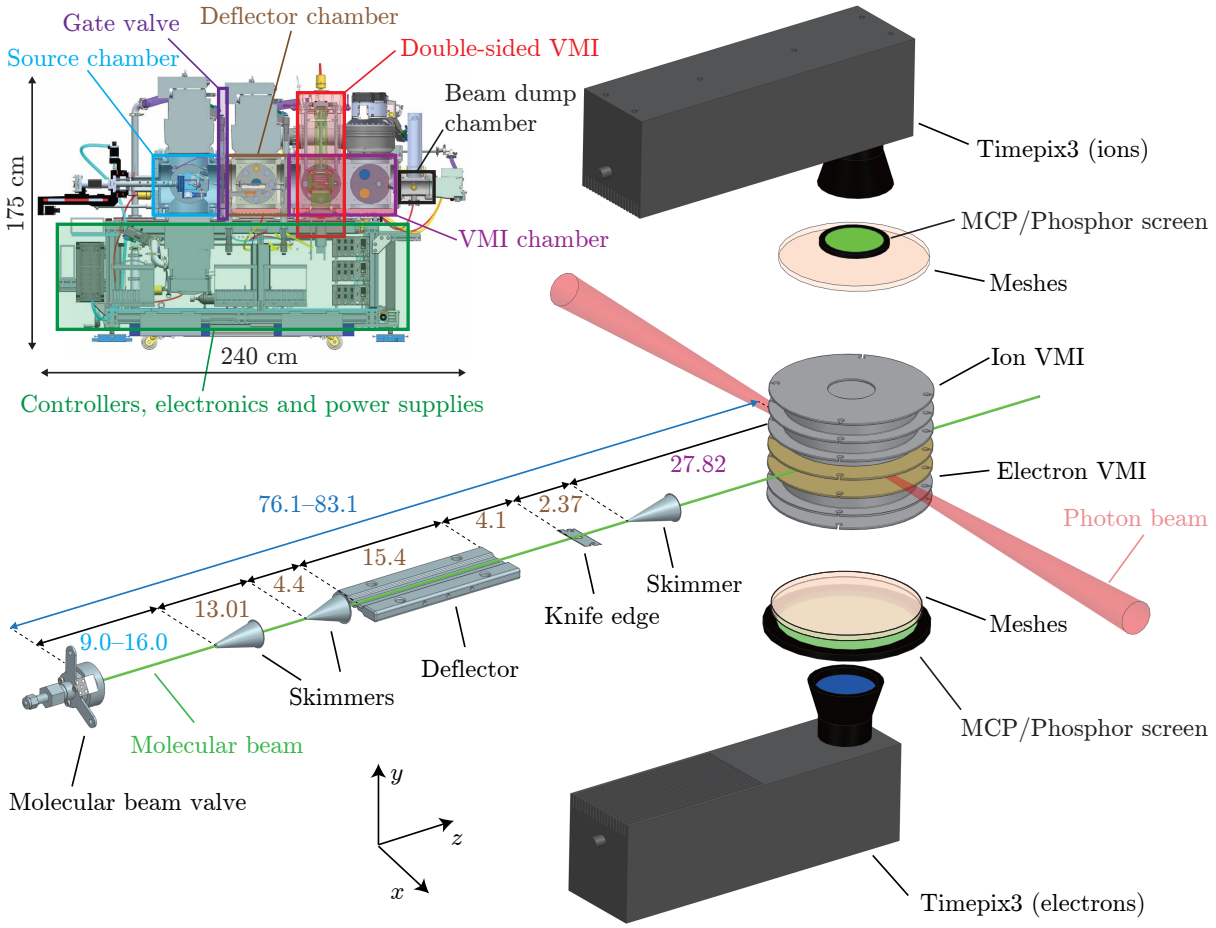

Figure 3.1.: Sketch of the experimental setup consisting of a molecular beam valve, an electrostatic *b*-type deflector, a double-sided VMI, and two Timepix3 cameras. The inset provides a side view from a CAD model, where colored frames depict the different parts of the setup. All distances are provided in cm. See the text for details.

chamber with a home-built automatic DN250 CF gate valve [256] to allow sample changes without breaking the vacuum of the deflector chamber and the spectrometer. The deflector chamber is also pumped with a turbomolecular pump with a pumping speed on the order of ~1800 l/s for helium (Pfeiffer Vacuum ATH2303 M). Next, the VMI chamber is pumped by two turbomolecular pumps (Pfeiffer Vacuum PM P06 302 and PM P06 312) resulting in an overall pumping speed of ~4000 l/s for helium. Finally, the beam dump is pumped with a turbomolecular pump (Pfeiffer Vacuum PM P04 024), resulting in a pumping speed of ~470 l/s for helium. In addition, a 250 mm diameter copper shield connected to a Dewar for liquid nitrogen cooling is located in the VMI chamber to increase the pumping speed for molecules with freezing points above the liquid nitrogen temperature. The Dewar is designed such that liquid nitrogen must be refilled every ~7 hours to keep the shield cold.

In order to achieve better vacuum, the VMI chamber can be baked. All non-metallic components of the VMI spectrometer are made of glass ceramic (Macor) with an operating temperature of up to >600 °C. The temperature limiting components of the setup are the O-ring and copper seals with a maximum temperature of 200 °C each. It must also be noted that the pumps must not exceed a temperature of 120 °C with possible additional air cooling. In addition, the pressure gauges must not be operated

above 55 °C. So far, baking was performed at 120 °C. After one week of baking and subsequent cooldown, a pressure of 3×10^{-11} mbar was achieved.

The first pre-vacuum line that provides vacuum to the source chamber and to the second low pressure pre-vacuum line, is pumped by a pre-vacuum pump (Pfeiffer Vacuum PR P00 009) with a nominal pumping speed of ~130 m^3/h. The second pre-vacuum line is pumped by a turbomolecular pump (Pfeiffer Vacuum PM P03 900) with a pumping speed of 255 l/s for helium. The second pre-vacuum line provides vacuum to the deflector-, VMI-, and beam dump chambers. This line is needed to compensate for the low helium compression ratio given for, e. g., the pumps of the VMI chamber by 3×10^5. When operating the molecular beam valve at a repetition rate of 100 Hz, the typical pressures in the source-, deflector-, VMI-, and beam dump chambers are ~10^{-6}, ~10^{-8}, ~10^{-10}, and ~10^{-10} mbar, respectively. Under such conditions, the typical pressure in the first and second pre-vacuum lines is ~10^{-3} and ~10^{-7} mbar, respectively.

Further information on the vacuum system including the layout of gas lines, the interlock system with its logic to control the gate valves, and voltage power supplies, is provided in the supplementary information. The primary purpose of the interlock system is to ensure operation monitoring of the eCOMO vacuum system and to automatically protect the setup and spectrometer in case of sudden emergency situations.

3.2.2. Molecular beam setup

The main part of Fig. 3.1 shows the molecular beam setup. All molecular beam components including the valve, skimmers, deflector, and knife edge are mounted on motorized translation stages in the x–y plane. The individual positions can therefore be adjusted perpendicular to the molecular beam propagation direction using linear feedthroughs and stepper motors (Thorlabs, DRV014), which can be controlled remotely. The maximum travel range for the whole molecular beam is ~11 and ~12 mm in x- and y-directions, respectively. The implemented motors enable the alignment and vertical scanning of the molecular beam with respect to any general photon source, enabling the investigation of different sections of the quantum-state-dispersed molecular beam.

An Even-Lavie valve [121] is used to deliver the molecular beam by a supersonic expansion of 10–100 bar helium with typically a few mbar of sample molecules into vacuum [257]. The valve temperature can be adjusted between room temperature and 250 °C to control the vapor pressure of the sample under investigation and can be operated with a repetition rate of up to 500 Hz. The valve is mounted on a semi-motorized DN63 CF 3D manipulator (Caburn-MDC E-PSM-2504) with a travel range of 7 cm along the molecular beam propagation direction. The first conical skimmer (Beam Dynamics, model 50.8, ∅ = 3 mm) is used for skimming the molecular beam and to obtain differential pumping. The distance between the first skimmer and the valve can be adjusted between 9 and 16 cm by moving the valve along the molecular beam propagation direction. The first skimmer is mounted on a home-built flange with a built-in 2D translation stage to adjust the skimmer position in the x- and y directions. A second skimmer (Beam Dynamics, model 40.5, ∅ = 1.5 mm) is placed 13.01 cm behind the first skimmer tip for further collimation of the molecular beam. An electrostatic b-type deflector [132], which disperses the molecules in the molecular beam with respect to their quantum states [45, 140, 141, 143, 251] is located 4.4 cm behind the tip of the second skimmer. Both electrodes of the electrostatic deflector are connected through high-voltage feedthroughs (Pfeiffer 420XST040-30-30-1) allowing

voltages of up to ±30 kV on each electrode. The second skimmer and the electrostatic deflector are mounted together on an x–y translation stage to adjust their positions. The electrostatically dispersed molecular beam is then cut by a vertically adjustable knife edge placed 4.1 cm downstream of the deflector exit. This allows for both an improved sample separation and a higher column density of the molecular beam [258]. The molecular beam is further skimmed by a third conical skimmer (Beam Dynamics model 50.8, ∅ = 1.5 mm) placed 2.37 cm downstream of the knife edge, providing differential pumping against the VMI chamber. This third skimmer is again mounted on a 2D translation stage. The molecular beam enters the VMI chamber after the third skimmer. The distance between the tip of the third skimmer and the interaction region is 27.8 cm. The state-selected molecules are ionized by the photons used for the investigation inside the double-sided VMI spectrometer [198]. The resulting electrons and ions are velocity-mapped onto a 120 mm (Photonis Model: APD 3 PS 120/32/25 19 I 60:1 NR 10″FM P47) and a 75 mm (Photonis Model: APD 3 PS 75/32/25/8 I 60:1 NR MGO 8″FM P47) diameter position-sensitive detector, respectively. Each detector consists of three z-stacked multi-channel plates (MCPs) and a fast phosphor screen with a decay time on the order of 100 ns (P-47) [259]. Both detectors are captured by time and position-sensitive Timepix3 cameras built by Amsterdam Scientific Instruments based on homebuilt chips [8, 208]. The molecular beam enters the beam dump chamber through a ∅ = 2 cm aperture after passing the VMI. The beam dump chamber pump is mounted with a 22 mm offset regarding the z-axis, allowing the molecular beam to directly hit onto the rotors to prevent scattering of the direct beam back into the VMI chamber.

3.2.3. Double-sided VMI

The double-sided VMI setup specifically designed for eCOMO is illustrated in Fig. 3.2 a along with its relevant dimensions and the electrode labels. It allows for the simultaneous detection of electrons and ions and evolved from the initial concept of velocity imaging in photoionization coincidence studies [260]. The VMI's adaptable design permits both, vertical and horizontal installations within the VMI chamber, facilitating flexible use in different laboratories and photon-science facilities. By default, the eCOMO spectrometer is installed vertically in the VMI chamber. Alternatively, the spectrometer can be installed horizontally along the molecular beam direction replacing the beam dump. In this case, only the long side of the spectrometer can be used for either electrons or ions. Furthermore, this arrangement results in a higher background gas pressure inside the VMI, because the atoms and molecules only leave this region through the additional holes in the drift tubes after colliding with the detector and the walls inside the spectrometer. The total conductance of the relevant part of the VMI for helium is ~2500 l/s and the corresponding total relevant volume is ~3.6 l. This results in a $1/e$ time constant on the order of 1 ms. For the same molecular-beam-valve repetition rate as used here the resulting background-pressure increase is $\sim 6 \times 10^{-10}$ mbar for helium.

The VMI's point of origin is defined in the middle between the electrodes EE1 and IE1 as indicated by the red star. This is the location where the molecular beam interacts with the photons. Electrodes EE1 and IE1 are fabricated from oxygen-free copper (OF-Cu) with at least 5 μm of gold plating to obtain a higher work function compared to stainless steel for experiments using high energetic photons, e. g., UV light. The remaining electrodes are made of stainless steel (1.4429 ESU), with surfaces finely

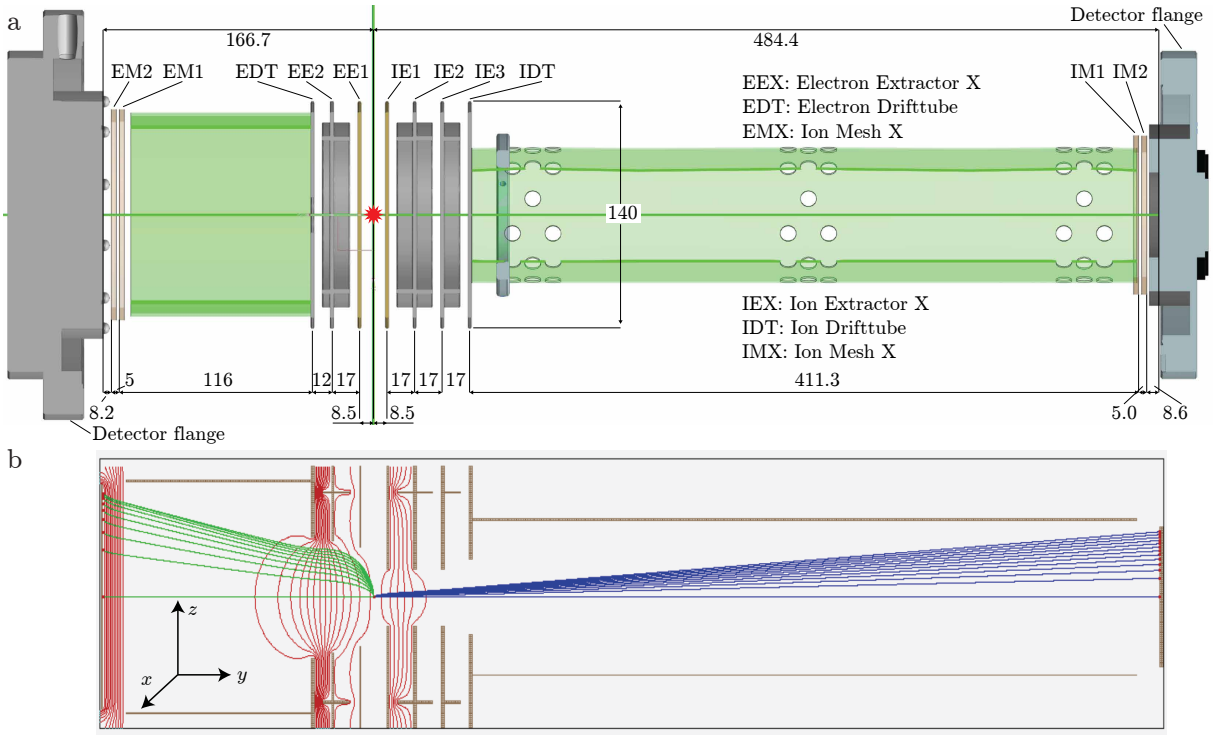

Figure 3.2.: (a) Schematic of the double-sided-VMI setup cut along the y-z plane, containing the symmetry axis. The left side represents the electron detector, while the right side represents the ion detector. All distances are in mm. Typical voltage settings for each electrode can be found in Table 3.1. The interaction region is indicated by the red star. (b) Simulation for the large velocity range mode calculated with SIMION. Equipotential lines are displayed in red. The trajectories of electrons are depicted in green, while ion trajectories are represented in blue. Electron kinetic energies parallel to the detector surface were chosen in steps of 70 eV from 0 to 630 eV and ion kinetic energies parallel to the detector surface were chosen in steps of 1 eV from 0 to 12 eV.

polished. Additionally, a rim structure is designed around the outer edge of each electrode to reduce the influence of the VMI holder on the shape of the electric field in the center of the spectrometer. All electrodes have an outer diameter of 140 mm and are separated by ceramic spacers (Macor) as electrical insulators. A cylindrical shield surrounding the VMI, depicted in green, with holes for the photons, molecular beam, potential diagnostic paddles for x-ray experiments as well as for pumping, is composed of μ-metal to provide shielding from stray fields and external magnetic fields. Double-layered meshes EM1–EM2 and IM1–IM2, with 80% transmission for each layer, are positioned on both sides of the spectrometer to ensure homogeneous drift tube fields close to the detector surfaces. The first mesh on both sides with respect to the interaction region is conductively connected to the corresponding drift tube. The VMI is completely mounted on the DN200 CF ion detector flange. Its design allows for straightforward installation or replacement entirely from the ion detector side. The electrode connections extend through wires to the DN200 CF flange, where they proceed to the exterior via electrical feedthroughs (CF16-SHV20-SH-SE-CE-NI, Vacom) with a maximum rated voltage of 20 kV each.

The spectrometer can operate in diverse photo-electron and photo-ion detection modes by adjusting the voltages across the electrodes as detailed in Table 3.1. This

Imaging mode	SMI	SVR–VMI	LVR–VMI
Electron mesh 2 (EM2)	0	-134	6864
Electron drift tube (EDT)	0	1956	9816
Electron extractor 2 (EE2)	0	490	673
Electron extractor 1 (EE1)	0	-277	-553
Ion extractor 1 (IE1)	0	-370	-593
Ion extractor 2 (IE2)	-420	-821	-4672
Ion extractor 3 (IE3)	-1600	-2373	-4717
Ion drift tube (IDT)	-1600	-2380	-4800
Ion mesh 2 (IM2)	-1600	-821	-4672

Table 3.1.: The voltage settings (in V) required for the corresponding electrodes, as displayed in Fig. 3.2 (a), to enable the operation of the double-sided VMI in the specified modes. See the text for details.

table lists, as examples, the implementation of a spatial map imaging (SMI) mode [41] – optimized exclusively for ions – and two VMI modes for different maximum energies for the velocity components parallel to the detection plane E_{p}. The VMI modes images both, electron and ion velocities. Each voltage setting is tailored for specific applications. In the SMI mode, the projected position on the detector correlates with the ion's initial position and is in the first order unaffected by its initial velocity, enabling precise imaging of the ionizing region. This functionality is particularly advantageous for the alignment of the experimental setup, ensuring accurate positioning of the light focus and the molecular beam. Conversely, the VMI mode allows electrons or ions with identical velocity vectors to converge to a single spot on the corresponding detector, in the first order irrespective of their initial positions. Different VMI modes allow different maximum kinetic energies to be collected on the detector, which can be adjusted depending on the experimental situation. The detection range for the electron kinetic energy parallel to the detector surface extends up to 700 eV in the large-velocity-range VMI (LVR–VMI) mode. Single-charged ions can be mapped here with a parallel energy up to 12 eV. The range for the parallel electron kinetic energy extends up to 100 eV and for single-charged ions up to 10 eV in the small-velocity-range VMI (SVR–VMI) mode.

The combination of MCP and phosphor screen amplifies each individual ion and electron after the particles hit the detector, by creating an avalanche of electrons that then scintillates on the phosphor screen. The light-flashes are captured with a Timepix3 camera [8, 205] operated and controlled by our open source library PymePix [209, 261]. PymePix is also utilized to extract the raw physics events from the Timepix3 data stream, converting them into centroided events recognized as single particle events [8]. The data-driven cameras, with a temporal resolution of ~1.6 ns, enable us to operate in multi-mass detection mode and to directly obtain the VMI images of all fragments by slicing the TOF coordinate in software during analysis. The performance evaluation of the Timepix3 camera is beyond the scope of this article and was extensively discussed in other publications [8, 262, 263]. The relative positions and relative TOFs measured by the cameras can be converted to velocities in VMI conditions.

The energy resolution of the double-sided VMI was determined through SIMION simulations. It is in the first approximation linearly dependent on the source size so the volume in which the ions and electrons are produced. In addition, it depends on the specific mode of spectrometer operation. In our specific simulation, we used a cylinder for the focal volume with the length given by the diameter of the molecular beam D = 2 mm, and the radius given by the standard deviation of the transverse

laser intensity distribution $\sigma_r = 21$ μm resembling our experimental conditions. Taking LVR–VMI as an example, we obtain $\Delta E_\mathrm{p}/E_\mathrm{p} = 0.004$ for the ion side, which is to first order constant for all energies that can be mapped. This results in an energy resolution of $\Delta E_\mathrm{p} = 0.02$ eV for, e. g., a parallel ion energy of $E_\mathrm{p} = 5$ eV. For electrons, using the same settings, we obtain $\Delta E_\mathrm{p}/E_\mathrm{p} = 0.003$. Both resolutions are in good agreement with results obtained on similar systems [80]. Further settings to meet special experimental requirements are possible, but must be again found by simulations.

3.2.4. Portability and Installation

The eCOMO setup is designed for easy and convenient transport between different light sources, which is facilitated by four integrated wheels. Once eCOMO is positioned, four adjustable home-built support feet connected to a screw jack with standing screw (Nozag NSE25), capable of both, horizontal and vertical adjustments, allow precise 2D positioning with a travel range of ±3 cm. The overall height of the interaction center can be adjusted between 103 and 135 cm. The source, deflector, and VMI chambers are mounted on profile guide rails attached to the stainless steel platform by guide carriages, allowing further adjustments along the molecular beam direction. The eCOMO setup incorporates all necessary equipment, as depicted schematically in the upper left corner of Fig. 3.1 in the green highlighted area, except for the computer used to control eCOMO and acquire data [209]. Integrated within the setup are all required power supplies with ports allowing quick installation, including three power cables capable of handling the necessary electrical load, a pair of inlet and outlet pipes for water circulation to cool the molecular pumps, an exhaust pipe for the vacuum system, and multiple gas sources such as nitrogen, compressed air, and the molecular carrier gas. The total weight of eCOMO including the pumps and electronics is ~1800 kg. The overall dimensions of eCOMO are 90, 175, and 240 cm in width, height, and length, respectively.

3.3. Characterization of the setup

3.3.1. Molecular beam spatial profiles

We used OCS as a sample to characterize the molecular beam and VMI performance to commission eCOMO [264, 265]. OCS was ionized by pulses from a commercial Ti:sapphire femtosecond laser system (Coherent Astrella) operated at a repetition rate of 1 kHz. The laser beam was compressed to approximately 40 fs with a standard grating-based compression setup. The laser beam was directed through a 75 cm focal-length lens, which resulted in a peak intensity of $I_0 \approx 3 \times 10^{14}$ W/cm^2. The laser focus was spatially and temporally overlapped with the molecular beam in the interaction center of the VMI spectrometer. The pulsed molecular beam was produced by expanding a mixture of 100 bar helium and ~10 mbar OCS. The gas mixture was expanded into the source chamber through the Even–Lavie valve operated at a temperature of 50 °C and at a repetition rate of 250 Hz. Laser shots without the molecular beam were used for background measurements. Optimized operation conditions of the valve allowed for the generation of a dense ($> 10^7$ cm^{-3}) molecular beam in the interaction volume. The OCS sample was displaced toward negative y positions when a total voltage of 25 kV was applied across the deflector, i. e., *de facto* the populated quantum states of OCS exhibited a strong-field-seeking character at the relevant electric field strengths in the

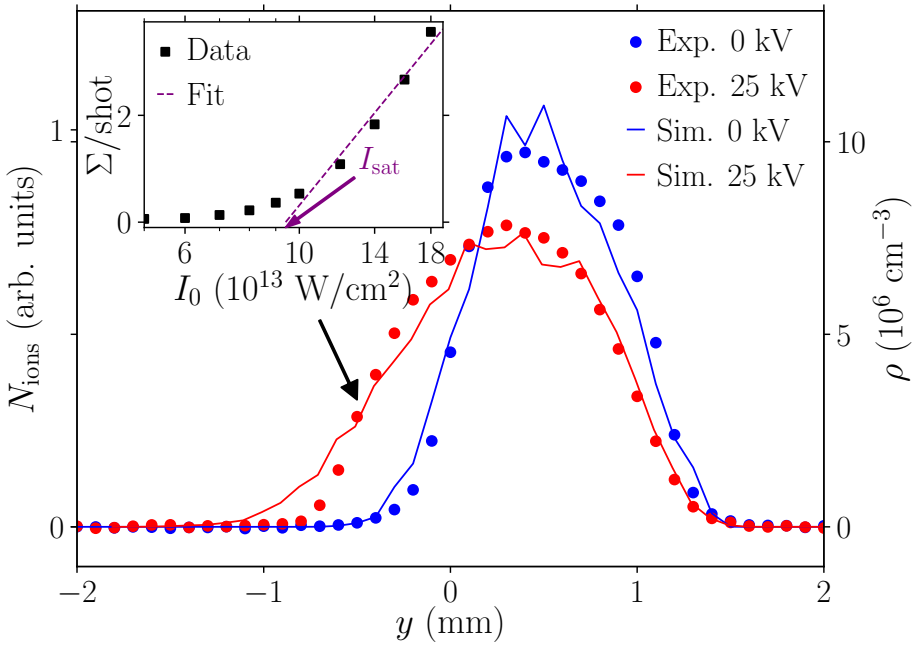

Figure 3.3.: Measured molecular beam density profiles (points) and simulation (solid lines) for the deflector switched off (blue) and at a total voltage of 25 kV (red) applied across the electrodes. The inset shows the number of OCS^+ ions Σ per shot (black squares) as a function of the laser peak-intensity natural logarithm $\ln I_0$. The purple dashed line represents the fit of the asymptotic slope. The data in the inset was measured at $y = -0.5$ mm in the deflected molecular beam profile, marked by the black arrow.

deflector. The measured deflection profile of OCS is shown in Fig. 3.3 as red dots. Solid lines represent simulated OCS beam profiles, computed through Monte-Carlo sampling combined with trajectory calculations that incorporate the geometrical constraints of the mechanical apertures in the experimental setup. These simulated deflection profiles of OCS match the experimental data, assuming an initial rotational temperature of $T_{\text{rot}} = 0.5$ K for the molecular beam entering the deflector. The results affirm that the eCOMO setup can generate cold and stable molecular beams.

The OCS beam sample density was determined using a strong-field ionization model [264, 266]. The asymptotic slope of an integral ionization signal $\Sigma(I_0)$, with respect to natural logarithm of the peak intensity $\ln I_0$ approaches a limiting value as I_0 approaches infinity. This slope can be expressed as:

$$\lim_{I_0 \to \infty} \left(\frac{d\Sigma}{d \ln I_0} \right) = 2\pi\alpha\sigma_r^2 D\rho \tag{3.1}$$

where ρ represents the sample density, σ_r the standard deviation of the transverse laser intensity distribution, α the instrument sensitivity, D the length of the focal volume in the molecular beam, and Σ the total number of detected ions. The inset of Fig. 3.3 illustrates the parent-ion signal count Σ per shot as a function of the laser peak intensity I_0 on a semi-logarithmic scale. The data was measured at $y = -0.5$ mm in the deflection profile as indicated by the black arrow. The asymptotic slope and saturation onset were obtained by fitting a straight line through the highest peak-intensity points, resulting in a saturation onset of $I_{\text{sat}} = (9.4 \pm 0.3_{\text{stat}} \pm 1.9_{\text{syst}}) \times 10^{13}$ W/cm^2. The subscripts indicate statistical and estimated systematic errors. This is in good agreement with the previously reported saturation intensity of OCS measured under similar experimental conditions

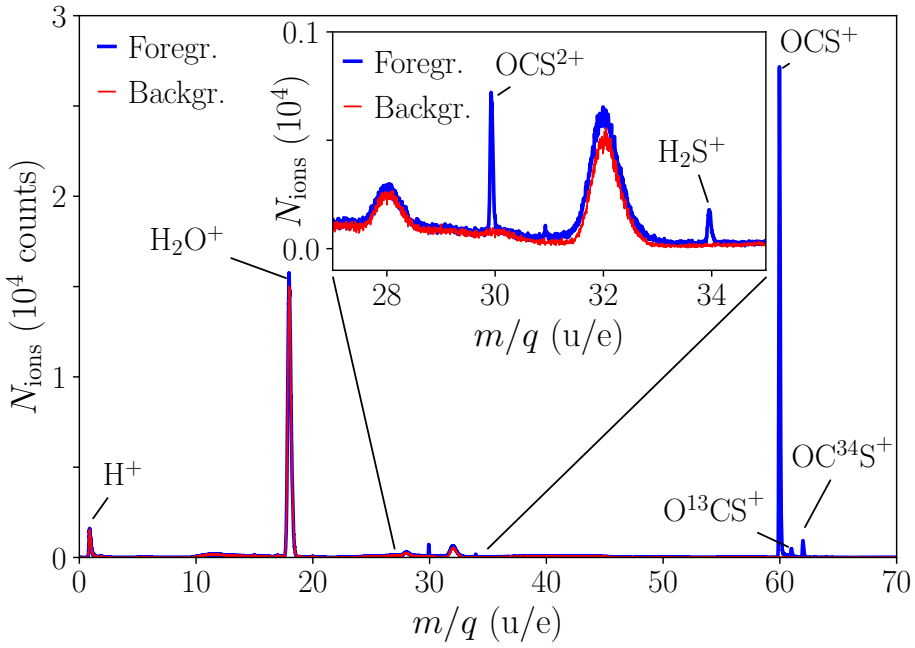

Figure 3.4.: TOF-MS spectrum of ions originating from the molecular beam containing OCS (blue) and from VMI-chamber background gases (red). The inset provides a magnified view of the specific region where OCS fragment ions and more-highly-charged ions occur.

given by $I_{sat} = 7.2 \times 10^{13}$ W/cm^2 [264]. To extract the sample density we determined the combined sensitivity of the meshes and the MCP detector to be $\alpha = 35.9\% \pm 1.3\%$ as described in subsection 3.3.3. In addition we use $\sigma_r = 21$ μm and $D = 2$ mm for the laser intensity standard deviation and the molecular beam width, respectively. The resulting sample density at $y = -0.5$ mm is given by $\rho = (2.86 \pm 0.58_{stat} \pm 0.57_{syst}) \times 10^6$ cm^{-3}. The maximum density is $\rho \approx 10^7$ cm^{-3} in the direct beam as shown in Fig. 3.3, which is one order of magnitude lower than previously reported on a similar experimental setup [264], which is attributed to a lower concentration of OCS in the helium mixture.

3.3.2. Time-of-flight mass spectrum (TOF-MS)

Fig. 3.4 shows the time-of-flight mass spectrum (TOF-MS) resulting from strong-field ionization of OCS and from the background gas in the VMI chamber measured with the Timepix3 camera [8, 205, 209]. The figure displays two distinct regions: The first region depicts the OCS parent ion and its isotopologues $O^{13}CS$ and $OC^{34}S$, which correspond to $m/q = 60$ u/e, $m/q = 61$ u/e, and $m/q = 62$ u/e, respectively. The respective signal strength is in good agreement with the corresponding natural abundance of OCS's most abundant atmospheric isotopologues [267]. The isotopologues with masses $m/q = 63$ u/e, and $m/q = 64$ u/e are also present in the data, but are not visible in the graph shown because of their natural abundance below 0.1%. The second feature is the presence of fragments, as also seen in the zoomed-in subfigure of the graph. Two broad peaks correspond to CO^+ with $m/q = 28$ u/e and S^+ with $m/q = 32$ u/e ions, which exhibit a broad ion velocity distribution due to Coulomb explosion of OCS^{2+}. The broad velocity distribution is directly reflected in the broad TOF distribution. The relatively strong background here originates from impurities of O_2 and N_2 gases present

in the VMI chamber and the molecular beam. Additionally, two narrow peaks are observed in the inset, which correspond to doubly ionized OCS and singly ionized H_2S, which is an impurity also present in the molecular beam. The significant water ion peak can also be mostly attributed to poor background pressure conditions, which at the time, were not fully optimized and given by $P_{\mathrm{VMI}} = 4 \times 10^{-9}$ mbar when the molecular beam was switched off. Additionally, there are small contributions of water ions that arose from impurities in the molecular beam. Recent modifications of the setup showed considerable improvement, achieving pressures as low as $P_{\mathrm{VMI}} = 3 \times 10^{-11}$ mbar. Furthermore, the purity of the gas line was also improved by installing a cooling thermostat (ECO RE 1050 S, LAUDA).

3.3.3. Performance of the double-sided VMI

In order to experimentally characterize the double-sided VMI, both electrons and ions from the molecular beam containing OCS were examined after strong-field ionization. Fig. 3.5 a and Fig. 3.5 c show the background subtracted cation-fragment velocity maps for $m/q = 28$ u/e and $m/q = 32$ u/e, respectively. The laser-peak-intensity here was $I_0 = 2.5 \times 10^{14}$ W/cm^2. The velocity maps show the commonly known features of OCS fragments after strong field ionization [91, 265]. The central circular parts of both velocity maps are attributed to fragmentation to CO^+ and S^+ following single ionization. The intense central spots are attributed to N_2^+ and O_2^+ in the $m/q = 28$ u/e and $m/q = 32$ u/e velocity maps, respectively. These were impurities present in the molecular beam. The outer rings are ascribed to the Coulomb explosion channels $OCS + nh\nu \rightarrow OCS^{+2} \rightarrow CO^+ + S^+$. The reduced counts right above the central regions are attributed to strong signals from background ions such as H_2O^+ arriving shortly before the selected ions in combination with the dead time of the Timepix3 camera, which was on the order of 1 μs in our case [8]. In addition, the detector could be less sensitive there because all background ions hit this area. The projected radial velocity distributions are shown in Fig. 3.5 e. The multiple channels corresponding to the VMIs are visible again.

The ion information can be used to determine the electron velocity map corresponding to specific ionization or fragmentation channels. To do so, both Timepix3 cameras have to be first synchronized as they independently record electrons and ions. To correlate the ion and electron cameras we simultaneously took ion and electron data at low laser intensities ($I_0 = 3 \times 10^{13}$ W/cm^2) at an average event rate of 0.02 ions or electrons per shot. The number of ions $N_{\mathrm{i}}(N_{\mathrm{trg;i}})$ or electrons $N_{\mathrm{e}}(N_{\mathrm{trg;e}})$ were assigned to the camera-specific trigger numbers $N_{\mathrm{trg;i}}$ and $N_{\mathrm{trg;e}}$, respectively. The normalized convolution $N_{\mathrm{i}} * N_{\mathrm{e}}$ of this signal is shown in Fig. 3.5 g as a function of the relative trigger number $\Delta N_{\mathrm{trg}} = N_{\mathrm{trg;i}} - N_{\mathrm{trg;e}}$. The peak indicates the required relative trigger number shift for both cameras to be synchronized.

To demonstrate ion-electron correlations, we ionized OCS with a laser-peak-intensity of $I_0 = 8 \times 10^{13}$ W/cm^2 to have both, parent ions and fragments present. In this case, the mean number of detected ions per shot was ~2 so specific ions and electrons from single laser shots can not be correlated directly. We can, however, obtain the statistically averaged electron image using the covariance of the electron velocity maps with the boolean operation on a specific ion detected [268]. Fig. 3.5 b displays the photoelectron velocity distribution after the covariance analysis where an OCS^+ was measured in coincidence. The figure reveals intricate angular and radial structures as previously reported [264]. Specifically, the momentum distributions exhibit wide

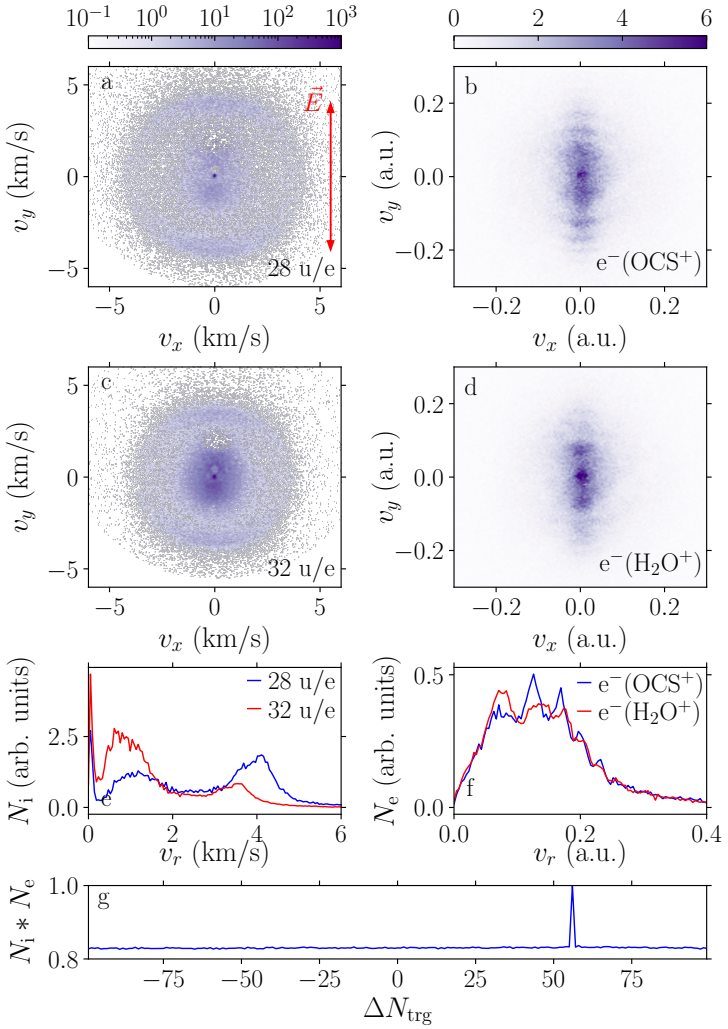

Figure 3.5.: (a) and (c) projected ion velocity maps for m/q = 28 u/e and for m/q = 32 u/e fragments, respectively. The laser polarization is indicated by the red arrow. (b) and (d) projected electron velocity maps for electrons correlated with OCS^+ and H_2O^+, respectively. (e) and (f) projected radial velocity distributions for ions and electrons, respectively. (g) Ion-electron Timepix3-camera-trigger correlation. See the text for more details.

radial patterns that repeat at integer multiples of the photon energy, which is commonly referred to as above-threshold ionization (ATI). A detailed discussion about the structure of the OCS electron momentum map is beyond the scope of this manuscript and further information can be found elsewhere [264]. Fig. 3.5 d displays the photoelectron momentum distribution accordingly when an H_2O^+ from ionization of the background gas was measured in coincidence with an electron. A clear difference in the image structure is observed in comparison with Fig. 3.5 b, which is attributed to the different ionization channels. The differences become even more obvious in the electron's speed distribution projected onto the detector shown in Fig. 3.5 f. In comparison with previous work [264], our short data acquisition time led to smaller experimental statistics, resulting in less detailed ATI structures. Further discussion about the underlying reason with respect to the differences in the electron velocity distributions is again beyond the scope of the manuscript. The clear differences between the two electron velocity maps however clearly show that eCOMO allows to correlate electron and ion momenta.

The low-intensity correlation measurements used for Fig. 3.5 g enabled us furthermore to obtain the detection efficiency for electrons and ions in our setup. From our data we obtain a final total detection efficiency of $\alpha_\mathrm{i} = 35.9\% \pm 1.3\%$ and $\alpha_\mathrm{e} = 35.4\% \pm 1.3\%$. Assuming a detection efficiency of the MCP given by $\alpha_\mathrm{MCP} = 50\%$ we obtain a transparency for a single mesh $\alpha_\mathrm{mesh} = 83.7\% \pm 1.5\%$, with the estimated transmission of 80%. The deviation is attributed to the fact that the effective transmission of the second grid is higher due to the shadow cast by the first grid.

3.4. Conclusions

In summary, eCOMO was developed, set up, and commissioned using experiments with an ultrashort-pulse table-top laser system. The performance of the cold ($T_\mathrm{rot} \leq 1$ K), pulsed, and dense ($\rho \approx 1 \times 10^7$ cm^{-3}) molecular beam was characterized. SIMION simulations of the double-sided VMI indicated that under experimental conditions, an energy resolution of $\Delta E/E < 0.4\%$ is achievable. We showed that the combination of the double-sided VMI and two synchronized Timepix3 cameras at eCOMO works and that the individual ions can be separated in the data analysis based on their mass over charge ratio. Furthermore, specific molecular dynamics can be separated for systems with many fragmentation channels as shown here for OCS after ionization. Using a covariance analysis, electron VMIs and corresponding projected electron velocity distributions were assigned to specific mass over charge ratios. The absolute detection efficiency of the setup was measured by coincidence methods to $\alpha_\mathrm{i} = 35.9\% \pm 1.3\%$ and $\alpha_\mathrm{e} = 35.4\% \pm 1.3\%$ for ions and electrons, respectively. The use of the *b*-type electrostatic deflector allows us to separate specific rotational quantum states, conformers and molecular cluster species with different effective-dipole-moment-to-mass ratios [45, 132]. This feature of the eCOMO setup has great potential in various areas, such as the separation and purification of complex clusters for chemical dynamics studies [7].

The eCOMO setup exhibits versatile applications in the production of purified cold gas-phase molecular beams and high-precision ion-electron coincidence and covariance measurements. It can be readily adapted to a wide range of photon-source facilities, making it suitable for diverse research activities spanning atomic, molecular, and cluster physics, as well as materials science, energy science, chemistry, and biology.

4. Methodology and application of resolution analysis for velocity map imaging spectrometers[1]

4.1. Introduction

Velocity map imaging (VMI) [26] has established itself as a powerful technique in probing molecular dynamics with high resolution. It can give insights on the atomistic details of molecular change by visualizing how singular molecular bonds can be formed or broken [27]. The dynamics of a molecule following a collisional process, this may stem from half-collisions with photons resulting in photodissociation [33] or with other molecules as a target in crossed-beam scattering experiments [28], are encoded within the kinematics of observed ionic fragments or electrons [269]. This leads to fragments with well-defined and sharp velocity distributions with concentric spherical symmetry, commonly referred to as a Newton sphere in momentum space. Imaging these Newton spheres was first pioneered in photodissociation experiments on iodomethane [29], where electrostatic lenses with a grid were used to create a homogenous electric field, enabling the capture of 2D spatial distributions of photofragmentation products. Leaving out the grid on their electrostatic lenses significantly improved the resolution of the technique [26]. Velocity-map imaging can be achieved with a three-plate electrode configuration, consisting of repelling, extracting, and grounding electrodes, which is commonly denoted as the Eppink-Parker geometry. The absence of a grid on these electrodes introduces an inhomogeneity to the electric field, which acts as a lens. The curved electric-field lines map a 3D volume of charged particles onto a position sensitive 2D detector irrespective of their initial position, e. g., at the time of their ionization. More specifically, it maps vector components of the Newton sphere parallel to the detector surface onto the same position of the detector, which provides a greater resolution compared to homogenous fields.

The full capture of a Newton sphere is only partially possible with a VMI spectrometer. The third velocity component along the spectrometer axis requires additional techniques to acquire, as the Newton sphere is initially crushed (pancaked) onto a two-dimensional imaging detector. Common well-established methods involve slice imaging to capture a center slice of the Newton sphere [270, 271], image reconstruction using an inverse Abel transformation [272, 273], measuring the time-of-flight along the spectrometer axis independently and correlating it to the 2D VMI data [40, 274], or using timestamping methods with delay-line detectors [275] or more advanced camera systems based, for instance, on PImMS [276] or TimePix [8, 205, 262].

[1] This chapter is based on the publication by Wuwei Jin, Ivo S. Vinklárek, Atilay Ayasli, Jochen Küpper, and Sebastian Trippel, "Methodology and application of resolution analysis for velocity map imaging spectrometers", *in preparation*. My contributions to this work were the implementation of the simulation setup, recording and analyzing of the data, and writing of the manuscript.

Using these techniques gives a kinematically complete description of of a Newton sphere, which enables us to extract the energetics and angular distributions of a system. This provides a snapshot of the underlying potential energy surface, and ultimately of the chemical dynamics by measuring translational velocity and angular distributions of products.

VMI has therefore become a central tool across a broad range of applications, delivering numerous high-resolution results for diverse molecular systems over the past decades, including studies of photodissociation with quantum-state specificity [30–33] and investigations conducted in the strong-field regime [34–37]. It has also been widely utilized in reactive crossed-beam neutral-neutral [28, 277] and ion-molecule [38–40] scattering experiments, as well as in studies of inelastic scattering [278]. These continued success highlights the growing demand for improved imaging resolution. Despite this, discussions regarding the achievable resolution of velocity mapping remain ongoing. Many studies propose tailored VMI designs [279–282], such as implementing additional electrodes or thick-lens geometries, to enhance resolution. However, these works typically provide only upper-bound estimates of the attainable resolution, without addressing how actual performance may vary under different experimental conditions or molecular systems.

A number of studies have investigated and derived the key factors influencing the resolution of velocity map imaging, e. g. extension of the source volume, lens spherical aberration, etc. These works often rely on simplifications to quantify resolution and are typically applied to tailored VMI designs. Notable previous literature includes the following: the theoretically achievable resolution of 3D VMI is discussed in [283]. Analytic derivations of VMI using quadratic potentials are provided in [42], demonstrating that a source volume of 80 mm in width can be focused to a spot of 0.1 mm on the detector. Numerical approaches based on second-order Taylor expansions for both velocity and spatial mapping are presented in [40, 41]. The impact of initial ionization volume on imaging performance has been examined using several representative particle distributions of varying source sizes in [284].

Beyond the conventional VMI geometry, numerous studies have introduced improved designs aimed at optimizing imaging resolution. An implementation of an additional dispersion-compensated field near the detector to compensate for kinetic energy dispersion was proposed to compensate the focusing effect [43, 284]. An analytical approach for optimizing electrode voltages was developed to achieve near-zero spherical aberration under various imaging conditions [42]. Other designs include increasing the number of electrodes or operating at higher voltages [283]. These approaches enhance resolution by design, yielding smaller focal spot sizes on the detector for specific source volumes.

Here, we present a comprehensive study of the achievable resolution in 3D Velocity Mapping Imaging based on the conventional design introduced by Eppink and Parker [26]. Charged-particle trajectory simulations were performed using SIMION [285, 286], focusing on the detailed mapping between the initial 3D momentum and spatial distributions of the particles and their corresponding time-of-flight and arrival positions on the detector. Within this framework, we develop a generalized computational methodology that quantitatively evaluates the attainable resolution under any specified experimental conditions. Importantly, the established mapping relationship from the initial particle phase space to the detected phase space is independent of the VMI geometry and electric field configuration, making the proposed

approach broadly applicable beyond the conventional VMI setup. This generality allows the method to be readily extended to any customized VMI design, providing a universal framework for predicting and optimizing resolution in a wide range of imaging configurations.

4.2. Prerequisites

4.2.1. Technical notation

In the subsequent discussion, we employ specific notations: lowercase letters denote the initial positions and velocity components of simulated particles, i. e., in Cartesian coordinates (x, y, z, v_x, v_y, v_z) and cylindrical coordinates (r, φ_r, z, v_r, v_φ, v_z), while the detected particle positions at the detector are represented by the capital letters, i. e., in Cartesian coordinates (Y, Z) and in polar coordinates (R, θ_R), and the time-of-flight (t_{ToF}).

Next, as is illustrated by (4.3), we can express the VMI mapping using energetic representation for all particles independently of their mass. This has a benefit for discussion of the VMI resolution as the obtained spectrometer description will be valid for detection of all particles independently of their masses. Further, we use $E_{\mathrm{K}\parallel}$ to label the particle's initial kinetic energy corresponding to velocity parallel to the detector plane $v_\parallel$(v_y or v_z. In this work, we only set velocity along y in the simulation), and $E_{\mathrm{K}\perp}$ for the kinetic energy corresponding to velocity perpendicular toward the detector plane $v_\perp$(v_x).

These notations will be utilized throughout the following analysis, with appropriate coordinate systems selected according to convenience.

4.2.2. Approach

In VMI experiments, charged particles present in an interaction region of spectrometer are accelerated by an electric field toward a position-sensitive detector. The position $\vec{R}$ on the detector is determined in first order approximation by the projection of the particle's initial velocities ($v_\parallel$) into the detector's plane given by

$$\vec{R} = f_M(\vec{v}_\parallel \cdot t_{\mathrm{ToF}}). \tag{4.1}$$

Here, t_{ToF} is the particle's time-of-flight from its initial position to the detector and f_M is the mapping function of the spectrometer. Assuming homogeneous electric fields, we can assume that t_{ToF} is linearly dependent on the term $\sqrt{m/q}$ [287] with the particles mass and charge denoted by m and q, respectively. The time-of-flight has, therefore, a functional form given by $t_{\mathrm{ToF}} = d_{\mathrm{ToF}}\sqrt{m/q}$ with $d_{\mathrm{ToF}} \neq f\left(m, q\right)$. Similarly, we can express $v_\parallel$ through a corresponding kinetic energy of the velocity components parallel to the detector $E_{\mathrm{K}\parallel}$ and thus rewrite (4.1) into

$$\vec{R} = f_M\left(\sqrt{\frac{E_{\mathrm{K}\parallel}}{m}} \cdot d_{\mathrm{ToF}}\sqrt{\frac{m}{q}} \cdot \frac{\vec{v}_\parallel}{|\vec{v}_\parallel|}\right) \tag{4.2}$$

$$= f_M\left(\sqrt{E_{\mathrm{K}\parallel}} \cdot \frac{d_{\mathrm{ToF}}}{\sqrt{q}} \cdot \frac{\vec{v}_\parallel}{|\vec{v}_\parallel|}\right). \tag{4.3}$$

Ideally, d_{ToF} is constant and the mapping function linear $f_M(\vec{k}) = M \cdot \vec{k}$, i. e.,

$$\vec{R} = M \cdot \sqrt{E_{\mathrm{K}\parallel}} \cdot \frac{d_{\mathrm{ToF}}}{\sqrt{q}} \cdot \frac{\vec{v}_\parallel}{|\vec{v}_\parallel|}, \tag{4.4}$$

which would yield from (4.3) a quadratic calibration function for the VMI spectrometer as

$$E_{\mathrm{K}\parallel} = \mathrm{Const.} \cdot R^2. \tag{4.5}$$

For a real VMI experiment, we usually try to search for such an electric field conditions that make M constant through the whole detector, i. e., fulfill the linear mapping condition. Unfortunately, small deviations from the linearity are typically obtained across the whole detector radius. Therefore, in the case of the simulations, we will present the characterization of the VMI using interpolation calibration, which makes our result effectively independent on a calibration function. A small changes to the results are expected when using quadratic and quartic calibration functions, which comparison with the interpolation calibration is discussed in Section B.1.

Next, we usually look for such a electric field conditions that diminish effects of initial particle's position and axial velocity on the VMI imaging. While the former is given by a charged particle ensemble preparation, e. g., laser focus size and molecular beam size, the latter is a particle's property, which might be also detected and analyzed for a direct 3D momentum detection. Unfortunately, both effects leads to a loss of resolution in VMI experiments.

4.2.3. Applied geometry of the conventional VMI spectrometer

We designed a conventional VMI geometry [198] and implemented into the SIMION program for illustration of our methodology for characterizing the VMI resolution.

The spectrometer, shown in Fig. 4.1 a, consists of three electrodes, i. e., the repeller, extractor, and grounding electrode, each has 2 mm thick and spaced 1.5 cm apart.

The openings of the second and third electrodes are 3 cm in diameter. The third electrode is connected to a drift tube with 45.97 cm in length, and the spectrometer is terminated by a detector with a diameter of 7.5 cm. The diameter of all electrodes and the drift tube is set to 20 cm. We did not observe any boundary effects when the electrodes' diameter was reduced to 14 cm. In the implementation of the geometry in the SIMION, we applied cylindrical symmetry and grid resolution of 10 points per mm.

4.2.4. Optimization of the VMI Voltages

As a necessary prerequisite for simulation of charged particles trajectories, we searched voltage setting across the spectrometers for the VMI focusing condition using Monte-Carlo simulations implemented in the SIMION program. In the voltage optimization procedure, we calculate trajectories for pairs of particles (m/q = 18 u/e) with initial position displacements of $\delta y_1 = +1$ mm and $\delta y_2 = -1$ mm with respect to the interaction center. The corresponding relative distance of 2 mm amounts to the typical width of our molecular beam in the interaction region. Furthermore, the velocities of all simulated particles are set parallel to the detector plane. Typically, in each optimization cycle, for a given voltage setting, we simulate the trajectories of four ion pairs with a linear sequence of velocity magnitudes. The accuracy of the voltage settings is judged based

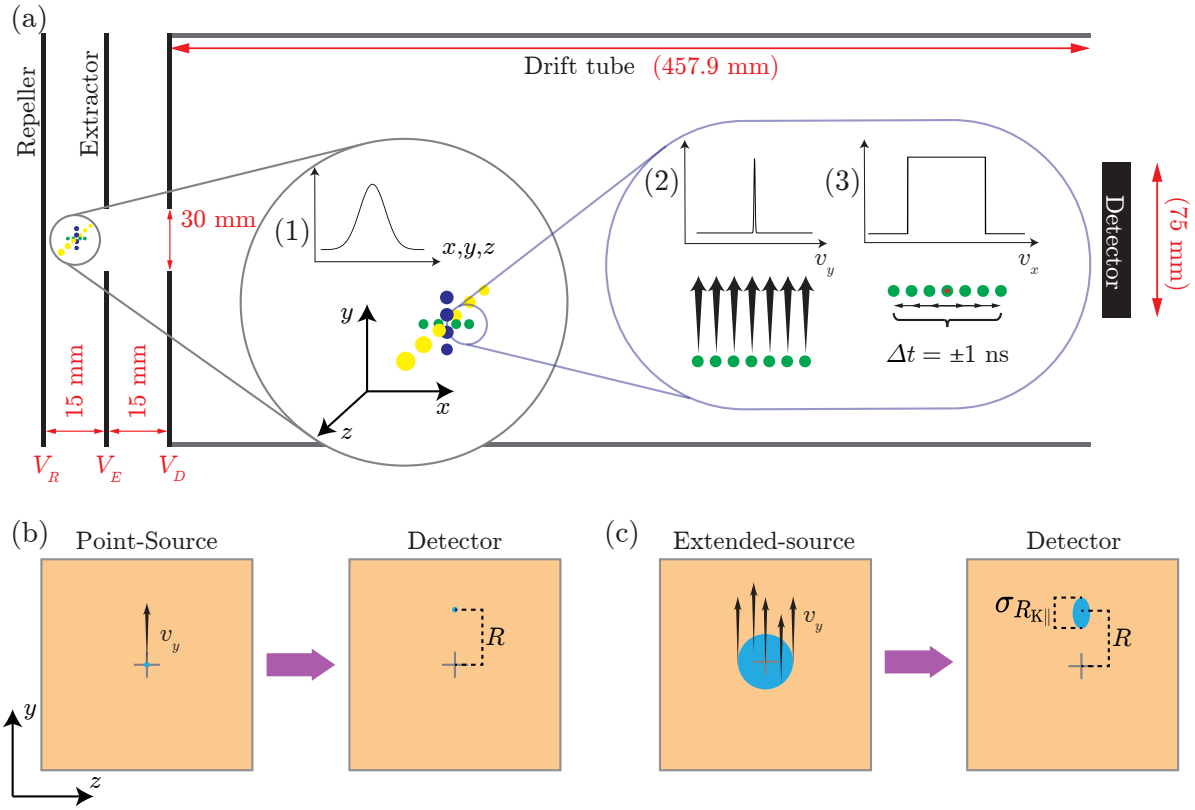

Figure 4.1.: (a) Schematic of the VMI spectrometer used in the simulations (not to scale). Insets illustrate the initial conditions for trajectory simulations investigating the effect of one-dimensional particle displacement from the center of the interaction region: (1) Charged particles are displaced along the x-, y-, or z-axis according to a Gaussian distribution (green, blue, and yellow markers, respectively). (2) All particles are assigned the same v_y component (example shown for displacement along the x-axis). (3) A v_x component is assigned from a uniform distribution such that the resulting t_{ToF} spans ±1 ns around $t_{\mathrm{ToF}}(v_x = 0$ marked with a red point). (b) Illustration for a point source: VMI mapping results in a single detection point on the detector. (c) Illustration for an extended source: VMI mapping results in a spatially delocalized detection.

on the mutual distance between the mapped particles within each pair and the linearity of the velocity mapping according to (4.4). Additionally, the optimized voltages must map the ion pair with the highest velocity at the edge of the detector to set the range of the detectable $E_{\mathrm{K}\|}$. The voltages applied to the repeller and extractor under the VMI focusing condition optimized for ions with $E_{\mathrm{K}\|}$ up to 8 eV are $U_{\mathrm{Rep}} = 4653.3$ V and $U_{\mathrm{Ext}} = 3520.3$ V.

4.3. Quantifying spatial resolution

4.3.1. VMI calibration

There are various practical approaches for the VMI calibration, including direct simulation of charged-particles trajectories, measurement of VMI images of particles with well known kinetic energy distributions, or in case of perpendicular geometry of

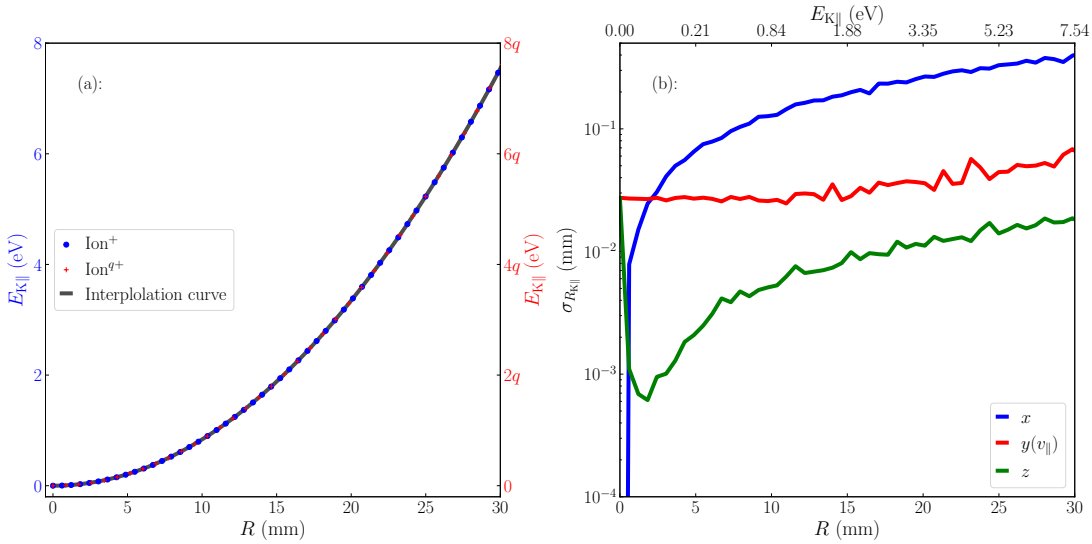

Figure 4.2.: (a) Dependence of $E_{K\parallel}$ on particles' radial position of arrival at detector R. Data obtained from trajectory simulations with singly- and multiply-charged particles are represented by blue and red markers, respectively, and are corresponding to the left-blue and right-red y-axes, respectively. Calibration of $E_{K\parallel}$ on R using interpolation model is shown in black curve. (b) Standard deviation of R as a function of the detector radius R for samples with one-dimensional Gaussian-distributed initial positions along the x-axis (blue), y-axis (red), and z-axis (green). In all three cases, particle trajectories were simulated with an initial velocity along the y-axis, following a uniform distribution corresponding to a slicing window of $\Delta t = \pm 1$ ns. The secondary y-axis (top) indicates the $E_{K\parallel}$ values corresponding to R.

the VMI spectrometer, fitting the zero-velocity positions-of-arrival of various charged particles according to their time-of-flights using known spectrometer's magnification factor and particles' mass-to-charge ratios. Regardless of the calibration approach, the given calibration formula is typically valid only for ideal conditions of no initial particle displacement and zero initial velocity.

To calibrate the modeled VMI spectrometer, we simulated trajectories of 5001 particles with stepwise velocity magnitudes corresponding to parallel kinetic energies up to $E_{K\parallel} = 8$ eV for singly charged ions and up to $E_{K\parallel} = 16$ eV for doubly charged ions, all starting from the initial position $\vec{r}_0 = (0, 0, 0)$. The resulting particles' radial positions of arrival R at the detector as a function of initial $E_{K\parallel}$ are presented in Fig. 4.2 a. The blue markers, associated with the left blue-colored y-axis represents the calibration curve for singly charged ions Ion^+. The red markers, associated with the right red-colored y-axis, corresponds to the trajectory simulations of multi-charged ions Ion^{q+}. Here, the notation q is used to emphasize the generalizability of the calibration result to multiply-charged ions, despite being derived from the simulations of doubly-charged particles.

In Fig. 4.2 a, the results for singly- and multi-charged particles are overlaid. This is because we set the limits for the y-axis of multi-charged particles by limits of y-axis for singly-charged particles multiplied by a factor q. This illustrates that also the VMI calibration obtained for singly-charged particles can be used to calculate the VMI calibration for multiply-charged particles when properly multiplied by q-factor. Similarly, all our findings for singly-charged particles can be easily applied to detection of multiply-charged particles through q-factor multiplication.

The solid black line in Fig. 4.2 a represents the VMI calibration curve obtained using

the interpolation model, which allows accurate calibration of mapping based on the simulated data points. Under ideal conditions, a quadratic fitting model can also provide a reliable calibration; however, this approach often becomes inadequate for non-conventional VMI spectrometers. For example, in double-sided VMI configurations, the voltage settings must compromise the resolution on both sides, often resulting in non-ideal linearity at higher kinetic energy region. In such cases, the interpolation method is always preferred as it effectively captures nonlinear relationship and enables more accurate calibration.

4.3.2. Effect of initial position

Firstly, we examine how initial position displacements along each of the Cartesian coordinates affect the resolution in VMI. For each axis (x, y, and z), a series of particle trajectory simulations was performed using the parameters illustrated in the insets of Fig. 4.1 a: (1) A set of $n = 500$ particles was generated with displacement along one axis according to a Gaussian distribution $G_l(\mu, \sigma)$, where $l \in \{x, y, z\}$, $\mu = 0$, and $\sigma = 851$ μm, corresponding to a full width at half maximum (FWHM) of 2000 μm. (2) All particles in the ensemble were assigned a single initial velocity along the y-axis (v_y) ranging from 0 km/s to 5 km/s, with a step size of 0.1 km/s. (3) The initial velocity along the x-axis (v_x) was assigned from a uniform distribution, with a range chosen such that the resulting t_{ToF} spanned $\Delta t = \pm 1$ ns relative to the reference point defined by $v_x = 0$, thereby simulating the temporal width introduced by signal slicing.

In practice, the detected particle signals are limited by the finite temporal resolution of the experimental detection apparatus. For example, the Timepix3 camera provides a timing resolution of 1.7 ns, which corresponds to a minimum measurable temporal window of $\Delta t = 1.7$ ns for detected particles. This finite resolution must be taken into account to realistically describe the temporal distribution of arrival times, rather than assuming an idealized Dirac delta function, i. e., $v_x = 0$ and $\Delta t = 0$. Incorporating this temporal spread is essential for accurately characterizing Newton sphere slices and reconstructing three–dimensional momentum distributions in the VMI applications.

Next, we evaluate the standard deviation of the particles' positions of arrival at the detector R. For each ensemble of particles $\{i\}, i \leq n$, with a given v_y and initial displacement along, e. g., the x-axis, we recorded the set of radial positions-of-arrival on the detector, $\{R_i(v_y, x_{0i})\}$, from the trajectory simulations. The standard deviation of R for a specific v_y from displacement along the x-axis was then calculated as

$$\sigma_{R_{\mathrm{K}\|}}\Big(G(0, \sigma_x), v_y\Big) = \sqrt{\frac{1}{n-1}\sum_{i=1}^{n}(R_i - R_{\mathrm{c}})^2}, \tag{4.6}$$

where R_{c} is the calibrated radial position of the ensemble for the given $E_{\mathrm{K}\|}$ based on the relationship from Fig. 4.2 a. The calculated standard deviation reflects the VMI spatial resolution at a given v_y corresponding to $E_{\mathrm{K}\|}$. And subsequently to the detector radius R using the mapping calibration, thereby directly associating the spatial resolution with a specific detector radius R. Similarly, standard deviations are also obtained for cases where the initial spatial displacements are applied along the y- and z-axes. The resulting dependencies of $\sigma_{R_{\mathrm{K}\|}}$ on detector radius R is also shown in Fig. 4.2 b.

As illustrated in Fig. 4.2 b, displacement along any of the Cartesian axes leads to a loss of spatial resolution, particularly for particles with higher kinetic energies. However,

the behavior differs markedly among the three directions. For the y- and z-axes, the initial standard deviation does not vanish and both curves start from the same non-zero value. This arises because in (4.6), the radius $R_c = \sqrt{Y^2 + Z^2}$ is used; although $E_{K\parallel} = 0$, the presence of an initial Gaussian distribution along y- and z-axes results in $R_c \neq 0$. In contrast, for the x-axis, the Gaussian distribution along x-axis projects onto the yz-plane at the zero point, yielding $R_c = 0$. As $E_{K\parallel}$ increases, the x-axis exhibits a much steeper growth compared to the z-axis, reaching approximately $3 \cdot 10^{-1}$ mm at the detector edge, whereas the z-axis reaches only about $1 \cdot 10^{-2}$ mm. The y-axis shows a different behavior due to the initial velocity being aligned with it. The standard deviation remains nearly constant at small $E_{K\parallel}$ and begins to increase slightly beyond $R > 12$ mm ($E_{K\parallel} > 1$ eV), rising from roughly $2 \cdot 10^{-2}$ mm to $4 \cdot 10^{-2}$ mm at the detector edge.

The particle ensembles used here for trajectory simulations follow the Gaussian distribution $G_l(0, 851\ \mu\text{m}), l \in \{x, y, z\}$. Similar and more detailed results for trajectory simulations using different FWHM are discussed in Section B.4 in Appendix.

4.3.3. Effect of initial axial velocity

In the prior section, we considered only the velocity components parallel to the detector surface, i. e., $E_{K\parallel}$, while introducing a small uniform distribution in v_x corresponding to $\Delta t = \pm 1$ ns, in order to mimic the finite temporal resolution of real detection systems. However, the effect of increasing v_x beyond this narrow range was neglected. This axial velocity component has a major impact on the time-of-flight t_{ToF}, leading not only to a broadening of the temporal resolution but also to a systematic shift in the measured flight times.

To evaluate the influence of $E_{K\perp}$ on VMI spatial resolution, we performed simulations under the conditions described in subsection 4.3.2, with an additional shift introduced along the v_x direction. Taking the time-of-flight (t) for $v_x = 0$ as the reference zero-point, we selected a range of v_x values such that the corresponding central arrival times were offset from this zero-point. Specifically, the simulated temporal shifting was set from $t = -20$ ns to $t = 20$ ns, with appropriately chosen time steps. The simulation results for the x-, y-, and z-directions are shown in Fig. B.2 in Appendix. While the x- and z-directions remain essentially unchanged, the y-direction exhibits an increase in $\sigma_{R_{K\parallel}}$ with increasing $|t|$. This increase closely follows a horizontal shift: taking the curve from $t = 0$ as a reference, we computed the difference between the distributions at each t and the reference curve, normalized by t, to quantify the change in standard deviation per unit temporal shift. The upper bound of this coefficient is approximately 0.008 mm/ns. More detailed results are discussed in Section B.2.

4.3.4. Calculating the final spatial resolution

From Fig. 4.2, we established both the calibration from R to $E_{K\parallel}$ for the VMI spectrometer and the base-line distributions of $\sigma_{R_{K\parallel}}$ as functions of R for initial displacements along the x-, y-, and z-axes respectively. Based on these results and (4.7), we can calculate the VMI spatial resolution for arbitrary initial particle distributions. Here, we focus on explaining the calculation procedure, discussing and comparing between calculated and simulated results.

$$f_{\sigma_{R_{K\parallel}}}(R) = \sqrt{\left(\frac{f_{\sigma_{R_{x_b}}} \cdot \sigma_x}{\sigma_{x_b}}\right)^2 + \left(\frac{f_{\sigma_{R_{y_b}}} \cdot \sigma_y}{\sigma_{y_b}} \cdot \left(1 + \frac{c \cdot \sigma_y}{\sigma_{y_b}} \cdot t\right)\right)^2 + \left(\frac{f_{\sigma_{R_{z_b}}} \cdot \sigma_z}{\sigma_{z_b}}\right)^2} \tag{4.7}$$

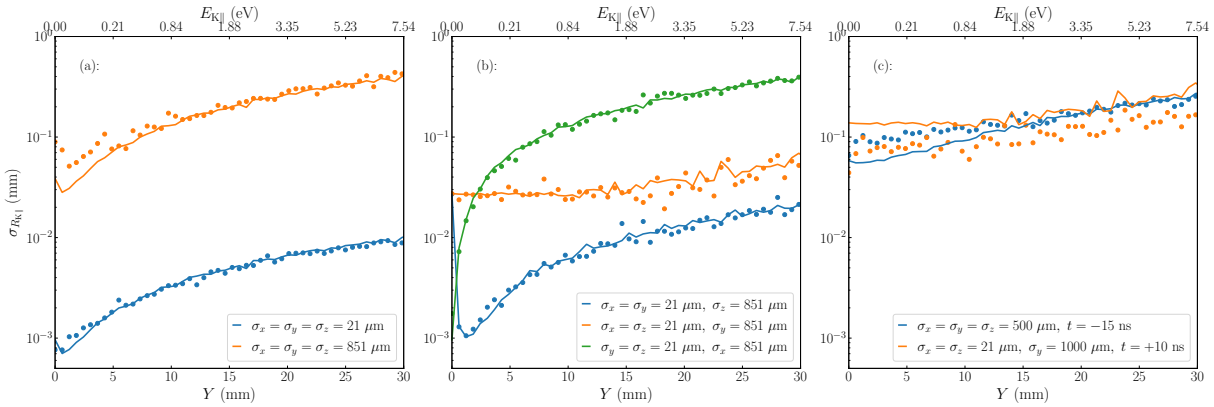

Figure 4.3.: Comparison of the simulated and calculated standard deviation of R as a function of the detector radius R under the corresponding initial particle distribution conditions. Scatter plots represent simulation results, while solid curves correspond to calculations based on (4.7). (a), (b), and (c) illustrate three representative cases: (a) uniform 3D Gaussian distribution, (b) non-uniform 3D Gaussian distribution, and (c) distribution with an applied temporal offset.

In (4.7), $f_{\sigma_{R_{i_b}}}$, where $i \in \{x, y, z\}$, denotes the base-line standard deviation of R along single x, y, or z-axes as a function of R, corresponding to the three curves in Fig. 4.2 b. The values σ_{i_b}, where $i \in \{x, y, z\}$, represents the σ of the 1D Gaussian distribution used for the base-line, which in this work is 851 μm. The coefficient c is the shifting coefficient for $\sigma_{R_{K\parallel}}$ per unit time in the curve, with an upper bound of $c = 0.008$ mm/ns in our analysis. $\sigma_{x,y,z}$ and t correspond to the standard deviations of the target initial particle distribution and the temporal shift relative to the zero point, respectively. The resulting $f_{\sigma_{R_{K\parallel}}}(R)$ gives the calculated standard deviation of R as a function of R for the given initial particle distribution.

In Fig. 4.3, we present several examples comparing the calculated results with the corresponding simulation data. Taking Fig. 4.3 a as an example, the blue scatter plot represents particles with initial positions following a 3D Gaussian distribution with $\sigma_x = \sigma_y = \sigma_z = 21.23$ μm (corresponding to FWHM = 50 μm), while the orange scatter plot corresponds to a broader distribution with $\sigma_x = \sigma_y = \sigma_z = 851$ μm (FWHM = 2000 μm). The simulation setup is as follows:(1) For each specific v_y value, a set of $n = 500$ particles is generated; (2) The initial velocity along the y-axis (v_y) is varied from 0 km/s to 5 km/s, with a step size of 0.1 km/s; (3) The initial velocity along the x-axis (v_x) follows a uniform distribution, with the range chosen such that the resulting t_{ToF} spans $\Delta t = \pm 1$ ns relative to the reference point defined by $v_x = 0$. The solid curves in the corresponding colors represent the results calculated using (4.7). The close agreement between the calculated and simulated values demonstrates the high predictive accuracy of our methodology.

We compared cases with non-uniform initial 3D particle distributions, see Fig. 4.3 b. Specifically, we use a broad distribution along a single axis (FWHM = 2000 μm) and a narrower distribution (FWHM = 50 μm) along the other two axes. This configuration closely mimics realistic experimental conditions in which the particle distribution is wider along the laser propagation direction than in the directions perpendicular to it. The results again demonstrate excellent agreement between the simulations and the calculations. Finally, in Fig. 4.3 c, we present results for various temporal offsets, comparing simulation data with our calculated predictions. Overall,

these comparisons confirm that by disentangling the displacement distribution into independent contributions along the x-, y-, and z-axes and recombining them, we can accurately calculate the spatial resolution under complex initial particle distributions. The key advantage of this approach is that only a single set of base-line standard deviation curves for 1D displacements along x, y, and z is required; once established, these base-lines can be extended to arbitrary distribution conditions without the need for repeated simulations, enabling one-time calibration for universal prediction.

Finally, the obtained $\sigma_{R_{\mathrm{K}\parallel}}$ values are converted into the corresponding $\Delta E_{\mathrm{K}\parallel}$, which represents the final energy resolution. By substituting $\sigma_{R_{\mathrm{K}\parallel}}$ into the calibration curve in Fig. 4.2 a, we determine the FWHM of R as $\Delta R = 2.35 \cdot \sigma_{R_{\mathrm{K}\parallel}}$ at each R position. As an example, for initial conditions of $\sigma_x = \sigma_y = 21.23$ μm and $\sigma_z = 851$ μm, the calculation at $E_{\mathrm{K}\parallel} = 5$ eV yields a corresponding energy resolution of $\Delta E_{\mathrm{K}\parallel} = 0.011$ eV(0.22%).

4.4. Temporal resolution

In the previous sections, we thoroughly analyzed the influence of initial position displacement and initial axial velocity on the spatial resolution of VMI and established a set of baseline conditions enabling the calculation of spatial resolution for arbitrary initial particle parameters. In the following sections, we shift our focus to the temporal resolution of VMI. In specific applications, such as mass spectrometry or 3D momentum reconstruction, the temporal resolution plays a critical role. Since time-of-flight is primarily determined by the axial velocity (v_x) and the mass-to-charge ratio (m/q), and is only weakly affected by the initial spatial displacement, our analysis will first focus on the effect of axial velocity followed by an investigation into how particle mass influences the temporal resolution.

Our experimental observations involving Newton spheres of neighboring mass-to-charge ratios frequently reveal peak-overlapping issues in the time-of-flight (t_{ToF}) spectra. These overlaps are primarily attributed to significant shifts in t_{ToF} induced by axial velocity components (v_x). In earlier sections, we only introduced small axial velocity components($\Delta t = 2$ ns in temporal space) to analyze their impact on the spatial resolution within slicing region. To further investigate the influence of axial velocity components, corresponding to the perpendicular kinetic energy $\pm E_{\mathrm{K}\perp}$, on t_{ToF}, we performed a series of numerical simulations using the following parameters: (a) Initial velocity directed along the $\pm x$-axis ($\pm v_x$), with corresponding kinetic energies ($\pm E_{\mathrm{K}\perp}$) ranging from -20 to 20 eV, incremented in steps of 0.5 eV; the other velocity components (v_y and v_z) are set to zero; (b) Mass-to-charge ratios (m/q) ranging from $m/q = 1$ u/e to $m/q = 100$ u/e; (c) The initial position is set at the origin, $\vec{r}_0 = (0, 0, 0)$. Fig. 4.4 a shows the relationship between t_{ToF} and $\pm E_{\mathrm{K}\perp}$ for three adjacent mass-to-charge ratios includes $m/q = 59$ u/e, $m/q = 60$ u/e, and $m/q = 61$ u/e as an illustrative example. The scatter plots show the distribution of SIMION simulation results. For clarity, we define $+E_{\mathrm{K}\perp}$ associated with an initial velocity along the $+x$ direction as positive, and along the $-x$ direction as negative. For all three mass-to-charge ratios, the distributions exhibit a trend that can be well approximated by the analytical expression in (B.33), with a detailed derivation provided in subsection B.6.3 in Appendix. This equation can be reformulated as a function of $E_{\mathrm{K}\perp}$ as:

$$t = a \cdot \sqrt{\frac{m}{q}} \mp b \cdot \frac{\sqrt{2mE_{\mathrm{K}\perp}}}{q} - c \cdot \frac{2\sqrt{m}E_{\mathrm{K}\perp}}{\sqrt{q}^3}. \tag{4.8}$$

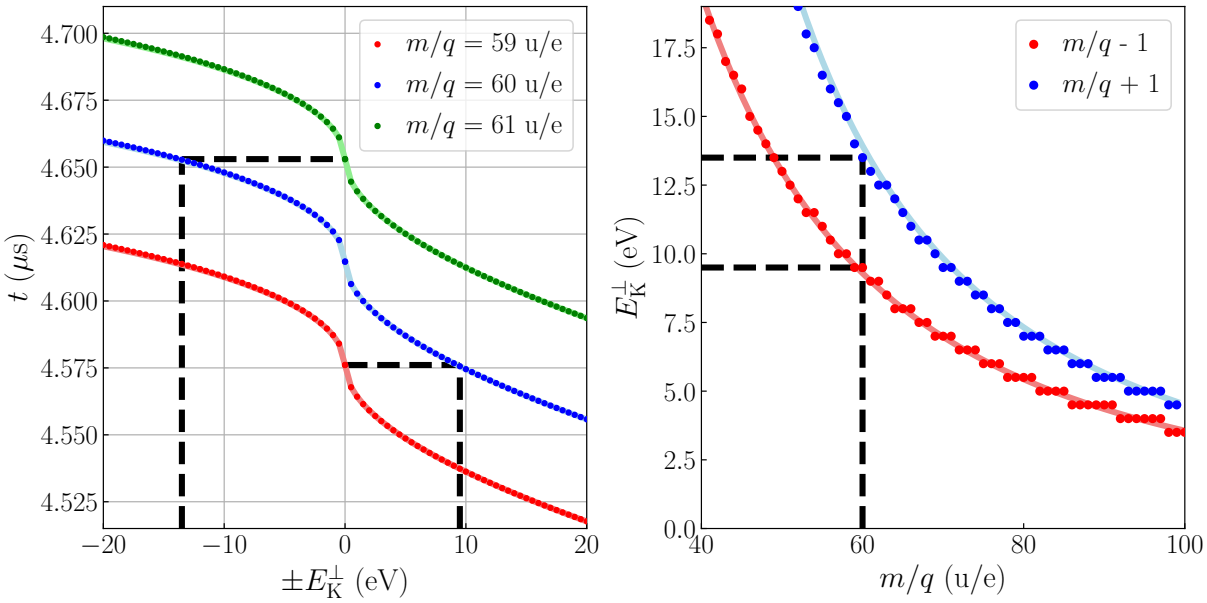

Figure 4.4.: (a) t as a function of $\pm E_{\mathrm{K}\perp}$ for three different mass-to-charge ratios (m/q = 59 u/e: red, m/q = 60 u/e: blue, and m/q = 61 u/e: green). The scatter plots represent the results from SIMION simulations, while the solid light-colored lines correspond to the fits based on (4.8). The black dashed line marks the $E_{\mathrm{K}\perp}$ required for m/q = 60 u/e to have the same t as its neighboring m/q when $E_{\mathrm{K}\perp}$ = 0. The sign of $E_{\mathrm{K}\perp}$ indicates the direction of the corresponding velocity; (b) Required $E_{\mathrm{K}\perp}$ for different mass-to-charge ratios when t overlaps with that of the adjacent m/q. Blue denotes overlap with the right-side neighbor ($m/q + 1$), while red denotes overlap with the left-side neighbor ($m/q - 1$). The scatter plots show SIMION simulation results, and the solid light-colored lines correspond to the fits based on (4.11) and (4.12). The black dashed line marks the $E_{\mathrm{K}\perp}$ required for m/q = 60 u/e to overlap in t with its neighboring m/q.

Ideally, the coefficients a, b, and c depend only on the geometry and voltage configuration of the VMI spectrometer. The fitting results obtained from (4.8) are shown as solid light-colored lines in Fig. 4.4 a. When $E_{\mathrm{K}\perp}$ reaches certain values, the corresponding t_{ToF} coincides with t_{ToF} for the neighboring mass-to-charge (m/q) when $E_{\mathrm{K}\perp}$ = 0, as indicated by the black dashed line in the figure. Such overlaps can cause ambiguity or misidentification of the m/q in experimental spectra.

Taking the case of m/q = 60 u/e as an example: if $E_{\mathrm{K}\perp}$ is approximately −13.5 eV on the left side of the graph and around +9.5 eV on the right side, ions with m/q = 60 u/e will overlap with the peak position of t for ions of adjacent mass-to-charge ratios of m/q = 59 u/e and m/q = 61 u/e, respectively. This presents a significant challenge in resolving mass-to-charge ratios in multi-mass imaging experiments. As an tool to evaluate this impact, we offer an analytical formula which provides a quantitative tool to evaluate the overlap of Newton spheres between ions with neighboring mass-to-charge ratios:

$$a \cdot \sqrt{\frac{m+1}{q}} = a\sqrt{\frac{m}{q}} + b\frac{\sqrt{2mE_{\mathrm{K}\perp(m+1)}}}{q} - c\frac{2\sqrt{m}E_{\mathrm{K}\perp(m+1)}}{\sqrt{q^3}}, \tag{4.9}$$

$$a \cdot \sqrt{\frac{m-1}{q}} = a\sqrt{\frac{m}{q}} - b\frac{\sqrt{2mE_{\mathrm{K}\perp(m-1)}}}{q} - c\frac{2\sqrt{m}E_{\mathrm{K}\perp(m-1)}}{\sqrt{q^3}}, \tag{4.10}$$

$$E_{\mathrm{K}\perp(m+1)} = \left(\frac{b\cdot\frac{\sqrt{2m}}{q} + \sqrt{\left(b\cdot\frac{\sqrt{2m}}{q}\right)^2 - 4A\cdot\left(-c\cdot\frac{2\sqrt{m}}{q^{3/2}}\right)}}{-4c\cdot\frac{\sqrt{m}}{q^{3/2}}} \right)^2, \tag{4.11}$$

$$E_{\mathrm{K}\perp(m-1)} = \left(\frac{b\cdot\frac{\sqrt{2m}}{q} + \sqrt{\left(b\cdot\frac{\sqrt{2m}}{q}\right)^2 - 4B\cdot\left(+c\cdot\frac{2\sqrt{m}}{q^{3/2}}\right)}}{+4c\cdot\frac{\sqrt{m}}{q^{3/2}}} \right)^2, \tag{4.12}$$

$$A = -a\left(\sqrt{\frac{m+1}{q}} - \sqrt{\frac{m}{q}}\right), \tag{4.13}$$

$$B = -a\left(\sqrt{\frac{m}{q}} - \sqrt{\frac{m-1}{q}}\right). \tag{4.14}$$

In the analytical expression, $E_{\mathrm{K}\perp(m+1)}$ and $E_{\mathrm{K}\perp(m-1)}$ denote the values of $E_{\mathrm{K}\perp}$ required for particles of a specific mass-to-charge ratio to have their t peaks overlap with those of adjacent mass-to-charge ratios' t with $v_x = 0$. Based on this formulation, we present in Fig. 4.4 b the calculated $E_{\mathrm{K}\perp}$ values required for the t of each ion to overlap with the temporal peak position ($t_{v_x=0}$) of its neighboring ions. Specifically, the required $E_{\mathrm{K}\perp}$ for overlap with $m/q-1$ (left-side) is shown in red, while overlap with $m/q+1$ (right-side) is shown in blue. The scatter plots represent the simulation results obtained from SIMION, whereas the solid lines correspond to the analytical results based on (4.11) and (4.12). The formula serves as a valuable aid for experimental design and for assessing the performance and resolution capabilities of a given VMI spectrometer.

4.5. Discussion

We established a quantitative model to evaluate the resolution of VMI spectrometers under specific experimental conditions by analyzing the mapping function from the initial particles' six-dimensional momentum and spatial distribution to the corresponding time-of-flight and arrival position on the detector.

We presented the characteristic mapping curve from detector radius R to $E_{\mathrm{K}\parallel}$ for particles started from the original point (0,0,0) in Fig. 4.2 a. We found $E_{\mathrm{K}\parallel}$ to be a well-defined physical variable. For particles with the same charges, their trajectories and arrival positions on the detector are determined solely by $E_{\mathrm{K}\parallel}$, independent of their masses. This allows us to describe all such particles using a single unified characteristic mapping curve. Furthermore, for ions with different charges, the same mapping can be restored by rescaling $E_{\mathrm{K}\parallel}$ according to the corresponding charges. The mapping curves of multiply-charged-particle can be mapped onto the singly-charged-particle case by applying a simple scaling factor to $E_{\mathrm{K}\parallel}$. This approach preserves the unified mapping function while requiring only a charge-dependent rescaling of the kinetic energy.

For the spatial resolution, a method based on a Taylor expansion approach was proposed in previous work [40, 41], in which electrostatic imaging was described as a mapping of the cylindrical phase-space coordinates (r, z, v_r, v_z) of a particle in the interaction region onto the detector coordinates (R, T). It is limited in that it only considers velocity components along the radial direction parallel to the detector plane, neglecting velocity components tangent to the radius in $x-y$ plane at positions away

from the origin. Our spatial resolution model disentangles the spatial contributions along the three Cartesian dimensions and considers the impact of tangential components, as shown by the green curve in Fig. 4.2 b. Under an equivalent initial displacement condition of $\sigma_x = \sigma_y = \sigma_z = 851$ μm and at $E_{\mathrm{K}\parallel} = 5$ eV, the relative contributions to the spatial spread from the perpendicular (blue), radial (red), and tangential (green) components follow an approximate ratio of $\sigma_{R_{\mathrm{K}\parallel x}} : \sigma R_{\mathrm{K}\parallel y} : \sigma R_{\mathrm{K}\parallel z} \approx 300 : 4 : 1$. This clearly indicates that spatial displacement along the x-axis imposes the strongest impact on the spatial resolution, while the tangential contribution (z) remains the smallest. Notably, this ratio is not constant but varies with $E_{\mathrm{K}\parallel}$. For instance, at lower $E_{\mathrm{K}\parallel}$ values, the x- and z-components decrease substantially, whereas the y-component remains nearly unchanged.

For other experimentally conditions, such as an interaction region that is elongated along the laser propagation direction while remaining tightly confined in the orthogonal directions due to laser focusing, where the initial particle distribution becomes anisotropic, resembling a cylinder-like source. In such cases, the spatial resolution must be evaluated using (4.7), where the weighting of each spatial displacement must be considered. For example, in the blue curve of Fig. 4.3 b, where $\sigma_x = \sigma_y = 21$ μm and $\sigma_z = 851$ μm at $E_{\mathrm{K}\parallel} = 5$ eV, the relative contributions to the spatial spread from the perpendicular (blue), radial (red), and tangential (green) components follows: $\sigma_{R_{\mathrm{K}\parallel x}} : \sigma R_{\mathrm{K}\parallel y} : \sigma R_{\mathrm{K}\parallel z} \approx 75 : 1 : 10$. In this scenario, the tangential term becomes even larger than the radial contribution and is no longer negligible. The computational model maintains good agreement with simulations over a broad range of source volumes (up to ~ 2000 μm). Beyond this range, the model cannot be further validated due to the limitations of the employed VMI geometry, where charged particles with larger volume inevitably hit on the electrodes.

The present work above does not aim to intrinsically improve the spatial resolution of VMI, but instead provides a general and quantitative framework for characterizing and estimating the achievable resolution. Within the adopted model, the dominant contribution to the resolution loss arises from the spatial displacement along the x-axis. Actual resolution enhancement would require other optimizations, such as increasing electrode voltages, designing of the electrode geometry, or introducing additional electrodes, which lie beyond the scope of this manuscript and further information can be found elsewhere [42, 43, 283]. The temporal slicing applied is restricted to a slice of $\Delta t = \pm 1$ ns around the arrival time for particles with $v_x = 0$. When considering the full Newton sphere, where the considered temporal slice extends over a broader temporal range, the corresponding spatial resolution will be modified by the superposition of multiple time slices. As illustrated in Fig. 4.3 c, the effect of temporal shifts on spatial broadening can be computed via (4.7), and summing over all relevant slices provides a methodology to prediction of the corresponding spatial resolution.

For the temporal resolution, the dominant contribution originates from the axial velocity component (v_x, or equivalently $E_{\mathrm{K}\perp}$), while the effects from v_y and v_z result primarily from electric-field inhomogeneities. In our simulations, varying $E_{\mathrm{K}\parallel}$ from 0 to 8 eV induces a time-of-flight difference of approximately 3 ns, which significantly lower than the contributions from the axial velocity component. Therefore, the subsequent analysis focuses on the influence of the axial velocity on temporal resolution. The functional dependence of t on $E_{\mathrm{K}\perp}$ is given in (4.8). Although the expression involves both $E_{\mathrm{K}\perp}$ and the mass-to-charge ratio, the coefficients a, b, and c, whose full forms are provided in (B.32) in the Appendix, depend solely on the VMI geometry and electrostatic

configuration. The derivation retains only the first-order term of the Taylor expansion, and the relative error associated with this approximation remains below 0.11% for $|v_x| \leq 30$ km/s, as shown in (B.20). Consequently, (4.8) provides a one-to-one mapping relationship between $E_{K\perp}$ and t, which agrees well with the trajectory simulations, as demonstrated for cases of $m/q = 59$ u/e, $m/q = 60$ u/e, and $m/q = 61$ u/e in Fig. 4.4 a.

Moreover, although spatial displacements along x, y, and z can in principle influence the time of flight t, the dominant contribution clearly arises from the x-direction, as it directly modifies the trajectory distance within the source region. As shown in the detailed derivation in Appendix subsection B.6.4, an initial displacement of $\sigma_x = 21$ μm induces variations in t on the order of several nanoseconds. In comparison, displacements along y and z act merely as perturbative terms superimposed on the effects of electric-field inhomogeneities and are negligible in magnitude. Therefore, our discussion of temporal resolution primarily focuses on the dependence on $E_{K\perp}$.

As illustrated in Fig. 4.4 a, ions with $m/q = 60$ u/e and $\pm E_{K\perp}$ of -13.5 eV or $+9.5$ eV exhibit time-of-flight values that coincide with those of neighboring ions with $m/q = 61$ u/e and $m/q = 59$ u/e at $E_{K\perp} = 0$ eV. In mass spectrometry, this overlap places different species within the same temporal slice, resulting in their contributions indistinguishable and hindering reliable reconstruction of full kinetic energy distributions. Such scenarios are undesirable in experimental design, as our aim is to achieve complete temporal separation of the peaks for different mass-to-charge ratios, thereby enabling accurate extraction of individual fragment yields and their corresponding $E_{K\perp}$ distributions.

Furthermore, by employing the expressions (4.11) and (4.12), we determine the maximum $E_{K\perp}$ that results in temporal overlap between adjacent mass-to-charge ratios as a function of m/q. In Fig. 4.4 b, the red and blue curves denote the conditions for overlap with the left- and right-hand neighboring species, respectively, thereby providing upper bounds on the resolvable kinetic energy range for each mass channel and enabling predictive assessment of temporal separation. The results reveal a clear trend: ions with larger m/q exhibit smaller limitation $E_{K\perp}$ for temporal overlap, indicating that higher-mass species are more difficult to resolve at the same kinetic energies. Conversely, the difference between the left- and right-hand overlap thresholds increases for lower m/q, reflecting enhanced asymmetry in temporal separation toward lighter species.

Such an analysis provides direct guidance for optimizing experimental parameters. Once the expected kinetic energy window of the target ionic fragments is given from a certain photon energy, the methodology described above enables an a prior assessment of whether the associated species can be porperly extracted and separated. Parameter optimization can then be performed accordingly. For example, doubling the electrode voltage compresses the mass spectrum in time. From the equation of motion: $q\varepsilon t^2/2m = s$, where q is the charge, ε is the electric field, m is the mass and s is flight distance. The ratio of t for the central peak position between the original and doubled voltages yields: $t_1 : t_2 = 2 : \sqrt{2}$; while the temporal spread scales as $\sigma_t = \sigma_P/(q\varepsilon)$, where P is the momentum, giving $\sigma_{t_1} : \sigma_{t_2} = 2 : 1$. This temporal shrinking facilitates channel isolation. However, it results in reducing the overall ToF range, increasing signal density and demanding the higher requirements on the temporal resolution of the detector. Overall, this provides an operational framework for evaluating whether a chosen of mass spectrometer is appropriate for the target molecular system in terms of separability.

4.6. Conclusion and Outlook

In this work, we employed SIMION-based simulations and analytical calculations to systematically investigate the multi-dimensional factors of both spatial and temporal resolution in VMI. For the spatial resolution, we established a general computational methodology that accounts for arbitrary initial particle distributions in arbitrary VMI configuration. The results demonstrate excellent agreement between theoretical predictions and simulation outcomes, thereby enabling reliable pre-evaluation of spatial resolution at specific kinetic energies. For the temporal resolution, we derived the relationship between the radial velocity distribution (v_x) and the corresponding time-of-flight t for different mass-to-charge ratios, and analyzed the resulting overlap issues in mass spectra. Furthermore, we provided explicit expressions for the upper kinetic energy limits at which adjacent mass-to-charge species become overlapped.

For the spatial resolution, the computational methodology presented here is based on a linear approximation. While this approach provides satisfactory accuracy at the order-of-magnitude level, it does not fully capture the behavior described by the Rayleigh length function. A more detailed discussion of this limitation is provided in Section B.4 from the Appendix. Moreover, as VMI electrostatic fields exhibit lens-like focusing effects at specific kinetic energies (see Fig. B.7, black arrows), the validity of the linear approximation is further compromised. The physical origin of the Rayleigh length function also requires a more thorough analysis; for example, a multi-dimensional analysis of the initial distributions from a phase space perspective would provide deeper insight. Finally, the present discussion is based solely on simulation data, and experimental validation remains absent and needed to further prove its validity.

5. Time-resolving the UV-initiated photoionization oscillation dynamics of carbonyl sulfide [1]

5.1. Introduction

Capturing ultrafast photochemical reactions with atomic-level spatial resolution and femtosecond temporal precision is a pivotal goal in physical chemistry and molecular sciences [7, 227, 288]. A variety of techniques including x-ray [214, 289] and electron diffractive imaging [290, 291], laser-induced electron diffraction (LIED) [292–294], and Coulomb-explosion ion imaging [173, 219] have been employed to achieve this goal. Further advancements in high-harmonic spectroscopy [295–297], time-of-flight mass spectrometer (TOF-MS) [298, 299] and time-resolved photoelectron spectroscopy [300–302] have significantly deepened our understanding of dynamical processes. In addition, state-of-the-art attosecond technologies [303, 304] are used to explore the dynamics of matter affected by light with high temporal precision.

Carbonyl sulfide(OCS) serves as a benchmark system and is essential for investigating photodissociation dynamics. It is particularly significant in the atmosphere as a source of sulfur, contributing to various crucial chemical catalytic reactions and attracting substantial scientific attention [89, 305–307]. For example, OCS is used as an agricultural fumigant, plays a role in the global sulfur cycle, undergoes photodissociation and photooxidation in the stratosphere, and participates in hydrolysis reactions when dissolved in ocean waters [308]. Although OCS is linear in its electronic ground state $X^1\Sigma^+$, it bends upon photoexcitation within the 190 nm to 255 nm range, in its first absorption band [309]. The structural simplicity of OCS as an asymmetric triatomic molecule is an additional advantage. This simplicity is underscored by the clear differences between the oxygen and sulfur atom, which aid in distinguishing between symmetric and antisymmetric stretching vibrations, which can is uncoupled [90]. Remarkably, the CO fragment usually remains in its electronic and vibrational ground state during the dissociation process, acting as a passive observer [310]. This stability simplifies the analysis of dissociation dynamics and facilitates the application of reduced-dimensional models [311]. The photodissociation dynamics of OCS within its first absorption band have been rigorously analyzed using both experimental [31, 310–321] and theoretical methods [311, 322–326], yielding critical insights into its

[1] This chapter is based on a manuscript in preparation by Wuwei Jin, Hubertus Bromberger, Ivo S. Vinklárek, Sergey Ryabchuk, Erik Månsson, Vincent Wanie, , Andrea Trabattoni, Francesca Calegari, Sebastian Trippel, and Jochen Küpper, "Time-resolving the UV-initiated photoionization oscillation dynamics of carbonyl sulfide", *in preparation*. My contributions to this work were participating in the experiment and recording of the data, the analysis of the data, and its interpretation with input from the collaboration. I also implemented the simulations and wrote the draft of the manuscript.

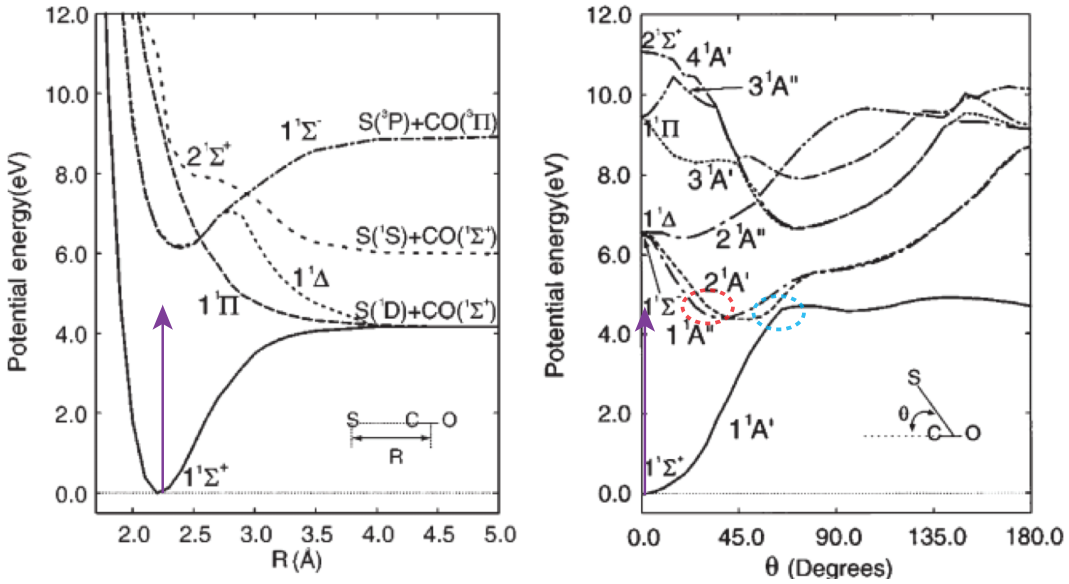

Figure 5.1.: Potential energy curves as a function of R(left) and θ(right). Figure is taken from [311].

photodissociation behavior. However, most of the studies listed focus primarily on fragmentation channels, leaving discussions on ionization and predissociation processes relatively scarce.

In the linear configuration of OCS, symmetry constraints typically inhibit dipole transitions to excited states [311]. However, Renner-Teller interactions induce bending that lifts these degeneracies, thereby allowing weakly these transitions [327]. The intensity of these transitions increases with the bending angle [327]. Predominantly, at its first absorption band at 222 nm, OCS dissociates into CO($X^1\Sigma^+$) + S($^1D_2$) or CO($X^1\Sigma^+$) + S(^3P_J) with a branching ratio of 95:5 [311] (shown in Fig. 5.1 left). For comprehensive energy diagrams of all electronic states involved, references [324, 328] should be consulted. Extensive research has detailed these dissociation pathways [90, 91, 314, 325]. The pathway leading to CO($X^1\Sigma^+$) + S($^1D_2$) is primarily associated with immediate dissociation following excitation to the $2^1A'(1^1\Delta)$ and $1^1A''(1^1\Sigma^-)$ states. Conversely, the formation of CO($X^1\Sigma^+$) + S(^3P_J) is linked to excitation to the $2^1A''(1^1\Delta)$ and the triplet $2^3A''(1^3\Sigma^-)$ metastable states, which undergo rapid predissociation through non-adiabatic transitions to the repulsive $1^3A''$ state, predissociate through non-adiabatic coupling to $1^1A''(1^1\Sigma^-)$ state or through spin-orbit coupling to the $2^1A'(1^1\Delta)$, respectively [328].

So far, the photodissociation studies of OCS have primarily utilized frequency-resolved spectroscopic methods with nanosecond lasers, such as laser-induced fluorescence (LIF) spectroscopy [90, 329, 330] and resonance-enhanced multiphoton ionization (REMPI) [31, 310, 311, 313–321, 331–337]. While these methods, coupled with computational studies [322–325, 338], have provided detailed insights into the final state distributions of photodissociation products, they lack the temporal resolution necessary to probe transient electronic and nuclear structures along the dissociation pathways. In contrast, studies of similar molecules like CS_2 have employed femtosecond UV pump pulses to excite molecules into a coherent superposition of scattering resonances within a linear geometry [339, 340]. This approach facilitates quasi-bound vibrational motions that ultimately lead to dissociation into both singlet and triplet states. Notably, the evolution of the photoelectron band, which signifies ionization into the vibrational

ground state of the cation, reveals quantum beats, underscoring the advantages of time-resolved techniques [341].

Therefore, we aim to overcome these limitations by implementing time-resolved methods to explore the ultrafast photodissociation dynamics of OCS post-UV excitation. We utilize techniques like laser-induced electron diffraction and photoelectron imaging to capture the structural and electronic state dynamics [35, 293, 294, 342]. Additionally, our quantum chemistry simulations, which model the immediate dissociation triggered by excitation to the $2^1A'(1^1\Delta)$ and $1^1A''(1^1\Sigma^-)$ states resulting in $S(^3P_J)$ products, include calculations of strong-field ionization rates [91]. Intriguingly, these models fail to replicate the rapid oscillations observed in the kinetic energy distributions of the S^+ fragments, suggesting the need for new theoretical models or modifications to existing theories to fully understand the dynamics observed in our experiments [91].

The primary aim of this study is to observe and manipulate coupled nuclear motion. By observing the time-dependent ion yields as a function of pump–probe delay, we investigate the intricate photoinduced chemical transformation dynamics of the molecule, effectively capturing high-resolution "molecular movies". Through this approach, we disentangle the bending dynamics that occur during the predissociation process. Using few-femtosecond UV pulses, we access and resolve molecular dynamics occurring on tens-of-femtosecond timescales. In particular, we employ a UV wavelength of 266 nm, positioned near the onset of the first electronically excited state, to study the underlying photoionization pathways of ground-state OCS and to probe the associated atomic motion patterns.

5.2. Method

5.2.1. Experimental setup

Details on the experimental setup were described previously [79]. Briefly, a cold molecular beam was generated through a supersonic expansion of ~10 mbar OCS seeded in 100 bar helium, utilizing a pulsed Even-Lavie valve operated at a temperature of 50 °C and at a repetition rate of 250 Hz [121]. Optimized operation conditions of the valve allowed for the generation of a dense ($> 10^7$ cm^{-3}) molecular beam in the interaction volume. A cold molecular beam with a rotational temperature in the order of $T_{\mathrm{rot}} = 0.5$ K was obtained. The sample was introduced into the ion velocity-map-imaging (VMI) spectrometer. The resulting ions are imaged using VMI combined with MCP and the converted light flashes signals are detected by a Timepix3-chip-based event-counting position-sensitive detector, which offers an effective spatial resolution of 8 megapixels with centroiding and a temporal resolution of 1.6 ns [8, 208, 209, 261].

As for the laser system employed in this experiment, carrier-phase stabilized 25 fs pulses from a Ti:sapphire amplified laser system are transmitted through a hollow-core fiber with a pressure gradient of helium for self-phase modulation. The pulse duration ((full width at half maximum)) is then compressed to approximately 5 fs using chirped mirrors, with a central wavelength around 750 nm and a repetition rate of 1 kHz [304, 343]. A beam splitter was employed to create two replicas of the NIR pulse. One pulse underwent polarization gating through waveplates [82, 344, 345] and was focused into a pulsed jet of krypton to generate an isolated UV pulse [236, 346]. An aluminum filter then selectively blocked the residual NIR light while allowing most of

the UV light to pass [347]. The resulting pulse was characterized by a 7 fs pulse duration and a central wavelength of 250 nm.

The second NIR pulse acted as a probe pulse that was collinearly recombined with the UV pulse using an annular mirror after navigating a piezoelectric delay stage, effectively forming a Mach-Zehnder-like interferometer. This configuration facilitates precise timing and control, essential for investigating ultrafast phenomena.

The UV-pump and NIR-probe pulses were temporally and spatially overlapped in the center of a VMI with their polarization parallel to the detector plane. The state-selected molecules were ionized by the pulses and the resulting ions were velocity-mapped onto a 75 mm diameter position-sensitive detector.

Normalized ion count ratios, defined as the number of detected ions divided by the total number of molecular beam pulses, were recorded for each ion channels over a range of pump-probe delay times (τ), with denser sampling intervals near the cross-correlation peak to improve temporal resolution at short delays. The OCS^+ parent ions were systematically recorded under varying UV pulse energies given by 30 nJ, 40 nJ, and 50 nJ and NIR pulse energies given by 20 μJ, 30 μJ, 40 μJ, and 60 μJ. All ion counting ratios presented in this manuscript were averaged over at least 60 seconds per time delay for each single scan. The number of scans varied under different laser energy conditions. For example, with the UV pulse energy of 40 nJ and the NIR pulse energy of 20 μJ, a total of ten scanswere recorded, corresponding to 600×250 laser pulses per time delay.

5.2.2. Simulation method

To further simulate and derive the ionization probability mapping of the molecule and compare it with the experimental results, we employed the Molecular Orbital Ammosov-Delone-Krainov (MO-ADK) model [166, 348]. This method was used to simulate the ionization probability distribution of the UV-initiated OCS. The calculation was performed for the HOMO-0 orbital, corresponding to the near ground-state molecular distribution, under the specific infrared field parameters used in the experiment. Jacobi coordinates (see Fig. 5.2) were adopted to describe the molecular geometry, where r denotes the CO bond length fixed at 1.15 Å, R is the distance between the S atom and the center of mass of the CO fragment, and θ is the angle between r and R. The CO bond length r was assumed to remain unchanged during the dynamics [310], with the primary structural change arising from the motion of the S atom. By systematically varying R and θ, the MO-ADK model yields the ionization probability (IP) for each molecular configuration, revealing how the ionization landscape evolves along the UV-triggered ionization.

5.3. Results and discussion

5.3.1. Mass spectrum for all ion channels

Fig. 5.3 presents the background-subtracted mass spectrum as a function of mass-to-charge ratio, obtained using a UV pulse energy of 50 nJ and an IR pulse energy of 30 μJ. The ion counts represent cumulative signals over all delay-time scans acquired under the specified pulse conditions. The dominant peak corresponds to OCS^+ at m/q = 60 u/e, while additional features arise from residual H_2O (m/q = 18 u/e) and

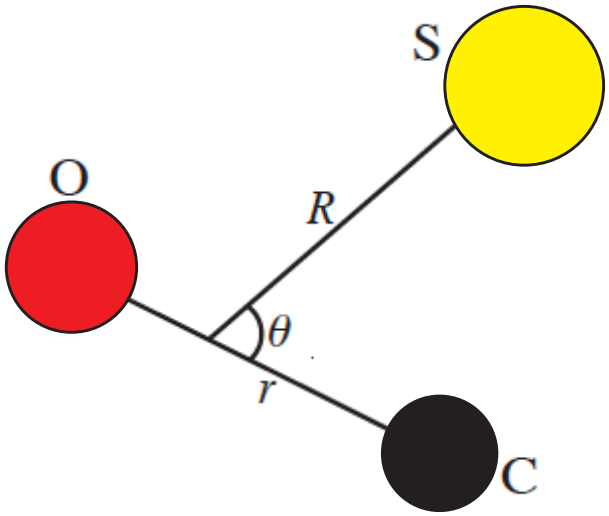

Figure 5.2.: Jacobi coordinates employed in the simulation.

chlorophenol (m/q = 128.5 u/e) originating from the molecular beam. A weak peak associated with H_2S impurities in the OCS sample appears at m/q = 34 u/e. Minor signals at m/q = 28 u/e and m/q = 32 u/e correspond to CO^+ and S^+, respectively. Owing to their low yields, these fragmentation channels lack statistical significance and are therefore excluded from further quantitative discussion. The low photodissociation yield is primarily due to the relatively low photon energy of the UV pulse employed in our experiment, which does not sufficiently overlap with the OCS absorption spectrum. Under these conditions, our analysis focuses on the dynamics of the ionized OCS^+ by examining the time-dependent yield of the parent fragmentation channel. Because parent ions inherit the motion of the carrier gas, their velocity distribution is sharply peaked. In the VMI imaging, this results in a single, localized intensity spot, enabling

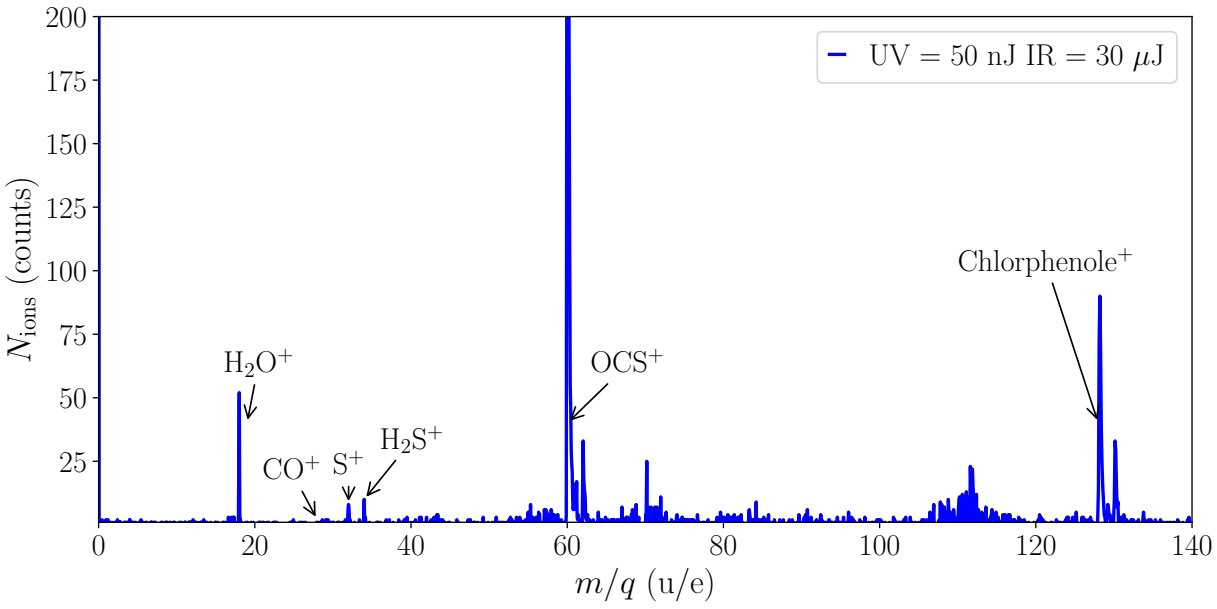

Figure 5.3.: Background substracted TOF-MS spectrum of cumulative ion counts from a single scan of total time delays under a certain pulse energy setting.

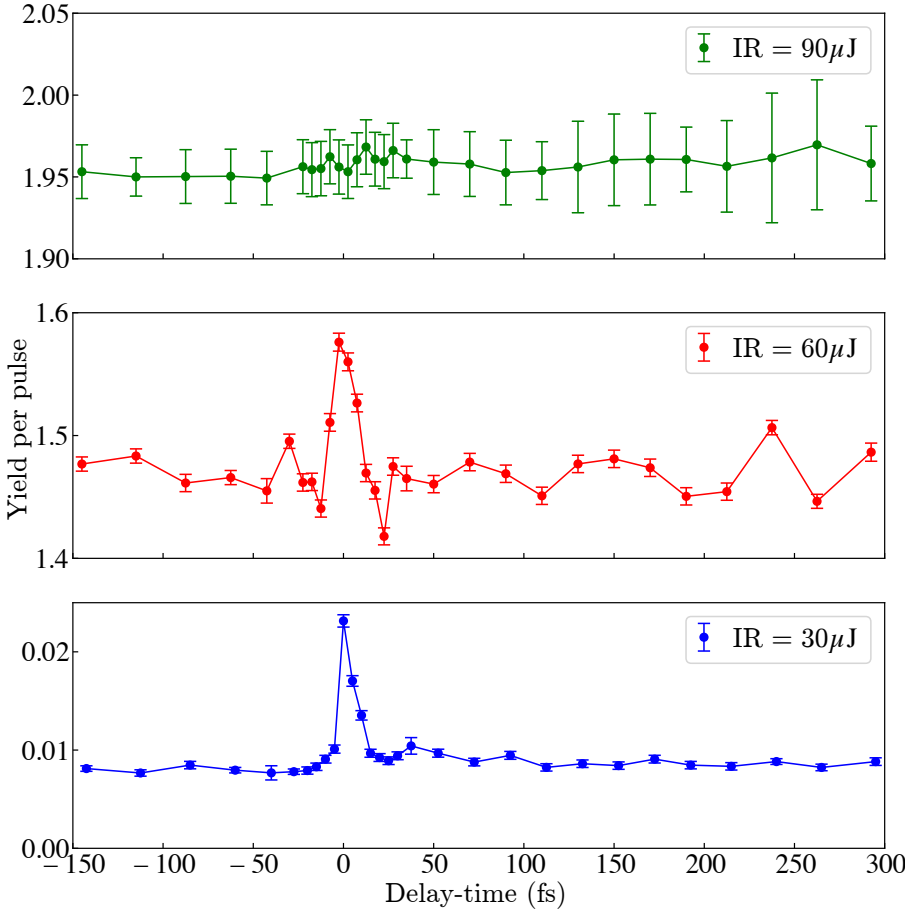

Figure 5.4.: Time-dependent OCS^+ yields signal were measured for a delay time range τ = -150 to 300 fs, using IR pulse energies of 30, 60 and 90 μJ

efficient separation of signal from background and contaminants during data processing. The following section will only present the time-resolved dynamics extracted from the OCS^+ channel.

5.3.2. IR-dependent photoionization dynamics

In Fig. 5.4, we analyze the time-dependent OCS^+ yield as a function of pump-probe delay time under different IR pulse energies. pump-probe scans were conducted over a temporal range of (-150, 300) fs to probe the ultrafast dynamics. A positive time delay indicates that the IR pulse follows the UV pulse, whereas a negative time delay corresponds to the UV pulse following the IR pulse. The three subplots (from bottom to top) correspond to increasing IR pulse energies. Although minor variations in low UV pulse conditions exist due to limited experimental statistics, the overall yield behavior is predominantly governed by the high IR intensity; a detailed discussion of UV pulse energy dependence is provided later. The results show that the primary role of the IR pulse is to establish a baseline level of OCS^+ yield. As the IR pulse energy increases, the yield per pulse at delay times away from the cross-correlation peak (where UV and IR pulses are both synchronized and delay-time is zero) increases uniformly, as illustrated in Fig. 5.4. This nearly constant enhancement across the full delay range indicates that the IR contribution is largely time-independent and originates from IR-only ionization of ground-state OCS.

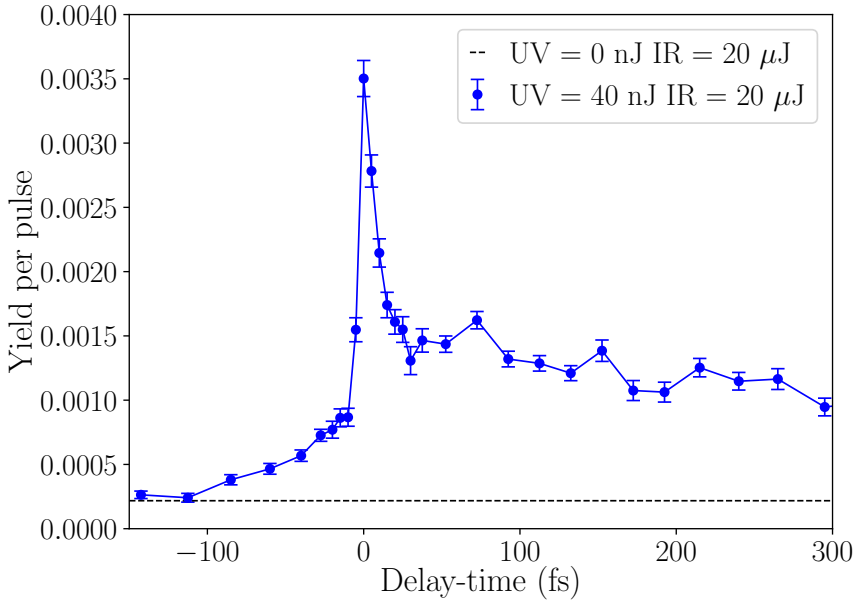

Figure 5.5.: Time-dependent OCS^+ yields were measured for a delay time range τ from -150 to 300 fs, using UV pulse energies of 40 nJ and IR pulse energies of 20 μJ in blue curve. A black dashed line indicates the OCS^+ baseline yield using IR-only.

This result allows us to disentangle the individual contributions of the IR and UV pulses. In the UV-IR pump-probe measurements, the black dashed line, called baseline (see Fig. 5.5), represents the ion yield obtained using only the IR pulse at the corresponding pulse energy, while the UV-only contribution is almost zero and therefore omitted for clarity. Any signal above this IR baseline is therefore attributed to the combined UV and IR interaction. This contribution appears primarily at positive delay times and vanishes for delays at approximately -100 fs. From the observed IR intensity dependence, we conclude that although the IR field sets the baseline level, it has minimal influence on the ultrafast temporal dynamics of the UV-IR process. This interpretation is consistent with Fig. 5.4, where higher IR pulse energies uniformly increase the yield without altering its temporal evolution.

5.3.3. UV-dependent UV-IR pump-probe photoionization dynamics

The cross-correlation peak in the OCS^+ yield near zero delay primarily originates from the temporal overlap of the two laser pulses. In Fig. 5.5, by comparing the ion yield before and after the zero-delay point, a distinct contrast is observed between the UV-IR and IR-UV pump-probe dynamics. For negative delays (IR-UV), the IR-excited state rapidly decay to the ground state within approximately 10 fs. Conversely, for positive delays (UV-IR), the OCS^+ yield exhibits a pronounced enhancement due to UV excitation, followed by a long decay extending over several hundred femtoseconds. Moreover, weak oscillatory modulations are observed between 50 fs and 300 fs, suggesting the involvement of vibrational wavepacket motion associated with excitation dynamics during the decay process.

To further quantify the role of the UV pulse, Fig. 5.6 displays the OCS^+ yield as a function of delay time for different UV pulse energies ranging from 30 nJ to 50 nJ, shown in distinct colors. The data has been normalized by dividing the yield per pulse at each delay by the sum of yields per pulse from all delays, enabling all curves to be compared

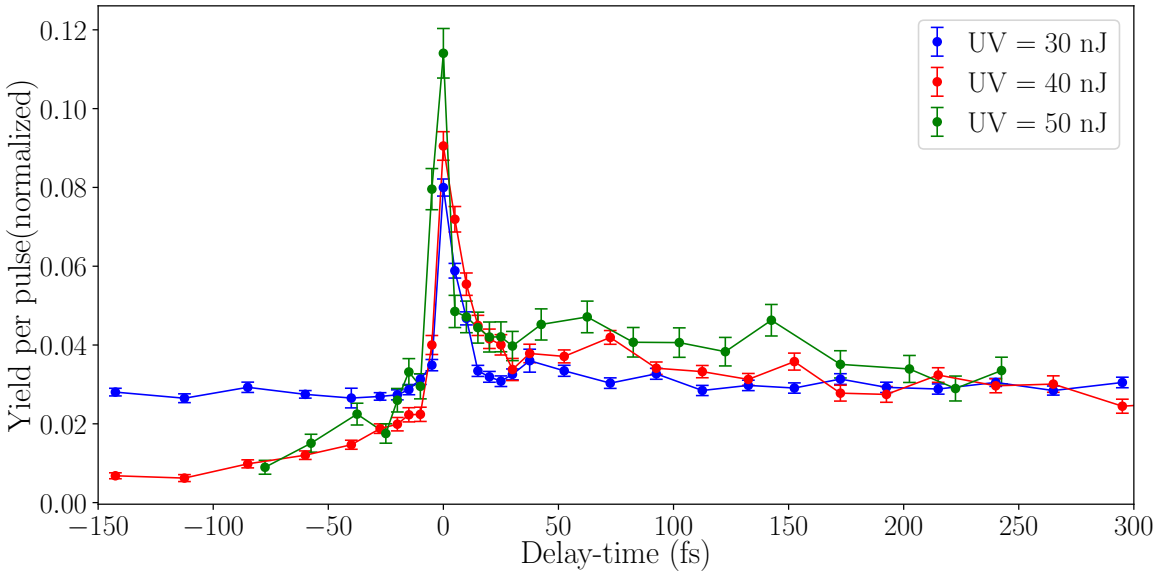

Figure 5.6.: Time-dependent OCS^+ yields signal were measured for a delay time range τ = -150 to 300 fs, using UV pulse energies of 30, 40 and 50 nJ and IR pulse energy of 20 μJ. yield per pulse has been normalized by divided the sums of yields per pulse from all delays. The changes in the baseline due to normalization are not shown in the figure.

on the same scale and highlighting differences in the dynamics. The IR pulse energy was kept approximately 20 μJ. The higher baseline of the blue curve arises from the weaker UV pulse at 30 nJ, for which the IR-only contribution becomes more prominent after normalization. As the UV pulse energy increases, both the absolute OCS^+ yield and the amplitude of the UV-IR dynamics increase, indicating enhanced excitation efficiency. At the lowest UV energy (30 nJ), the dynamics remain close to the IR-only baseline, while higher UV energies produce clear oscillatory features at positive delays. These oscillations appear slightly earlier and with larger amplitudes at higher UV energies, suggesting that stronger UV excitation more effectively populates coherently excited vibrational wavepackets or transient superposition states in OCS.

5.3.4. Simulation of ionization probability mapping

As described previously (see subsection 5.2.2), we varied the structural parameters R and θ to simulate the ionization probability (IP) of OCS using the MO-ADK model. The resulting IP distribution is shown in Fig. 5.7, plotted as a logarithmic color map with black contour lines. The red point in the upper-left corner marks the equilibrium position of OCS.

Two characteristic motion pathways emerge from the simulation. The first one is bond stretching (labelled as a blue arrow line in Fig. 5.7): When θ = 180° (no bending) and the S-CO separation R increases from 2.25 to 3.5 Å, the ionization probability exhibits an oscillatory behavior, initially rising to a local maximum at 2.75 Å, decreasing to a minimum near 3.1 Å, and then increasing again. The second one is bending motion (labelled as a yellow arrow line in Fig. 5.7): When R = 2.75 Å is held constant and the bending angle θ changes from 180° to 150°, the IP also decreases locally. Owing to the symmetry of the linear molecule of OCS, analogous oscillatory variations are observed for bending from 210° to 150°. These results demonstrate that both stretching and

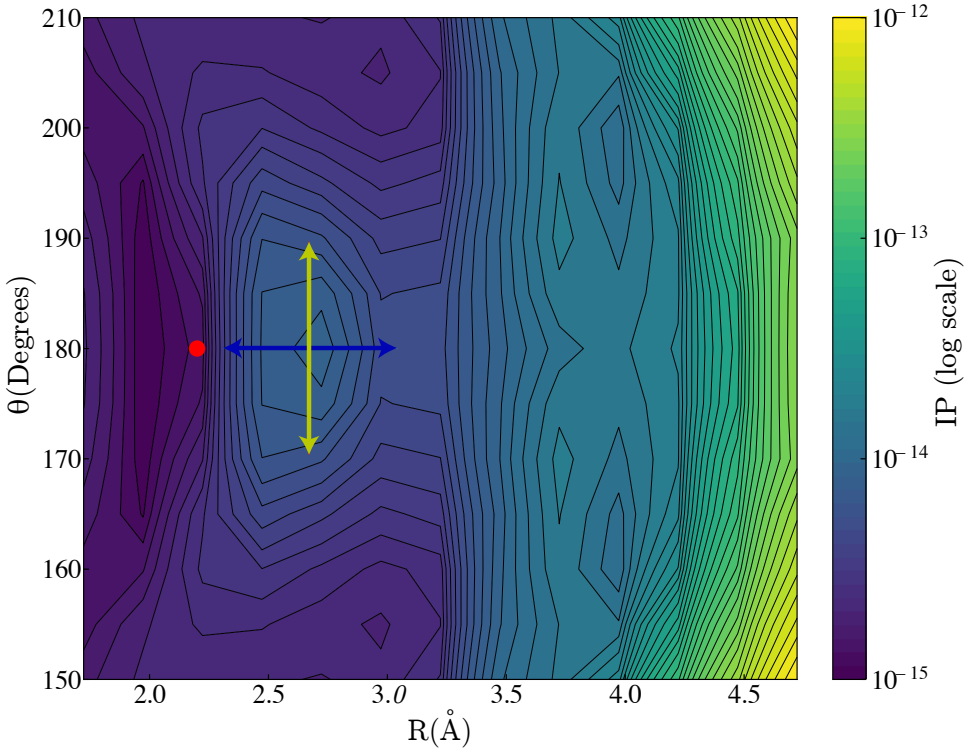

Figure 5.7.: The relative ionization probability(IP) of the OCS molecule in the IR field shown in log scale, simulated using the MO-ADK method for the HOMO-0 orbital, is shown as a function of θ and R. The red circular marker in the upper-left corner indicates the equilibrium geometry of the OCS molecule in its ground state. Blue and yellow arrow lines label two motion modes.

bending distortions of the molecular geometry lead to periodic increases and decreases in the ionization probability, suggesting a potential oscillatory signature in the ultrafast dynamics.

These results suggest that bond stretching and bending within this range can induce oscillatory variations in the ionization probability, reflecting the structural evolution of the HOMO-0 orbital during the predissociation process near the grounding states. However, it should be noted that this simulation only reveals the potential energy-dependent characteristics of the ionization probability and does not include the temporal evolution of the molecular wavepacket. Further theoretical modeling will be required to elucidate the precise origin of these ultrafast modulations.

In right panel of Fig. 5.1, the potential energy curve has been shown as a function of θ with r_{CO} = 1.13 Å and R = 2.2 Å. The purple arrow indicates the photon energy of the UV pulse used in experiment (4.66 eV, 266 nm). Within this energy range, the regions marked by the red dashed circle highlight that the $1^1A''(1^1\Sigma^-)$ and $2^1A'(1^1\Delta)$ states are nearly degenerate. This similarity arises because the former state originates from a single excitation of the $3a''$ molecular orbital, whose energy is almost similar to that of the $12a'$ orbital, reflecting the strong localization of the HOMO on the S atom in OCS [311]. If coupling occurs between these two states, such interaction may induce oscillatory behavior in the ionization probability. Furthermore, at $\theta = 60°$, the potential energy curves exhibit a conical intersection between $2^1A'$ and $1^1A'$, providing an efficient pathway for population transfer from the excited state back to the electronic ground state. This channel could potentially rationalizes the slowly relaxation dynamics

observed experimentally.

5.4. Conclusions and Outlook

This study presents a time-resolved investigation of the photoionization dynamics of OCS. By employing ultrashort UV and IR pulses, we resolve the temporal evolution of the OCS^+ yield in a UV-IR pump-probe scheme and observe a weak oscillatory features. Complementary MO-ADK calculations performed on the HOMO-0 orbital reveal that both stretching and bending motions can generate modulation patterns consistent with the experimentally observed oscillations. Despite these correlations, further advanced experimental and theoretical efforts are required to unambiguously identify the physical origin of the rapid modulations. Time-resolved electron–ion coincidence spectroscopy would provide critical insight into channel-specific dynamics and fragmentation pathways. Moreover, retrieving atomically resolved structural information, such as via laser-induced electron diffraction (LIED), would offer direct access to the transient geometries involved in the UV-initiated process.

The central wavelength and spectral bandwidth of the UV pulse play a important role in shaping the photoionization and photodissociation probability distributions of OCS. Optimizing these parameters will be essential for disentangling competing pathways and fully resolving the underlying ultrafast molecular dynamics. Fig. 5.8 shows the UV pulse spectrum used in the experiment alongside the absorption spectrum of OCS. The black curve corresponds to the experiment UV pulse spectrum (centered at approximately 266 nm), whereas the red curve represents the absorption band associated with the

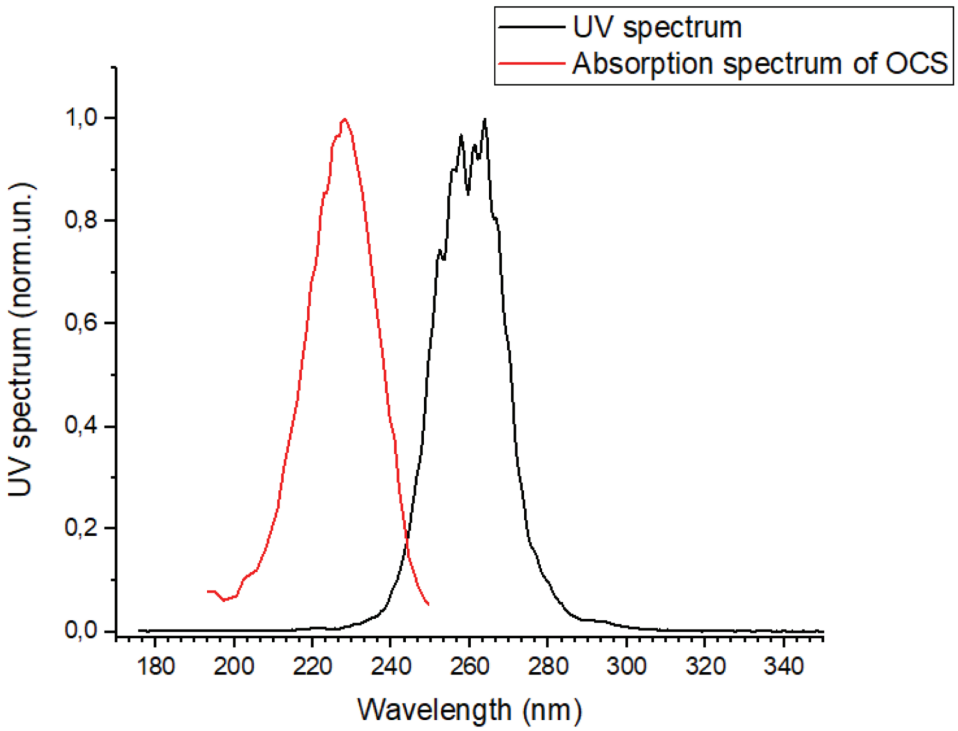

Figure 5.8.: Absorption spectrum of OCS displaying normalized absorption intensity as a function of wavelength (red line), with the UV pulse spectrum utilized in the experiment overlaid (black line).

dissociative channel of OCS (centered at 225 nm). The two spectra exhibit only a minor overlap around 245 nm. This limited spectral overlap accounts for the experimentally observed low yield of dissociative fragments (CO and S), which precludes statistical analysis, as the photon energy of the UV pulse is insufficient to excite OCS into its first absorption band at 222 nm. Instead, a significant portion of the excited population is likely promoted to intermediate states lying between the ground state and the first absorption band. To achieve higher yields of dissociation products, it would be necessary to employ UV photons with energies that correspond to the absorption peaks of OCS, thereby exciting the molecules to higher electronic states that facilitate dissociation.

During data acquisition, we encountered instability issues with the Timepix3 camera and the Pymepix software. These challenges have been addressed in subsequent software updates. To enhance temporal resolution in the critical 50-150 fs range, we recommend increasing the sampling density in these intervals during future experiments. This approach will enable a more precise analysis of the dynamic processes of the oscillation modes, thereby improving overall experimental accuracy statistically.

6. Unravelling charge transfer dynamics in microhydrated pyrrole after infrared and x-ray free electron laser ionization[1]

6.1. Introduction

Water-biomolecule interactions are vital for living organism due to their essential impact on an elementary phenomenona [57, 61, 92–94] such as biomacromolecule arrangment [62], molecule dissolvation [65, 95], biosynthetic reactions [62, 96, 97] and charge migration [349]. The asymmetric charge distribution of water molecules, with a negative charge shifted from hydrogens towards the oxygen atom, facilitates the formation of strong hydrogen bonds (H-bonds) between water and nucleophilic sites within biomolecules, thereby influencing their structures [350]. This strong H-bonding environment also opens complex reaction pathways involving charge migration and energy exchange between solute and solvent [351], as well as relaxation processes such as autoionization, fluorescence, and dissociation occurring in isolated molecules [352]. For instance, damage to various biomolecules buried in water environment can occur through secondary reactions with radicals and solvated electrons created by radiatively ionizing water [105]. Conversely, biomolecules that are directly excited or ionized can dissipate acquired energy and charge to the surrounding environment, thereby mitigating fragmentation [6, 353, 354]. Notably, electron dynamics induced by core ionization of solvated molecules [4] or supramolecular complexes lead to relaxation through photon and electron emissions via processes such as local Auger decay, or non-local intermolecular Auger and proton-mediated Auger decays [185, 355–357].

An atomic-scale insight into such processes for solvated molecules in bulk remains elusive with current experimental techniques. Consequently, experiments utilizing model systems of microsolvated biomolecules investigated in the gas phase [45] serve to narrow the gap between isolated and solvated molecules. One notable advantage of such studies is the direct investigation of specific interactions within a well-defined system, which can also be found in bulk [4].

The imaging of charge transfer using x-ray free-electron lasers (XFEL) of dissociating halomethanes provided spatiotemporal information on the critical distance for charge

[1]This chapter is based on the publication by Ivo S. Vinklárek, Wuwei Jin, Hubertus Bromberger, Thomas Kierspel, Sergey Usenko, Terry Mullins, Rebecca Boll, Yevheniy Ovcharenko, Matthew Robinson, Mukhtar Singh, Nidin Vadassery, Dimitrios Koulentianos, Michael Meyer, Sebastian Trippel, and Jochen Küpper, "Unravelling charge transfer dynamics in microhydrated pyrrole after infrared and x-ray free electron laser ionization", *in preparation*. My contributions to this work were preparing the experiment and sample-delivery setup, participating in the experiment and the recording of the data, and I assisted in analyzing of the data and writing of the manuscript.

migration between a halogen atom and a hydrocarbon residue [15, 358]. This linked collisional experiments investigating interatomic charge transfer with bio- and chemically relevant charge funnel studies in highly complex systems [15, 110, 111]. Here, we extended this approach to the prototypical biological solvated-molecule complex pyrrole-water (pyrrole-H_2O) to explore the solvation effect on the relaxation of a photoionized molecule through an infrared-pump-x-ray-probe experiment.

The pyrrole-H_2O cluster features a well-defined structure with a H-bonded water molecule acting as an H-bond acceptor bonded to the nitrogen within the pyrrole ring [106]. The pyrrole ring itself is a prominent building block of larger pyrrole-containing biomolecules, such as tryptophan, vitamin B12, chlorophyll, and hemoglobin, which makes it a highly relevant system for investigating interactions between aqueous environment and biological systems.

The excited state dynamics of pyrrole-$(H_2O)_n$ complexes was studied both by experiment and theory, mainly focusing on the role of environmental protection affecting the pyrrole dissociation [6, 106]. These studies emphasized the primary role in the dynamics played by σ N-H bond [359] for the pyrrole-H_2O complex together with π-hydrogen-bond interactions for polyhydrated pyrrole [94, 360], which through hydrogen bonding serve as a mediator for mass, energy, and charge transfer to the environments. In case of UV excitation a charge dislocation from the pyrrole aromatic ring to the hydrogen within the N-H group takes place [106], eventually leading to creation of pyrrole cation and an hydrated electron if more than 3 water molecules are present. This is a common characteristics of aromatic heterocyclic molecules practically leading to pyrrole ionic state dynamics in aqueus solution.

The orchestrated H-bond-mediated rearrangement of hydration structure was also reported for microhydrated pyrrole cation [360], breaking the ring H-bonding structure to form of linear H-bonding chain structure. Previous table-top experiments studying the fragementation of pyrrole-H_2O after outer-valence ionization revealed an environmental photoprotection by water [6], minimizing pyrrole-ring fragmentation compared to isolated pyrrole [361].

Here, we provide insights into the dynamics of charge and proton transfer in the pyrrole-H_2O dimer, mimicking the biomolecule in aqueous solution, through site-selective N(1s)-edge probing at various stages of near-infrared (NIR)-induced (pyrrole-H_2O)$^+$ fragmentation. Both strong-field NIR and XFEL pulses are expected to induce a redistribution of charges in the system through charge migration [6] and Auger processes. The outcome of these processes is anticipated to depend on the distance between pyrrole and H_2O [15, 362], thereby enabling the observation of time-dependent changes in the ion yields of the resulting products. Through the analysis of these changes, we obtain information on charge redistribution and proton transfer and their modification by solvation interactions. This not only helps to understand pyrrole-water interactions, but it also paves the way for studies of charge migration, proton transfer, and non-local Auger processes in more complex biological model systems, including hydrogen-bonding in protein interactions with aqueous environment.

6.2. Methods

6.2.1. Experimental setup and laser pulse parameters

The controlled-molecule experiments (COMO) setup [54] was used to provide a cold and pure pulsed beam of pyrrole-H_2O. Pyrrole and water were seeded in helium (80 bar) and co-expanded from the Even-Lavie valve [121], skimmed [54, 258], quantum-state dispersed, species selected and separated from the seed gas [45, 54] using the deflector at U_{defl} = 24 kV. The sample was injected to the center of the velocity-map-imaging (VMI) spectrometer installed in the Nano-sized Quantum Systems (NQS) endstation at the European x-ray free-electron laser (EuXFEL) [225]. All equipment in the COMO setup are motorized and positioning of the molecular beam in the VMI is facilitated through computer control. The density of the purified pyrrole(H_2O) sample at y = 2.33 mm(red arrow in Fig. 6.1 c) was estimated to $3 \cdot 10^7$ cm^{-3} from measurement of integral photoion yield [264], where y-axis is perpendicular to the molecular beam direction (z) and parallel to the deflection direction. See also subsection C.1.2 in the Appendix.

The molecular beam is intersected by NIR and XFEL pulses at the center of the VMI spectrometer to both trigger and probe the supramolecular dynamics. The generated ions are imaged using optimized voltages for VMI or spatial map imaging (SMI) conditions, converted to light flashes using a micro-channel-plate(MCP) and phosphor screen combination and detected using a Timepix3 event-counting pixelated detector with an effective spatial resolution of ~8 megapixel and a temporal resolution of ~1.7 ns [209, 261].

The experiment was operated at an overall 10 Hz repetition rate with an XFEL and NIR bunch structure with 18 pulses separated by ~4.9 μs, i. e., 180 pulse/s. Molecular beam pulses covered ~100 μs in the center of pulse train.

The Ti:Sapphire laser provided short (τ_{FWHM} = 12 fs) IR pulses centered at 800 nm. The size of IR laser focus was captured by a beam profiler and the profile was fitted with a 2D-Gaussian function resulting in an estimated waist of d_{FWHM_x} = 82 μm and d_{FWHM_y} = 135 μm. The peak intensity I_0 of applied laser pulses was set to $1.3 \cdot 10^{14}$ W/cm^2. The applied x-ray FEL laser centered slightly above nitrogen K-edge at 495 eV was set to energy per pulse equal to 67.5 μJ. The IR-only and FEL-only data were acquired every 1st pulse and 50th pulse of the pulse trains, respectively. See subsection C.1.1 for more calibration details.

6.2.2. Spatial separation of pyrrole-H_2O

Pyrrole-H_2O was separated from larger clusters and monomer molecules using the electrostatic deflection technique [6, 45, 144]. Fig. 6.1 illustrates the spatial profiles of undeflected pyrrole compared to deflected pyrrole and pyrrole-H_2O. Data acquisition involved scanning the molecular beam using motorized stages for the EL valve, all skimmers, and the deflector, with the spectrometer voltages optimized for spatial imaging. The top two panels Fig. 6.1 a, b depict ion-signal mapping based on time-of-arrival (ToA) and laser position within the molecular beam with the deflector off and on, respectively. The bottom plot compares the molecular beam profile without applied electrostatic deflection (black) and the molecular beam profiles of corrected Pyr^+ signal (blue) and (pyrrole-H_2O)$^+$ signal (red) when using electrostatic deflector. The correction of Pyr^+ signal involved removing contributions from (pyrrole-H_2O)$^+$ fragmentation,

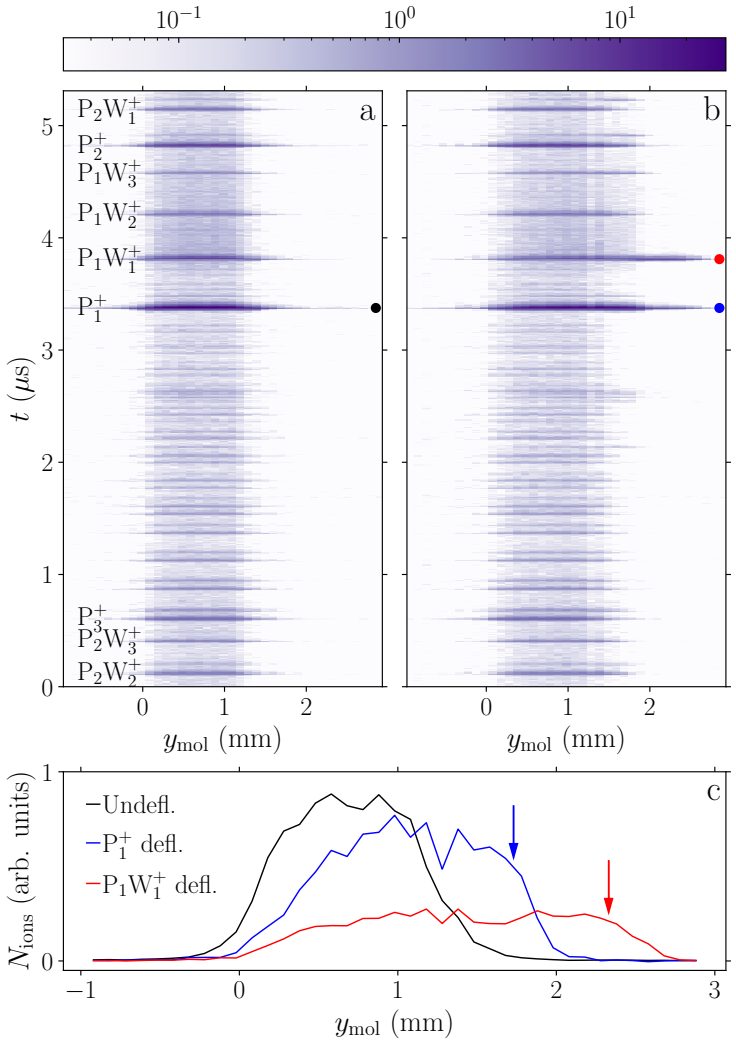

Figure 6.1.: Deflection of pyrrole-H_2O. The top two ion maps display the time-of-flight spectra corresponding to different positions of the molecular beam intersecting the ionizing laser under voltage-off (left) and deflection-voltage-on (right) conditions. P_nW_m denotes clusters composed of n pyrrole and m water molecules. The bottom graph shows comparison of molecular beam profiles of pyrrole-H_2O and corrected pyrrole. See text for details.

estimated from comparison of the relative signals of Pyr^+ and (pyrrole-H_2O)$^+$.

Experiments to investigate pyrrole-H_2O discussed in the subsequent chapters were conducted at position $y = 2.33$ mm, which is indicated by the red arrow in Fig. 6.1. The estimated pyrrole-H_2O purity was 95 %.

One source of impurity in this experiment was the distinct signal from ionized $(H_2O)_2$ and its ionic fragments. Using the ion yields from our table-top experiment [36] with $(H_2O)_2$ with similar IR laser intensities, we assume its contribution to the current results negligible. We also used a photoion-photoion coincidence (PIPICO) analysis to verify the origin of the detected H_2O^+ and H_3O^+ ions, see Fig. C.4 and Fig. C.5 in the Appendix. These PIPICO maps illustrate the origin of H_2O^+ and H_3O^+ ion signals from the pyrrole-H_2O ionization. This is in line with the 19-times larger photoionoization cross-section at 495 eV of pyrrole-H_2O than $(H_2O)_2^+$.

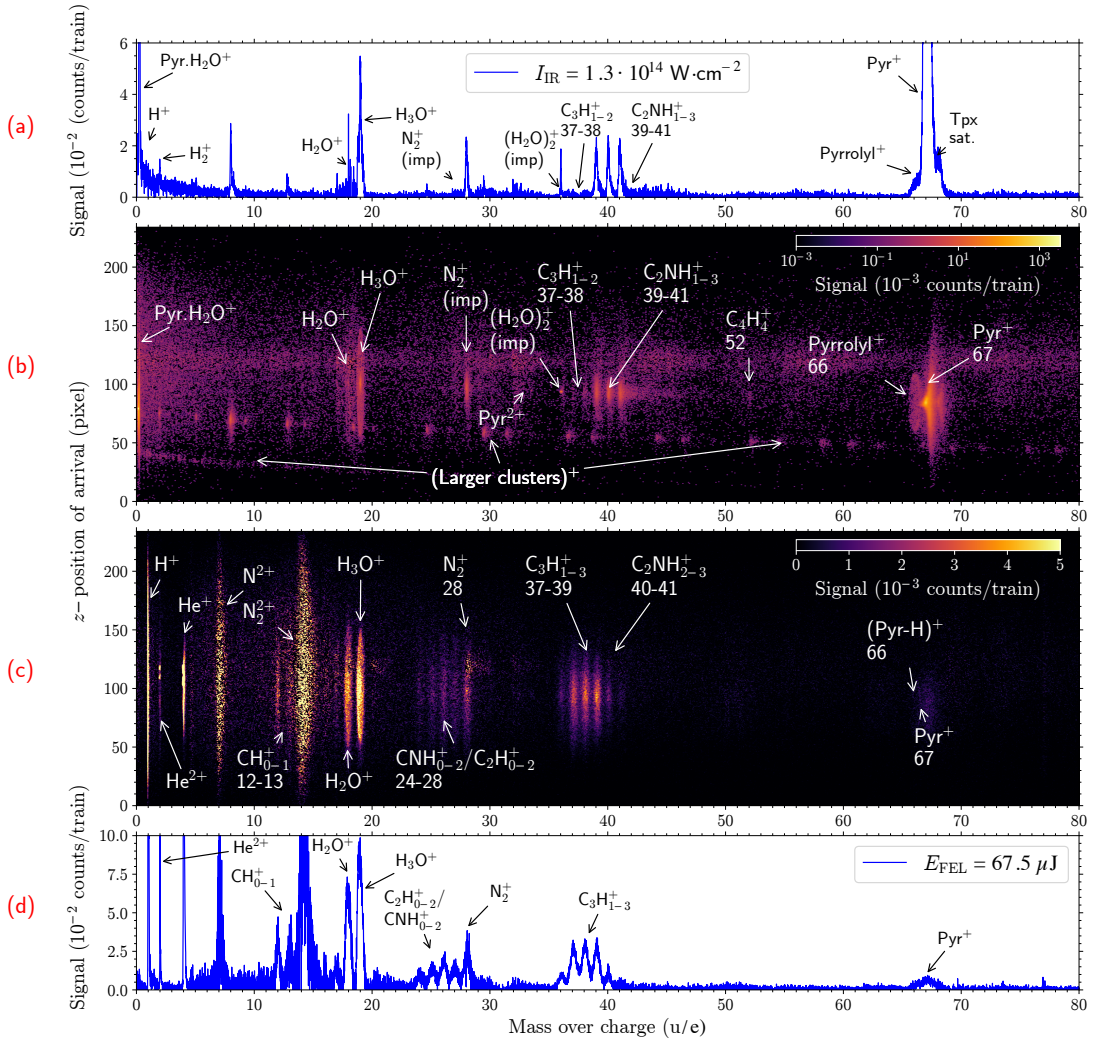

Figure 6.2.: Background corrected mass spectra and ion maps after IR-only ($\sim 3.9 \cdot 10^{14}$ W $\cdot$ cm^{-2}) and FEL-only ionization (10 % transmission). (a) Mass spectrum and (b) Ion maps of all detected ions from IR-only ionization. (c) Ion map and (d) Mass spectrum of all detected ions after FEL-only ionization. The ion maps have their vertical axes assigned to position of arrival at the detector parallel to molecular beam velocity and horizontal axes assigned to mass over charge. See text for more details.

6.3. Results

6.3.1. IR-only and FEL-only fragmentation

Fig. 6.2 (a) and Fig. 6.2 (b) show the acquired ion signal after IR-only ionization. The spectrum was measured at deflected position of pyrrole-H_2O molecular beam. The detected ions predominantly originated from singly and doubly ionized pyrrole-H_2O clusters. The use of VMI detection enabled us to distinguish between different ion sources. The ion map in Fig. 6.2 (b) provides an overview of the acquired data, where the horizontal axis represents calibrated mass-over-charge and the vertical axis denotes the z-position of arrival, which is parallel to the molecular beam direction. Each ion Newton sphere is depicted by a vertical oval structure, with its center position shifted downward proportionally to $\sqrt{m/q}$ due to the velocity of the molecular beam [36]. The time window between individual pulses in the pulse-train was approximately ~4.9 μs, resulting in

ions with $m/q < 80$ u/e appearing as displaced blobs with a systematic downward shift. Fig. 6.2 (a) shows the mass spectrum obtained by projecting Fig. 6.2 (b) onto the mass-over-charge axis. Although the spectra were acquired using deflection, there is at the bottom of the ion map weak signal corresponding to non-fragmented ions originating from the higher cluster ionization (pyrrole)$_l$-(H_2O)$_k$. See also subsection C.2.1 in the Appendix for more details about IR-only-ionization induced pyrrole-H_2O fragmentation at laser intensities in the range from $1 \cdot 10^{14}$ W $\cdot$ cm^{-2} to $4 \cdot 10^{14}$ W $\cdot$ cm^{-2}.

In addition to IR-only ionization, we also investigated FEL-only ionization of pyrrole-H_2O clusters. In contrast to IR-only ionization, which involves the ejection of valence electrons, x-ray absorptions leads to the core electron ejection, predominantly localized at the pyrrole ring ($\sim$ 97.5 %) of the pyrrole-H_2O complex. This process leads to Auger electron decay through local or non-local pathways, resulting in the production of multi-charged pyrrole-H_2O complexes [185, 355–357]. As a result, we do not detect any signal of (pyrrole-H_2O)$^+$ fragmentation following FEL ionization, apart from a minor channel associated with valence ionization by FEL, in contrast to IR ionization.

The ion map corresponding the FEL-only ionization in Fig. 6.2 (c) and mass spectrum in Fig. 6.2 (d) show that the predominant channels are H_2O^+ and H_3O^+ (designated as H_2O^+:+1 and H_3O^+:+1 channels) with similar signal magnitudes, both arising from Coulomb channels. However, the minimal signal of (Pyr-H)$^+$ and Pyr$^+$ ions implies that the generated ions undergo immediate fragmentation following Coulomb explosion. Furthermore, the secondary fragmentation of the pyrrole ring appears to slightly blur the H_3O^+ and H_2O^+ Coulomb explosion rings, resulting in less sharp profiles compared to those induced via IR ionization.

The abrupt secondary fragmentation of the pyrrole ring also results in ion signals attributed to various pyrrole residuals, including CH^+_{0-1}, $C_2H^+_{0-2}$, CNH^+_{0-2}, $C_3H^+_{0-3}$, and $C_2NH^+_{0-3}$. Unfortunately, the background nitrogen signal hinders the distinction of the N^+/NH^+ signal originating from pyrrole ring fragmentation. Nonetheless, we observe a markedly different pattern of secondary pyrrole ring fragmentation compared to the IR-only experiment. The most prominent ions derived from pyrrole ring residuals consist of (hydro)carbon-only fragments with masses in the range of $m/q = 37 - 39$ u/e. A weaker ion signal observed between $m/q = 24 - 28$ u/e does not exhibit any significant differentiation between nitrocarbon and carbon-only ion residuals.

A weak signals at (Pyr-H)$^+$ ($m/q = 66$ u/e), Pyr$^+$ ($m/q = 67$ u/e) can be also attributed to valence ionization of (pyrrole-H_2O)$^+$ via FEL photons. Nevertheless, the PIPICO map shown in Fig. C.5 in the Appendix supports that part of (Pyr-H)$^+$ and Pyr$^+$ signal originates in Coulomb explosion channels. An intriguing observation is the absence of ion signals corresponding to larger pyrrole$_n$-(H_2O)$_m$ clusters, in contrast to IR ionization, despite identical molecular beam conditions. Finally, using the FEL pulses with half of the energy (33.7 μJ), we observe exactly half of the ion yield. This indicates a single FEL photon absorption regime.

6.3.2. Dynamics of ionized pyrrole-H_2O

Since most of the dynamics related to charge, energy, and mass transfer are expected to occur on an ultrafast timescale, we conducted pump-probe scans over temporal ranges of (-0.3, 0.3) ps to probe fast dynamics. We study the dynamics of the ionized pyrrole-H_2O complex by examining the behavior of water/hydronium signals and ions generated from pyrrole ring fragmentation. Timepix3 saturation at the Pyr$^+$ signal

makes it practically impossible to determine true signal intensities. The FEL energy per pulse and IR peak intensity per pulse were set to 67.5 μJ and $1.3 \cdot 10^{14}$ W $\cdot$ cm^{-2}, respectively.

All data were calibrated to assign 3D momentum and kinetic energy, enabling the separation of different channels of individual ions: (1) Slow ions (usually $E_{tr} < 1$ eV) from singly charged pyrrole-H_2O; (2) Fast ions (usually 1.5 eV $< E_{tr} <$ 3 eV) originating from the first Coulomb explosion channels after double ionization of pyrrole-H_2O clusters; (3) Very fast ions (usually $E_{tr} > 3$ eV) from the second (or higher) Coulomb explosion channels after triple (or multi-) ionization of pyrrole-H_2O. It should be emphasize that this separation and precise assignment of ion origins are feasible in IR-only/FEL-only measurements or at delays close to zero between pump and probe pulses. At later delays, the second pulse probes complexes undergoing dynamics following the first ionizing pulse, potentially shifting the kinetic energy distribution of the channels [15, 358].

Ion maps, e. g. Fig. C.6 in the Appendix of Section C.3, used for acquired data illustration are shown in two versions. The top ion maps (with green-magenta scale) show the ion kinetic energy distribution for different pump-probe delays with subtracted incoherent sum of IR-only and FEL-only signal. The bottom ion maps show the ion kinetic energy distribution for different pump-probe delays with subtracted the specific energy-dependent delay-averaged ion yield to emphasize the observed dynamical changes. The second set of maps is especially beneficial to track relative changes of kinetic energy distribution from average pump-probe signal, which amplify the flow of ion kinetic energy distribution.

In all the plots shown in the Appendix of Section C.3, the horizontal axis represents the temporal delay. The positive direction indicates that the x-ray FEL pulse follows the IR pulse, while the negative direction indicates that the IR pulse follows the x-ray FEL pulse. Furthermore, the dependencies were normalized on the incoherent sum of IR-only and FEL-only signals indicated by the black horizontal line, which is also used for the acquired signal description and the undergoing process interpretation.

Most of the ion signal previously discussed in the static IR-only or FEL-only measurements exhibit time-dependent signals. An overview of selected signal dependencies on IR-FEL delay is available in the Appendix of Section C.3.

6.4. Discussion

6.4.1. Single color ionization

In this section, we will focus mainly on ion signal after the FEL-only ionization and its comparison to the case of IR-only ionization. The FEL-only ionization leading predominantly to double ionization of pyrrole-H_2O via Auger processes, shows vastly different fragmentation pattern compared to the IR-only ionization. Although 97.5 % FEL photons is absorbed within the pyrrole ring of pyrrole-H_2O cluster, we detect predominantly H_2O^+ and H_3O^+ signal coming from Coulomb explosion channels. We tested the acquired data by photoion-photoion coincidence analysis, see the resulting PIPICO maps in Fig. C.5 in the Appendix. The maps are shown in full range and zoomed-in areas. No observation of $(H_2O)_2^{2+}$ fragmentation coincidences and contrary, a weak coincidence observed in the area of (pyrrole-H_2O)$^{2+}$ fragmentation enable us assign H_2O^+ and H_3O^+ origin to fragmentation of doubly ionized pyrrole-H_2O clusters after charge transfer or non-local Auger decay. Nevertheless, the fragmentation seems

to be much severe as almost no singly (after Coulomb explosion channel) and no doubly-ionized pyrrole or pyrrolyl ions are detected. The charge transfer to the water after pyrrole-H_2O ionization, seems to be inefficient in preventing of the fragmentation of ionized pyrrole ring.

The FEL ionization of pyrrole-H_2O results preferentially in formation of carbon-only-containing three-atomic-ring fragments, $C_3H^+_{1-3}$, and a small contribution of $C_2NH^+_{1-3}$ ion fragments. Also, we also detect two-atomic-ring fragments $C_2H^+_{1-2}$ and CNH^+_{1-2}, and a significant contributions of H^+, C^+, and CH^+ ion signals. Contrary, the IR ionization of pyrrole-H_2O shows preference for three-atomic-ring nitro-carbon fragments and no two-atomic-ring fragments. Unfortunately, the strong background signal from doubly charged molecular nitrogen and its fragments does not allow for further investigation of smaller nitrogen containing fragments.

Interestingly, we do not observe any signal corresponding to ions of larger clusters after the FEL ionization at the exactly same molecular beam condition as in the IR-only measurement. As we would expected, the double ionization via Auger decay should cause much stronger fragmentation than the single ionization by IR, nevertheless, we would still expect to see fragments of the large clusters after charge transfer or inter-molecular Auger decay to the surrounding aqueous environment. Similarly, the ion maps reveal a stabilization of doubly charged pyrrole after the IR ionization contrary to their no detection after the FEL ionization.

The reason for our inability to observe any signal can also come directly from low ion yield originating from molecular beam after FEL-only ionization. The total signal after FEL ionization was very high in range of ~ 120 ions per train, but most of it originated from the background gas in the chamber due to the long Rayleigh length of FEL laser beam.

6.4.2. Dynamics induced by IR or FEL ionization

In this section, we offer a phenomenological perspective on the observed dynamical processes presented in Section C.3. Our goal is to understand the significance of the aqueous environment, represented by a single water molecule, in influencing the charge and energy transfer within the pyrrole-H_2O cluster.

Firstly, we assume that irradiation by an IR laser leads predominantly to single ionization followed by cluster stabilization as (pyrrole-H_2O)$^+$ or cluster fragmentation as (pyrrole)$^+$ + H_2O. Furthermore, channels of H_3O^+ + pyrrolyl and $C_2NH^+_{1-3}$ + neutral co-fragments should be populated with an one-order lower probability. Only a small fraction of clusters is also double ionized at set IR laser power conditions of $1.3 \cdot 10^{14}$ W/cm^2. These IR-doubly ionized clusters either lead to the Coulomb explosion pathway of H_3O^+ + (Pyr-H)$^+$/(pyrrole fragments)$^+$ or pyrrole^{2+} stabilization. The outcome of the IR-only ionization was investigated in IR-only static VMI/mass spectra, see the Appendix.

Depending on the pump-probe delay, we disrupt different phases of the IR-induced process by bringing additional energy and charge ($n \geq 2$). As the majority of the FEL absorption is carried out by the pyrrole ring, we can assume that the critical point of the probe-following dynamics is whether the water molecule can still work as a sink for charge and energy, or, due to its previous ejection, the gained energy and charge must be redistributed within the pyrrole residual, i. e., neutral or charged pyrrole, and its fragments for the $C_2NH^+_{1-3}$ channel.

On the other side of the pump-probe scan, the pyrrole-H_2O cluster is first predominantly doubly ionized by FEL photons leading to Coulomb explosion channels including H_2O^+ + (pyr. fragments)$^+$/pyrrole$^+$, H_3O^+ + (pyr. fragments)$^+$/pyrrolyl$^+$, H^+ + ionized co-fragments. Again, during the undergoing FEL-induced processes, an additional IR strong-field ionization is causing disrupting by bringing additional single charge and energy.

The fundamental difference between the current and previous case of the pump-probe experiment is that IR can cause ejection of valence electrons only. Secondly, the negative pump-probe direction is probing predominantly fast Coulomb explosion channels, whereas the positive pump-probe direction should reveal underlying dynamics of the slow fragmentation dynamics after single ionization of pyrrole-H_2O. Another good assumption is that the IR ionization in the negative pump-probe delay can only cause ejection of electrons from singly ionized pyrrole as the FEL-produced H_2O^+ and H_3O^+ ions have significantly higher second ionization energy.

Previous similar experiment with ability of charge spatiotemporal tracking were done on isolated halomethanes CH_3I and CH_3F [15, 358]. Those experimental results are a very good benchmark for similar studies, nevertheless, we should emphasize that our system of pyrrole-H_2O is far more complex and we cannot reach such a high multi-ionized states. Also, especially in the case of CH_3I, the experiment reached highly multi-charged iodine >+7, whereas in our experiment, we can undoubtedly see only pathways coming from triply and quadruply charged pyrrole-H_2O cluster. Therefore, we do not assume such a strong role for charge transfer across long donor acceptor distances as was presented in [15].

6.5. Conclusion and outlook

In this study, we demonstrate the use of an electrostatic deflector to purify pyrrole-H_2O clusters, which were subsequently investigated using NIR-FEL pump-probe experiments. The full-channel ion fragment maps were recorded with a data-driven Timepix3 camera. We first analyzed the fragment distributions in the NIR-only and FEL-only measurements and provided pathway analyses for the ionization processes observed in each situation.

Next, we extracted the time-dependent evolution of the ion yields at different kinetic energies from the NIR-FEL pump-probe experiments. The current yields were separated into high-, medium-, and low-kinetic-energy channels, and the corresponding reaction pathways were analyzed on the basis of Coulomb explosion dynamics.

The primary obstacle of the data acquisition, which also significantly complicated their analysis, was an enormous signal background from FEL radiation. The background-corrected figure shown in Fig. 6.2 reveal that the ion signal origin for FEL-created ions is mainly in the background. This was caused by rather high background pressure in the spectrometer chamber ($\sim 10^{-9}$ mbar) and long Rayleigh range of FEL beam. A significant improvement of the acquired data should be gain from lowering the background pressure by one to two orders. Although one should have in mind that the FEL energy per pulse should not be increased as we want to stay in one-FEL-photon absorption regime.

7. Summary and Outlook

7.1. Summary

This thesis presents the conception, realization, and application of a set of experiments designed for probing the interaction between purified neutral molecular beams and specific light fields, enabling real-time imaging of relaxation pathways across multiple channels following photoexcitation or ionization. The work spans the entire development chain, from hardware construction and spectrometer calibration to quantitative resolution analysis and experimental demonstrations using diverse laser sources, thereby providing both a technical foundation and new insight into molecular dynamics driven by intense laser fields.

In Chapter 3, the eCOMO setup was developed, assembled, and commissioned using a table-top laser system. The apparatus integrates a cold ($T_{\mathrm{rot}} \leq 1$ K), pulsed, and dense (up to $\sim 10^9$ cm^{-3}) molecular beam source with a double-sided velocity map imaging (VMI) spectrometer and two synchronized Timepix3 cameras. The *b*-type electrostatic deflector incorporated into the setup allowed spatial separation of rotational quantum states, conformers, and cluster species with distinct effective dipole-moment-to-mass ratios. The data-driven detection system enables clear separation of individual particles by their mass-to-charge ratios and facilitates the reconstruction of specific ionization channels in multi-fragmentation 3D momentum measurement. Covariance analyses further demonstrated the capability to assign electron VMIs and projected velocity distributions to distinct ion channels. Collectively, these developments establish eCOMO as a highly adaptable platform for experiments across a wide range of photon-source facilities, enabling applications in atomic, molecular, and cluster physics, as well as in chemistry, biology, and materials science.

Chapter 4 developed a generalized computational methodology for the quantitative evaluation and prediction of attainable resolution under arbitrary experimental conditions. This framework combines SIMION-based numerical simulations with analytical modeling to systematically assess both the spatial and temporal resolution of VMI spectrometers. It accommodates arbitrary initial particle distributions and electrode geometries, thereby ensuring broad applicability. The excellent agreement between calculated and simulated results validates the model's predictive capability for determining spatial resolution at specific kinetic energies. On the temporal side, the relationship between perpendicular velocity distributions and the corresponding time-of-flight for different mass-to-charge ratios was derived, identifying overlap conditions in mass spectra and providing analytical expressions for the kinetic energy thresholds at which spectral separation becomes compromised. While the linear approximation used in the spatial calculation in (4.7) offers sufficient first-order accuracy, it does not fully describe focusing effects governed by the quasi-Rayleigh-length distribution. This analysis thus highlights the need for multidimensional phase-space treatments and experimental verification to further refine resolution predictions.

Chapter 5 presented a time-resolved investigation of the UV-initiated photoionization

oscillation dynamics of OCS molecules implemented on the eCOMO setup. The study revealed ultrafast oscillatory features in the photoionization signals of OCS^+. Complementary MO-ADK calculations indicate the possible involvement of two potential molecular bond motion modes, suggesting that the observed dynamics arise from complex coupled electronic and nuclear motion that warrants deeper theoretical interpretation. This study establishes important benchmarks for future UV-induced pump-probe experiments on OCS, highlighting the critical role of optimizing pulse conditions and photon energy in selectively addressing specific molecular electronic states and in controlling the evolution of their relaxation pathways.

In Chapter 6, we extended the application to study charge-transfer dynamics in microhydrated pyrrole clusters following infrared pump and x-ray probe implemented on the COMO setup, which is an extension of the endstation at EuXFEL. The electrostatic deflector was successfully employed to purify pyrrole-H_2O clusters, and the subsequent NIR-FEL pump-probe experiments were recorded using a fully time-resolved Timepix3 detection system. Fragmentation pathways were systematically analyzed under both NIR-only and FEL-only conditions, with the NIR-only results found to be consistent with previous work [6]. Time-dependent ion yields were extracted from the pump-probe measurements and classified into high-, medium-, and low-kinetic-energy channels, enabling detailed examination of energy-dependent dissociation mechanisms. This work demonstrated the applicability of the COMO setup under high-intensity photon sources and provided a quantitative framework for analyzing ultrafast charge-transfer processes in hydrogen-bonded molecular samples.

7.2. Outlook

The research presented in this thesis establishes the eCOMO as a robust, adaptable, and high-resolution molecular beam platform, capable of addressing a wide range of scientific questions concerning molecular structure, dynamics, and reactivity. Nevertheless, several aspects can be further improved and expanded in future work.

From an instrumentation perspective, improving the vacuum level of the VMI chamber by one to two orders of magnitude would substantially suppress background noise and significantly enhance the signal-to-noise ratio in coincidence detection. Owing to momentum conservation, electrons originating from the same parent ion are emitted with much higher velocities, resulting in a single broad peak in the electron time-of-flight spectrum with FWHM of several tens of nanoseconds. Under such conditions, it becomes impossible to separate reaction channels via electron time-of-flight alone, and the measurements are particularly susceptible to background contributions. In subsequent experiments, we mitigated this issue by installing additional turbomolecular pumps and repairing a leakage at the interface on the detector. Further optimization can be achieved through pre-experimental baking of the chamber and by improving the molecular beam source, such as implementing pre-cooling procedures, to further reduce background signals. These measures have already been implemented in later experiments, resulting in a VMI chamber pressure of approximately 5×10^{-11} mbar with molecular beam off.

Because eCOMO enables full-channel detection of the 3D momentum of ions, it is particularly well suited for the analysis of reaction pathways involving multiple ionic fragments. For example, pump-probe disruptive probing method [189] can be

employed to resolve the dissociation pathways of water dimers. Beyond this, we plan to extend to more complex molecular samples, such as uracil-water clusters or chiral molecules. Owing to the transportable design of eCOMO, the setup can be relocated to different light sources as required, enabling a broad spectrum of future experiments and scientific applications. Integrating eCOMO with next-generation light sources, such as seeded free-electron lasers (FELs), will facilitate detailed investigations of Auger decay and the subsequent dissociation pathways of ionic fragments, processes that are directly relevant to radiation-induced damage and protection mechanisms in biological molecules. Furthermore, pump-probe experiments employing attosecond pulse beamlines will open new avenues for probing ultrafast electronic dynamics at even higher spatiotemporal resolution. Together, these advances will not only deepen our understanding of fundamental photo-induced processes but also bring us closer to the long-standing goal of recording molecular movies that capture chemical reactions in real time.

Methodologically, future work should focus on extending the resolution analysis framework developed in Chapter 4. A comprehensive $E_{K\|}$-dependent non-linear approximation could replace the current linear model, enabling more accurate descriptions of field-induced focusing effects at specific positions and providing deeper insight into the quasi-Rayleigh-length dependence. Experimental benchmarking of these theoretical predictions will be essential. The next step is to employ the eCOMO for dedicated measurements to further validate the applicability of the model and the accuracy of the calculated predictions.

For the OCS sample, several experimental limitations were identified during experiment, including insufficient vacuum level in the VMI chamber, imperfect molecular beam alignment, and restricted laser intensity and bandwidth, all of which led to reduced signal statistics. Furthermore, the UV excitation spectrum exhibited a redshift relative to the OCS absorption band (Fig. 5.8), implying that the photon energy was inadequate to reach dissociative excited states. Consequently, the experiment predominantly probed lower-lying electronic states, resulting in minimal fragmentation yields. Further work employing UV pulses that coincide with the absorption maxima would enable excitation into dissociative states and yield statistically significant fragmentation data. In addition, acquiring more experimental data, particularly with denser temporal sampling steps for delay-time between 50 fs to 200 fs, would allow for a more detailed verification of the oscillatory features observed in the ultrafast dynamics. Complementary detection of electron signals would further enhance the characterization of the underlying processes, while theoretical simulations of wavefunction evolution at the relevant electronic states are also required to achieve a comprehensive understanding of the time-resolved dynamics.

For the pyrrole-H_2O sample, the primary experimental challenge in this study arose from the substantial background induced by FEL radiation, mainly caused by the relatively high chamber pressure ($\sim 10^{-9}$ mbar) and the extended Rayleigh length of the FEL beam. Reducing FEL-induced background signals while maintaining single-photon absorption conditions will allow for a more detailed investigation of ultrafast charge migration and proton transfer dynamics within hydrogen-bonded networks. In addition, several reaction channels currently lack statistically significant data, and acquiring extended datasets will be essential to resolve finer details of the underlying dynamical processes. Looking ahead, future experiments at the EuXFEL combining COMO with the Reaction Microscope (REMI) will provide new opportunities

to investigate Coulomb explosion or roaming dynamics in complex chemical reactions for specific purified samples.

A. Appendix to Chapter 3

This appendix provides more configuration parameters and design details applied in the eCOMO setup.

A.1. Vacuum system

Fig. A.1 illustrates the vacuum setup, including the high-pressure gas line of the eCOMO system. The source-, deflector-, VMI- and beam-dump chambers are indicated as the light blue structure. The gas flow is depicted by red arrows starting from the Even-Lavie (EL) valve in the source chamber. The turbomolecular pumps are indicated as yellow rectangles and are discussed in the main manuscript. The roughing-line pump is indicated as OTB. The automatic gate valves are shown as blue symbols. Here, gate valves 1 and 4 are DN40-ISO-KF mini gate valves (VAT 01232-KA44). Gate valve 3 is a DN16 ISO-KF mini gate valve (VAT 01224-KA44). Gate valve 4 indicates an updated home-built automatic DN250 CF gate valve [256], which allows separating the source from the deflector chamber. This gate valve is driven by a solenoid valve (Festo VUVS-LK20-M52-AD-G18-1C1-S). All gate valves are controlled by a home-built NIM-based controller. Vacuum monitoring is accomplished by the gauges shown in Fig. A.1 as green rectangles (Pfeiffer Vacuum PKR 251, PBR260, and IKR270). All gauges are controlled and monitored by a controller (Pfeiffer TPG 366).

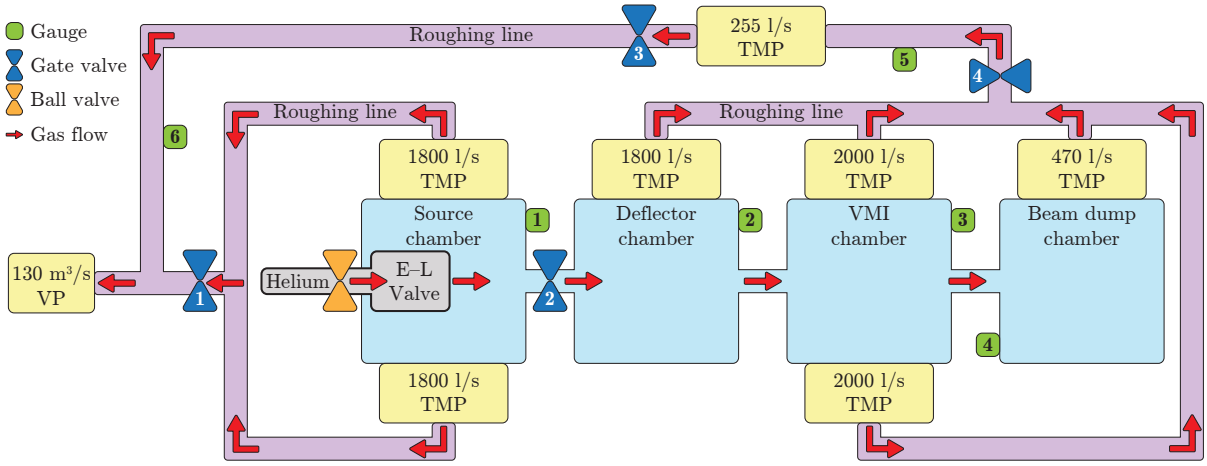

Figure A.1.: Schematic of the eCOMO vacuum system together with the high pressure gas line. Gauges and pumps are indicated as green and yellow rectangles, respectively. Red arrows depict the gas flow. Ball and gate valves are indicated by orange and blue symbols, respectively. The high-vacuum part of the setup is depicted in light blue. The roughing lines are shown in light purple. The high-pressure line and the Even-Lavie valve (EL valve) are shown by the gray shaded structure.

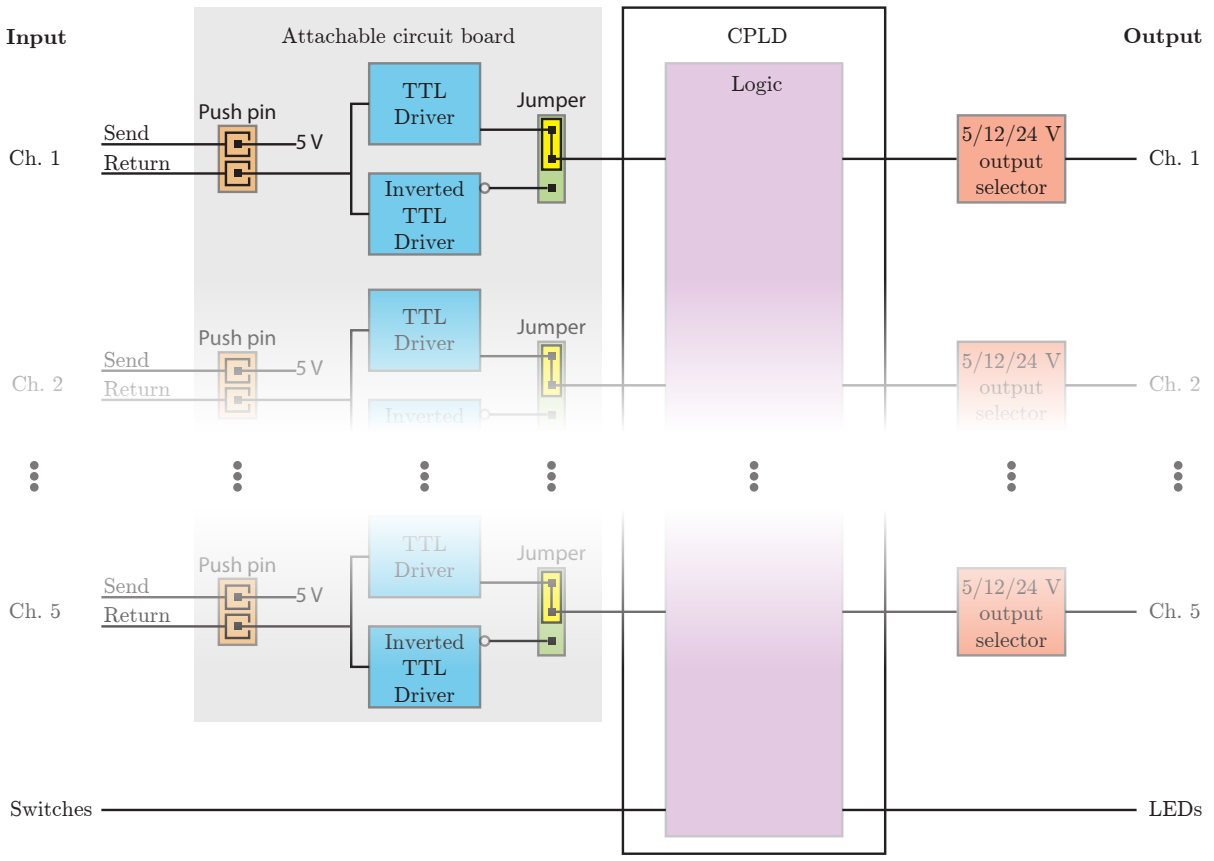

Figure A.2.: General concept of the interlock controller. The middle section is hidden for space reasons.

A.2. Interlock system

The general concept of the interlock controller logic is illustrated in Fig. A.2. The box has 5 two-wire LEMO inputs and 5 one-wire LEMO outputs. One of the two-wire input wires delivers 5 V ("Send"). The second wire is used to drive the transistor-transistor logic (TTL) driver integrated circuits (ICs) labeled as "Return" in Fig. A.2. All input channels are connected via push pins with an attachable circuit board in the interlock controller. The push pins can be used to select a specific pin assignment of the input connectors with respect to Send and Return. The Return signal drives two ICs, a TTL driver, and an inverted TTL driver, respectively. In this way, the input logic can be inverted making use of the jumpers right behind the TTL drivers. The TTL driver ICs serve also as a protection of the interlock controller regarding over voltages. The attachable circuit board can be easily replaced if necessary since it is connected to a main circuit board via push pins. A complex programmable logic (CPLD) device is used to logically connect the input signals and interlock hardware switches with the output channels and LEDs. In this way, the logical program can be changed quickly. The output voltage can be switched between 5, 12, and 24 V depending on the specific requirements of the corresponding device attached.

The front and back panel of the interlock controller are shown in Fig. A.3. The upper half of the front panel contains LED indicators and switches for the input channels. The lower half of the front panel contains LED indicators and switches to indicate the status and control the output channels. Input and output channels are provided via the back

Figure A.3.: Front- (left) and back-panel (right) of the interlock controller.

plate of the module. LEDs on the front panel indicate the status of the box depending on the logic of the CPLD.

Fig. A.4 illustrates how the interlock system monitors and protects the vacuum system. The pressure-gauge controller records the vacuum from each gauge and, depending on whether the respective threshold conditions are met, sends a 5 V trigger signal to the interlock box. The interlock box then processes these input signals and transmits corresponding output trigger signals to the gate valves controller box and electrode power supplies to control their operation. In this special case, a gate valve can only be opened if all vacuum systems connected by this valve are within the permitted pressure range. Additionally, voltage can only be applied to the electrodes when the pressure in the VMI chamber is below the threshold.

A.3. Detection efficiency

The low-power correlation measurements used for Fig. 3.5 enabled us to determine the detection efficiency for electrons and ions in our setup. For each detected electron, we examined whether there was a simultaneous detection of an ion for the same laser shot. The detection efficiency for ions α_i and electrons α_e is given by:

$$\alpha_\mathrm{i} = \frac{N_\mathrm{i} \cdot N_\mathrm{e} - N_\mathrm{uncor.}}{N_{\mathrm{i}|\mathrm{e}>1}}, \quad \alpha_\mathrm{e} = \frac{N_\mathrm{i} \cdot N_\mathrm{e} - N_\mathrm{uncor.}}{N_{\mathrm{e}|\mathrm{i}>1}} \tag{A.1}$$

Here, we have the number of electrons N_e, the number of ions N_i, the number of uncorrelated events on both detectors $N_\mathrm{uncor.}$, the number of ions with at least one detected electron $N_{\mathrm{i}|\mathrm{e}>1}$, and the number of electrons with at least one detected ion $N_{\mathrm{e}|\mathrm{i}>1}$. From our data we obtain a final total detection efficiency of $\alpha_\mathrm{i} = 35.90\%$ and $\alpha_\mathrm{e} = 35.35\%$. Assuming a detection efficiency of the MCP given by $\alpha_\mathrm{MCP} = 50\%$ we obtain a transparency for a single mesh $\alpha_\mathrm{mesh} = 83.7\%$, which is in agreement with the nominal transmission of 80%. The deviation is attributed to the fact that the effective transmission of the second grid is higher due to the geometric overlap with the shadow cast by the first grid.

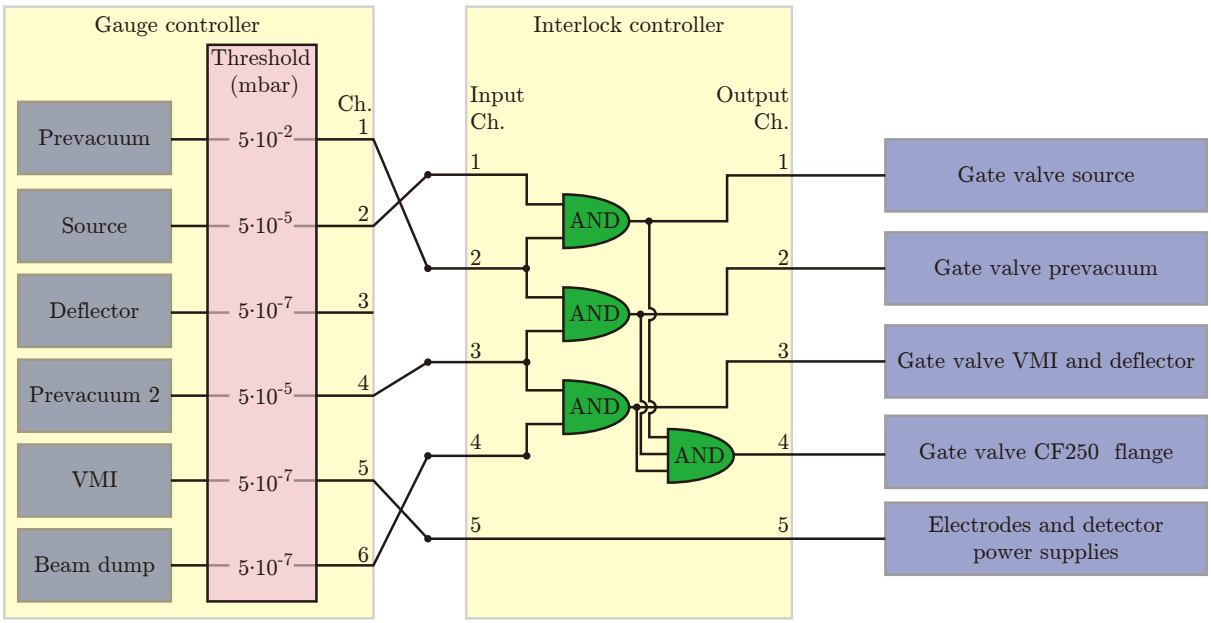

Figure A.4.: Interlock logic used at eCOMO. Thresholds for pressures are set on the gauge controller on the left. The corresponding outputs are send to the input of the interlock controller. The CPLD of the interlock controller is programmed as illustrated in the figure. The logic output of the interlock controller drives the gate valves and the logic for the power supplies as indicated on the right.

B. Appendix to Chapter 4

B.1. Method of VMI calibration

In subsection 4.3.1, we discussed that under ideal conditions, the calibration model mapping R to $E_{K\|}$ can be approximated using a quadratic function. However, in practical scenarios, direct interpolation offers higher accuracy.

Here we compare the results of $E_{K\|}$ dependencies for two alternative calibration models using quadratic and quartic function:

$$E_{K\|} = m_1 \cdot R^2 \quad \text{(Quadratic)}, \tag{B.1}$$

$$E_{K\|} = n_1 \cdot R^2 + n_2 \cdot R^4 \quad \text{(quartic)}, \tag{B.2}$$

and direct interpolation method. The calibration fits and their differences are shown in Fig. B.1. The interpolation method yields significantly higher accuracy compared to the polynomial models. However, in practical experiments, calibration is often limited by the availability of only a few data points. Therefore, polynomial-based calibration models remain a feasible and convenient option for most applications.

B.2. Effect of t-shift on $\sigma_{R_{K\|}}$

In this section, we analyze how the initial v_x distribution, which refers to equivalently the t distribution, affects the spatial resolution. We first define the t-shift. In previous work, particles were selected within a slice width of $\Delta t = \pm 1$ ns, with t_0 defined by $v_x = 0$ and $v_x(\text{max})$ and $v_x(\text{min})$ corresponding to $t = t_0 - 1$ ns and $t = t_0 + 1$ ns, respectively;

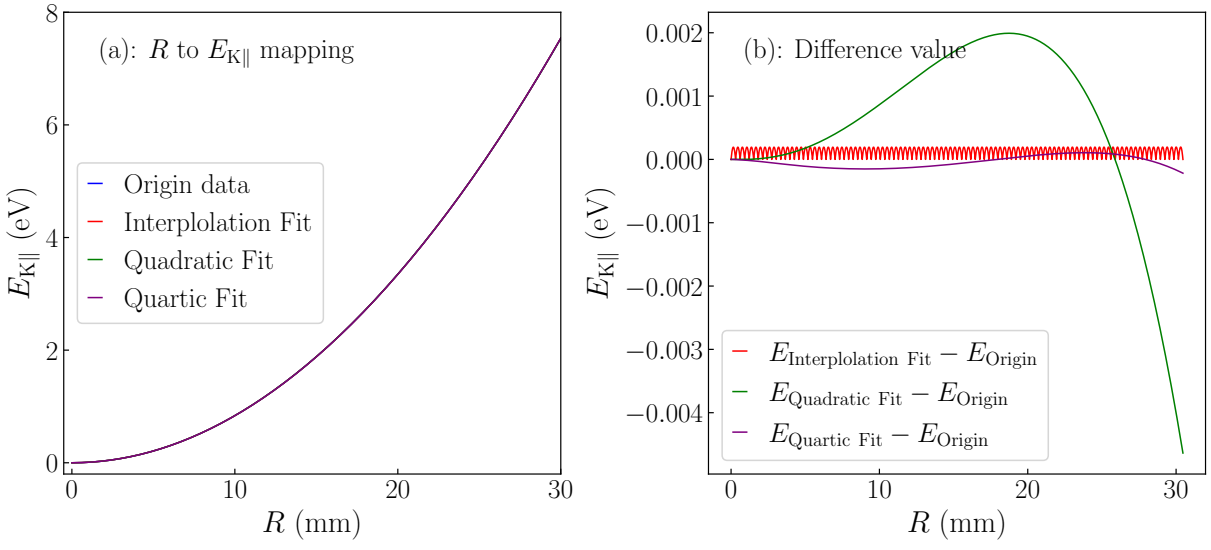

Figure B.1.: Compare different Fitting function for mapping between R to $E_{K\|}$

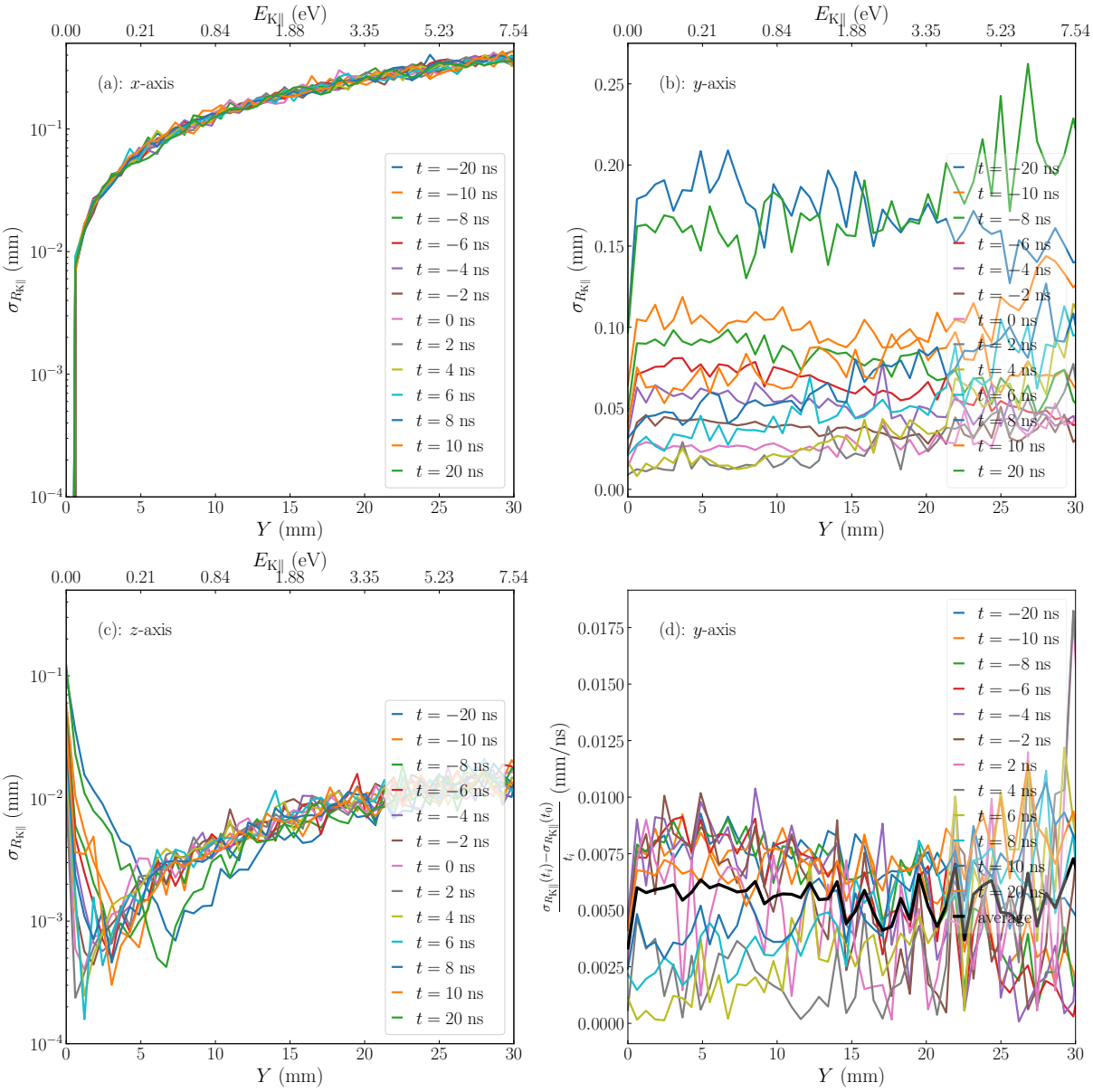

Figure B.2.: (a–c): show $\sigma_{R_{K\parallel}}$ as a function of Y for 1D Gaussian initial position distributions along the x, y, and z axes under various t-shift conditions; (d) presents the offset for each t-shift relative to the $t = 0$ case, normalized by t to obtain the per-unit-t offset as a function of Y. The thick black line denotes the average per-unit-t offset over all t-shift conditions.

v_x was uniformly distributed within this range. Here, we keep $\Delta t = \pm 1$ ns but shift the slice region. For example, for $t = 5$ ns, v_x(max) corresponds to $t = t_0 + 5 - 1$ ns and v_x(min) to $t = t_0 + 5 + 1$ ns, again with a uniform v_x distribution.

Simulation parameters are as follows: (1) $n = 100$ particles for each v_y value; (2) v_y ranges from 0 km/s to 5 km/s in 0.1 km/s steps; (3) Initial positions follow a 1D Gaussian $G(\mu, \sigma)$ with $\mu = 0$ and $\sigma = 851$ μm (FWHM = 2000 μm), applied along x, y, or z only; (4) Slice width is $\Delta t = \pm 1$ ns, with t varying from −20 ns to +20 ns in proper steps listed in Fig. B.2.

In Fig. B.2 a-c, $\sigma_{R_{K\parallel}}$ as a function of Y is shown for 1D Gaussian initial position distributions along the x, y, and z axes under various t-shift conditions. For the x- and

z-axis cases, the t-shift has negligible influence, while for the y-axis it produces a vertical offset in the distribution, i. e., an increase in $\sigma_{R_{K\|}}$. This offset is uniform with respect to Y and grows with the absolute value of t. Taking $t = 0$ as the reference, the offset for each t-shift is calculated relative to the $t = 0$ case, normalized by t to obtain the per-unit-t offset. The resulting distributions are shown in Fig. B.2 d. The results indicate that the average per-unit-t offset does not exceed ~0.008 mm/ns. The thick black line represents the average per-unit-t offset over all t-shifts. For estimation purposes, this upper bound (0.008 mm/ns) can be used to approximate the offset for a given t-shift relative to t_0.

B.3. Effect of σ from 1D Gaussian case on $\sigma_{R_{K\|}}$

In subsection 4.3.2, we introduced the value $\sigma_{R_{K\|}}$ to characterize the spatial resolution of the VMI system for each individual component of the parallel kinetic energy($E_{K\|}$). This results was derived specifically under the condition that the initial spatial distribution of particles follows a one-dimensional (1D) Gaussian distribution with a fixed standard deviation (σ = 851 μm). This constraint significantly limits the general applicability of the analysis in characterizing the spatial resolution of VMI systems under more variable initial distribution conditions.

In this section, we extend our analysis to encompass a broader range of initial spatial distributions by systematically varying the standard deviation σ of the particles' initial Gaussian position distribution. We begin with the case of a one-dimensional (1D) Gaussian distribution along a single spatial axis and subsequently generalize the model to a three-dimensional (3D) Gaussian distribution encompassing all axes. We then examine how the standard deviation of the detected particle positions, σ_R, varies with the initial spatial spread $\sigma_{x,y,z}$ across different values of axial velocity $v_{\|}$. By summarizing and characterizing the observed trends, we establish a generalized mapping between $\sigma_{x,y,z}$ and $\sigma_{R_{K\|}}$. This relationship forms the theoretical foundation for calculating the VMI spatial resolution under arbitrary initial particle conditions.

In our SIMION simulation for one-dimensional (1D) Gaussian distribution of the initial particle positions along a single axis, the initial particle distribution satisfies the following conditions: for each set of specified parameters, a group of $n = 100$ particles is generated; The initial velocity along the y-axis (v_y) is varied from 0 km/s to 5 km/s and step of 1 km/s; The initial positions are sampled from a 1-D Gaussian distribution $G(\mu, \sigma)$, where the mean $\mu = 0$, and the standard deviation σ is varied between 1 μm and 1000 μm. The distribution is applied along only one given axis at a time (x, y, or z). In Fig. B.3, we show the relationship between $\sigma_{R_{K\|}}$ and the standard deviation of initial position displacement (σ) for all three individual axis (x, y, or z). Different colors represent different initial velocities v_y, with specific values and corresponding kinetic energy labelled. (a)–(c) correspond to the 1-D Gaussian distribution along the x-, y-, and z-axes, respectively. For x-axis case in (a), we observe that the standard deviation of R ($\sigma_{R_{K\|}}$) exhibits a linear relationship with σ_x for each fixed value of v_y. Additionally, $\sigma_{R_{K\|}}$ increases with increasing v_y. In (b) and (c), which correspond to displacements along the y- and z-axes respectively, display qualitatively similar trends: $\sigma_{R_{K\|}}$ is approximately linearly proportional to the corresponding spatial spread σ_y or σ_z, but the dependence on v_y is non-monotonic strictly. This nonlinearity arises from the presence of velocity-dependent focusing effects, which is particularly obvious at unique values of σ.

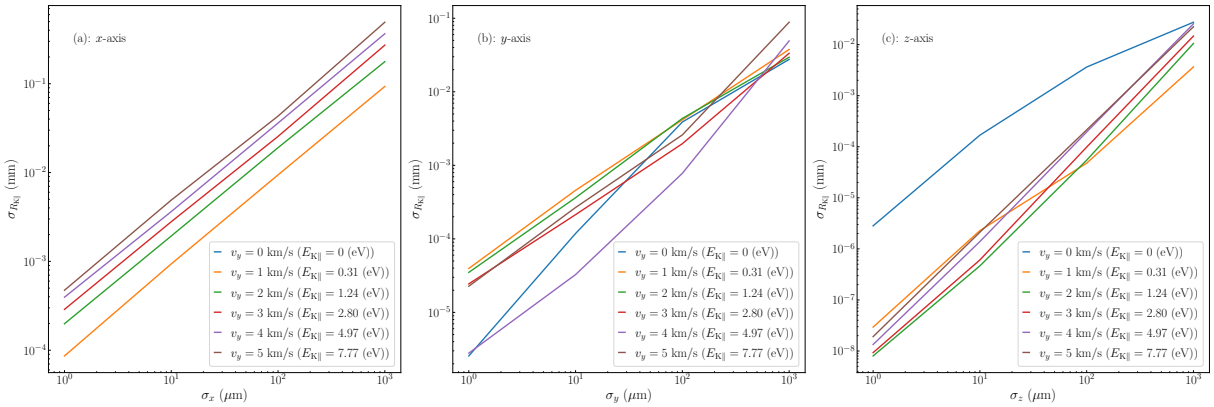

Figure B.3.: Standard deviation of R ($\sigma_{R_{K\|}}$) as a function of the initial spatial spread σ, for different values of initial velocity along the y-axis (v_y), represented by different colored curves. (a)–(c) correspond to the cases where the initial position distribution is applied along the x-, y-, and z-axes, respectively.

B.4. Effect of σ from 3D Gaussian case on $\sigma_{R_{K\|}}$

In Section B.3, we conducted a detailed analysis of the effect of the width of the initial position displacement on $\sigma_{R_{K\|}}$ at various kinetic energy levels, assuming a 1D Gaussian distribution as the initial conditions for samples. In this section, we extend the analysis to a more general scenario where the initial particle distribution follow a 3D Gaussian distribution.

We use SIMION to simulate the spatial distribution of particle impacts on the detector and examine how this distribution evolves with respect to the standard deviation (σ) of the initial 3D Gaussian distribution for different $E_{K\|}$. The simulation setup adheres to the following conditions: for each parameter set, a total of $n = 2000$ particles are generated; The initial velocity along the y-axis (v_y) is varied from 0 km/s to 6 km/s, with a step size of 0.25 km/s from 0 to 1 km/s, and a step size of 1 km/s from 1 km/s to 6 km/s; The initial positions are sampled from a 3D Gaussian distribution $G(\mu, \sigma)$, with mean $\mu = 0$ and identical standard deviation in all directions ($\sigma_x = \sigma_y = \sigma_z$). The value of σ is varied from 10 μm to 1500 μm, with step sizes selected according to the magnitude of the standard deviation, denser sampling is used for smaller σ values, while sparser sampling is adopted for larger ones. All the selected values are listed in Fig. B.6 a.

As an example, we consider the 3D case where the initial spatial standard deviation is $\sigma = 21.23$ μm. For each value of v_y, the corresponding particle distributions on the detector are shown as 2D histograms in Fig. B.4, arranged in order from low to high v_y. In each subplot, the x- and y-axes represent the particles' positions in the y and z directions, respectively, relative to their mean values ($\bar{y}$, $\bar{z}$).The figures reveal a clear trend: as v_y increases, the distribution becomes increasingly elongated only along the y-axis (the direction of motion), while the spread along the z-axis (where $v_z = 0$) remains essentially unchanged. This behavior indicates that the spatial distributions along the y and z directions are largely decoupled. Moreover, the increasing elongation along the y-axis with rising v_y suggests a clear decline in the spatial resolution of the VMI system along the direction of the particle's velocity. To further quantitatively evaluate this trend, we project the 2D distributions onto the y- and z-axes and extract the corresponding projected 1D histograms, respectively, as shown in Fig. B.5 a-j. Gaussian

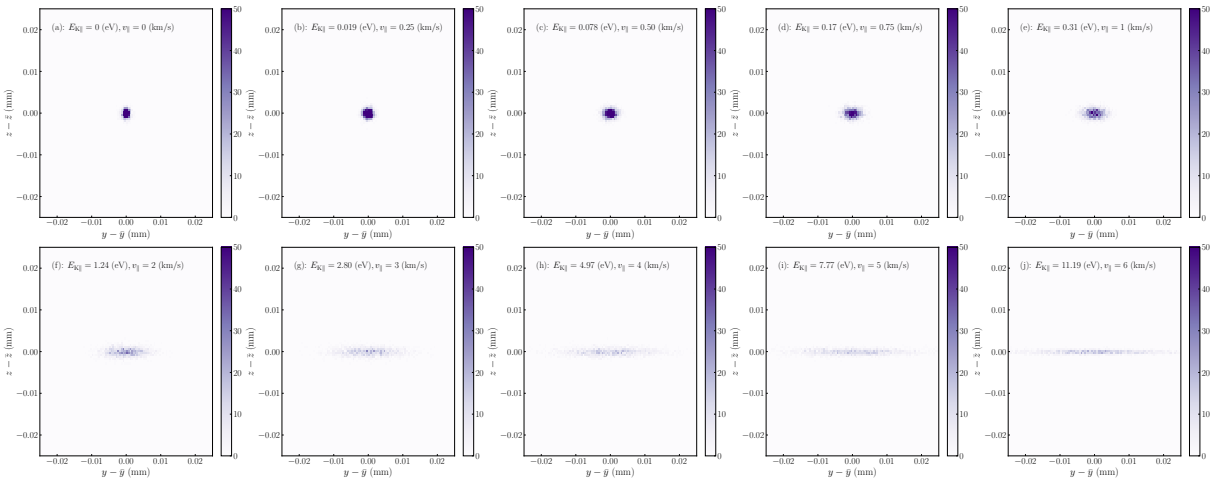

Figure B.4.: From (a) to (j), The initial velocity along y-axis changing from 0 to 6 km/s with a step size of 0.25 km/s between 0 and 1 km/s and a step size of 1 km/s between 1 and 6 km/s. For all subplots, the initial particles follow a 3D Gaussian spatial distribution with standard deviations $\sigma_x = \sigma_y = \sigma_z = 21.23$ μm and a total of n = 2000 particles are sampled. The histogram of particle's arrived spatial distribution on the detector is represented in the relative molecular distribution center frame ($y - \bar{y}$ and $z - \bar{z}$).

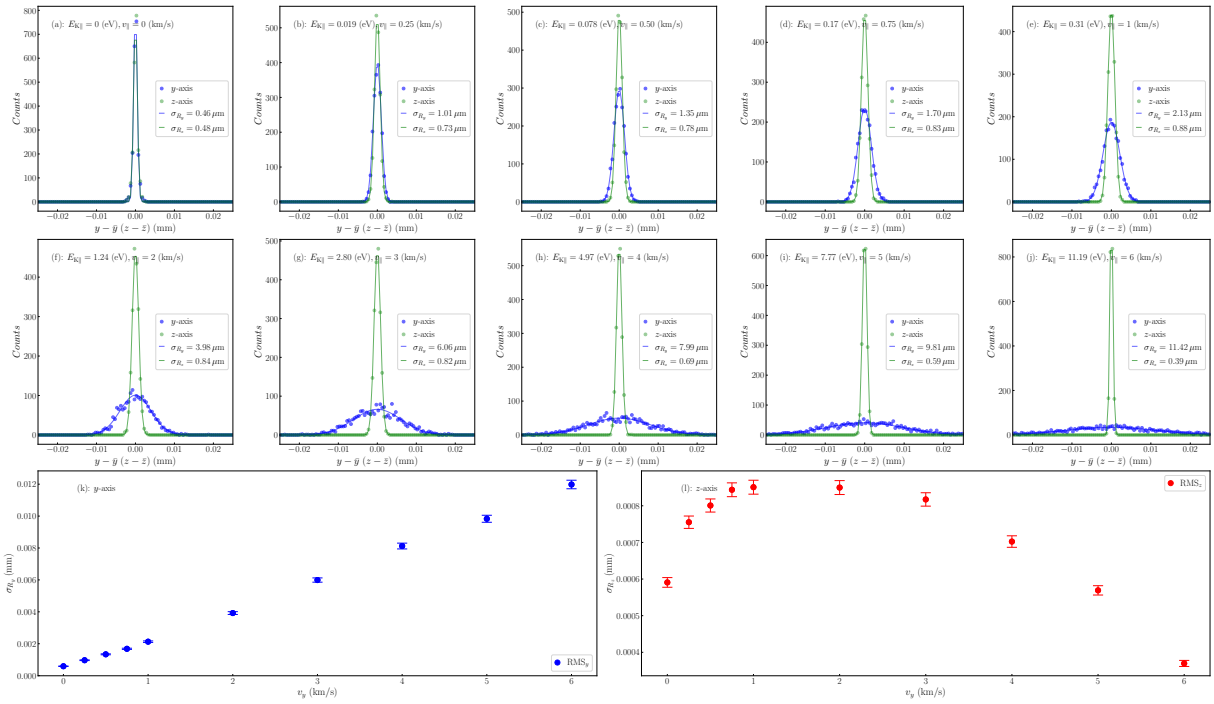

Figure B.5.: (a-j): Projection histogram along y and z for the position of arrivals at each v_y from Fig. B.4 and the corresponding Gaussian fitting. The according fitting $\sigma_{R_{y,z}}$ has been given in the labels; (k-l): σ_{R_y} and σ_{R_z} as the function of the initial velocity along the y-axis(v_y).

fits are applied to each of these projections, and the resulting fitting standard deviations ($\sigma_{R_{y,z}}$) are labelled in the legends.

In Fig. B.5 k-l, we present the relationship between the $\sigma_{R_{y,z}}$ of R as a function of the initial velocity (v_y). For σ_{R_y}, the distribution exhibits an approximately linear increase with v_y. In contrast, the trend along the z-axis may appear to increase and then decrease with rising v_y; however, this apparent behavior is misleading and primarily results from the relatively small absolute values involved. To further investigate the $\sigma_{R_{y,z}}$, we extend the analysis to include a broader range of standard deviation (σ) for initial sample conditions from the simulation. The resulting $\sigma_{R_{y,z}}$ distributions are shown in Fig. B.6 a–b with a logarithmic scale is applied to the y-axis in the figure to better visualize the distribution of smaller values. Specifically, in Fig. B.6 b, where a wider range and a larger set of σ_z values are considered, it becomes evident that σ_{R_z} remains effectively constant as v_y increases. Moreover, when comparing across different cases of σ_z, the variations in σ_{R_z} can be regarded just as a simple fluctuation which also shown in Fig. B.5 l. This behavior demonstrates that σ_{R_z} exhibits minimal sensitivity to changes in the initial v_y. These observations confirm our earlier interpretation that the spatial resolution in the z-direction is largely unaffected by the initial perpendicular velocity along the y-direction. Therefore, in the subsequent analysis, we will focus on the dependence of σ_{R_y}, as illustrated in Fig. B.6 a.

Similar to previous observations, the σ_{R_y} exhibits an approximately linear relationship with the initial velocity v_y. However, for larger values of σ, the slope near $v_y = 0$ is noticeably reduced to zero, indicating a deviation from strict linearity in this region. Given the similarity between particle convergence and motion in VMI and the focusing behavior of optical lenses, we adopt the Gaussian beam distribution function and the concept of Rayleigh length to fit the corresponding σ_{R_y}. The functional relationship is defined as:

$$w(v_y) = \omega_0 \sqrt{1 + \left(\frac{v_y}{v_{y\mathrm{R}}}\right)^2}, \tag{B.3}$$

where ω_0 is the minimum beam waist, and $v_{y\mathrm{R}}$ is the Rayleigh range characterizing the spread ratio of the distribution.

The corresponding fitting coefficients are presented in Fig. B.6 c. In particular, the ratio $\omega_0/v_{y\mathrm{R}}$ is shown to facilitate the subsequent fitting procedure. To further explore the functional dependence of these coefficients on σ, we perform curve fitting using the complete set of data points. The beam waist ω_0 is found to approximately follow an exponential dependence on σ, expressed as:

$$\omega_0(\sigma) = a \cdot (e^{b\cdot\sigma} - 1), \tag{B.4}$$

where a and b are fitting parameters.

The coefficient $\omega_0/v_{y\mathrm{R}}$, which reflects the asymptotic slope of σ_{R_y} curve at large values of v_y, exhibits an approximately homogeneous linear relationship with σ showing below:

$$\frac{\omega_0}{v_{y\mathrm{R}}}(\sigma) = c \cdot \sigma, \tag{B.5}$$

where c is also a fitting parameter. In Fig. B.6 d, we apply the fitted functions for ω_0 and $v_{y\mathrm{R}}$ from previously obtained parameters of a, b and c, to recalculate the corresponding parameters for each value of σ. The results are then compared with the simulated data. The calculated values(dashed curves) from the fitted function exhibit excellent agreement

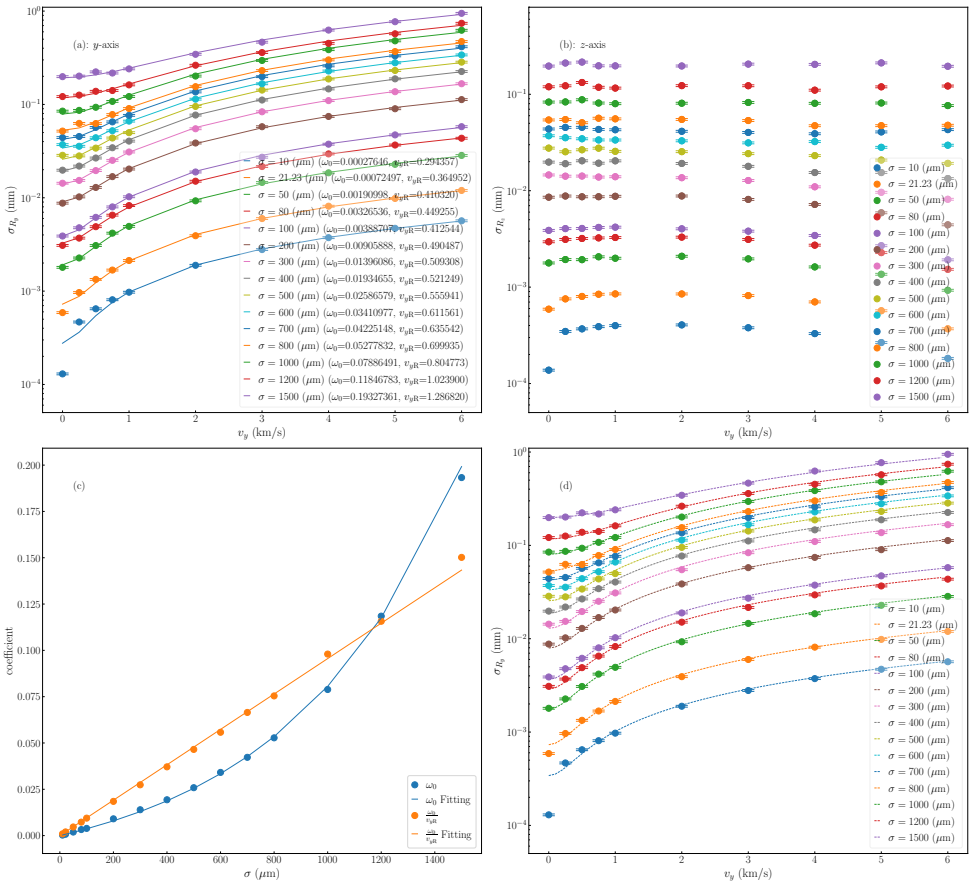

Figure B.6.: (a) and (b) illustrate $\sigma_{R_{y,z}}$ of the detected particle positions on the detector along the y- and z-axes, respectively, as functions of the initial velocity along the y-axis (v_y) for various values of the initial Gaussian 3D distribution width σ (shown as scatter plots in different colors). In (a), the curves are fitted using (B.3), with the corresponding fitting parameters ω_0 and v_{yR} annotated; (c) presents the extracted fitting parameters ω_0 and $\frac{\omega_0}{v_{yR}}$ from (a) as functions of σ (scatter plots). The fitted dependence of ω_0 on σ follows an exponential function, while ω_0/v_{yR} exhibits a linear relationship (shown in solid lines); In (d), the fitted functions from (c) are used to compute ω_0 and v_{yR} for each σ, and the Gaussian beam function is reconstructed accordingly (shown in dashed lines in different colors). These reconstructed curves are compared with the simulation results (scatter plots in corresponding colors).

with the simulated results(points), validating the reliability of the functional forms. This consistency also enables the extrapolation of the model to predict the behavior of σ_{R_y} distributions for a broader range of σ values and the Gaussian beam-based model demonstrates superior performance, particularly in regions with higher σ, where it also ensures continuous differentiability of the slope around $v_y = 0$, thereby aligning better with the intrinsic symmetry of the VMI system.

B.5. Apply Rayleigh length function on $\sigma_{R_{K\|}}$ for 1D Gaussian case

In Section B.3, we qualitatively examined the dependence of $\sigma_{R_{K\|}}$ on $\sigma_{x,y,z}$ for 1D Gaussian initial position distributions, and in Section B.4, we showed that for 3D

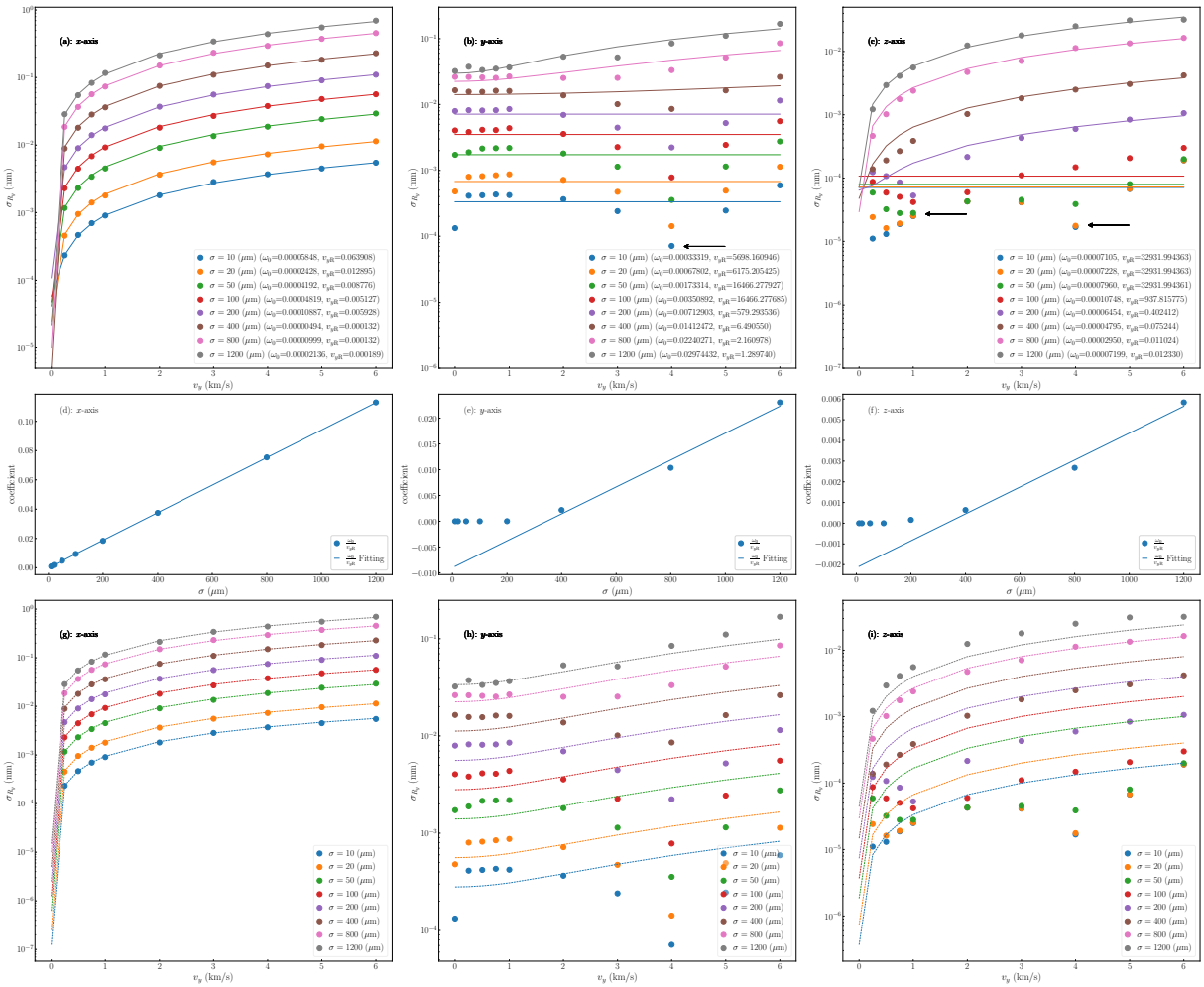

Figure B.7.: (a–c): $\sigma_{R_{K\|}}$ as a function of $\sigma_{x,y,z}$ for 1D Gaussian initial position distributions along the x, y, and z axes. Simulation results are shown as scatter plots, and Rayleigh length function fits are plotted as solid curves. Distortions caused by focusing effects are indicated by black arrows. (d–f): Corresponding ratios $\frac{\omega_0}{v_{yR}}$ as functions of σ (scatter plots) with linear fits (solid lines) along the x, y, and z axes. (g–i): $\sigma_{R_{K\|}}$ for different σ values calculated using a proportional scaling from a single base-line distribution ($\sigma_{\text{base}} = 800$ μm)(shown in dashed lines) compared with simulation results (scatter plots) along the x, y, and z axes.

Gaussian distributions this dependence on σ is well described by a Rayleigh length function. Here, we extend this approach to quantitatively isolate the contributions from individual spatial directions in the 1D case, using the Rayleigh length function as the fitting model.

Simulations are performed in SIMION with $n = 2000$ particles per parameter set. The initial y-axis velocity v_y is scanned from 0 to 6 km/s, with 0.25 km/s steps for 0 to 1 km/s and 1 km/s steps for 1 to 6 km/s. Initial positions follow a 1D Gaussian $G(\mu = 0, \sigma_{x,y,z})$. The standard deviation σ ranges from 10 μm to 1200 μm, with denser sampling for smaller values. In Fig. B.7 a-c, we present $\sigma_{R_{K\|}}$ as a function of $\sigma_{x,y,z}$ for 1D Gaussian initial position distributions along the x, y, and z axes. Simulation results are shown as scatter plots, with Rayleigh length function fits plotted as solid curves. In (a), the x-axis case shows excellent agreement, with $\sigma_{R_{K\|}} \approx 0$ at $v_y = 0$, as expected due to the absence of perpendicular velocity and electric field effects—analogous to the

z-axis case. Thus, all contributions at $v_y = 0$ originate from the y-axis distribution. In (b) and (c), smaller $\sigma_{y,z}$ values yield poorer fits due to focusing effects at specific v_y (e. g., $v_y = 4$ km/s for y; $v_y = 1$ or 4 km/s for z), which distort the distribution and reduce $\sigma_{R_{\mathrm{K}\parallel}}$. These effects diminish for larger σ, leading to better fits in that regime.

Based on the linear relationship of $\sigma_{R_{\mathrm{K}\parallel}}$ as the function of σ observed in Fig. B.3 and the linear relationship of $\omega_0/v_{y\mathrm{R}}$ in Fig. B.6, we calculate $\sigma_{R_{\mathrm{K}\parallel}}$ for different σ values using one single distribution as a base-line ($\sigma_{\mathrm{base}} = 800$ μm). Assuming proportionality, the relation is:

$$\frac{\sigma_{R_i}(v_y)}{\sigma_i} = \frac{\sigma_{R_{\mathrm{base}}}(v_y)}{\sigma_{\mathrm{base}}}. \tag{B.6}$$

The results, shown as dashed lines in Fig. B.7 g–i, are compared with simulations (scatter plots). The x-axis case matches very well, while y and z show deviations due to focusing effects that distort the distributions and cannot be fully captured by the linear scaling. Nevertheless, the method reproduces the correct order of magnitude for all directions, especially for small $\sigma_{y,z}$. At $v_y = 0$, the exponential distribution is not fully accounted for, leading to larger local errors. However, since $E_{\mathrm{K}\parallel}$ is small at this point, its impact on the energy resolution is minimal. Overall, this demonstrates a practical methodology for extending results from a base-line σ to a larger range of distributions.

B.6. Time-of-flight calculation from the general equation of motion

B.6.1. Generalization of the Wiley-McLaren approach

The ideas are inspired by Edwins Kukk [287] and the Wiley-McLaren's paper [199]. The particles start at 0 and the total length of the spectrometer is given by D. We divide the total length in N parts with a specific length $\Delta s = D/N$. The electric fields ε_i inside the small distance pieces are assumed to be constant (the electric field between the starting point and the first Δs is denoted as ε_1, the next one ε_2 ...). From the Wiley-McLaren paper we find for the time between two points s_{i+1} and s_i on the way to the detector

$$t_{i+1} = \frac{\sqrt{2m}}{q} \frac{\sqrt{E_{\mathrm{kin};i+1}} - \sqrt{E_{\mathrm{kin};i}}}{\varepsilon_i}. \tag{B.7}$$

Here the kinetic energy at position s_i is denoted as $E_{\mathrm{kin};i}$, the mass and charge is denoted as m and q, respectively. In addition we have $t_0 = 0$ and $E_{\mathrm{kin};0}$ is the initial axial kinetic energy which we would like to extract from the final time-of-flight. The above equation also assumes that the initial velocity is pointing towards the detector (the general case needs to be worded out, here some of the numerators will have a + sign instead of a −).

The total time-of-flight is then given by:

$$\begin{aligned} t_{\mathrm{ToF}} &= \sum_{i=1}^{N} t_i \\ &= \frac{\sqrt{2m}}{q}\left[\frac{\sqrt{E_{\mathrm{kin};0}+q\Delta s\,\varepsilon_1}-\sqrt{E_{\mathrm{kin};0}}}{\varepsilon_1}\right. \\ &\quad +\frac{\sqrt{E_{\mathrm{kin};0}+q\Delta s(\varepsilon_1+\varepsilon_2)}-\sqrt{E_{\mathrm{kin};0}+q\Delta s\,\varepsilon_1}}{\varepsilon_2} \\ &\quad +\frac{\sqrt{E_{\mathrm{kin};0}+q\Delta s(\varepsilon_1+\varepsilon_2+\varepsilon_3)}-\sqrt{E_{\mathrm{kin};0}+q\Delta s(\varepsilon_1+\varepsilon_2)}}{\varepsilon_3} \\ &\quad \left.+\ldots\right]. \end{aligned} \tag{B.8}$$

So assuming we know all electric fields at the positions s_i we can calculate the time-of-flight. Or by inverting the equation we get the initial kinetic energy. An additional improvement could be the solutions to linear fields as shown for two in Edwins Kukk's paper [287]. This also nicely shows that the $t_{\mathrm{ToF}} \propto \sqrt{m/q}$ satisfied only holds for 0 initial axial velocity($v_x = 0$).

B.6.2. Path of the particle in a homogeneous electric field

The path of a particle through any electric field just depends on the initial energy and the direction of the velocity vector. So for particles with different masses the path will be the same. The particles will just travel the path faster or slower depending on the mass. We did not find a proof at the moment in time so we try to get an idea why that is the case by ourselves. Without restriction of generality we restrict ourselves to two dimension. This is in general just the plane defined by the velocity vector $\vec{v}$ and the electric field vector $\vec{\varepsilon}$. The idea of the proof is to show that for a single step using the Euler method we obtain:

1. A path independent on the particle's mass.
2. A final velocity where again $v_x \propto 1/\sqrt{m}$ and $v_y \propto 1/\sqrt{m}$.

The model for a single Euler step is shown in Fig. B.8 So we assume a particle with charge q and mass m to enter a region of length l where a homogeneous electric field $\vec{\varepsilon}$ along the y-coordinate is present. Outside that area there is no field. The initial velocity is given by v_{x_i} and v_{y_i} in x and y directions, respectively. Since the initial kinetic energy is assumed to be independent of the mass m and since we always want to have the same direction for the velocities implies that $v_{x_i} = C_x/\sqrt{m}$ and $v_{y_i} = C_y/\sqrt{m}$ with two constants C_x and C_y. In addition without restriction of generality we assume that the particle enters the homogeneous field at the coordinates $(x_0, y_0) = (0, 0)$. Since there is no force along the x coordinate the velocity v_{x_i} is constant and we can calculate the time it takes to fly through the homogeneous field by $t = l/v_{x_i}$. The initial velocity can be expressed by the initial kinetic energy $E_{\mathrm{kin;i}}$ by

$$v_{x_i} = \sqrt{\frac{2E_{\mathrm{kin;i}}}{m} - v_{y_i}^2} = \sqrt{\frac{2E_{\mathrm{kin;i}}}{m} - \frac{C_y^2}{m}} \propto \frac{1}{\sqrt{m}}. \tag{B.9}$$

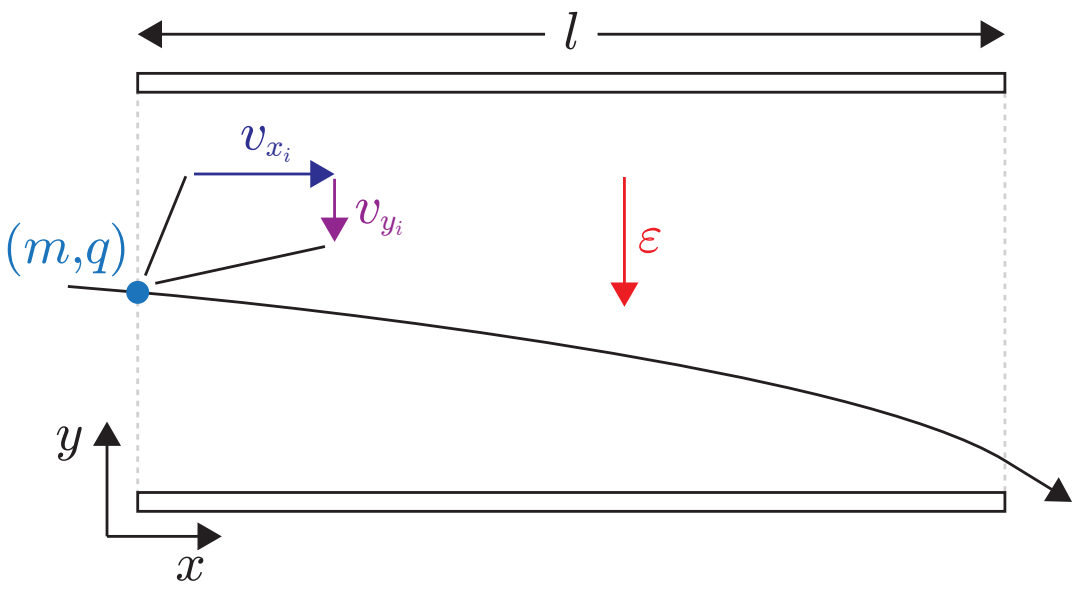

Figure B.8.: Trajectory of a particle with mass m and charge q through a constant electric field ε of length l. Initial velocities along x and y are denoted as v_{x_i} and v_{y_i}, respectively.

This implies that it should work for fixed initial kinetic energy. Furthermore we have $t \propto \sqrt{m}$ and therefore also $t^2 \propto m$. The acceleration is given by $a = e\varepsilon/m$ and the solution of the equation of motion along y is

$$v_y(t) = at + v_{y_i} \propto \frac{1}{\sqrt{m}} \tag{B.10}$$

$$y(t) = \frac{1}{2}at^2 + v_{y_i}t \neq f(m). \tag{B.11}$$

So the position $y(t)$ is independent of the mass m and both items stated above are fulfilled.

If we have now an arbitrary field we can use the Euler method to obtain the trajectory. For every single step we get a trajectory that is independent of the mass. The final velocity components after performing one step are both again $\propto 1/\sqrt{m}$. Since for decreasing individual time steps $\Delta t \longrightarrow 0$ we converge to the real solution and since every single step is independent of the mass in terms of the position the real curve is also independent on the mass for the same $E_{\text{kin,i}}$ and the velocity vectors pointing into the same direction.

B.6.3. Time-of-flight calculation

We assume that the field in the source and acceleration region is homogeneous. Therefore, the problem can be studied only in the dimension in which the electric field is pointing to. In the other two dimensions, the motion could potentially be described by a constant straight line motion.

A simplified model describing the axial motion of a charged particle in a VMI spectrometer across different regions is illustrated in Fig. B.9. From left to right, the system includes the source region, acceleration region, and drift tube region. A charged particle (represented by the blue spheres) with mass m and charge q is placed at the point of origin inside the source regions with a distance s to the second plate. In this

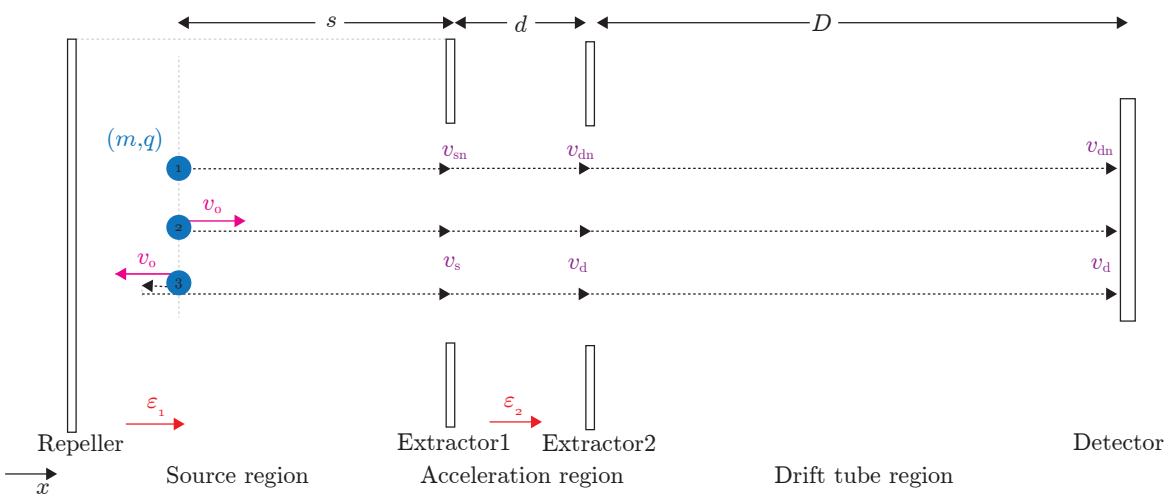

Figure B.9.: Trajectory of a particle with mass m and charge q traveling with an initial velocity v_0 through a conventional Wiley McLaren spectrometer. The spectrometer consists of three regions: the source region, the acceleration region, and the drift tube region, with respective flight distances denoted by s, d, and D. The electric fields in the source region ($\vec{\varepsilon}_1$) and the acceleration region ($\vec{\varepsilon}_2$) are assumed to be homogeneous and directed along the x-axis.

model, we first neglect the effects of the initial spatial displacement. Furthermore in contrast to a VMI we assume homogeneous fields which can be to good approximation obtained by separating the different regions with grids. Also the size of the field plates is assumed to be infinite radially. The thickness of the plates is assumed to be zero. We analyze three initial axial velocity conditions:

(1) Initial velocity $v_0 = 0$

(2) Initial velocity $v_0 > 0$, i.e., towards the detector

(3) Initial velocity $v_0 < 0$, i.e., away from the detector

Each of the three regions has a defined length:

- Source region: s
- Acceleration region: d
- Drift tube region: D

The electric fields in the source region($\vec{\varepsilon}_1$) and acceleration region($\vec{\varepsilon}_2$) are assumed to be homogeneous along the x-cooridnate. The following numerical values are used in the simulations presented in Fig. B.10. These values are consistent with the parameters previously employed for the conventional VMI configuration:

- $q = 1\ e$
- $m = 10\ u$
- $\vec{\varepsilon}_1 = 66666.7\ \mathrm{V/m}$
- $\vec{\varepsilon}_2 = 233333.3\ \mathrm{V/m}$

- $s = 0.0075$ m
- $d = 0.015$ m
- $D = 0.46$ m
- $v_0 \in [-30000, +30000]$ m/s
- $v_{\mathrm{sn}} = 97881$ m/s
- $v_{\mathrm{dn}} = 276851$ m/s

The general one dimensional equation of motion in a source region with a constant field is given by $ma_{\mathrm{s}} = q\varepsilon_{\mathrm{s}}$. Here, m is the mass, a_{s} is the acceleration in the source region, q is the charge, and ε_{s} is the electric field. The general solution is given by

$$x(t) = \frac{1}{2}a_{\mathrm{s}}t^2 + v_0 t + s_0. \tag{B.12}$$

Here, s_0 and v_0 represent the initial position and velocity, respectively along the x-direction. If we set the starting position of the particle to $s_0 = 0$ we obtain a condition for the time t_{s} when the particle is at the exit of the source region at distance s with respect to the starting position. This is given by

$$\frac{1}{2}a_{\mathrm{s}}t_{\mathrm{s}}^2 + v_0 t_{\mathrm{s}} - s = 0. \tag{B.13}$$

(B.13) has in general two solutions for t_{s}. Since we set the starting time to $t_0 = 0$, we are only interested in the positive solution given by

$$t_{\mathrm{s}} = \frac{-v_0 + \sqrt{v_0^2 + 2a_{\mathrm{s}}s}}{a_{\mathrm{s}}}. \tag{B.14}$$

The velocity of the particle at the exit of the source region v_{s} is obtained by inserting (B.14) into $v(t) = a_{\mathrm{s}}t_{\mathrm{s}} + v_0$ for t. This is given by $v_{\mathrm{s}} = \sqrt{v_0^2 + 2a_{\mathrm{s}}s}$. To simplify (B.14), we define the nominal velocity v_{sn} as the final velocity of a particle with the initial velocity $v_0 = 0$ under acceleration in the source region:

$$v_{\mathrm{sn}} = \sqrt{2a_{\mathrm{s}}s}. \tag{B.15}$$

Using this, (B.14) becomes:

$$t_{\mathrm{s}} = \frac{-v_0 + v_{\mathrm{sn}}\sqrt{1 + \frac{v_0^2}{v_{\mathrm{sn}}^2}}}{a_{\mathrm{s}}}. \tag{B.16}$$

When $v_0 \ll v_{\mathrm{sn}}$, the square root can be approximated by a Taylor expansion:

$$\sqrt{1 + \frac{v_0^2}{v_{\mathrm{sn}}^2}} = \lim_{\frac{v_0}{v_{\mathrm{sn}}} \to 0} \left(1 + \frac{1}{2}\left(\frac{v_0}{v_{\mathrm{sn}}}\right)^2 - \frac{1}{8}\left(\frac{v_0}{v_{\mathrm{sn}}}\right)^4 + O((\frac{v_0}{v_{\mathrm{sn}}})^6)\right), \tag{B.17}$$

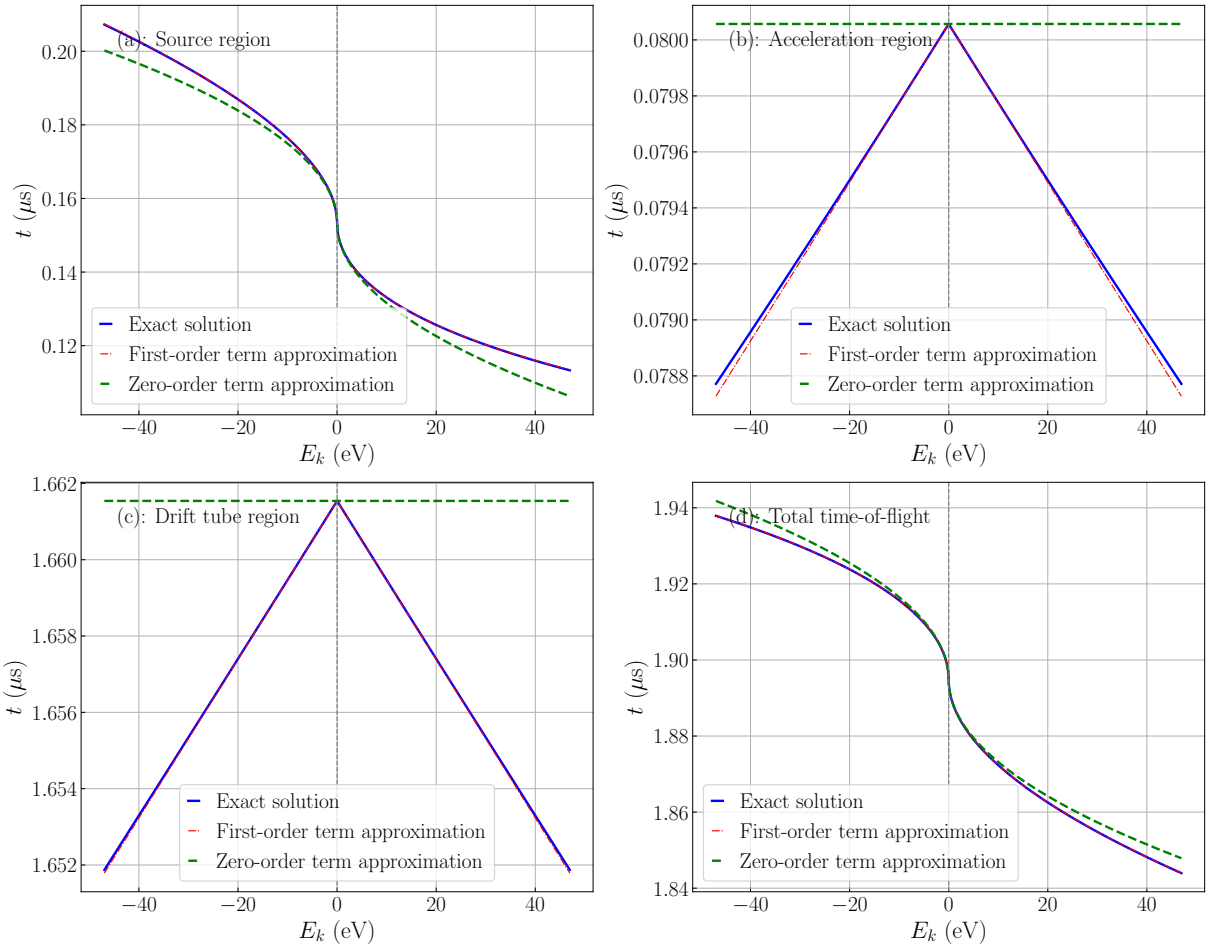

Figure B.10.: (a–c) show the flight time t as a function of the initial kinetic energy within the source region, acceleration region, and drift tube region, respectively. (d) presents the total flight time, i.e., the sum across all three regions. The blue curves represent the results from exact solution based on Newton's laws. The red dashed lines correspond to the first-order retained approximation derived from a Taylor expansion, while the green dashed lines represent the zero-order retained approximation.

with a remainder term smaller than $(v_0/v_{sn})^4/8$. Retaining only the first-order term in the Taylor expansion and substituting into the expression for (B.16) gives the approximate form:

$$t_s \approx \frac{v_{sn}}{a_s} - \frac{v_0}{a_s} + \frac{v_0^2}{2v_{sn}a_s} = t_{sn} - \frac{v_0}{a_s} + \frac{v_0^2}{2v_{sn}a_s}. \tag{B.18}$$

Here, the nominal time, so the time with $v_0 = 0$ is denoted as t_{sn}. It is instructive to consider the signs of the three terms. Due to the definition of the coordinate system, the first term is always greater than 0. The second term depends on the direction of the initial velocity. It (including the minus sign in front of it) is positive when the particle first moves away from the detector and negative for the opposite case. The third term is again positive for all initial velocities. This different behavior of the last two terms regarding the initial velocity sign causes an asymmetry with respect to the nominal time. We present the results for t_s as a function of the initial kinetic energy in Fig. B.10 a. Here, positive and negative initial kinetic energy values corresponding to the direction of the initial velocity. The blue curve shows t_s from the exact results based on Newton's law

by (B.16). The red dashed line corresponds to the approximation from (B.18), and the green dashed line includes only the zero-order term of the Taylor expansion in (B.17). The results indicate that the quadratic term in v_0 contributes noticeably to an increase in t_s within the source region.

To further evaluate the accuracy of the approximation. The resulting v_{sn} in exact solution is 97881 m/s(compare to $\max v_0 = \pm 30000$ m/s) and typical value becomes

$$\epsilon = \left| \frac{v_0}{v_{sn}} \right| \approx 0.306. \tag{B.19}$$

Substituting this into the Taylor remainder estimate, the relative error from retaining the expansion at first order (neglecting the $O(\epsilon^4)$ term) is approximately:

$$\text{Relative error} \approx \frac{1}{8}\epsilon^4 \approx \frac{1}{8}(0.306)^4 \approx 1.1 \times 10^{-3}. \tag{B.20}$$

This corresponds to an error of only 0.11% and this approximation in (B.18) is deemed sufficiently accurate over a broader range of v_0.

The second acceleration region contains again a homogeneous electric field pointing along x in the same direction as the one in the source region. For the time the particle spends in the second acceleration region t_d we can therefore again make use of (B.12). Here we set $s_0 = 0$, $v_0 = v_s$ and $t_0 = 0$ and we are interested when the particle is at d. This leads to a condition for t_d in the same way as in (B.13) given by

$$\frac{1}{2}a_d t_d^2 + v_s t_d - d = 0. \tag{B.21}$$

Here, $a_d = q\varepsilon_d/m$ is the acceleration in the acceleration region, v_s is the velocity of the particle upon exiting the source region, and d is the distance through the acceleration region.

As shown in Fig. B.9, due to the symmetry of the system, particles with $\pm v_0$ undergo symmetric motion. A negative initial velocity ($-v_0$) experiences a turning point near the origin and then follows a trajectory identical to that of the positive initial velocity ($+v_0$). Therefore, v_s, the velocity upon leaving the source region, is the same for both $+v_0$ and $-v_0$. The corresponding time t_d through the second acceleration region and the terminal velocity at the end of the second acceleration region is given by

$$t_d = \frac{-v_s + \sqrt{v_s^2 + 2a_d d}}{a_d} = \frac{-v_s + v_d}{a_d}, \tag{B.22}$$

$$v_d = \sqrt{v_s^2 + 2a_d d} = \sqrt{v_0^2 + 2a_s s + 2a_d d} = \sqrt{v_0^2 + v_{dn}^2} \tag{B.23}$$

with nominal velocity $v_{dn} = \sqrt{2a_s s + 2a_d d}$. We similarly expand v_d using Taylor expansion making use of $v_0 \ll v_{dn}$:

$$v_d = \sqrt{v_0^2 + v_{dn}^2} = \lim_{\frac{v_0}{v_{dn}} \to 0} \left(v_{dn} \left(1 + \frac{1}{2}\left(\frac{v_0}{v_{dn}}\right)^2 - \frac{1}{8}\left(\frac{v_0}{v_{dn}}\right)^4 + O((\frac{v_0}{v_{dn}})^6) \right) \right). \tag{B.24}$$

With a remainder term smaller than $(v_0/v_{\mathrm{dn}})^4/8$. Substituting the approximations for v_{s} and v_{d} into (B.22), we obtain:

$$t_{\mathrm{d}} \approx \frac{-v_{\mathrm{sn}}\left(1+\frac{1}{2}\frac{v_0^2}{v_{\mathrm{sn}}^2}\right)+v_{\mathrm{dn}}\left(1+\frac{1}{2}\frac{v_0^2}{v_{\mathrm{dn}}^2}\right)}{a_{\mathrm{d}}} \tag{B.25}$$

$$= \frac{v_{\mathrm{dn}}-v_{\mathrm{sn}}}{a_{\mathrm{d}}}+\frac{1}{2a_{\mathrm{d}}}\left(\frac{v_0^2}{v_{\mathrm{dn}}}-\frac{v_0^2}{v_{\mathrm{sn}}}\right) \tag{B.26}$$

$$= t_{\mathrm{dn}}+\frac{1}{2a_{\mathrm{d}}}\left(\frac{1}{v_{\mathrm{dn}}}-\frac{1}{v_{\mathrm{sn}}}\right)v_0^2, \tag{B.27}$$

with the nominal time t_{dn} for the acceleration region. Again, the signs of the two terms can be considered. The first term is strictly positive for the acceleration fields defined above. It could theoretically be negative if the particles are slowed down in the second acceleration stage. But this is not the situation we evaluate here. The second term is strictly negative because of $v_{\mathrm{sn}} < v_{\mathrm{dn}}$.

Fig. B.10 b shows t_{d} as a function of the initial kinetic energy in blue for the exact solution of (B.22). The red dashed line corresponds to the approximation from (B.27), and the green dashed line shows the result when only the zero-order term in the Taylor expansion is retained (t_{dn}). The results demonstrate that in the acceleration region, the flight time is symmetric with respect to $\pm v_0$, and the strictly negative sign of the first-order term in (B.27) causes a decrease in t_{d}.

Similarly, the resulting v_{dn} in exact solution is 276851 m/s and typical value becomes

$$\epsilon = \left|\frac{v_0}{v_{\mathrm{dn}}}\right| \approx 0.108. \tag{B.28}$$

This is even smaller when compare to case for v_{sn}.

For the last drift tube region—where the electric field is zero—the particles undergo uniform straight line motion. The corresponding time spend in the drift tube is:

$$t_{\mathrm{D}} = \frac{D}{v_{\mathrm{d}}}. \tag{B.29}$$

The approximate expression for t_{D}, derived via a Taylor expansion of v_{d} and retaining only the first-order term, is given by:

$$t_{\mathrm{D}} = D\left(v_0^2+v_{\mathrm{dn}}^2\right)^{-\frac{1}{2}} = \lim_{\frac{v_0}{v_{\mathrm{dn}}}\to 0}\left(\frac{D}{v_{\mathrm{dn}}}\left(1-\frac{1}{2}\left(\frac{v_0}{v_{\mathrm{dn}}}\right)^2+\frac{3}{8}\left(\frac{v_0}{v_{\mathrm{dn}}}\right)^4+\mathcal{O}((\frac{v_0}{v_{\mathrm{dn}}})^6)\right)\right) \approx t_{\mathrm{Dn}}-\frac{t_{\mathrm{Dn}}}{2}\left(\frac{v_0}{v_{\mathrm{dn}}}\right)^2. \tag{B.30}$$

Here, the first term which is the nominal time in the drift tube t_{Dn} is strictly positive while the second term (including the sign) is strictly negative. In Fig. B.10 c, the results are presented for the drift tube. The blue curve denotes the exact solution of drift tube time-of-flight t_{D} as a function of the initial kinetic energy. The red dashed line corresponds to the expression derived above, while the green dashed line represents the result obtained by retaining only the zero-order term in the Taylor expansion. The results demonstrate that similar to the acceleration region, the trajectories for $\pm v_0$ are symmetric, and the first-order contributions of v_0 lead to a reduction in t_{D}.

The total time-of-flight is therefore given by

$$t_{\text{sum}} = t_{\text{s}}+t_{\text{d}}+t_{\text{D}} = t_{\text{sn}}+t_{\text{dn}}+t_{\text{Dn}}-\frac{v_0}{a_{\text{s}}}+\frac{v_0^2}{2v_{\text{sn}}a_{\text{s}}}+\frac{1}{2a_{\text{d}}}\left(\frac{1}{v_{\text{dn}}}-\frac{1}{v_{\text{sn}}}\right)v_0^2-\frac{t_{\text{Dn}}}{2}\left(\frac{v_0}{v_{\text{dn}}}\right)^2. \quad \text{(B.31)}$$

Here, the first three terms represent the nominal times in the corresponding sections of the spectrometer. The remaining terms are the corrections caused by initial velocities along the x-direction. These terms correspond to Equation [23] in Kukk's paper [287].

In Fig. B.10 d, the total time-of-flight t_{sum} is shown. The blue curve depicts the exact results based on Newtonian mechanics, the red dashed line represents the approximation incorporating first-order corrections, and the green dashed line shows the approximation using only the zero-order term. Overall, the quadratic dependence on v_0 leads to a reduction when summing the times across all three regions.

To further validate these results, we employed SIMION simulations based on the same conventional VMI geometry as described earlier in Fig. 4.4. The electric fields in this case account for non-zero plate thickness and the absence of grids or meshes, which introduces field inhomogeneities near the edges, deviating from the ideal homogeneous field assumption.

In Fig. B.11, we present the simulated time-of-flight t as a function of the initial kinetic energy along the x-direction. Specifically, we recorded:

(a) $t_1 = t_s$ at which particles exit the source region,

(b) $t_2 = t_s + t_d$ at which particles exit the acceleration region, and

(c) $t_3 = t_s + t_d + t_D$ at which particles reach the detector.

In each subplot, the dotted line represents the SIMION simulation results, the light-colored curve indicates the fitting using the approximation from (B.31), and the black line denotes the result when only the zero-order term is retained.

The results demonstrate excellent agreement between the theoretical calculations and SIMION simulations for the time-of-flight t. The dominant contribution to t originates from the drift tube region, whereas the deviation Δt due to the initial velocity component v_x primarily arises from the source region. Moreover, accurate modeling of the temporal resolution must rigorously account for first-order effects not only in the source region but also in the acceleration and drift regions. These first-order corrections are critical to capturing the influence of initial axial velocities on t with high precision. From (B.31), we extract all terms involving the mass-to-charge ratio m/q and reorganize the expression, yielding the following form:

$$\begin{aligned} t_{\text{sum}} = &\left(\sqrt{\frac{2s}{\varepsilon_{\text{s}}}}+\frac{1}{\varepsilon_{\text{d}}}\left(\sqrt{2(\varepsilon_{\text{s}}s+\varepsilon_{\text{d}}d)}-\sqrt{2\varepsilon_{\text{s}}s}\right)+D\sqrt{\frac{1}{2(\varepsilon_{\text{s}}s+\varepsilon_{\text{d}}d)}}\right)\cdot\sqrt{\frac{m}{q}} \\ &-\frac{v_0}{\varepsilon_{\text{s}}}\cdot\sqrt{\frac{m}{q}}^2+\left(\frac{v_0^2}{\sqrt{8\varepsilon_{\text{s}}^3s}}+\frac{v_0^2}{2\varepsilon_{\text{d}}}\left(\frac{1}{\sqrt{2(\varepsilon_{\text{s}}s+\varepsilon_{\text{d}}d)}}-\frac{1}{\sqrt{2\varepsilon_{\text{s}}s}}\right)-\frac{Dv_0^2}{4\sqrt{2}\cdot(\varepsilon_{\text{s}}s+\varepsilon_{\text{d}}d)^{3/2}}\right)\cdot\sqrt{\frac{m}{q}}^3. \end{aligned} \quad \text{(B.32)}$$

The simplest fitting expression for t as a function of the initial velocity(v_0) can be summarized in the following simple form:

$$t_{\text{sum}} = a\cdot\sqrt{\frac{m}{q}}-b\cdot\sqrt{\frac{m}{q}}^2\cdot v_0-c\cdot\sqrt{\frac{m}{q}}^3\cdot v_0^2. \quad \text{(B.33)}$$

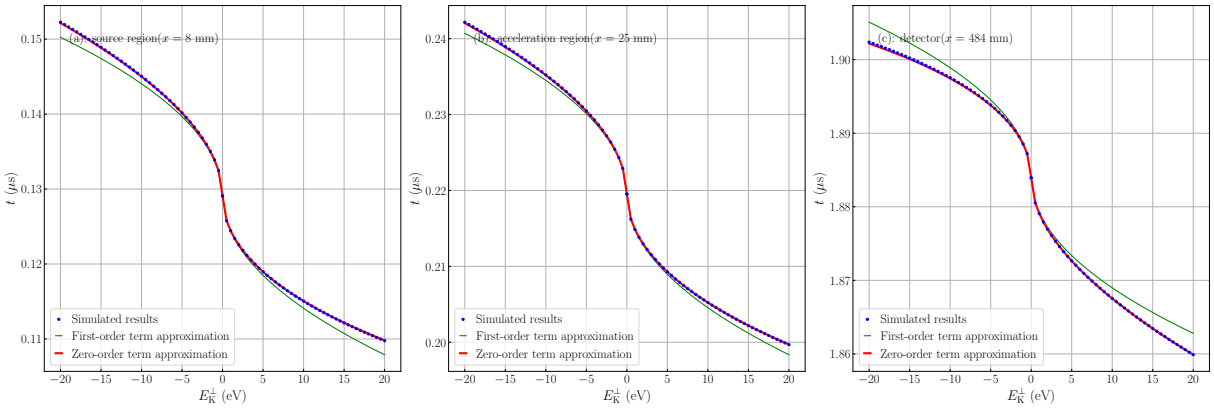

Figure B.11.: (a–c) show the flight time t as a function of the initial kinetic energy along the x-axis when particles exit the source region, the acceleration region, and finally reach the detector, respectively. The blue dotted lines represent the results obtained from SIMION simulations. The red curves correspond to the first-order approximation fitting derived from (B.31), while the green curves represent the zero-order approximation.

Here, the fitting coefficients a, b, and c depend solely on the geometry and voltage configuration of the VMI system, and are independent of the particle species.

B.6.4. Effect of a Small Perturbation s_0 on the Total Time t_{sum}

In the previous derivation of t_{sum}, we assumed for simplicity initial displacement $s_0 = 0$ from the center of source region. Now, we consider the effect of $s_0 \neq 0$ assuming $s_0 \ll s$. It is known from (B.32) that most of the terms are depend on the s. To investigate the sensitivity of the total time-of-flight t_{sum} to small perturbations in the initial position, we apply initial displacement given by:

$$s' = s + s_0, \tag{B.34}$$

where $s_0 \ll s$. Our goal is to understand how the induced perturbation of initial displacement from the source center influences t_{sum}. Therefore, we apply the first-order retained Taylor expansion of (B.32) and derive it as a function of s' to investigate the effect.

Considering (B.34), the expression for v'_{sn} becomes:

$$v'_{\text{sn}} = \sqrt{2a_{\text{s}}(s + s_0)} = \sqrt{2a_{\text{s}}s} \cdot \sqrt{1 + \frac{s_0}{s}} \approx v_{\text{sn}} \left(1 + \frac{1}{2}\frac{s_0}{s}\right). \tag{B.35}$$

The corresponding perturbed time t'_{s} in the source region is then:

$$\begin{aligned} t'_{\text{s}} &\approx \left(\frac{v_{\text{sn}}}{a_{\text{s}}} + \frac{v_{\text{sn}}}{2a_{\text{s}}} \cdot \frac{s_0}{s}\right) - \frac{v_0}{a_{\text{s}}} + \left(\frac{v_0^2}{2v_{\text{sn}}a_{\text{s}}} - \frac{v_0^2}{4v_{\text{sn}}a_{\text{s}}} \cdot \frac{s_0}{s}\right) \\ &= \left(\frac{v_{\text{sn}}}{a_{\text{s}}} - \frac{v_0}{a_{\text{s}}} + \frac{v_0^2}{2v_{\text{sn}}a_{\text{s}}}\right) + \left(\frac{v_{\text{sn}}}{2a_{\text{s}}} - \frac{v_0^2}{4v_{\text{sn}}a_{\text{s}}}\right) \cdot \frac{s_0}{s} \\ &= t_{\text{s}} + \left(\frac{v_{\text{sn}}}{2a_{\text{s}}} - \frac{v_0^2}{4v_{\text{sn}}a_{\text{s}}}\right) \cdot \frac{s_0}{s}, \end{aligned} \tag{B.36}$$

where the second term represents the correction due to the initial displacement s_0.

Similarly, the perturbed nominal velocity in the acceleration region becomes:

$$v'_{\mathrm{dn}} = \sqrt{2a_{\mathrm{s}}(s+s_0)+2a_{\mathrm{d}}d} = \sqrt{v_{\mathrm{dn}}^2+2a_{\mathrm{s}}s_0} \approx v_{\mathrm{dn}}\left(1+\frac{a_{\mathrm{s}}s_0}{v_{\mathrm{dn}}^2}\right). \tag{B.37}$$

The perturbed time t'_{d} in the acceleration region is given by:

$$\begin{aligned} t'_{\mathrm{d}} &= \frac{v'_{\mathrm{dn}}-v'_{\mathrm{sn}}}{a_{\mathrm{d}}} + \frac{1}{2a_{\mathrm{d}}}\left(\frac{v_0^2}{v'_{\mathrm{dn}}}-\frac{v_0^2}{v'_{\mathrm{sn}}}\right) \\ &\approx \frac{1}{a_{\mathrm{d}}}\left[v_{\mathrm{dn}}\left(1+\frac{a_{\mathrm{s}}s_0}{v_{\mathrm{dn}}^2}\right)-v_{\mathrm{sn}}\left(1+\frac{1}{2}\cdot\frac{s_0}{s}\right)\right] \\ &\quad + \frac{1}{2a_{\mathrm{d}}}\left[\frac{v_0^2}{v_{\mathrm{dn}}}\left(1-\frac{a_{\mathrm{s}}s_0}{v_{\mathrm{dn}}^2}\right)-\frac{v_0^2}{v_{\mathrm{sn}}}\left(1-\frac{1}{2}\cdot\frac{s_0}{s}\right)\right] \\ &= t_{\mathrm{d}} + \frac{1}{a_{\mathrm{d}}}\left(\frac{a_{\mathrm{s}}s_0}{v_{\mathrm{dn}}}-\frac{v_{\mathrm{sn}}}{2}\cdot\frac{s_0}{s}\right)+\frac{v_0^2}{2a_{\mathrm{d}}}\left(-\frac{a_{\mathrm{s}}s_0}{v_{\mathrm{dn}}^3}+\frac{1}{2v_{\mathrm{sn}}s}s_0\right), \end{aligned} \tag{B.38}$$

which simplifies to:

$$t'_{\mathrm{d}} \approx t_{\mathrm{d}} + s_0\cdot\left[\frac{1}{a_{\mathrm{d}}}\left(\frac{a_{\mathrm{s}}}{v_{\mathrm{dn}}}-\frac{v_{\mathrm{sn}}}{2s}\right)+\frac{v_0^2}{2a_{\mathrm{d}}}\left(-\frac{a_{\mathrm{s}}}{v_{\mathrm{dn}}^3}+\frac{1}{2v_{\mathrm{sn}}s}\right)\right], \tag{B.39}$$

where again the second term represents the linear correction due to s_0.

Finally, the perturbed time-of-flight in the drift tube region is:

$$t'_{\mathrm{D}} = \frac{D}{\sqrt{v_0^2+\left(v'_{\mathrm{dn}}\right)^2}} = \frac{D}{\sqrt{v_0^2+v_{\mathrm{dn}}^2+2a_{\mathrm{s}}s_0}} \tag{B.40}$$

$$\approx \frac{D}{\sqrt{v_0^2+v_{\mathrm{dn}}^2}}\left(1-\frac{a_{\mathrm{s}}s_0}{\left(v_0^2+v_{\mathrm{dn}}^2\right)}\right) \tag{B.41}$$

$$= t_{\mathrm{D}} - \frac{Da_{\mathrm{s}}s_0}{\left(v_0^2+v_{\mathrm{dn}}^2\right)^{3/2}}. \tag{B.42}$$

In summary, the influence of a small displacement s_0 on the total flight time in each region can be represented as a linear correction term added to the nominal time.

C. Appendix to Chapter 6

C.1. Experimental conditions

C.1.1. IR laser calibration

Fig. C.1 shows calibration curve of the IR peak intensity dependence on the half-wave plate rotation angle (Θ). The data were fitted by the function $I(\Theta) = I_{\max}/2 \cdot \left(\cos(4\Theta) + 1\right)$ [363]. The fitted factor $I_{\max} = 6.62 \cdot 10^{14}$ W/cm^2. The IR laser peak intensity was set to $1.27 \cdot 10^{14}$ W/cm^2 in the experiments (corresponding to the half-wave plate angle set to 32°).

C.1.2. Molecular beam density

The electrostatic deflector enabled us to create a target ensemble of pyrrole-H_2O clusters with a purity of $\sim$ 95 %. Fig. C.2 illustrates an estimation of the pyrrole-H_2O beam density ρ through fitting the ion count slope at saturation conditions [6, 264, 266].

$$\lim_{I_0 \to \infty} \left(\frac{\mathrm{d}\Sigma_r}{\mathrm{d} \ln I_0} \right) = 2\pi\alpha\sigma_r^2 D\rho, \tag{C.1}$$

where D is the molecular beam length, Σ_r is the standard deviation of the transverse laser intensity distribution, and α_r is an instrument sensitivity given by transparency of the meshes and sensitivity of the microchannel plate detector. The signal was measured at deflected position of molecular beam (y = 2.33 mm). The resulting molecular beam density at y = 2.33 mm is $\sim 2.9 \cdot 10^7$ cm^{-3}. The saturation intensity $I_{\text{sat}} = 2 \cdot 10^{14}$ W/cm^2 is approximately 2-3 times larger than the previously reported value from [6]. The

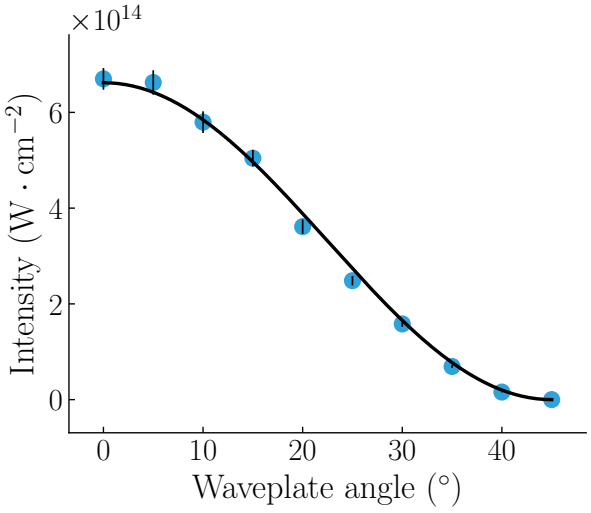

Figure C.1.: Calibration of the IR laser peak intensity on the half-wave plate angle Θ.

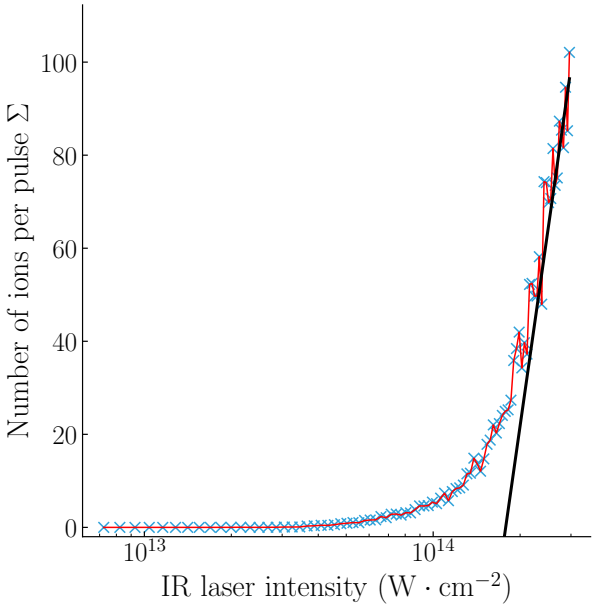

Figure C.2.: Blue x marker and red curve show the number of ions signal from all mass over charge channels per pulse as a function of the IR laser peak-intensity natural logarithm ln I_0. The black line represents the fit of the asymptotic slope of (C.1) from the last 10 data points, see more details from [264].

discrepancy between the values can be explained by a strong detector saturation in the reported measurement [6].

Similarly, we estimate the molecular beam density to $\sim 7.1 \cdot 10^7$ cm^{-3} from the ion yield detected after FEL ionization. Here, we approximated the cross section of pyrrole-water by $\sigma_{\text{pyrrole-H}_2\text{O}} = 1.66$ Mbarn given by the sum $\sigma_{\text{pyrrole-H}_2\text{O}} = 4 \cdot \sigma_{\text{C}} + \sigma_{\text{N}} + \sigma_{\text{O}} + 7 \cdot \sigma_{\text{H}}$ [364]. The FEL energy per pulse was set to 67.5 μJ and the photon energy was set slightly above the K-edge of nitrogen, i. e., $E_{\text{FEL}} = 495$ eV. Furthermore, we assumed that each FEL photon leads to two detected ion particles to estimate upper limit for the molecular beam density.

The both estimates gives us range of densities of $10^7 - 10^8$ cm^{-3}, which are in very good agreement with our laboratory experiments [144, 145, 264].

C.2. Single color ionization

C.2.1. IR-only induced fragmentation with different laser intensities

Our previous table-top experiments [6] also applied 800 nm photoionization to trigger dynamics by ionizing pyrrole-H_2O with a nominal peak intensity around 10^{14} W/cm^2. The current peak intensity was used in the range from $1.3 \cdot 10^{14}$ W $\cdot$ cm^{-2} to $3.9 \cdot 10^{14}$ W/cm^2.

Fig. C.3 shows the TOF-MS of pyrrole-H_2O after strong field ionization for four different laser pulse energies. Fig. C.3 (a) and Fig. C.3 (b) show zoomed-in areas covering the ranges of $m/q = 27 - 42$ u/e and $m/q = 65 - 69$ u/e, respectively. Particularly at higher applied IR-laser intensities ($3.0 - 3.9 \cdot 10^{14}$ W/cm^2), the signal from Pyr$^+$ saturates the camera, rendering precise estimation of the Pyr$^+$ ion yields practically unfeasible. The similar problem exhibits signal at virtual mass of $m/q = 0.4$ u/e assigned to

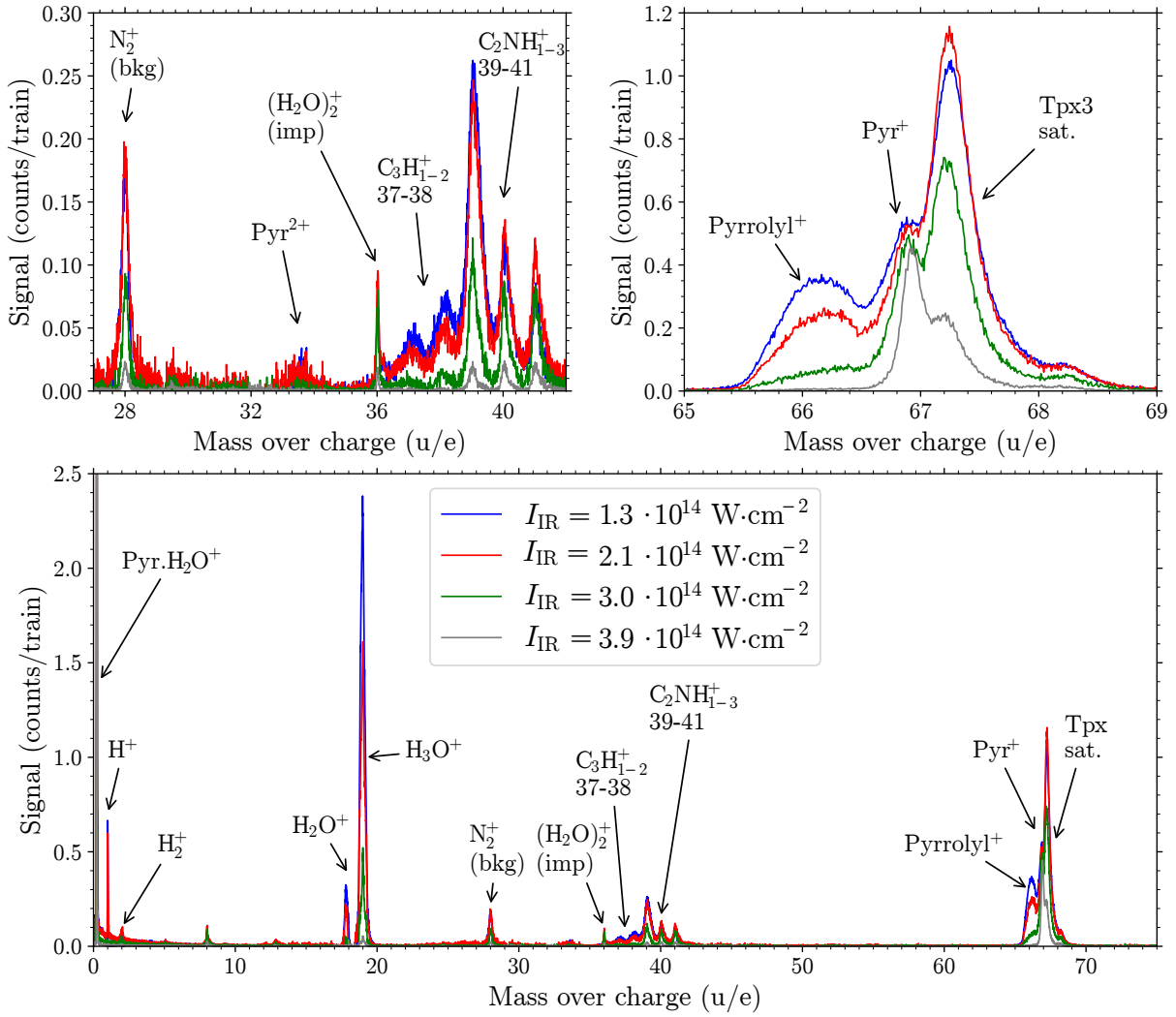

Figure C.3.: Mass spectrum comparison of detected ions after IR-only ionization for different laser intensities. The two upper plots show zoomed-in ranges the mass spectrum below.

(pyrrole-H_2O)$^+$ (m/q = 85 u/e). The virtual shift of its mass-over-charge ratio is due to the bunch structure of the ionizing pulses with pulse temporal separation of 4.9 μs.

The less prominent channels, exhibiting roughly an order lower ion yields, involve proton transfer yielding H_3O^+ + pyrrolyl ((Pyr-H), labeled as H_3O^+ channel) and pyrrole ring fragmentation, resulting in $C_2NH_{1-3}^+$ ions ($m/q = 39-41$ u/e, labeled as $C_2NH_{1-3}^+$ channel), evident as distinctive three peaks in the mass spectrum of Fig. C.3, respectively, with similar signal intensities.

Other significantly less prominent (3-4 orders less) fragmentation channels of singly ionized pyrrole-H_2O generate $C_3H_{1-3}^+$ ions (37-39 m/u, labeled as C_3^+ channel). The ion $C_3H_3^+$ overlaps with the $C_2NH_1^+$ signal, complicating precise ion signal assignment. Nevertheless, the three-peak structure at $m/q = 39-41$ u/e and absence of C_3^+ ions without hydrogens suggest a higher propensity for charge localization at the three atomic residuals of the fragmented pyrrole ring containing nitrogen. Interestingly, the charged fragment exhibits a tendency to bond at least one hydrogen atom. The last detected minor channel manifests ions at m/q = 52 u/e, attributed to the production of $C_4H_4^+$ ions (labeled as channel $C_4H_4^+$) following charged pyrrole ring fragmentation. No

additional signals could be unequivocally assigned to (pyrrole-H_2O)$^+$ fragmentation, suggesting that their contribution should be at least 5-6 orders of magnitude lower than the ion yield of the stabilized (pyrrole-H_2O)$^+$ channel.

Furthermore, even at the lowest applied laser power, we observe double ionization of pyrrole-H_2O complexes, leading to the (weak) Coulomb explosion channel of H_3O^+ + (Pyr-H)$^+$ (channel labelled as (Pyr-H)$^+$: +1 or H_3O^+: +1). At higher laser peak intensities ($I_0 = 3.9 \cdot 10^{14}$ W/cm^2) the channel is strongly enhanced. Also, additional Coulomb channels emerge, yielding H_2O^+, Pyr^+, and $C_2NH^+_{1-3}$ ions (along with very minor signals of $C_2H^+_{1-3}$/CNH^+_{0-2} ions), characterized by ions with high kinetic energy represented by blurred commas around the central blobs. As no other counter-fragment in the $C_2H^+_{0-2}$/CNH^+_{0-2} region is observed for $C_2NH^+_{1-3}$ ions, we hypothesize that new pathways involve abrupt H_2O^+ + Pyr^+ dissociation and secondary fragmentation of the charged pyrrole ring. Lastly, we also detect stabilized Pyr^{2+} ions, indicating either the repulsion of neutral water following double ionization or possibly stabilization of doubly charged isolated pyrrole present as an impurity of our molecular beam.

At the highest applied laser intensities, we additionally detect a small fraction of triple-ionized pyrrole-H_2O fragmentation, evidenced by the presence of high kinetic energy ions such as H_3O^+, H_2O^+, and Pyr^{2+} exhibiting the typical sharp Coulomb explosion structure. It is assumed that triple ionization also leads to the formation of $C_3H^+_{1-3}$/$C_2NH^+_{1-3}$ products. However, direct assignment is challenging due to the blurring of Coulomb rings caused by secondary fragmentation. Surprisingly, no significant $C_2H^+_{0-2}$/CN^+_{0-2} ion signal is observed, contrary to the presence of high kinetic energy CH^+_{0-1} and H^+ ion signals.

It is noteworthy that we also detect the parent signal of the water dimer $(H_2O)^+_2$ at $m/q = 36$ u/e, which is considered an impurity in our experiment. Unfortunately, the high effective dipole moment to mass ratio of $(H_2O)_2$ hinders its spatial separation via electrostatic deflection from pyrrole-H_2O clusters. Utilizing ion yields of $(H_2O)^+_2$ fragmentation following IR ionization from our table-top experiment [36], we can infer its minor contribution to the H_2O^+ and H_3O^+ signals. Moreover, a small fraction of higher Pyr_n-$(H_2O)^+_m$ clusters, where $n > 1$ or $m > 1$, is observed with a signal ratio to the parent (pyrrole-H_2O)$^+$ ion of less than 10^{-2}.

In summary, our observations on IR-only ionized pyrrole-H_2O clusters align well with our previous findings [6], also supporting the photoprotective role of H_2O in the pyrrole-H_2O complex after single ionization.

C.2.2. Photoion-photoion coincidence maps

Fig. C.4 and Fig. C.5 show coincidence maps of detected photoions after IR-only and FEL-only ionization, respectively. The maps are shown in full range in subfigures (A) and two zoomed-in ranges of $m/q = (16-20, 16-20)$ u/e and $m/q = (16-20, 64-68)$ u/e in subfigures (B) and (C), respectively, to investigate origin of H_2O^+ and H_3O^+ signal. The coincidence maps show that the detected H_2O^+ and H_3O^+ originate predominantly from fragmentation of ionized pyrrole-H_2O clusters.

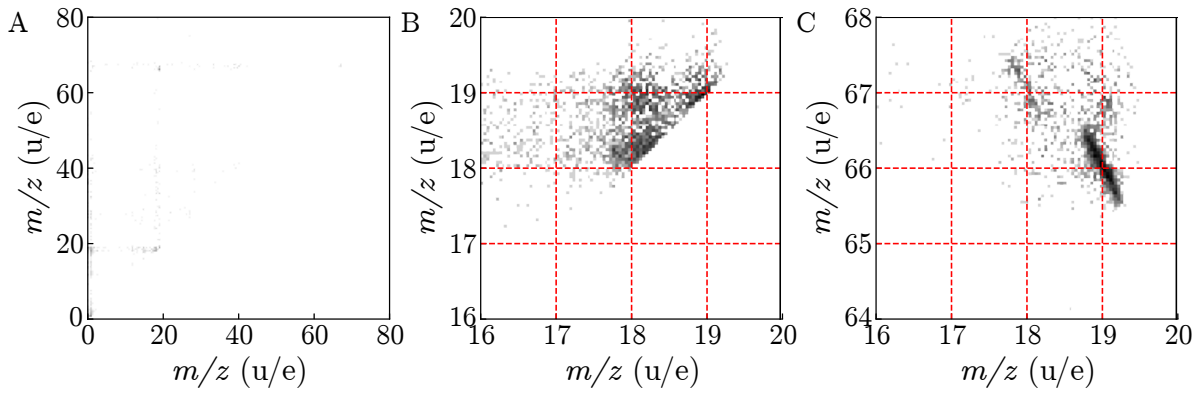

Figure C.4.: Coincidence maps after IR-only ionization in (A) full range, (B) range of m/q = (16 – 20, 16 – 20) u/e, and (C) range of m/q = (16 – 20, 64 – 68) u/e.

C.3. Dynamics of individual fragments

C.3.1. H_2O^+ and H_3O^+ fragments

At IR laser intensities of $1.3 \cdot 10^{14}$ W · cm^{-2}, the H_2O^+ and H_3O^+ signals are represented by the delay-dependent kinetic energy maps in Fig. C.6. The specific energy-dependent delay-averaged ion yield was subtracted from its energy-corresponding pump-probe dynamics to highlight the relative changes in the false colors. Both channels exhibit a particularly strong signal increase around time zero at very high kinetic energies above 3 eV. Such a high kinetic energy can be gained when the H_2O^+ and H_3O^+ ions are expelled from multicharged (n ≥ 2) counter-partner. At both, positive and negative pump-probe delays, the ions' kinetic energy is decreasing fastly. This can be observed directly in the ion maps. Around t_0, they show intensive positive (red) blob at high kinetic energies ($E_t > 3$ eV) and negative (blue) signal at lower kinetic energies ($E_t < 3$ eV). Contrary, at the late delays, the positive signal is shifted mainly to the area of the lower kinetic energies.

The signal dependences of the very-fast ions are shown in the plots below the corresponding delay-dependent kinetic energy maps. The applied very-fast ion region

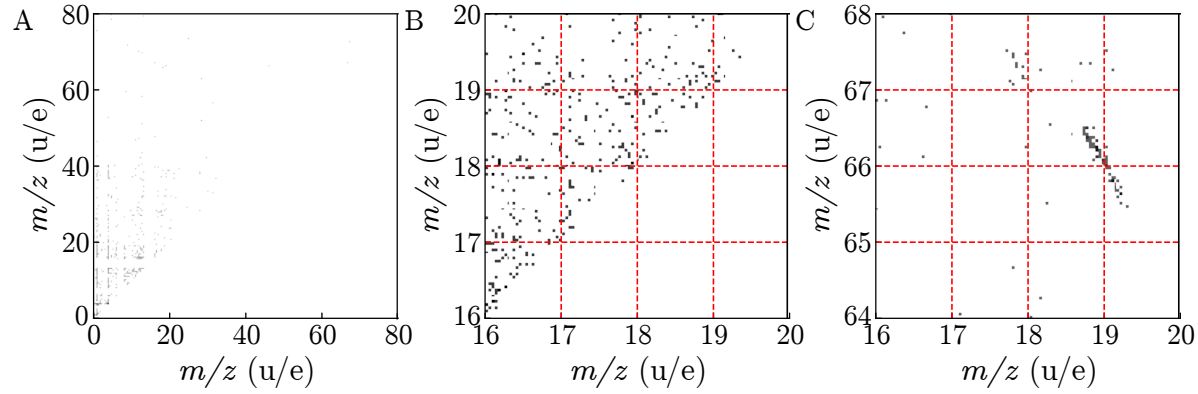

Figure C.5.: Coincidence maps after FEL-only ionization in (A) full range, (B) range of m/q = (16 – 20, 16 – 20) u/e, and (C) range of m/q = (16 – 20, 64 – 68) u/e.

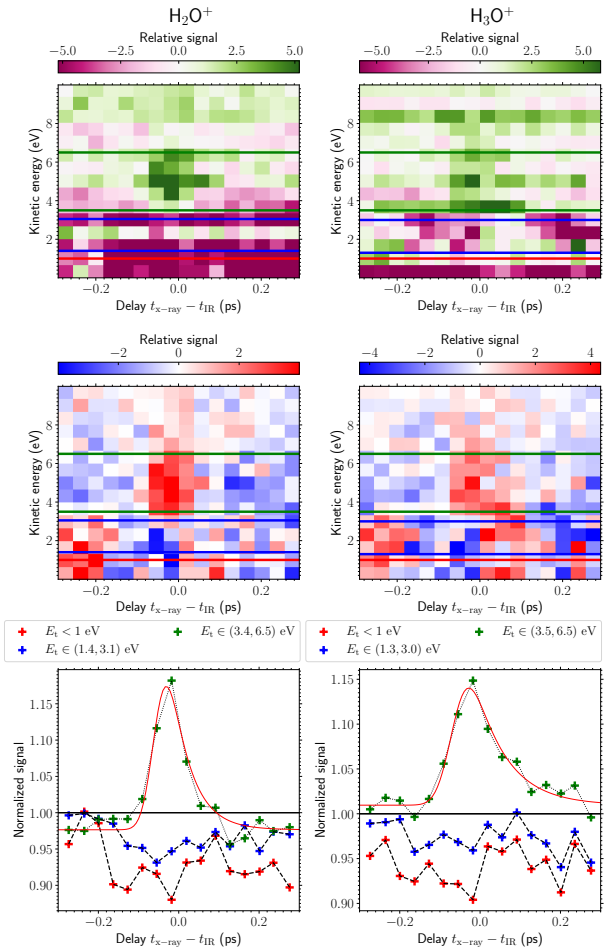

Figure C.6.: Time-dependent signal of H_2O^+ and H_3O^+. The ion maps at the top show the ion kinetic energy distribution for different pump-probe delays with subtracted incoherent sum of IR-only and FEL-only signal. The middle ion maps show the ion kinetic energy distribution for different pump-probe delays with subtracted the specific energy-dependent delay-averaged ion yield to emphasize the observed dynamical changes. Here it was normalized to the incoherent sum. The plots below display the measured signal yield for the selected region of interest, i. e., (green) $E_t(H_2O^+) \in (3.4, 6.5)$ eV, $E_t(H_3O^+) \in (3.5, 6.5)$ eV, (blue) $E_t(H_2O^+) \in (1.4, 3.1)$ eV, $E_t(H_3O^+) \in (1.3, 3.0)$ eV, and (red) H_2O^+: $E_t < 1$ eV and H_3O^+: $E_t < 1$ eV. The very-fast ion data are fitted with exponentially modified Gaussian distribution function to characterize the decay.

of interest used for the cut is indicated by green horizontal lines on the maps. The selection was made to fit to the region of H_2O^+: +2 ($E_t(H_2O^+) \in (3.4, 6.5)$ eV) and H_3O^+: +2 ($E_t(H_3O^+) \in (3.5, 6.5)$ eV) channels, which gives us estimation on the expected charge for counter-partner of ejected water ions. Whereas the H_2O^+ signal shows a close to Gaussian shape, the H_3O^+ exhibits significant wing at positive delays. Both channels were fitted with exponentially modified Gaussian distribution functions to characterize the dependence with estimated lifetimes of $\tau_{H_2O^+:+2} = 50$ fs and $\tau_{H_3O^+:+2} = 79$ fs. The peak maxima of H_3O^+:+2 and H_2O^+:+2 channels is shifted slightly to the negative pump-probe delays, which might be however artificially caused by the assignment of time zero to the center of signal step decrease at N^{2+} signal similar to the assignment in [365].

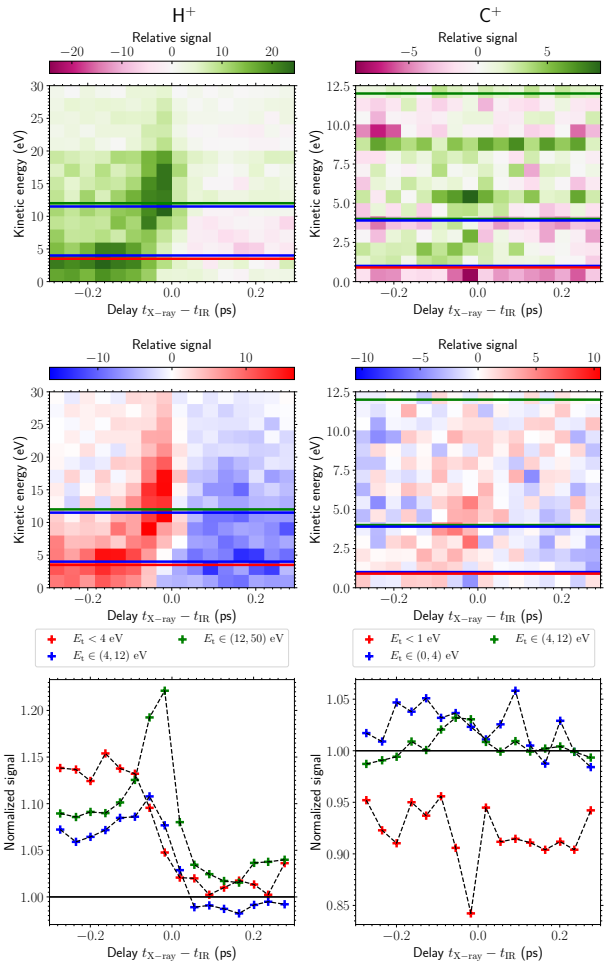

Figure C.7.: Time-dependent signal of H^+ and C^+. The ion maps at the top show the ion kinetic energy distribution for different pump-probe delays with subtracted incoherent sum of IR-only and FEL-only signal. The middle ion maps show the ion kinetic energy distribution for different pump-probe delays with subtracted the specific energy-dependent delay-averaged ion yield to emphasize the observed dynamical changes. The plots below display the measured signal yield for the selected region of interest, i. e., (green) $E_t(H^+) \in (12, 50)$ eV, $E_t(C^+) \in (4, 12)$ eV, (blue) $E_t(H^+) \in (4, 12)$ eV, $E_t(C^+) \in (1, 4)$ eV, and (red) H^+: $E_t < 4$ eV and C^+: $E_t < 1$ eV.

The other two data sets (blue) and (red) correspond to the ions with lower kinetic energy. Again, the regions of interest were selected in a regions of (blue) 1st Coulomb explosion channel of H_2O^+: +1 ($E_t(H_2O^+) \in (1.4, 3.1)$ eV) and H_3O^+: +1 ($E_t(H_3O^+) \in (1.3, 3.0)$ eV), and (red) singly charged fragmentation of (pyrrole-H_2O)$^+$ ($E_t < 1$ eV). Ion signals in both regions of interest exhibit relative signal bleaching in the ion map around −50 fs, which is also visible in the absolute signal illustrated in the kinetics below. The H_2O^+ ions in H_2O^+: +1 region show fast signal increase between −100 fs and −200 fs reaching the plato of incoherent sum of background signal. Contrary, the H_2O^+: +1 ion signal in positive pump-probe delay direction shows slow signal increase between −50 fs and 200 fs rising to only half of the signal bleach compared to the background signal. The H_3O^+: +1 signal show similar behavior in the negative pump-probe delays with sudden signal increase around −200 fs, whereas in the positive pump-probe delays, we observe signal peaking at 100 fs followed by slow signal decrease. Finally, the slow ions $E_t < 1$ eV of the H_2O^+ ions at H_2O^+ regions exhibit similar sudden signal increase in

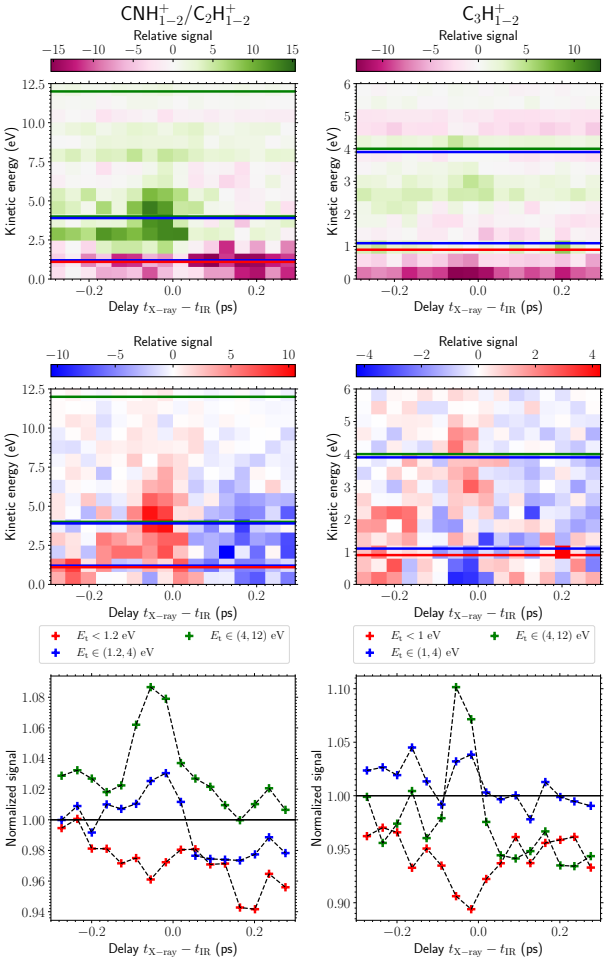

Figure C.8.: Time-dependent signal of $CNH^+_{1-2}/C_2H^+_{1-2}$ and $C_3H^+_{1-2}$. The ion maps at the top show the ion kinetic energy distribution for different pump-probe delays with subtracted incoherent sum of IR-only and FEL-only signal. The middle ion maps show the ion kinetic energy distribution for different pump-probe delays with subtracted the specific energy-dependent delay-averaged ion yield to emphasize the observed dynamical changes. The plots below display the measured signal yield for the selected region of interest, i. e., (green) $E_t(CNH_{1-2}/C_2H^+_{1-2}) \in (4, 12)$ eV, $E_t(C_3H^+_{1-2}) \in (4, 12)$ eV, (blue) $E_t(CNH_{1-2}/C_2H^+_{1-2}) \in (1, 4)$ eV, $E_t(C_3H^+_{1-2}) \in (1.2, 4)$ eV, and (red) $CNH_{1-2}/C_2H^+_{1-2}$: $E_t < 1.2$ eV and $C_3H^+_{1-2}$: $E_t < 1$ eV.

the negative delays as in the previous case shifted slightly to more negative delays. The positive delays reveal a sudden positive step at 0 fs for H_3O^+ ions followed by slow signal decrease. Nevertheless, the changes in the kinetics are rather small at the level of noise and should be taken carefully. Importantly, the ion yields of slow H_2O^+ and H_3O^+ ions stay below the incoherent background signal sum in the positive pump-probe delays.

C.3.2. Pyrrole ring fragments

All H_2O^+ and H_3O^+ ions together indicate production of ions with high kinetic energy around time zero and the deceleration of ion velocities at later delays. Similar features can also be observed in the pump-probe signal dependencies of the ring fragments. More significant dynamical changes in signal intensity can be observed in the time

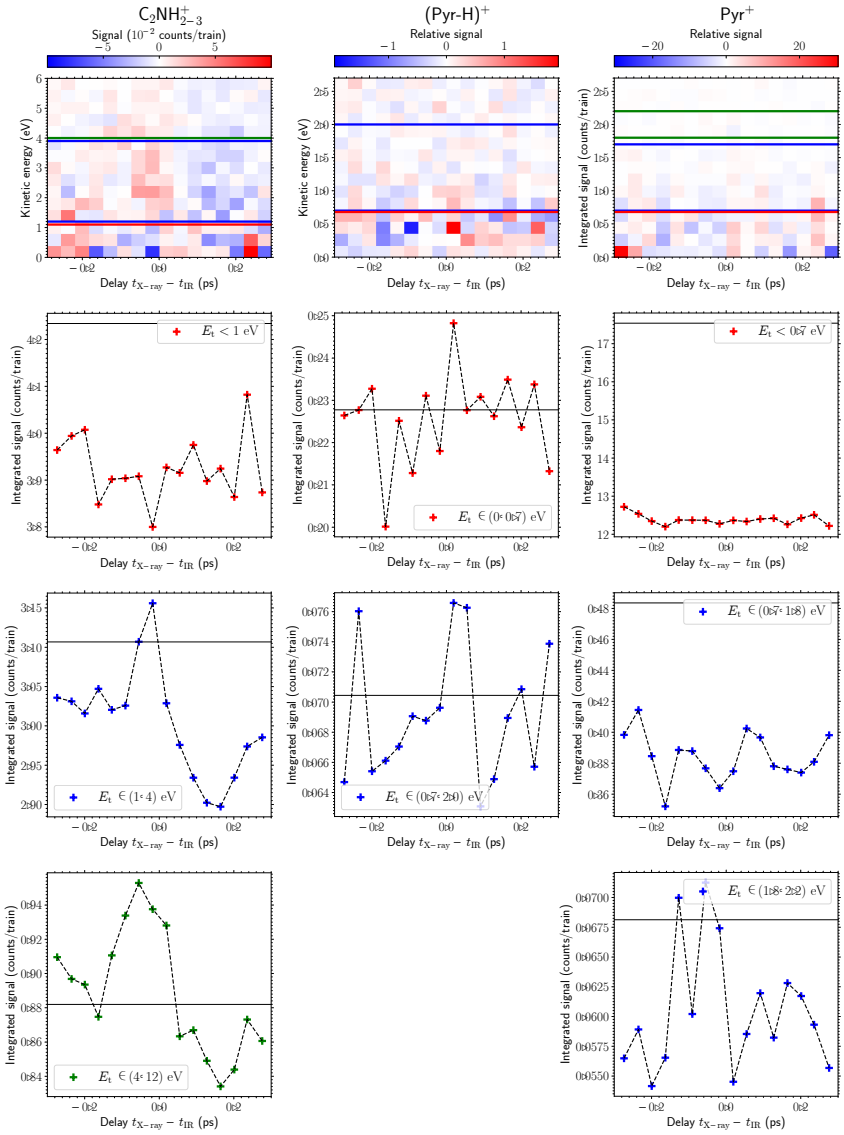

Figure C.9.: Time-dependent signal of $C_2NH^+_{2-3}$, pyrrole (Pyr^+) and pyrrolyl $(Pyr\text{-}H)^+$. The ion maps at the top show the kinetic energy distribution of ions for different pump-probe delays with subtracted the specific energy-dependent delay-averaged ion yield. The plots below display the measured signal yield for the selected region of interest.

dependence of the ring fragments H^+, C^+, $C_2H^+_m/CNH^+_{1-2}$, and $C_3H^+_{1-2}$, as shown in Fig. C.7 and Fig. C.8. Other channels, such as $C_2NH^+_{2-3}$, pyrrole (Pyr^+), and pyrrolyl ($(Pyr\text{-}H)^+$) are shown in Fig. C.9. The kinetic energy region of interest in the graphs below is chosen such that it resembles the selection for H_2O^+ and H_3O^+ ions as the observed ions due not show any obvious ring structure, which would enable simple assignment to different levels of Coulomb explosion channels.

The H^+ ion map in Fig. C.7 shows a strong cross-correlation signal for ions with kinetic energy around 12 eV at -15 fs and a visible step in the signal for ions with lower kinetic energy. The step delay shifts with kinetic energy, moving from -20 fs for the ions at 5-10 eV kinetic energy to -50 fs for ions with kinetic energy below 5 eV. This is also evident in the summed signal for different regions shown in the plot below the H^+ ion map, with indicated regions of interest. Additionally, the plots reveal that the signal level is at the background level at positive delays, while at negative delays, there is a

strong increase in the signal compared to the sum of incoherent signal from IR and FEL irradiation $S_{sum}^{FEL/IR}$.

The dynamical change for the C^+ signal is shown in the ion map shown on right of Fig. C.7 revealing rather unstructured kinetic energy distributions with signal bleach for slow C^+ and slight signal increase of ions with higher kinetic energy compared to $S_{sum}^{FEL/IR}$. Looking closely into the signal dependencies below the ion map, we observe a significant negative dip for slow ions with $E_t < 1$ eV (in red) at -15 fs and signal maximum for ions with $E_t > 5$ eV at -40 fs.

Similar features to the H^+ signal can be observed in the $CNH_{1-2}^+/C_2H_{1-2}^+$ signal, as shown in Fig. C.8, with a strong cross-correlation signal for ions with kinetic energy higher than 3 eV and a relative negative signal step in positive pump-probe delays. The ion map also reveals two dynamical changes in ion kinetic energy distributions: the first, similar to the H^+ signal, occurs at negative pump-probe delays; the second occurs at slightly positive delays. The plots for selected region of interest below the ion maps shows the relative signal to $S_{sum}^{FEL/IR}$. The dependencies are very similar to the H^+ signal. In contrast, we observe a signal decrease below $S_{sum}^{FEL/IR}$ for ions with $E_t < 3$ eV at positive pump-probe delays.

The larger pyrrole fragments containing three ring atoms, such as $C_3H_{1-2}^+$ and $C_2NH_{2-3}^+$, exhibit similar behavior. The acquired signal of $C_3H_{1-2}^+$ is shown in Fig. C.8, see also Fig. C.9 for $C_2NH_{2-3}^+$ signal. Both show a sharp positive cross-correlation peak for ions with higher kinetic energy—above 2.5 eV and 1.8 eV, respectively—and a negative bleaching for ions with lower kinetic energy. The signal dependencies also display a negative slope from negative to positive delays, with signal intensity lower by 10 % compared to the incoherent sum of the FEL-only and IR-only signals.

The behavior of intact pyrrole (Pyr^+), pyrrolyl ($(Pyr\text{-}H)^+$) ions was also studied, as shown in Fig. C.9. The Pyr^+ and $(Pyr\text{-}H)^+$ ions do not exhibit any significant signal dependence on the pump-probe delay. The small cross-correlation peak and slight signal increase of $(Pyr\text{-}H)^+$ are at the noise level. However, the magnitude of the Pyr^+ signal is significantly reduced compared to the incoherent sum of IR-only and FEL-only signals, indicating strong bleaching of the intact pyrrole ring signal. In contrast, the pump-probe signal level for $(Pyr\text{-}H)^+$ remains the same in the IR-FEL experiment as in their incoherent sum.

Bibliography

[1] Brian C. Dian, Gordon G. Brown, Kevin O. Douglass, and Brooks H. Pate. Measuring picosecond isomerization kinetics via broadband microwave spectroscopy. *Science*, 320(5878):924–928, 2008. doi: 10.1126/science.1155736. URL http://www.sciencemag.org/cgi/content/abstract/320/5878/924.

[2] Olga A. Sytina, Derren J. Heyes, C. Neil Hunter, Maxime T. Alexandre, Ivo H. M. Van Stokkum, Rienk Van Grondelle, and Marie Louise Groot. Conformational changes in an ultrafast light-driven enzyme determine catalytic activity. *Nature*, 456(7224):1001–1004, 2008. ISSN 14764687. doi: 10.1038/nature07354. URL https://doi.org/10.1038/nature07354.

[3] Tomas Ekeberg, Dameli Assalauova, Johan Bielecki, Rebecca Boll, Benedikt J. Daurer, Lutz A. Eichacker, Linda E. Franken, Davide E. Galli, Luca Gelisio, Lars Gumprecht, Laura H. Gunn, Janos Hajdu, Robert Hartmann, Dirk Hasse, Alexandr Ignatenko, Jayanath Koliyadu, Olena Kulyk, Ruslan Kurta, Markus Kuster, Wolfgang Lugmayr, Jannik Lübke, Adrian P. Mancuso, Tommaso Mazza, Carl Nettelblad, Yevheniy Ovcharenko, Daniel E. Rivas, Max Rose, Amit K. Samanta, Philipp Schmidt, Egor Sobolev, Nicusor Timneanu, Sergej Usenko, Daniel Westphal, Tamme Wollweber, Lena Worbs, P. Lourdu Xavier, Hazem Yousef, Kartik Ayyer, Henry N. Chapman, Jonas A. Sellberg, Carolin Seuring, Ivan A. Vartanyants, Jochen Küpper, Michael Meyer, and Filipe R.N.C. Maia. Observation of a single protein by ultrafast x-ray diffraction. *Light Sci. Appl.*, 13 (15):15, 2024. doi: 10.1038/s41377-023-01352-7. URL https://www.nature.com/articles/s41377-023-01352-7.

[4] Lanhai He, Lukáš Tomaník, Sebastian Malerz, Florian Trinter, Sebastian Trippel, Michal Belina, Petr Slavíček, Bernd Winter, and Jochen Küpper. Specific versus non-specific solvent interactions of a biomolecule in water. *J. Phys. Chem. Lett.*, 14 (46):10499–10508, 2023. doi: 10.1021/acs.jpclett.3c01763. URL https://doi.org/10.1021/acs.jpclett.3c01763.

[5] Jia Wang, Lanhai He, Jovana Petrovic, Ahmed Al-Refaie, Helen Bieker, Jolijn Onvlee, Karol Długołęcki, and Jochen Küpper. Spatial separation of 2-propanol monomer and its ionization-fragmentation pathways. *J. Mol. Struct.*, 1208:127863, 2020. doi: 10.1016/j.molstruc.2020.127863. URL http://www.sciencedirect.com/science/article/pii/S0022286020301873.

[6] Melby Johny, Constant A. Schouder, Ahmed Al-Refaie, Lanhai He, Joss Wiese, Henrik Stapelfeldt, Sebastian Trippel, and Jochen Küpper. Water is a radiation protection agent for ionised pyrrole. *Phys. Chem. Chem. Phys.*, 26:13118–13130, 2024. doi: 10.1039/D3CP03471B. URL http://dx.doi.org/10.1039/D3CP03471B.

[7] Jolijn Onvlee, Sebastian Trippel, and Jochen Küpper. Ultrafast light-induced dynamics in the microsolvated biomolecular indole chromophore with water. *Nat. Commun.*, 13:7462, 2022. doi: 10.1038/s41467-022-33901-w. URL https://dx.doi.org/10.1038/s41467-022-33901-w.

[8] Hubertus Bromberger, Christopher Passow, David Pennicard, Rebecca Boll,

Jonathan Correa, Lanhai He, Melby Johny, Christina Papadopoulou, Atia Tul-Noor, Joss Wiese, Sebastian Trippel, Benjamin Erk, and Jochen Küpper. Shot-by-shot 250 kHz 3D ion and MHz photoelectron imaging using Timepix3. *J. Phys. B*, 55(14):144001, June 2022. doi: 10.1088/1361-6455/ac6b6b. URL https://doi.org/10.1088/1361-6455/ac6b6b.

[9] Constant Schouder, Adam S Chatterley, Melby Johny, Flora Hübschmann, Ahmed F Al-Refaie, Florent Calvo, Jochen Küpper, and Henrik Stapelfeldt. Laser-induced Coulomb explosion imaging of $(C_6H_5Br)_2$ and C_6H_5Br-I_2 dimers in helium nanodroplets using a Tpx3Cam. *J. Phys. B*, 54:184001, 2021. doi: 10.1088/1361-6455/ac04c4. URL https://iopscience.iop.org/article/10.1088/1361-6455/ac04c4.

[10] Jan Rothhardt, Steffen Hädrich, Yariv Shamir, Maxim Tschnernajew, Robert Klas, Armin Hoffmann, Getnet K Tadesse, Arno Klenke, Thomas Gottschall, Tino Eidam, Jens Limpert, Andreas Tünnermann, Rebecca Boll, Cédric Bomme, Hatem Dachraoui, Benjamin Erk, Michele Di Fraia, Daniel A. Horke, Thomas Kierspel, Terence Mullins, Andreas Przystawik, Evgeny Savelyev, Joss Wiese, Tim Laarmann, Jochen Küpper, and Daniel Rolles. High-repetition-rate and high-photon-flux 70 eV high-harmonic source for coincidence ion imaging of gas-phase molecules. *Opt. Express*, 24(16):18133–18147, 2016. doi: 10.1364/OE.24.018133. URL http://www.osapublishing.org/viewmedia.cfm?uri=oe-24-16-18133&seq=0.

[11] Tony Heinz, Oleg Shpyrko, Dimitri Basov, Nora Berrah, Phil Bucksbaum, Tom Devereaux, David Fritz, Kelly Gaffney, Oliver Gessner, Venkat Gopalan, Zahid Hasan, Alessandra Lanzara, Todd Martinez, Andy Millis, Shaul Mukamel, Margaret Murnane, Keith Nelson, Rohit Prasankumar, David Reis, Ken Schafer, Greg Scholes, Z.-X. Shen, Albert Stolow, Haidan Wen, Martin Wolf, Di Xiao, Linda Young, Bruce Garrett, Linda Horton, Helen Kerch, Jeff Krause, Tom Settersten, Lane Wilson, Katie Runkles, Terry Anderson, Glennda Chui, and Eiko Rutherford. Basic energy sciences roundtable: Opportunities for basic research at the frontiers of xfel ultrafast science. Technical report, 10 2017. URL https://www.osti.gov/biblio/1616251.

[12] RE Carley, E Heesel, and HH Fielding. Femtosecond lasers in gas phase chemistry. *Chemical Society Reviews*, 34(11):949–969, 2005.

[13] Deborah S Jin and Jun Ye. Introduction to ultracold molecules: New frontiers in quantum and chemical physics. *Chem. Rev.*, 112(9):4801–4802, September 2012. doi: 10.1021/cr300342x.

[14] Musahid Ahmed and Oleg Kostko. From atoms to aerosols: probing clusters and nanoparticles with synchrotron based mass spectrometry and x-ray spectroscopy. *Phys. Chem. Chem. Phys.*, 22:2713–2737, 2020. doi: 10.1039/C9CP05802H. URL http://dx.doi.org/10.1039/C9CP05802H.

[15] Benjamin Erk, Rebecca Boll, Sebastian Trippel, Denis Anielski, Lutz Foucar, Benedikt Rudek, Sascha W Epp, Ryan Coffee, Sebastian Carron, Sebastian Schorb, Ken R Ferguson, Michele Swiggers, John D Bozek, Marc Simon, Tatiana Marchenko, Jochen Küpper, Ilme Schlichting, Joachim Ullrich, Christoph Bostedt, Daniel Rolles, and Artem Rudenko. Imaging charge transfer in iodomethane upon x-ray photoabsorption. *Science*, 345(6194):288–291, July 2014. doi: 10.1126/science.1253607.

[16] Richard Neutze, Remco Wouts, David van der Spoel, Edgar Weckert, and Janos Hajdu. Potential for biomolecular imaging with femtosecond x-ray pulses. *Nature*,

406(6797):752–757, August 2000. doi: 10.1038/35021099. URL `http://dx.doi.org/10.1038/35021099`.

[17] J Feldhaus, M Krikunova, M Meyer, Th Möller, R Moshammer, A Rudenko, Th Tschentscher, and J Ullrich. AMO science at the FLASH and European XFEL free-electron laser facilities. *J. Phys. B*, 46(16):164002, aug 2013. doi: 10.1088/0953-4075/46/16/164002.

[18] R. Abela, A. Aghababyan, M. Altarelli, C. Altucci, G. Amatuni, P. Anfinrud, P. Audebert, V. Ayvazyan, N. Baboi, J. Baehr, V. Balandin, R. Bandelmann, J. Becker, B. Beutner, C. Blome, I. Bohnet, A. Bolzmann, C. Bostedt, Y. Bozhko, A. Brandt, S. Bratos, C. Bressler, O. Brovko, H. Brück, J.-P. Carneiro, S. Casalbuoni, M. Castellano, P. Castro, L. Catani, A. Cavalleri, S. Celik, H. Chapman, D. Charalambidis, J. Chen, M. Chergui, S. Choroba, A. Cianchi, M. Clausen, E. Collet, H. Danared, C. David, W. Decking, M. Dehler, H. Delsim-Hashemi, G. Dipirro, B. Dobson, M. Dohlus, S. Duesterer, A. Eckhardt, H.-J. Eckoldt, H. Edwards, B. Faatz, M. Fajardo, A. Fateev, J. Feldhaus, Y. Filipov, K. Floettmann, R. Follath, B. Fominykh, M. French, J. Frisch, L. Froehlich, E. Gadwinkel, L. García-Tabarcés, J. J. Gareta, T. Garvey, F. Gel'mukhanov, U. Gensch, C. Gerth, M. Goerler, N. Golubeva, H. Graafsma, W. Graeff, O. Grimm, B. Griogoryan, G. Grübel, C. Gutt, K. Hacker, L. Haenisch, U. Hahn, J. Hajdu, J. H. Han, M. Hartrott, J. Havlicek, O. Hensler, K. Honkavaara, V. Honkimäki, T. Hott, M. R. Howells, M. Huening, H. Ihee, F. Ö. Ilday, R. Ischebeck, M. Jablonka, E. Jaeschke, K. Jensch, J.-P. Jensen, S. Johnson, L. Juha, F. Kaerntner, R. Kammering, H. Kapitza, V. Katalev, B. Keil, S. Khodyachykh, R. Kienberger, J.-W. Kim, Y. Kim, K. Klose, V. Kocharyan, W. Koehler, M. Koerfer, M. Kollewe, Q. Kong, W. Kook, D. Kostin, O. Kozlov, D. Kraemer, M. Krasilnikov, B. Krause, O. Krebs, J. Krzywinski, G. Kube, M. Kuhlmann, H. Laich, R. Lange, M. Larsson, R. W. Lee, A. Leuschner, H. Lierl, L. Lilje, T. Limberg, A. Lindenberg, D. Lipka, F. Loehl, K. Ludwig, M. Luong, C. Magne, A. Maquet, J. Marangos, C. Masciovecchio, M. Maslov, A. Matheisen, E. Matyushevskiy, O. Matzen, H.-J. May, I. McNulty, D. McCormick, P. Meulen, N. Meyners, P. Michelato, N. Mildner, V. Miltchev, M. Minty, W.-D. Moeller, T. Möller, L. Monaco, M. Nagl, O. Napoly, G. Neubauer, P. Nicolosi, A. Nienhaus, D. Noelle, T. Nunez, F. Obier, A. Oppelt, C. Pagani, R. Paparella, H. B. Pedersen, B. Petersen, B. Petrosyan, L. Petrosyan, A. Petrov, P. Piot, J. Pflueger, A. Plech, E. Ploenjes, L. Poletto, G. Pöplau, E. Prat, S. Prat, J. Prenting, D. Proch, D. Pugachov, H. Quack, B. Racky, D. Ramert, H. Redlin, K. Rehlich, R. Reininger, H. Remde, D. Reschke, D. Richter, M. Richter, S. Riemann, D. Riley, I. Robinson, J. Roensch, F. Rosmej, M. Ross, J. Rossbach, V. Rybnikov, M. Sachwitz, E. Saldin, W. Sandner, J. Schäfer, T. Schilcher, H. Schlarb, M. Schloesser, V. Schlott, B. Schmidt, M. Schmitz, P. Schmueser, J. Schneider, E. Schneidmiller, F. Schotte, S. Schrader, S. Schreiber, C. Schroer, R. Schuch, H. Schulte-Schrepping, A. Schwarz, M. Seidel, J. Sekutowicz, P. Seller, D. Sellmann, F. Senf, D. Sertore, A. Shabunov, S. Simrock, W. Singer, H. Sinn, R. Smith, E. Sombrowski, A. A. Sorokin, E. Springate, M. Staack, L. Staykov, B. Steffen, B. Stephenson, F. Stephan, F. Stulle, E. Syresin, K. Sytchev, V. Sytchev, G. Tallents, S. Techert, N. Tesch, H. Thom, K. Tiedtke, M. Tischer, M. Tolan, S. Toleikis, F. Toral, R. Treusch, D. Trines, V. Tsakanov, I. Tsakov, T. Tschentscher, F. R. Ullrich, U. van Rienen, A. Variola, I. Vartaniants, E. Vogel, J. Vogel, R. Vuilleumier, H. Wabnitz, R. Wanzenberg, J. S. Wark, H. Weddig, T. Weiland, H. Weise, M. Wendt, R. Wenndorff, R. Wichmann, I. Will, A. Winter,

K. Witte, K. Wittenburg, P. Wochner, T. Wohlenberg, J. Wojtkiewicz, A. Wolf, M. Wulff, M. Yurkov, I. Zagorodnov, P. Zambolin, K. Zapfe, P. Zeitoun, V. Ziemann, A. Zolotov, R. Brinkmann, H.-J. Grabosch, and DESY. XFEL: The European X-Ray Free-Electron Laser – Technical Design Report. Technical report, DESY, Hamburg, Germany, Jun 2006. URL https://bib-pubdb1.desy.de/record/77248.

[19] Siqi Li, Taran Driver, Philipp Rosenberger, Elio G. Champenois, Joseph Duris, Andre Al-Haddad, Vitali Averbukh, Jonathan C. T. Barnard, Nora Berrah, Christoph Bostedt, Philip H. Bucksbaum, Ryan N. Coffee, Louis F. DiMauro, Li Fang, Douglas Garratt, Averell Gatton, Zhaoheng Guo, Gregor Hartmann, Daniel Haxton, Wolfram Helml, Zhirong Huang, Aaron C. LaForge, Andrei Kamalov, Jonas Knurr, Ming-Fu Lin, Alberto A. Lutman, James P. MacArthur, Jon P. Marangos, Megan Nantel, Adi Natan, Razib Obaid, Jordan T. O'Neal, Niranjan H. Shivaram, Aviad Schori, Peter Walter, Anna Li Wang, Thomas J. A. Wolf, Zhen Zhang, Matthias F. Kling, Agostino Marinelli, and James P. Cryan. Attosecond coherent electron motion in Auger-Meitner decay. *Science*, 375(6578): 285–290, 2022. doi: 10.1126/science.abj2096. URL https://www.science.org/doi/10.1126/science.abj2096.

[20] Christopher J. Milne, Thomas Schietinger, Masamitsu Aiba, Arturo Alarcon, Jürgen Alex, Alexander Anghel, Vladimir Arsov, Carl Beard, Paul Beaud, Simona Bettoni, Markus Bopp, Helge Brands, Manuel Brönnimann, Ingo Brunnenkant, Marco Calvi, Alessandro Citterio, Paolo Craievich, Marta Csatari Divall, Mark Dällenbach, Michael D'Amico, Andreas Dax, Yunpei Deng, Alexander Dietrich, Roberto Dinapoli, Edwin Divall, Sladana Dordevic, Simon Ebner, Christian Erny, Hansrudolf Fitze, Uwe Flechsig, Rolf Follath, Franziska Frei, Florian Gärtner, Romain Ganter, Terence Garvey, Zheqiao Geng, Ishkhan Gorgisyan, Christopher Gough, Andreas Hauff, Christoph P. Hauri, Nicole Hiller, Tadej Humar, Stephan Hunziker, Gerhard Ingold, Rasmus Ischebeck, Markus Janousch, Pavle Juranić, Mario Jurcevic, Maik Kaiser, Babak Kalantari, Roger Kalt, Boris Keil, Christoph Kittel, Gregor Knopp, Waldemar Koprek, Henrik T. Lemke, Thomas Lippuner, Daniel Llorente Sancho, Florian Löhl, Carlos Lopez-Cuenca, Fabian Märki, Fabio Marcellini, Goran Marinkovic, Isabelle Martiel, Ralf Menzel, Aldo Mozzanica, Karol Nass, Gian Luca Orlandi, Cigdem Ozkan Loch, Ezequiel Panepucci, Martin Paraliev, Bruce Patterson, Bill Pedrini, Marco Pedrozzi, Patrick Pollet, Claude Pradervand, Eduard Prat, Peter Radi, Jean-Yves Raguin, Sophie Redford, Jens Rehanek, Julien Réhault, Sven Reiche, Matthias Ringele, Jochen Rittmann, Leonid Rivkin, Albert Romann, Marie Ruat, Christian Ruder, Leonardo Sala, Lionel Schebacher, Thomas Schilcher, Volker Schlott, Thomas Schmidt, Bernd Schmitt, Xintian Shi, Markus Stadler, Lukas Stingelin, Werner Sturzenegger, Jakub Szlachetko, Dhanya Thattil, Daniel M. Treyer, Alexandre Trisorio, Wolfgang Tron, Seraphin Vetter, Carlo Vicario, Didier Voulot, Meitian Wang, Thierry Zamofing, Christof Zellweger, Riccardo Zennaro, Elke Zimoch, Rafael Abela, Luc Patthey, and Hans-Heinrich Braun. SwissFEL: the Swiss x-ray free electron laser. *Appl. Sci.*, 7(7):720, 2017. doi: 10.3390/app7070720. URL https://www.mdpi.com/2076-3417/7/7/720.

[21] Zhentang Zhao, Dong Wang, Qiang Gu, Lixin Yin, Ming Gu, Yongbin Leng, and Bo Liu. Status of the SXFEL Facility. *Appl. Sci.*, 7(6):607, 2017. doi: 10.3390/app7060607. URL https://www.mdpi.com/2076-3417/7/6/607.

[22] K Nagaya, K Motomura, E Kukk, Y Takahashi, K Yamazaki, S Ohmura,

H Fukuzawa, S Wada, S Mondal, T Tachibana, Y Ito, R Koga, T Sakai, K Matsunami, K Nakamura, M Kanno, A Rudenko, C Nicolas, X J Liu, C Miron, Y Zhang, Y Jiang, J Chen, M Anand, D E Kim, K Tono, M Yabashi, M Yao, H Kono, and K Ueda. Femtosecond charge and molecular dynamics of I-containing organic molecules induced by intense x-ray free-electron laser pulses. *Faraday Disc.*, 194(6):537–562, 2016. doi: 10.1039/c6fd00085a. URL `http://pubs.rsc.org/en/content/articlelanding/2016/fd/c6fd00085a#!divAbstract`.

[23] Sébastien Boutet, Lukas Lomb, Garth J. Williams, Thomas R. M. Barends, Andrew Aquila, R. Bruce Doak, Uwe Weierstall, Daniel P. DePonte, Jan Steinbrener, Robert L. Shoeman, Marc Messerschmidt, Anton Barty, Thomas A. White, Stephan Kassemeyer, Richard A. Kirian, M. Marvin Seibert, Paul A. Montanez, Chris Kenney, Ryan Herbst, Philip Hart, Jack Pines, Gunther Haller, Sol M. Gruner, Hugh T. Philipp, Mark W. Tate, Marianne Hromalik, Lucas J. Koerner, Niels van Bakel, John Morse, Wilfred Ghonsalves, David Arnlund, Michael J. Bogan, Carl Caleman, Raimund Fromme, Christina Y. Hampton, Mark S. Hunter, Linda C. Johansson, Gergely Katona, Christopher Kupitz, Mengning Liang, Andrew V. Martin, Karol Nass, Lars Redecke, Francesco Stellato, Nicusor Timneanu, Dingjie Wang, Nadia A. Zatsepin, Donald Schafer, James Defever, Richard Neutze, Petra Fromme, John C. H. Spence, Henry N. Chapman, and Ilme Schlichting. High-resolution protein structure determination by serial femtosecond crystallography. *Science*, 337(6092):362–364, 2012. doi: 10.1126/science.1217737. URL `http://www.sciencemag.org/content/337/6092/362.abstract`.

[24] Marcus Gallagher-Jones, Yoshitaka Bessho, Sunam Kim, Jaehyun Park, Sangsoo Kim, Daewoong Nam, Chan Kim, Yoonhee Kim, Osamu Miyashita, Florence Tama, et al. Macromolecular structures probed by combining single-shot free-electron laser diffraction with synchrotron coherent x-ray imaging. *Nat. Commun.*, 5:3798, 2014.

[25] D H Bilderback, P Elleaume, and E Weckert. Review of third and next generation synchrotron light sources. *J. Phys. B*, 38(9):S773–S797, 2005. doi: 10.1088/0953-4075/38/9/022. URL `http://stacks.iop.org/0953-4075/38/i=9/a=022?key=crossref.fff50e96d91376df49e03a0a29977070`.

[26] D. H. Parker and A. Eppink. Photoelectron and photofragment velocity map imaging of state-selected molecular oxygen dissociation/ionization dynamics. *J. Chem. Phys.*, 107:2357–2362, Aug 1997. doi: 10.1063/1.474624. URL `http://dx.doi.org/10.1063/1.474624`.

[27] R. D. Levine and R. B. Bernstein. *Molecular Reaction Dynamics and Chemical Reactivity*. Oxford University Press, New York, 1987.

[28] Stuart J. Greaves, Rebecca A. Rose, and Andrew J. Orr-Ewing. Velocity map imaging of the dynamics of bimolecular chemical reactions. *Phys. Chem. Chem. Phys.*, 12(32):9129–9143, 2010. ISSN 1463-9076. doi: 10.1039/c001233e.

[29] D.W. Chandler and P.L. Houston. Two-dimensional imaging of state-selected photodissociation products detected by multiphoton ionization. *J. Chem. Phys.*, 87 (2):1445, 1987. doi: 10.1063/1.453276. URL `https://aip.scitation.org/doi/10.1063/1.453276`.

[30] A. I. Chichinin, T. Einfeld, C. Maul, and K.-H. Gericke. Three-dimensional imaging technique for direct observation of the complete velocity distribution of state-selected photodissociation products. *Rev. Sci. Instrum.*, 73(4):1856–1865, 2002. doi: 10.1063/1.1453505. URL `https://doi.org/10.1063/1.1453505`.

[31] M. Laura Lipciuc and Maurice H. M. Janssen. Slice imaging of quantum state-to-state photodissociation dynamics of OCS. *Phys. Chem. Chem. Phys.*, 8:3007–3016, 2006. doi: 10.1039/B605108A. URL http://dx.doi.org/10.1039/B605108A.

[32] Joseph R. Roscioli and David J. Nesbitt. Quantum state resolved velocity-map imaging spectroscopy : A new tool for collision dynamics at gas/self-assembled monolayer interfaces. *Faraday Disc.*, 150(0):471–479, 2011. ISSN 1359-6640. doi: 10.1039/c0fd00023j.

[33] Arthur G. Suits. Invited Review Article: Photofragment imaging. *Rev. Sci. Instrum.*, 89(11):111101, 11 2018. ISSN 0034-6748. doi: 10.1063/1.5045325. URL https://doi.org/10.1063/1.5045325.

[34] L.F. Dimauro and P. Agostini. Ionization dynamics in strong laser fields. *Adv. Atom. Mol. Opt. Phys.*, 35:79–120, 1995. ISSN 1049-250X. doi: 10.1016/s1049-250x(08)60161-5.

[35] Joss Wiese, Jolijn Onvlee, Sebastian Trippel, and Jochen Küpper. Strong-field ionization of complex molecules. *Phys. Rev. Research*, 3:013089, 2020. doi: 10.1103/PhysRevResearch.3.013089. URL https://doi.org/10.1103/PhysRevResearch.3.013089.

[36] Ivo S. Vinklárek, Hubertus Bromberger, Nidin Vadassery, Wuwei Jin, Jochen Küpper, and Sebastian Trippel. Reaction pathways of water dimer following single ionization. *J. Phys. Chem. A*, 128(9):1593–1599, 2024. doi: 10.1021/acs.jpca.3c07958. URL https://pubs.acs.org/doi/10.1021/acs.jpca.3c07958.

[37] D. Dimitrovski, J. Maurer, H. Stapelfeldt, and L. B. Madsen. Strong-field ionization of three-dimensionally aligned naphthalene molecules: orbital modification and imprints of orbital nodal planes. *J. Phys. B*, 48(24):245601, 2015. doi: 10.1088/0953-4075/48/24/245601. URL https://doi.org/10.1088/0953-4075/48/24/245601.

[38] Atilay Ayasli, Arnab Khan, Thomas Gstir, Tim Michaelsen, Dóra Papp, Yan Wang, Hongwei Song, Minghui Yang, Gábor Czakó, and Roland Wester. A dynamic isotope effect in the nucleophilic substitution reaction between F^- and CD_3I. *Nat. Commun.*, 16(1):2318, 2025. doi: 10.1038/s41467-025-57086-0.

[39] S. Trippel, M. Stei, J. A. Cox, and R. Wester. Differential Scattering Cross-Sections for the Different Product Vibrational States in the Ion-Molecule Reaction $Ar^+ + N_2$. *Phys. Rev. Lett.*, 110(16):163201, 2013. doi: 10.1103/PhysRevLett.110.163201. URL https://link.aps.org/doi/10.1103/PhysRevLett.110.163201.

[40] Roland Wester. Velocity map imaging of ion–molecule reactions. *Phys. Chem. Chem. Phys.*, 16(2):396–405, 2013. ISSN 1463-9076. doi: 10.1039/c3cp53405g.

[41] M. Stei, J. von Vangerow, R. Otto, A. H. Kelkar, E. Carrascosa, T. Best, and R. Wester. High resolution spatial map imaging of a gaseous target. *J. Chem. Phys.*, 138:214201, 2013. doi: 10.1063/1.4807482.

[42] Yehuda Ben-Shabo, Adeliya Kurbanov, Claus Dieter Schröter, Robert Moshammer, Holger Kreckel, and Yoni Toker. Velocity map imaging with no spherical aberrations. *Phys. Chem. Chem. Phys.*, 25(37):25122–25129, 2023.

[43] Peng Zhang, Pengfei Lan, Zhengpeng Feng, Qingbin Zhang, and Peixiang Lu. Method to compensate the dispersion of kinetic energy resolution in a velocity map imaging spectrometer. *Meas. Sci. Technol.*, 25(10):105202, 2014. ISSN 0957-0233. doi: 10.1088/0957-0233/25/10/105202.

[44] Hans Pauly. *Atom, Molecule, and Cluster Beams*, volume 1 & 2 of *Springer Series on*

Atomic, Optical, and Plasma Physics. Springer Verlag, 2000.

[45] Yuan-Pin Chang, Daniel A. Horke, Sebastian Trippel, and Jochen Küpper. Spatially-controlled complex molecules and their applications. *Int. Rev. Phys. Chem.*, 34: 557–590, 2015. doi: 10.1080/0144235X.2015.1077838. URL https://dx.doi.org/10.1080/0144235X.2015.1077838.

[46] Jianfu Zhou, Alexandra E. Panaitiu, and Gevorg Grigoryan. A general-purpose protein design framework based on mining sequence-structure relationships in known protein structures. *Proc. Natl. Acad. Sci. U.S.A.*, 117(2):1059–1068, 2019. doi: 10.1073/pnas.1908723117.

[47] John Jumper, Richard Evans, Alexander Pritzel, Tim Green, Michael Figurnov, Olaf Ronneberger, Kathryn Tunyasuvunakool, Russ Bates, Augustin Žídek, Anna Potapenko, Alex Bridgland, Clemens Meyer, Simon A. A. Kohl, Andrew J. Ballard, Andrew Cowie, Bernardino Romera-Paredes, Stanislav Nikolov, Rishub Jain, Jonas Adler, Trevor Back, Stig Petersen, David Reiman, Ellen Clancy, Michal Zielinski, Martin Steinegger, Michalina Pacholska, Tamas Berghammer, Sebastian Bodenstein, David Silver, Oriol Vinyals, Andrew W. Senior, Koray Kavukcuoglu, Pushmeet Kohli, and Demis Hassabis. Highly accurate protein structure prediction with AlphaFold. *Nature*, 596(7873):583–589, 2021. doi: 10.1038/s41586-021-03819-2.

[48] S. Beaulieu, A. Comby, A. Clergerie, J. Caillat, D. Descamps, N. Dudovich, B. Fabre, R. Géneaux, F. Légaré, S. Petit, B. Pons, G. Porat, T. Ruchon, R. Taïeb, V. Blanchet, and Y. Mairesse. Attosecond-resolved photoionization of chiral molecules. *Science*, 358(6368):1288–1294, December 2017. doi: 10.1126/science.aao5624. URL https://doi.org/10.1126/science.aao5624.

[49] Frank Filsinger, Jochen Küpper, Gerard Meijer, Jonas L. Hansen, Jochen Maurer, Jens H. Nielsen, Lotte Holmegaard, and Henrik Stapelfeldt. Pure samples of individual conformers: The separation of stereo-isomers of complex molecules using electric fields. *Angew. Chem. Int. Ed.*, 48:6900–6902, 2009. doi: 10.1002/anie.200902650. URL http://onlinelibrary.wiley.com/doi/10.1002/anie.200902650/abstract.

[50] Daniel A. Horke, Yuan-Pin Chang, Karol Długołęcki, and Jochen Küpper. Separating para and ortho water. *Angew. Chem. Int. Ed.*, 53:11965–11968, 2014. doi: 10.1002/anie.201405986. URL http://onlinelibrary.wiley.com/doi/10.1002/anie.201405986/abstract.

[51] R. D. Suenram and F. J. Lovas. Millimeter wave spectrum of glycine - a new conformer. *J. Am. Chem. Soc.*, 102:7180–7184, 1980. doi: 10.1021/ja00544a002.

[52] T[homas] R. Rizzo, Y[ong] D. Park, L. Peteanu, and D[onald] H. Levy. Electronic spectrum of the amino acid tryptophan cooled in a supersonic molecular beam. *J. Chem. Phys.*, 83:4819–4820, 1985. doi: 10.1063/1.449009.

[53] Frank Filsinger, Gerard Meijer, Henrik Stapelfeldt, Henry N. Chapman, and Jochen Küpper. State- and conformer-selected beams of aligned and oriented molecules for ultrafast diffraction studies. *Phys. Chem. Chem. Phys.*, 13(6):2076–2087, 2011. doi: 10.1039/C0CP01585G. URL https:dx.doi.org/10.1039/C0CP01585G.

[54] Lanhai He, Melby Johny, Thomas Kierspel, Karol Długołęcki, Sadia Bari, Rebecca Boll, Hubertus Bromberger, Marcello Coreno, Alberto De Fanis, Michele Di Fraia, Benjamin Erk, Mathieu Gisselbrecht, Patrik Grychtol, Per Eng-Johnsson, Tommaso Mazza, Jolijn Onvlee, Yevheniy Ovcharenko, Jovana Petrovic, Nils Rennhack,

Daniel E. Rivas, Artem Rudenko, Eckart Rühl, Lucas Schwob, Marc Simon, Florian Trinter, Sergey Usenko, Joss Wiese, Michael Meyer, Sebastian Trippel, and Jochen Küpper. Controlled molecule injector for cold, dense, and pure molecular beams at the european x-ray free-electron laser. *Rev. Sci. Instrum.*, 95(11):113301, 2024. doi: 10.1063/5.0219086. URL https://pubs.aip.org/aip/rsi/article/95/11/113301/3320596/Controlled-molecule-injector-for-cold-dense-and.

[55] Albert Szent-Györgyi. Biology and pathology of water. *Perspectives in Biology and Medicine*, 14(2):239–249, 1971. doi: 10.1353/pbm.1971.0014. URL https://doi.org/10.1353/pbm.1971.0014.

[56] Philip Ball. Water is an active matrix of life for cell and molecular biology. *Proc. Natl. Acad. Sci. U.S.A.*, 114(51):13327–13335, 2017. doi: 10.1073/pnas.1703781114. URL https://doi.org/10.1073/pnas.1703781114.

[57] Lynn J Rothschild and Rocco L Mancinelli. Life in extreme environments. *Nature*, 409(6823):1092–1101, February 2001. doi: 10.1038/35059215. URL http://www.nature.com/doifinder/10.1038/35059215.

[58] Frances Westall and A Brack. The importance of water for life. *Space Science Reviews*, 214(2):50, 2018. doi: 10.1007/s11214-018-0476-7.

[59] R. Lynden-Bell, S. Morris, J. Barrow, J. Finney, and C. Harper, editors. *Water and Life*. CRC Press, Boca Raton, 2010. ISBN 9780429191039. URL https://doi.org/10.1201/EBK1439803561.

[60] Philip Ball. Seeking the solution. *Nature*, 436:1084–1085, 2005. doi: 10.1038/4361084a. URL https://doi.org/10.1038/4361084a.

[61] Samir Kumar Pal, Jorge Peon, and Ahmed H. Zewail. Biological water at the protein surface: Dynamical solvation probed directly with femtosecond resolution. *Proc. Natl. Acad. Sci. U.S.A.*, 99(4):1763–1768, 2002. doi: 10.1073/pnas.042697899. URL https://www.pnas.org/content/99/4/1763.

[62] Marie-Claire Bellissent-Funel, Ali Hassanali, Martina Havenith, Richard Henchman, Peter Pohl, Fabio Sterpone, David van der Spoel, Yao Xu, and Angel E Garcia. Water determines the structure and dynamics of proteins. *Chem. Rev.*, 116(13):7673–7697, 2016. doi: 10.1021/acs.chemrev.5b00664. URL https://doi.org/10.1021/acs.chemrev.5b00664.

[63] Carlos E Crespo-Hernández, Boiko Cohen, Patrick M Hare, and Bern Kohler. Ultrafast excited-state dynamics in nucleic acids. *Chem. Rev.*, 104:1977–2020, 2004. doi: 10.1021/cr0206770. URL https://doi.org/10.1021/cr0206770.

[64] Damien Laage, Thomas Elsaesser, and James T Hynes. Water dynamics in the hydration shells of biomolecules. *Chem. Rev.*, 117(16):10694–10725, 2017. ISSN 0009-2665. doi: 10.1021/acs.chemrev.6b00765. URL https://pubs.acs.org/doi/10.1021/acs.chemrev.6b00765.

[65] Biman Bagchi. Water dynamics in the hydration layer around proteins and micelles. *Chem. Rev.*, 105(9):3197–3219, 2005. ISSN 0009-2665. doi: 10.1021/cr020661+. URL https://pubs.acs.org/doi/10.1021/cr020661%2B.

[66] Marcio F. Colombo, Donald C. Rau, and V. Adrian Parsegian. Protein solvation in allosteric regulation: A water effect on hemoglobin. *Science*, 256(5057):655–659, 1992. doi: 10.1126/science.1585178. URL http://science.sciencemag.org/content/256/5057/655.

[67] Catherine A. Royer. Probing protein folding and conformational transitions with fluorescence. *Chem. Rev.*, 106(5):1769–1784, 2006. doi: 10.1021/cr0404390.

[68] Jun Ma, Furong Wang, Sergey A. Denisov, Amitava Adhikary, and Mehran Mostafavi. Reactivity of prehydrated electrons toward nucleobases and nucleotides in aqueous solution. *Sci. Adv.*, 3(12):1–7, 2017. doi: 10.1126/sciadv.1701669. URL https://advances.sciencemag.org/content/3/12/e1701669.

[69] Jun Ma, Anil Kumar, Yusa Muroya, Shinichi Yamashita, Tsuneaki Sakurai, Sergey A. Denisov, Michael D. Sevilla, Amitava Adhikary, Shu Seki, and Mehran Mostafavi. Observation of dissociative quasi-free electron attachment to nucleoside via excited anion radical in solution. *Nat. Commun.*, 6:1, 2019. doi: 10.1038/s41467-018-08005-z. URL https://doi.org/10.1038/s41467-018-08005-z.

[70] M. Smyth, J. Kohanoff, and I. I. Fabrikant. Electron-induced hydrogen loss in uracil in a water cluster environment. *J. Chem. Phys.*, 140:184313, 2014. doi: 10.1063/1.4874841. URL https://doi.org/10.1063/1.4874841.

[71] T. Ito, S. C. Baker, C. D. Stickley, J. G. Peak, and M. J. Peak. Dependence of the yield of strand breaks induced by γ-rays in DNA on the physical conditions of exposure: Water content and temperature. *Int. J. Radiat. Biol.*, 63:289–296, 1993. doi: 10.1080/09553009314550391. URL https://doi.org/10.1080/09553009314550391.

[72] J Kočišek, A Pysanenko, M Fárník, and J Fedor. Microhydration prevents fragmentation of uracil and thymine by low-energy electrons. *J. Phys. Chem. Lett.*, 27:3401–3405, 2016. doi: 10.1021/acs.jpclett.6b01601. URL https://doi.org/10.1021/acs.jpclett.6b01601.

[73] Milan Ončák, Hans Lischka, and Petr Slavíček. Photostability and solvation: photodynamics of microsolvated zwitterionic glycine. *Phys. Chem. Chem. Phys.*, 12 (19):4906–14, 2010. ISSN 1463-9076. doi: 10.1039/b925246k. URL https://pubs.rsc.org/en/content/articlelanding/2010/cp/b925246k#!divAbstract.

[74] Andrew J Orr-Ewing. Taking the plunge: chemical reaction dynamics in liquids. *Chem. Soc. Rev.*, 46(24):7597–7614, December 2017. doi: 10.1039/C7CS00331E.

[75] Olivier Collet. How does the first water shell fold proteins so fast? *J. Chem. Phys.*, 134(8):085107, 2011. doi: 10.1063/1.3554731. URL https://doi.org/10.1063/1.3554731.

[76] L. Dunoyer. Sur la théorie cinétique des gaz et la réalisation d'un rayonnement matériel d'origine thermique. *Cŕ. hebd. séances Acad. sci.*, 152:592–595, 1911. doi: 10.1051/radium:0191100804014201. URL http://visualiseur.bnf.fr/Visualiseur?Destination=Gallica&O=NUMM-3105.

[77] Ronald G. J. Fraser. *Molecular Rays*. Cambridge University Press, London, GB, 1931.

[78] Dudley R. Herschbach. Reactive collisions in crossed molecular beams. *Discuss. Faraday Soc.*, 33(0):149–161, 1962. doi: 10.1039/df9623300149. URL https://pubs.rsc.org/en/content/articlelanding/1962/DF/df9623300149.

[79] Wuwei Jin, Hubertus Bromberger, Lanhai He, Melby Johny, Ivo S Vinklárek, Karol Długołęcki, Andrey Samartsev, Francesca Calegari, Sebastian Trippel, and Jochen Küpper. A versatile and transportable endstation for controlled molecule experiments. *Rev. Sci. Instrum.*, 96(2):023305, 2025. doi: 10.1063/5.0228913.

[80] Linnea Rading, Jan Lahl, Sylvain Maclot, Filippo Campi, Hélène Coudert-Alteirac, Bart Oostenrijk, Jasper Peschel, Hampus Wikmark, Piotr Rudawski, Mathieu Gisselbrecht, and Per Johnsson. A versatile velocity map ion-electron covariance imaging spectrometer for high-intensity XUV experiments. *Appl. Sci.*, 8(6):998, 2018. doi: 10.3390/app8060998. URL http://www.mdpi.com/2076-3417/8/6/998.

[81] Xavier Llopart, Rafael Ballabriga, Michael Campbell, Lukas Tlustos, and Winnie Wong. Timepix, a 65k programmable pixel readout chip for arrival time, energy and/or photon counting measurements. *Nucl. Instrum. Methods Phys. Res. A*, 581 (1):485–494, 2007. doi: 10.1016/j.nima.2007.08.079. URL https://doi.org/10.1016/j.nima.2007.08.079.

[82] F. Calegari, G. Sansone, S. Stagira, C. Vozzi, and M. Nisoli. Advances in attosecond science. *J. Phys. B*, 49(6):062001, 2016. doi: 10.1088/0953-4075/49/6/062001.

[83] F Remacle and RD Levine. An electronic time scale in chemistry. *Proc. Natl. Acad. Sci. U.S.A.*, 103(18):6793–6798, January 2006. doi: 10.1073/pnas.0601855103. URL http://www.pnas.org/content/103/18/6793.

[84] P. B. Corkum and F. Krausz. Attosecond Science. *Nat. Phys.*, 3:381–387, 2007. doi: 10.1038/nphys620. URL https://www.nature.com/articles/nphys620.

[85] P. M. Paul, E. S. Toma, P. Breger, G. Mullot, F. Augé, Ph. Balcou, H. G. Muller, and P. Agostini. Observation of a train of attosecond pulses from high harmonic generation. *Science*, 292(5522):1689–1692, 2001. ISSN 0036-8075. doi: 10.1126/science.1059413. URL http://science.sciencemag.org/content/292/5522/1689.

[86] M. Hentschel, R. Kienberger, C. Spielmann, G. A. Reider, N. Milosevic, T. Brabec, P. Corkum, U. Heinzmann, M. Drescher, and F. Krausz. Attosecond metrology. *Nature*, 414:509–513, 2001. doi: 10.1038/35107000. URL https://doi.org/10.1038/35107000.

[87] Mingxuan Li, Leshi Zhao, Huiyong Wang, Jialong Li, Wentao Wang, Jiaao Cai, Xiaochun Hong, Xiaosen Shi, Ming Zhang, Xinning Zhao, Robin Weissenbilder, David Busto, Mathieu Gisselbrecht, Kiyoshi Ueda, Sizuo Luo, Zheng Li, and Dajun Ding. Attosecond spectroscopy reveals spontaneous symmetry breaking in molecular photoionization. *Sci. Adv.*, 11(38):eadw5415, 2025. doi: 10.1126/sciadv.adw5415.

[88] Ahmed H Zewail. Laser femtochemistry. *Science*, 242(4886):1645–1653, December 1988. doi: 10.1126/science.242.4886.1645. URL https://doi.org/10.1126/science.242.4886.1645.

[89] C. Brühl, J. Lelieveld, P. J. Crutzen, and H. Tost. The role of carbonyl sulphide as a source of stratospheric sulphate aerosol and its impact on climate. *Atmos. Chem. Phys.*, 12(3):1239–1253, 2012. doi: 10.5194/acp-12-1239-2012.

[90] N. Sivakumar, G. E. Hall, P. L. Houston, J. W. Hepburn, and I. Burak. State-resolved photodissociation of OCS monomers and clusters. *J. Chem. Phys.*, 88(6):3692–3708, 1988. doi: 10.1063/1.453869. URL https://doi.org/10.1063/1.453869.

[91] Evangelos Karamatskos, Suresh Yarlagadda, Serguei Patchkovskii, Marc Vrakking, Ralph Welsch, Jochen Küpper, and Arnaud Rouzée. Time-resolving the UV-initiated photodissociation dynamics of OCS. *Faraday Disc.*, 228:413, 2021. doi: 10.1039/d0fd00119h.

[92] Daniela Russo, Jacques Ollivier, and José Teixeira. Water hydrogen bond analysis on hydrophilic and hydrophobic biomolecule sites. *Phys. Chem. Chem. Phys.*, 10:4968–4974, 2008. doi: 10.1039/B807551B. URL https://pubs.rsc.org/en/content/articlelanding/2008/cp/b807551b.

[93] Pavel Jungwirth. Biological water or rather water in biology? *J. Phys. Chem. Lett.*, 6(13):2449–2451, 2015. doi: 10.1021/acs.jpclett.5b01143. URL https://doi.org/10.1021/acs.jpclett.5b01143.

[94] Otto Dopfer and Masaaki Fujii. Probing solvation dynamics around aromatic and biological molecules at the single-molecular level. *Chem. Rev.*, 116(9):5432–5363, 2016. doi: 10.1021/acs.chemrev.5b00610.

[95] Sayantan Mondal, Saumyak Mukherjee, and Biman Bagchi. Protein hydration dynamics: Much ado about nothing? *J. Phys. Chem. Lett.*, 8(19):4878–4882, 2017. doi: 10.1021/acs.jpclett.7b02324. URL https://doi.org/10.1021/acs.jpclett.7b02324. PMID: 28978201.

[96] J Lucas-Lenard and F Lipmann. Protein biosynthesis. *Annu. Rev. Biochem.*, 40 (1):409–448, 1971. doi: 10.1146/annurev.bi.40.070171.002205. URL https://www.annualreviews.org/doi/abs/10.1146/annurev.bi.40.070171.002205.

[97] Katarzyna Świderek, Sergio Marti, Iñaki Tuñón, Vicent Moliner, and Juan Bertran. Peptide bond formation mechanism catalyzed by ribosome. *J. Am. Chem. Soc.*, 137 (37):12024–12034, 2015. doi: 10.1021/jacs.5b05916. URL https://doi.org/10.1021/jacs.5b05916.

[98] Shirley Lehnert. *Biomolecular Action of Ionizing Radiation*. Taylor & Francis, London, 2007. doi: 10.1201/9781420011920. URL https://www.taylorfrancis.com/books/9780429145117.

[99] Elahe Alizadeh, Thomas M. Orlando, and Léon Sanche. Biomolecular damage induced by ionizing radiation: The direct and indirect effects of low-energy electrons on DNA. *Annu. Rev. Phys. Chem.*, 66:379–398, 2015. doi: 10.1146/annurev-physchem-040513-103605. URL https://www.annualreviews.org/doi/pdf/10.1146/annurev-physchem-040513-103605.

[100] Hong-Keun Kim, Jasmin Titze, Markus Schöffler, Florian Trinter, Markus Waitz, Jörg Voigtsberger, Hendrik Sann, Moritz Meckel, Christian Stuck, Ute Lenz, Matthias Odenweller, Nadine Neumann, Sven Schössler, Klaus Ullmann-Pfleger, Birte Ulrich, Rui Costa Fraga, Nikos Petridis, Daniel Metz, Annika Jung, Robert Grisenti, Achim Czasch, Ottmar Jagutzki, Lothar Schmidt, Till Jahnke, Horst Schmidt-Böcking, and Reinhard Dörner. Enhanced production of low energy electrons by alpha particle impact. *Proc. Natl. Acad. Sci. U.S.A.*, 108:11821–11824, 2011. doi: 10.1073/pnas.1104382108. URL https://www.pnas.org/content/108/29/11821.

[101] Badia Boudaïffa, Pierre Cloutier, Darel Hunting, Michael A. Hues, and Leon Sanche. Resonant formation of DNA strand breaks by low-energy (3 to 20 eV) electrons. *Science*, 287(5458):1658–1660, 2000. doi: 10.1126/science.287.5458.1658. URL https://science.sciencemag.org/content/287/5458/1658.

[102] F Martin, P. D. Burrow, Z Cai, D Cloutier, Pand Hunting, and L Sanche. DNA strand breaks induced by 0–4 eV electrons: The role of shape resonances. *Phys. Rev. Lett.*, 93:068101, Aug 2004. doi: 10.1103/PhysRevLett.93.068101. URL https://link.aps.org/doi/10.1103/PhysRevLett.93.068101.

[103] Barry D. Michael and Peter O'Neill. A sting in the tail of electron tracks. *Science*, 187(5458):1603–1604, 2000. doi: 10.1126/science.287.5458.1603. URL https://science.sciencemag.org/content/287/5458/1603.

[104] Z.-H. Loh, G. Doumy, C. Arnold, L. Kjellsson, S. H. Southworth, A. Al Haddad, Y. Kumagai, M.-F. Tu, P. J. Ho, A. M. March, R. D. Schaller, M. S. Bin Mohd Yusof, T. Debnath, M. Simon, R. Welsch, L. Inhester, K. Khalili, K. Nanda, A. I. Krylov, S. Moeller, G. Coslovich, J. Koralek, M. P. Minitti, W. F. Schlotter, J.-E. Rubensson, R. Santra, and L. Young. Observation of the fastest chemical processes in the

radiolysis of water. *Science*, 367:179–182, 2020. doi: 10.1126/science.aaz4740. URL https://science.sciencemag.org/content/367/6474/179.

[105] Vít Svoboda, Rupert Michiels, Aaron C. LaForge, Jakub Med, Frank Stienkemeier, Petr Slavíček, and Hans Jakob Wörner. Real-time observation of water radiolysis and hydrated electron formation induced by extreme-ultraviolet pulses. *Sci. Adv.*, 6:eaaz0385, 2020. doi: 10.1126/sciadv.aaz0385. URL https://advances.sciencemag.org/content/6/3/eaaz0385.

[106] Andrzej L Sobolewski and Wolfgang Domcke. Photoejection of electrons from pyrrole into an aqueous environment: ab initio results on pyrrole-water clusters. *Chem. Phys. Lett.*, 321(5-6):479–484, May 2000. doi: 10.1016/S0009-2614(00)00404-8. URL http://linkinghub.elsevier.com/retrieve/pii/S0009261400004048.

[107] Andrew T. Ulijasz, Gabriel Cornilescu, Claudia C. Cornilescu, Junrui Zhang, Mario Rivera, John L. Markley, and Richard D. Vierstra. Structural basis for the photoconversion of a phytochrome to the activated Pfr form. *Nature*, 463:250–254, 2010. doi: 10.1038/nature08671. URL https://www.nature.com/articles/nature08671.

[108] M. N. R. Ashfold, B. Cronin, A. L. Devine, R. N. Dixon, and M. G. D. Nix. The role of $\pi\sigma^*$ excited states in the photodissociation of heteroaromatic molecules. *Science*, 312:1637–1640, 2006. doi: 10.1126/science.1125436. URL http://science.sciencemag.org/content/312/5780/1637/tab-pdf.

[109] A. L. Sobolewski, W. Domcke, C. Dedonder-Lardeux, and C. Jouvet. Excited-state hydrogen detachment and hydrogen transfer driven by repulsive $^1\pi\sigma^*$ states: A new paradigm for nonradiative decay in aromatic biomolecules. *Phys. Chem. Chem. Phys.*, 4:1093–1100, 2002. doi: 10.1039/B110941N. URL http://dx.doi.org/10.1039/B110941N.

[110] Louise Belshaw, Francesca Calegari, Martin J Duffy, Andrea Trabattoni, Luca Poletto, Mauro Nisoli, and Jason B Greenwood. Observation of ultrafast charge migration in an amino acid. *J. Phys. Chem. Lett.*, 3(24):3751–3754, December 2012. doi: 10.1021/jz3016028. URL http://pubs.acs.org/doi/abs/10.1021/jz3016028.

[111] Gerhard L Closs and John R Miller. Intramolecular long-distance electron transfer in organic molecules. *Science*, 240(4851):440–447, 1988.

[112] G. Scoles, editor. *Atomic and molecular beam methods*, volume 1 & 2. Oxford University Press, New York, NY, USA, 1988 & 1992.

[113] Norman F. Ramsey. *Molecular Beams*. The International Series of Monographs on Physics. Oxford University Press, London, GB, 1956. reprinted in *Oxford Classic Texts in the Physical Sciences* (2005).

[114] Wolfgang Demtröder. *Laser Spectroscopy 1: Basic Principles*. Springer Verlag, Berlin, 2008. ISBN 978-3-540-73418-5. doi: 10.1007/978-3-540-73418-5.

[115] Jens Als-Nielsen and Des McMorrow. *Elements of Modern X-ray Physics*. John Wiley & Sons, Chichester, West Sussex, United Kingdom, 2001. ISBN 978-0-471-49858-2.

[116] C. D. Lin, Anh-Thu Le, Cheng Jin, and Hui Wei. *Attosecond and Strong-Field Physics: Principles and Applications*. Cambridge University Press, 2018. doi: 10.1017/9781108181839.010.

[117] F. Reif. *Fundamentals of statistical and thermal physics*. McGraw-Hill, Singapore, international edition, 1985. ISBN 0-07-085615-X.

[118] O. F. Hagena and W. Obert. Cluster formation in expanding supersonic jets: Effect

of pressure, temperature, nozzle size, and test gas. *J. Chem. Phys.*, 56(5):1793–1802, 1972. doi: 10.1063/1.1677455. URL http://link.aip.org/link/?JCP/56/1793/1.

[119] Richard E. Smalley, Lennard Wharton, and Donald H. Levy. Molecular optical spectroscopy with supersonic beams and jets. *Acc. Chem. Res.*, 10(4):139–145, 1977. doi: 10.1021/ar50112a006. URL https://doi.org/10.1021/ar50112a006.

[120] U. Even. Pulsed supersonic beams from high pressure source: Simulation results and experimental measurements. *Adv. Chem.*, 2014:636042, 2014. doi: 10.1155/2014/636042.

[121] Uzi Even. The Even-Lavie valve as a source for high intensity supersonic beam. *Eur. Phys. J. Techn. Instrumen.*, 2(1):17, December 2015. doi: 10.1140/epjti/s40485-015-0027-5. URL https://doi.org/10.1140/epjti/s40485-015-0027-5.

[122] U. Even, J. Jortner, D. Noy, N. Lavie, and N. Cossart-Magos. Cooling of large molecules below 1 K and He clusters formation. *J. Chem. Phys.*, 112:8068–8071, 2000. doi: 10.1063/1.481405. URL http://dx.doi.org/10.1063/1.481405.

[123] Matthias Hillenkamp, Sharon Keinan, and Uzi Even. Condensation limited cooling in supersonic expansions. *J. Chem. Phys.*, 118(19):8699–8705, 2003. doi: 10.1063/1.1568331. URL http://link.aip.org/link/?JCP/118/8699/1.

[124] Donald H. Levy. The Spectroscopy of Very Cold Gases. *Science*, 214(4518):263–269, 1981. ISSN 0036-8075. doi: 10.1126/science.214.4518.263.

[125] Wolfgang Christen, Klaus Rademann, and Uzi Even. Supersonic beams at high particle densities: Model description beyond the ideal gas approximation. *J. Phys. Chem. A*, 114(42):11189–11201, 2010. doi: 10.1021/jp102855m.

[126] S. Carles, F. Lecomte, J. P. Schermann, and C. Desfrançois. Gas-phase experimental and theoretical studies of adenine, imidazole, pyrrole, and water non-covalent complexes. *J. Phys. Chem. A*, 104:10662–10668, 2000. doi: 10.1021/jp002157j. URL https://doi.org/10.1021/jp002157j.

[127] O. G. Danylchenko, S. I. Kovalenko, and V. N. Samovarov. Experimental verification of the hagena relation for large clusters formed in a conical nozzle. *Tech. Phys. Lett.*, 34:1037–1040, 2008. doi: 10.1134/S1063785008120146. URL https://doi.org/10.1134/S1063785008120146.

[128] Wolfgang Demtröder. *Atoms, Molecules and Photons An Introduction to Atomic-, Molecular- and Quantum Physics*. Graduate Texts in Physics: SpringerLink: Bücher. Springer Verlag, third edition edition, 2018. doi: 10.1007/978-3-662-55523-1.

[129] Daniel Irimia, Dimitar Dobrikov, Rob Kortekaas, Han Voet, Daan A. van den Ende, Wilhelm A. Groen, and Maurice H. M. Janssen. A short pulse (7 μs FWHM) and high repetition rate (dc–5kHz) cantilever piezovalve for pulsed atomic and molecular beams. *Rev. Sci. Instrum.*, 80(11):113303, 2009. doi: 10.1063/1.3263912.

[130] J. Stark and G. Wendt. Beobachtungen über den Effekt des elektrischen Feldes auf Spektrallinien. II. Längseffekt. *Ann. Phys.*, 348(7):983–990, 1914. ISSN 1521-3889. doi: 10.1002/andp.19143480703. URL http://dx.doi.org/10.1002/andp.19143480703.

[131] Y.-P. Chang, F. Filsinger, B. G. Sartakov, and J. Küpper. CMIstark: Python package for the Stark-effect calculation and symmetry classification of linear, symmetric and asymmetric top wavefunctions in dc electric fields. *Comp. Phys. Comm.*, 185: 339–349, 2014. doi: 10.1016/j.cpc.2013.09.001. URL http://www.sciencedirect.

com/science/article/pii/S0010465513003019. Current version available from https://gitlab.desy.de/CMI/CMI-public/cmistark.

[132] Jens S. Kienitz, Karol Długołęcki, Sebastian Trippel, and Jochen Küpper. Improved spatial separation of neutral molecules. *J. Chem. Phys.*, 147(2):024304, 2017. doi: 10.1063/1.4991479. URL https://doi.org/10.1063/1.4991479.

[133] F H de Leeuw and A Dymanus. Electric and magnetic properties of OCS measured by molecular-beam electric-resonance spectroscopy. *Chem. Phys. Lett.*, 7(2):288–292, October 1970.

[134] W. Gordy and R. L. Cook. *Microwave Molecular Spectra*. John Wiley & Sons, New York, NY, USA, 3 edition, 1984.

[135] M. Born and R. Oppenheimer. Zur Quantentheorie der Molekeln. *Ann. Physik*, 84:457–484, 1927. doi: 10.1002/andp.19273892002. URL https://doi.org/10.1002/andp.19273892002.

[136] C. Eckart. Some studies concerning rotating axes and polyatomic molecules. *Phys. Rev.*, 47:552, 1935. doi: 10.1103/PhysRev.47.552. URL https://link.aps.org/doi/10.1103/PhysRev.47.552.

[137] Adrian J de Nijs and Hendrick L Bethlem. On deflection fields, weak-focusing and strong-focusing storage rings for polar molecules. *Phys. Chem. Chem. Phys.*, 13 (42):19052–8, November 2011. ISSN 1463-9084. doi: 10.1039/c1cp21477b. URL http://www.ncbi.nlm.nih.gov/pubmed/21979152.

[138] Jens S. Kienitz, Sebastian Trippel, Terry Mullins, Karol Długołęcki, Rosario González-Férez, and Jochen Küpper. Adiabatic mixed-field orientation of ground-state-selected carbonyl sulfide molecules. *Chem. Phys. Chem.*, 17(22): 3740–3746, 2016. doi: cphc.201600710R2. URL http://dx.doi.org/10.1002/cphc.201600710.

[139] Jens H. Nielsen, Paw Simesen, Christer Z. Bisgaard, Henrik Stapelfeldt, Frank Filsinger, Bretislav Friedrich, Gerard Meijer, and Jochen Küpper. Stark-selected beam of ground-state OCS molecules characterized by revivals of impulsive alignment. *Phys. Chem. Chem. Phys.*, 13:18971–18975, 2011. doi: 10.1039/c1cp21143a. URL https://dx.doi.org/10.1039/c1cp21143a.

[140] Frank Filsinger, Jochen Küpper, Gerard Meijer, Lotte Holmegaard, Jens H. Nielsen, Iftach Nevo, Jonas L. Hansen, and Henrik Stapelfeldt. Quantum-state selection, alignment, and orientation of large molecules using static electric and laser fields. *J. Chem. Phys.*, 131:064309, 2009. doi: 10.1063/1.3194287. URL http://scitation.aip.org/content/aip/journal/jcp/131/6/10.1063/1.3194287.

[141] Nicole Teschmit, Daniel A. Horke, and Jochen Küpper. Spatially separating the conformers of a dipeptide. *Angew. Chem. Int. Ed.*, 57(42):13775–13779, October 2018. doi: 10.1002/anie.201807646. URL https://onlinelibrary.wiley.com/doi/abs/10.1002/anie.201807646.

[142] Thomas Kierspel, Daniel A. Horke, Yuan-Pin Chang, and Jochen Küpper. Spatially separated polar samples of the *cis* and *trans* conformers of 3-fluorophenol. *Chem. Phys. Lett.*, 591:130–132, 2014. ISSN 0009-2614. doi: 10.1016/j.cplett.2013.11.010. URL http://www.sciencedirect.com/science/article/pii/S0009261413014000.

[143] Sebastian Trippel, Yuan-Pin Chang, Stephan Stern, Terry Mullins, Lotte Holmegaard, and Jochen Küpper. Spatial separation of state- and size-selected neutral clusters. *Phys. Rev. A*, 86:033202, September 2012. doi: 10.1103/PhysRevA.

86.033202. URL http://pra.aps.org/abstract/PRA/v86/i3/e033202.

[144] Melby Johny, Jolijn Onvlee, Thomas Kierspel, Helen Bieker, Sebastian Trippel, and Jochen Küpper. Spatial separation of pyrrole and pyrrole-water clusters. *Chem. Phys. Lett.*, 721:149–152, 2019. ISSN 0009-2614. doi: 10.1016/j.cplett.2019.01.052. URL https://doi.org/10.1016/j.cplett.2019.01.052.

[145] Helen Bieker, Jolijn Onvlee, Melby Johny, Lanhai He, Thomas Kierspel, Sebastian Trippel, Daniel A Horke, and Jochen Küpper. Pure molecular beam of water dimer. *J. Phys. Chem. A*, 123:7486–7490, August 2019. doi: 10.1021/acs.jpca.9b06460. URL https://doi.org/10.1021/acs.jpca.9b06460.

[146] M Abd El Rahim, R Antoine, M Broyer, D Rayane, and Ph Dugourd. Asymmetric top rotors in electric fields: influence of chaos and collisions in molecular beam deflection experiments. *J. Phys. Chem. A*, 109(38):8507–8514, September 2005. doi: 10.1021/jp053127p. URL http://www.ncbi.nlm.nih.gov/pubmed/16834247.

[147] Kaoru Yamanouchi, Wendell T Hill III, and Gerhard G Paulus. *Progress in Ultrafast Intense Laser Science XIII*. Springer, December 2017. ISBN 978-3-319-64840-8. doi: 10.1007/978-3-319-64840-8_1. URL https://doi.org/10.1007/978-3-319-64840-8_1.

[148] P. Lambropoulos. Topics on multiphoton processes in atoms. In D.R. Bates and Benjamin Bederson, editors, *Advances in atomic and molecular physics*, volume 12, pages 87–164. Adv. Phys., 1976. doi: 10.1016/S0065-2199(08)60043-3. URL http://www.sciencedirect.com/science/article/pii/S0065219908600433.

[149] Misha Yu Ivanov, Michael Spanner, and Olga Smirnova. Anatomy of strong field ionization. *J. Mod. Opt.*, 52(2-3):165–184, 2005. doi: 10.1080/0950034042000275360. URL https://doi.org/10.1080/09500340420002753 60.

[150] T. Ditmire, J. W. G. Tisch, E. Springate, M. B. Mason, N. Hay, R. A. Smith, J. Marangos, and M. H. R. Hutchinson. High-energy ions produced in explosions of superheated atomic clusters. *Nature*, 386(6620):54–56, 1997. ISSN 0028-0836. doi: 10.1038/386054a0.

[151] Jonas Hansen. *Imaging molecular frame dynamics using spatially oriented molecules*. PhD thesis, University of Aarhus, Aarhus, Denmark, 2012.

[152] L.V. Keldysh. Ionization in the field of a strong electromagnetic wave. *J. Exp. Theor. Phys.*, 20(5):1307–1314, 1965. URL http://jetp.ras.ru/cgi-bin/e/index/e/20/5/p1307?a=list.

[153] S V Popruzhenko. Keldysh theory of strong field ionization: history, applications, difficulties and perspectives. *J. Phys. B*, 47(20):204001, 2014. doi: 10.1088/0953-4075/47/20/204001. URL http://stacks.iop.org/0953-4075/47/i=20/a=204001.

[154] S G Walt, N B Ram, M Atala, N I Shvetsov-Shilovski, A von Conta, D Baykusheva, M Lein, and H J Wörner. Dynamics of valence-shell electrons and nuclei probed by strong-field holography and rescattering. *Nat. Commun.*, 8:15651, 2017. doi: 10.1038/ncomms15651. URL https://www.nature.com/articles/ncomms15651.

[155] Jean-Patrick Connerade. *Highly excited atoms*. Number 9. Cambridge University Press, 1998.

[156] P. B. Corkum. Plasma perspective on strong-field multiphoton ionization. *Phys. Rev. Lett.*, 71:1994–1997, 1993. doi: 10.1103/PhysRevLett.71.1994. URL https://journals.aps.org/prl/abstract/10.1103/PhysRevLett.71.1994.

[157] W. Becker, F. Grasbon, R. Kopold, D. B. Milošević, G. G. Paulus, and H. Walther.

Above-threshold ionization: From classical features to quantum effects. *Adv. Atom. Mol. Opt. Phys.*, 48:35–98, 2002. doi: 10.1016/S1049-250X(02)80006-4. URL http://adsabs.harvard.edu/abs/2002AAMOP..48...35B.

[158] P Agostini, F Fabre, G Mainfray, G Petite, and N K Rahman. Free-free transitions following six-photon ionization of xenon atoms. *Phys. Rev. Lett.*, 42(17):1127–1130, 1979. ISSN 0031-9007. doi: 10.1103/physrevlett.42.1127.

[159] C.-H. Yang, G. Sarma, J. J. ter Meulen, D. H. Parker, and C. M. Western. REMPI spectroscopy and predissociation of the $\tilde{C}\ ^1B_1(v = 0)$ rotational levels of H_2O, HOD and D_2O. *Phys. Chem. Chem. Phys.*, 12:13983–13991, 2010. doi: 10.1039/C0CP00946F. URL http://dx.doi.org/10.1039/C0CP00946F.

[160] Christer Z. Bisgaard and Lars Bojer Madsen. Tunneling ionization of atoms. *Am. J. Phys.*, 72(2):249–254, 2004. doi: 10.1119/1.1603274. URL https://doi.org/10.1119/1.1603274.

[161] A L'Huillier, D Descamps, A Johansson, J Norin, J Mauritsson, and C G Wahlstrom. Applications of high-order harmonics. *Eur. Phys. J. D*, 26(1):91–98, October 2003. doi: 10.1140/epjd/e2003-00072-2. URL http://www.springerlink.com/openurl.asp?genre=article&id=doi:10.1140/epjd/e2003-00072-2.

[162] H. Niikura, F. Légaré, R. Hasbani, A. D. Bandrauk, M. Y. Ivanov, D. M. Villeneuve, and P. B. Corkum. Sub-laser-cycle electron pulses for probing molecular dynamics. *Nature*, 417:917–922, 2002. doi: 10.1038/nature00787. URL https://www.nature.com/articles/nature00787.

[163] S Augst, D D Meyerhofer, D Strickland, and S L Chint. Laser ionization of noble gases by coulomb-barrier suppression. *J. Opt. Soc. Am. B*, 8(4):858, 1991. ISSN 0740-3224. doi: 10.1364/josab.8.000858.

[164] M. V. Ammosov, N. B. Delone, and V. P. Krainov. Tunnel ionization of complex atoms and of atomic ions in an alternating electromagnetic field. *Sov. Phys. JETP*, 64(6):1191–1194, 1986. URL http://www.jetp.ac.ru/cgi-bin/e/index/e/64/6/p1191?a=list.

[165] Howard R. Reiss. Effect of an intense electromagnetic field on a weakly bound system. *Phys. Rev. A*, 22:1786–1813, Nov 1980. doi: 10.1103/PhysRevA.22.1786. URL https://link.aps.org/doi/10.1103/PhysRevA.22.1786.

[166] X. M. Tong, Z. X. Zhao, and C. D. Lin. Theory of molecular tunneling ionization. *Phys. Rev. A*, 66:033402, Sep 2002. doi: 10.1103/PhysRevA.66.033402. URL https://link.aps.org/doi/10.1103/PhysRevA.66.033402.

[167] T. Zuo and A. D. Bandrauk. Charge-resonance-enhanced ionization of diatomic molecular ions by intense lasers. *Phys. Rev. A*, 52:R2511–R2514, 1995. doi: 10.1103/PhysRevA.52.R2511. URL https://link.aps.org/doi/10.1103/PhysRevA.52.R2511.

[168] Irina Bocharova, Reza Karimi, Emmanuel F. Penka, Jean-Paul Brichta, Philippe Lassonde, Xiquan Fu, Jean-Claude Kieffer, André D. Bandrauk, Igor Litvinyuk, Joseph Sanderson, and Fran çois Légaré. Charge resonance enhanced ionization of co_2 probed by laser coulomb explosion imaging. *Phys. Rev. Lett.*, 107(6):063201, 2011. doi: 10.1103/PhysRevLett.107.063201. URL https://link.aps.org/doi/10.1103/PhysRevLett.107.063201.

[169] Stefan Roither, Xinhua Xie, Daniil Kartashov, Li Zhang, Markus Schöffler, Huailiang Xu, Atsushi Iwasaki, Tomoya Okino, Kaoru Yamanouchi, Andrius Baltuska, and Markus Kitzler. High energy proton ejection from hydrocarbon

molecules driven by highly efficient field ionization. *Phys. Rev. Lett.*, 106(16):163001, 2011. URL https://link.aps.org/doi/10.1103/PhysRevLett.106.163001.

[170] Christian Siedschlag and Jan M. Rost. Electron release of rare-gas atomic clusters under an intense laser pulse. *Phys. Rev. Lett.*, 89(17):173401, 2002. ISSN 0031-9007. doi: 10.1103/physrevlett.89.173401.

[171] A Giustisuzor, FH Mies, LF Dimauro, E Charron, and B Yang. Dynamics of h-2(+) in intense laser fields. *Journal of Physics B-Atomic Molecular & Optical Physics*, 28(3): 309–339, 1995.

[172] Z. Vager, R. Naaman, and E. P. Kanter. Coulomb explosion imaging of small molecules. *Science*, 244(4903):426–431, 1989. doi: 10.1126/science.244.4903.426. URL http://www.sciencemag.org/cgi/doi/10.1126/science.244.4903.426.

[173] Martin Pitzer, Maksim Kunitski, Allan S. Johnson, Till Jahnke, Hendrik Sann, Felix Sturm, Lothar Ph. H. Schmidt, Horst Schmidt-Böcking, Reinhard Dörner, Jürgen Stohner, Julia Kiedrowski, Michael Reggelin, Sebastian Marquardt, Alexander Schießer, Robert Berger, and Markus S. Schöffler. Direct determination of absolute molecular stereochemistry in gas phase by Coulomb explosion imaging. *Science*, 341(6150):1096–1100, 2013. doi: 10.1126/science.1240362. URL http://www.sciencemag.org/cgi/doi/10.1126/science.1240362.

[174] David Attwood. *Soft x-rays and extreme ultraviolet radiation: principles and applications*. Cambridge University Press, University of California, Berkeley, 2000. ISBN 0521652146.

[175] Grant Bunker. *X-RAY ABSORPTION SPECTROSCOPY*, pages 2499–2527. John Wiley and Sons, Ltd, 2016. ISBN 9781119244752. doi: https://doi.org/10.1002/9781119244752.ch69. URL https://onlinelibrary.wiley.com/doi/abs/10.1002/9781119244752.ch69.

[176] A. Thompson, I. Lindau, D. Attwood, Y. Liu, E. Gullikson, P. Pianetta, M. Howells, A. Robinson, K.-J. Kim, J. Scofield, J. Kirz, J. Underwood, J. Kortright, G. Williams, and H. Winick. *X-Ray Data Booklet*. Center for X-Ray Optics and Advanced Light Source, Lawrence Berkeley National Laboratory, Berkeley, CA, 2009. URL http://xdb.lbl.gov/.

[177] Elettra Web Page, 2017. URL https://vuo.elettra.eu/services/elements/WebElements.html. Atomic Calculation of Photoionization Cross-Sections and Asymmetry Parameters.

[178] Robin Santra. Concepts in x-ray physics. *J. Phys. B*, 42(2):023001, January 2009. doi: 10.1088/0953-4075/42/2/023001. URL http://iopscience.iop.org/article/10.1088/0953-4075/42/2/023001.

[179] Svante Svensson, Bengt Eriksson, Nils Mårtensson, Göran Wendin, and Ulrik Gelius. Electron shake-up and correlation satellites and continuum shake-off distributions in x-ray photoelectron spectra of the rare gas atoms. *J. Electron. Spectrosc. Relat. Phenom.*, 47:327–384, January 1988. doi: 10.1016/0368-2048(88)85020-5. URL https://doi.org/10.1016/0368-2048(88)85020-5.

[180] Burhop. *The Auger Effect and Other Radiationless Transitions*. Cambridge University Press, 1952. ISBN 9781107641105.

[181] T Jahnke. Interatomic and intermolecular Coulombic decay: the coming of age story. *J. Phys. B*, 48(8):082001, 2015. doi: 10.1088/0953-4075/48/8/082001. URL http://doi.org/10.1088/0953-4075/48/8/082001.

[182] L S Cederbaum, J Zobeley, and F Tarantelli. Giant intermolecular decay and

fragmentation of clusters. *Phys. Rev. Lett.*, 79(24):4778–4781, December 1997. doi: 10.1103/PhysRevLett.79.4778. URL https://doi.org/10.1103/PhysRevLett.79.4778.

[183] Melanie Mucke, Markus Braune, Silko Barth, Marko Förstel, Toralf Lischke, Volker Ulrich, Tiberiu Arion, Uwe Becker, Alex Bradshaw, and Uwe Hergenhahn. A hitherto unrecognized source of low-energy electrons in water. *Nat. Phys.*, 6:143–146, 2010. doi: 10.1038/nphys1500. URL https://www.nature.com/articles/nphys1500.

[184] J Zobeley, R Santra, and L S Cederbaum. Electronic decay in weakly bound heteroclusters: Energy transfer versus electron transfer. *J. Chem. Phys.*, 115(11):5076–5088, 2001. doi: 10.1063/1.1395555. URL https://doi.org/10.1063/1.1395555.

[185] Clemens Richter, Daniel Hollas, Clara Magdalena Saak, Marko Förstel, Tsveta Miteva, Melanie Mucke, Olle Björneholm, Nicolas Sisourat, Petr Slavíček, and Uwe Hergenhahn. Competition between proton transfer and intermolecular Coulombic decay in water. *Nat. Commun.*, 9:4988, 2018. doi: 10.1038/s41467-018-07501-6. URL https://www.nature.com/articles/s41467-018-07501-6.

[186] Petr Slavíček, Bernd Winter, Lorenz S. Cederbaum, and Nikolai V. Kryzhevoi. Proton-transfer mediated enhancement of nonlocal electronic relaxation processes in X-ray irradiated liquid water. *J. Am. Chem. Soc.*, 136(52):18170–18176, June 2014. doi: 10.1021/ja5117588. URL https://doi.org/10.1021/ja5117588.

[187] J. W. L. Lee, D. S. Tikhonov, P. Chopra, S. Maclot, A. L. Steber, S. Gruet, F. Allum, R. Boll, X. Cheng, S. Düsterer, B. Erk, D. Garg, L. He, D. Heathcote, M. Johny, M. M. Kazemi, H. Köckert, J. Lahl, A. K. Lemmens, D. Loru, R. Mason, E. Müller, T. Mullins, P. Olshin, C. Passow, J. Peschel, D. Ramm, D. Rompotis, N. Schirmel, S. Trippel, J. Wiese, F. Ziaee, S. Bari, M. Burt, J. Küpper, A. M. Rijs, D. Rolles, S. Techert, P. Eng-Johnsson, M. Brouard, C. Vallance, B. Manschwetus, and M. Schnell. Time-resolved relaxation and fragmentation of polycyclic aromatic hydrocarbons investigated in the ultrafast XUV-IR regime. *Nat. Commun.*, 12:6107, 2021. doi: 10.1038/s41467-021-26193-z. URL https://www.nature.com/articles/s41467-021-26193-z.

[188] A. Assion, M. Geisler, J. Helbing, V. Seyfried, and T. Baumert. Femtosecond pump-probe photoelectron spectroscopy: Mapping of vibrational wave-packet motion. *Phys. Rev. A*, 54:R4605–R4608, Dec 1996. doi: 10.1103/PhysRevA.54.R4605. URL https://link.aps.org/doi/10.1103/PhysRevA.54.R4605.

[189] Bethany Jochim, Lindsey DeJesus, and Marcos Dantus. Ultrafast disruptive probing: Simultaneously keeping track of tens of reaction pathways. *Rev. Sci. Instrum.*, 93(3):033003, 03 2022. doi: 10.1063/5.0084837. URL https://doi.org/10.1063/5.0084837.

[190] Shuai Li, Lixin Lu, Swarnendu Bhattacharyya, Carolyn Pearce, Kai Li, Emily T. Nienhuis, Gilles Doumy, R. D. Schaller, S. Moeller, M.-F. Lin, G. Dakovski, D. J. Hoffman, D. Garratt, Kirk A. Larsen, J. D. Koralek, C. Y. Hampton, D. Cesar, Joseph Duris, Z. Zhang, Nicholas Sudar, James P. Cryan, A. Marinelli, Xiaosong Li, Ludger Inhester, Robin Santra, and Linda Young. Attosecond-pump attosecond-probe x-ray spectroscopy of liquid water. *Science*, 383(6687):1118–1122, 2024. doi: 10.1126/science.adn6059.

[191] K Schnorr, A Senftleben, G Schmid, A Rudenko, M Kurka, K Meyer, L Foucar, M Kuebel, M F Kling, Y H Jiang, S Duesterer, R Treusch, C D Schroeter, J Ullrich, T Pfeifer, and R Moshammer. Multiple ionization and fragmentation dynamics

of molecular iodine studied in ir-xuv pump-probe experiments. *Faraday Discuss.*, 171(0):41–56, 2014. doi: 10.1039/c4fd00031e. URL http://xlink.rsc.org/?DOI=C4FD00031E.

[192] C. S. Lehmann, A. Picón, C. Bostedt, A. Rudenko, A. Marinelli, D. Moonshiram, T. Osipov, D. Rolles, N. Berrah, C. Bomme, M. Bucher, G. Doumy, B. Erk, K. R. Ferguson, T. Gorkhover, P. J. Ho, E. P. Kanter, B. Krässig, J. Krzywinski, A. A. Lutman, A. M. March, D. Ray, L. Young, S. T. Pratt, and S. H. Southworth. Ultrafast x-ray-induced nuclear dynamics in diatomic molecules using femtosecond x-ray-pump–x-ray-probe spectroscopy. *Phys. Rev. A*, 94:013426, 2016. doi: 10.1103/PhysRevA.94.013426. URL https://link.aps.org/doi/10.1103/PhysRevA.94.013426.

[193] Till Stensitzki, Yang Yang, Valeri Kozich, Ashour A. Ahmed, Florian Kössl, Oliver Kühn, and Karsten Heyne. Acceleration of a ground-state reaction by selective femtosecond-infrared-laser-pulse excitation. *Nat. Chem.*, 10(2):126–131, 2018. ISSN 1755-4330. doi: 10.1038/nchem.2909. URL https://dx.doi.org/10.1038/nchem.2909.

[194] Ondrej Marsalek, Christopher G Elles, Piotr A Pieniazek, Eva Pluhařová, Joost VandeVondele, Stephen E Bradforth, and Pavel Jungwirth. Chasing charge localization and chemical reactivity following photoionization in liquid water. *J. Chem. Phys.*, 135(22), 2011. doi: 10.1063/1.3664746.

[195] L Strüder, Sascha Epp, Daniel Rolles, Robert Hartmann, Peter Holl, Gerhard Lutz, Heike Soltau, Rouven Eckart, Christian Reich, Klaus Heinzinger, Christian Thamm, Artem Rudenko, Faton Krasniqi, K Kühnel, Christian Bauer, Claus-Dieter Schroeter, Robert Moshammer, Simone Techert, Danilo Miessner, Matteo Porro, Olaf Haelker, Norbert Meidinger, Nils Kimmel, Robert Andritschke, Florian Schopper, Georg Weidenspointner, Alexander Ziegler, Daniel Pietschner, Sven Herrmann, Ullrich Pietsch, Albert Walenta, Wolfram Leitenberger, Christoph Bostedt, Thomas Moeller, Daniela Rupp, Marcus Adolph, Heinz Graafsma, Helmut Hirsemann, Klaus Gaertner, Rainer Richter, Lutz Foucar, Robert L Shoeman, Ilme Schlichting, and Joachim Ullrich. Large-format, high-speed, x-ray pnCCDs combined with electron and ion imaging spectrometers in a multipurpose chamber for experiments at 4th generation light sources. *Nucl. Instrum. Methods Phys. Res. A*, 614(3):483–496, Jan 2010. doi: 10.1016/j.nima.2009.12.053.

[196] Gihan Basnayake, Yasashri Ranathunga, Suk Kyoung Lee, and Wen Li. Three-dimensional (3d) velocity map imaging: from technique to application. *J. Phys. B*, 55(2):023001, feb 2022. doi: 10.1088/1361-6455/ac4b42. URL https://dx.doi.org/10.1088/1361-6455/ac4b42.

[197] J Bull, J Lee, S Gardiner, and C Vallance. An introduction to velocity-map imaging mass spectrometry (vmimms). *Eur. J. Mass Spectrom.*, 20(2):117–129, 2014.

[198] André T. J. B. Eppink and David H. Parker. Velocity map imaging of ions and electrons using electrostatic lenses: Application in photoelectron and photofragment ion imaging of molecular oxygen. *Rev. Sci. Instrum.*, 68(9):3477–3484, 1997. doi: 10.1063/1.1148310. URL https://aip.scitation.org/doi/abs/10.1063/1.1148310.

[199] W C Wiley and I H Mclaren. Time-of-flight mass spectrometer with improved resolution. *Rev. Sci. Instrum.*, 26(12):1150–1157, 1955. doi: 10.1063/1.1715212. URL https://doi.org/10.1063/1.1715212.

[200] A.S. Tremsin and J.V. Vallerga. Unique capabilities and applications of

microchannel plate (MCP) detectors with Medipix/Timepix readout. *Radiat. Meas.*, 130:106228, 2020. ISSN 1350-4487. doi: 10.1016/j.radmeas.2019.106228. URL https://www.sciencedirect.com/science/article/pii/S1350448719305141.

[201] Joseph Ladislas Wiza. Microchannel plate detectors. *Nucl. Instrum. Methods*, 162 (1-3):587–601, 1979. ISSN 0029-554X. doi: 10.1016/0029-554x(79)90734-1.

[202] A Nomerotski, M Brouard, E Campbell, A Clark, J Crooks, J Fopma, J J John, A J Johnsen, C Slater, R Turchetta, C Vallance, E Wilman, and W H Yuen. Pixel imaging mass spectrometry with fast and intelligent pixel detectors. *J. Instrum.*, 5(7):C07007, July 2010. doi: 10.1088/1748-0221/5/07/C07007. URL https://doi.org/10.1088/1748-0221/5/07/C07007.

[203] Andrew T. Clark, Jamie P. Crooks, Iain Sedgwick, Renato Turchetta, Jason W. L. Lee, Jaya John John, Edward S. Wilman, Laura Hill, Edward Halford, Craig S. Slater, Benjamin Winter, Wei Hao Yuen, Sara H. Gardiner, M. Laura Lipciuc, Mark Brouard, Andrei Nomerotski, and Claire Vallance. Multimass Velocity-Map Imaging with the Pixel Imaging Mass Spectrometry (PImMS) Sensor: An Ultra-Fast Event-Triggered Camera for Particle Imaging. *J. Phys. Chem. A*, 116(45):10897–10903, 2012. doi: 10.1021/jp309860t. URL https://doi.org/10.1021/jp309860t.

[204] L. Montgomery Smith, Dennis R. Keefer, and S. I. Sudharsanan. Abel inversion using transform techniques. *J. Quant. Spectrosc. Radiat. Transf.*, 39(5):367–373, 1988. ISSN 0022-4073. doi: 10.1016/0022-4073(88)90101-X. URL https://www.sciencedirect.com/science/article/pii/002240738890101X.

[205] Arthur Zhao, Martin van Beuzekom, Bram Bouwens, Dmitry Byelov, Irakli Chakaberia, Chuan Cheng, Erik Maddox, Andrei Nomerotski, Peter Svihra, Jan Visser, Vaclav Vrba, and Thomas Weinacht. Coincidence velocity map imaging using Tpx3Cam, a time stamping optical camera with 1.5 ns timing resolution. *Rev. Sci. Instrum.*, 88(11):113104, 2017. doi: 10.1063/1.4996888. URL https://doi.org/10.1063/1.4996888.

[206] T Poikela, J Plosila, T Westerlund, M Campbell, M De Gaspari, X Llopart, V Gromov, R Kluit, M. van Beuzekom, F. Zappon, V Zivkovicd, C. Brezinae, K. Desche, Y. Fue, and A. Kruth. Timepix3: a 65 k channel hybrid pixel readout chip with simultaneous ToA/ToT and sparse readout. *J. Instrum.*, 9(5):C05013, 2014. doi: 10.1088/1748-0221/9/05/C05013. URL https://doi.org/10.1088/1748-0221/9/05/C05013.

[207] J. Visser, M. van Beuzekom, Henk Boterenbrood, B. van der Heijden, J.I. Muñoz, S. Kulis, B. Munneke, and F. Schreuder. SPIDR: a read-out system for Medipix3 & Timepix3. *J. Instrum.*, 10(12):C12028, December 2015. doi: 10.1088/1748-0221/10/12/c12028. URL https://doi.org/10.1088%2F1748-0221%2F10%2F12%2Fc12028.

[208] B. van der Heijden, J. Visser, M. van Beuzekom, H. Boterenbrood, S. Kulis, B. Munneke, and F. Schreuder. SPIDR, a general-purpose readout system for pixel ASICs. *J. Instrum.*, 12(02):C02040, 2017. doi: 10.1088/1748-0221/12/02/c02040. URL https://doi.org/10.1088%2F1748-0221%2F12%2F02%2Fc02040.

[209] Ahmed Al-Refaie, Melby Johny, Jonathan Correa, David Pennicard, Peter Svihra, Andrei Nomerotski, Sebastian Trippel, and Jochen Küpper. PymePix: A Python library for SPIDR readout of Timepix3. *J. Instrum.*, 14(10):P10003, 2019. doi: 10.1088/1748-0221/14/10/P10003. URL https://iopscience.iop.org/article/10.1088/1748-0221/14/10/P10003/meta.

[210] CFEL Controlled Molecule Imaging. PymePix. Code repository, URL: https://gitlab.desy.de/CMI/CMI-public/pymepix, 2020. URL https://gitlab.desy.de/CMI/CMI-public/pymepix.

[211] J Feldhaus, J Arthur, and J B Hastings. X-ray free-electron lasers. *J. Phys. B*, 38(9): S799, 2005. doi: 10.1088/0953-4075/38/9/023. URL https://iopscience.iop.org/article/10.1088/0953-4075/38/9/023.

[212] Richard Neutze and Keith Moffat. Time-resolved structural studies at synchrotrons and x-ray free electron lasers: opportunities and challenges. *Current opinion in structural biology*, 22(5):651–659, October 2012.

[213] H. N. Chapman, A. Barty, M. J. Bogan, S. Boutet, S. Frank, S. P. Hau-Riege, S. Marchesini, B. W. Woods, S. Bajt, W. H. Benner, London W. A., E. Plönjes, M. Kuhlmann, R. Treusch, S. Düsterer, T. Tschentscher, J. R. Schneider, E. Spiller, T. Möller, C. Bostedt, M. Hoener, D. A. Shapiro, K. O. Hodgson, D. van der Spoel, F. Burmeister, M. Bergh, C. Caleman, G. Huldt, M. M. Seibert, F. R. N. C. Maia, R. W. Lee, A. Szöke, N. Timneanu, and J. Hajdu. Femtosecond diffractive imaging with a soft-x-ray free-electron laser. *Nat. Phys.*, 2:839–843, 2006. doi: 10.1038/nphys461. URL http://dx.doi.org/10.1038/nphys461.

[214] Jochen Küpper, Stephan Stern, Lotte Holmegaard, Frank Filsinger, Arnaud Rouzée, Artem Rudenko, Per Johnsson, Andrew V. Martin, Marcus Adolph, Andrew Aquila, Saša Bajt, Anton Barty, Christoph Bostedt, John Bozek, Carl Caleman, Ryan Coffee, Nicola Coppola, Tjark Delmas, Sascha Epp, Benjamin Erk, Lutz Foucar, Tais Gorkhover, Lars Gumprecht, Andreas Hartmann, Robert Hartmann, Günter Hauser, Peter Holl, Andre Hömke, Nils Kimmel, Faton Krasniqi, Kai-Uwe Kühnel, Jochen Maurer, Marc Messerschmidt, Robert Moshammer, Christian Reich, Benedikt Rudek, Robin Santra, Ilme Schlichting, Carlo Schmidt, Sebastian Schorb, Joachim Schulz, Heike Soltau, John C. H. Spence, Dmitri Starodub, Lothar Strüder, Jan Thøgersen, Marc J. J. Vrakking, Georg Weidenspointner, Thomas A. White, Cornelia Wunderer, Gerard Meijer, Joachim Ullrich, Henrik Stapelfeldt, Daniel Rolles, and Henry N. Chapman. X-ray diffraction from isolated and strongly aligned gas-phase molecules with a free-electron laser. *Phys. Rev. Lett.*, 112:083002, 2014. doi: 10.1103/PhysRevLett.112.083002. URL https://dx.doi.org/10.1103/PhysRevLett.112.083002.

[215] Henry N. Chapman, Carl Caleman, and Nicusor Timneanu. Diffraction before destruction. *Phil. Trans. R. Soc. B*, 369(1647):20130313, 2014. ISSN 0962-8436. doi: 10.1098/rstb.2013.0313. URL https://doi.org/10.1098/rstb.2013.0313.

[216] A Rudenko, L Inhester, K Hanasaki, X Li, S J Robatjazi, B Erk, R Boll, K Toyota, Y Hao, O Vendrell, C Bomme, E Savelyev, B Rudek, L Foucar, S H Southworth, C S Lehmann, B Kraessig, T Marchenko, M Simon, K Ueda, K R Ferguson, M Bucher, T Gorkhover, S Carron, R Alonso-Mori, J E Koglin, J Correa, G J Williams, S Boutet, L Young, C Bostedt, S K Son, R Santra, and D Rolles. Femtosecond response of polyatomic molecules to ultra-intense hard x-rays. *Nature*, 546(7656):129–132, 2017. doi: 10.1038/nature22373. URL https://doi.org/10.1038/nature22373.

[217] Egor Sobolev, Serguey Zolotarev, Klaus Giewekemeyer, Johan Bielecki, Kenta Okamoto, Hemanth K. N. Reddy, Jakob Andreasson, Kartik Ayyer, Imrich Barak, Sadia Bari, Anton Barty, Richard Bean, Sergey Bobkov, Henry N. Chapman, Grzegorz Chojnowski, Benedikt J. Daurer, Katerina Dörner, Tomas Ekeberg, Leonie Flückiger, Oxana Galzitskaya, Luca Gelisio, Steffen Hauf, Brenda G. Hogue, Daniel A. Horke, Ahmad Hosseinizadeh, Vyacheslav Ilyin, Chulho Jung, Chan Kim,

Yoonhee Kim, Richard A. Kirian, Henry Kirkwood, Olena Kulyk, Romain Letrun, Duane Loh, Marc Messerschmidt, Kerstin Mühlig, Abbas Ourmazd, Natascha Raab, Andrei V. Rode, Max Rose, Adam Round, Takushi Sato, Robin Schubert, Peter Schwander, Jonas A. Sellberg, Marcin Sikorski, Alessandro Silenzi, Changyong Song, John C. H. Spence, Stephan Stern, Jolanta Sztuk-Dambietz, Anthon Teslyuk, Nicusor Timneanu, Martin Trebbin, Charlotte Uetrecht, Britta Weinhausen, Garth J. Williams, P Lourdu Xavier, Chen Xu, Ivan Vartanyants, Victor Lamzin, Adrian Mancuso, and Filipe R. N. C. Maia. Megahertz single-particle imaging at the European XFEL. *Commun. Phys.*, 3:97, 2020. doi: 10.1038/s42005-020-0362-y.

[218] Jordan T. O'Neal, Elio G. Champenois, Solène Oberli, Razib Obaid, Andre Al-Haddad, Jonathan Barnard, Nora Berrah, Ryan Coffee, Joseph Duris, Gediminas Galinis, Douglas Garratt, James M. Glownia, Daniel Haxton, Phay Ho, Siqi Li, Xiang Li, James MacArthur, Jon P Marangos, Adi Natan, Niranjan Shivaram, Daniel S. Slaughter, Peter Walter, Scott Wandel, Linda Young, Christoph Bostedt, Philip H. Bucksbaum, Antonio Picón, Agostino Marinelli, and James P. Cryan. Electronic population transfer via impulsive stimulated x-ray raman scattering with attosecond soft-x-ray pulses. *Phys. Rev. Lett.*, 125(7):073203, 2020. doi: 10.1103/physrevlett.125.073203. URL `https://journals.aps.org/prl/abstract/10.1103/PhysRevLett.125.073203`.

[219] Rebecca Boll, Julia M. Schäfer, Benoît Richard, Kilian Fehre, Gregor Kastirke, Zoltan Jurek, Markus S. Schöffler, Malik M. Abdullah, Nils Anders, Thomas M. Baumann, Sebastian Eckart, Benjamin Erk, Alberto De Fanis, Reinhard Dörner, Sven Grundmann, Patrik Grychtol, Alexander Hartung, Max Hofmann, Markus Ilchen, Ludger Inhester, Christian Janke, Rui Jin, Max Kircher, Katharina Kubicek, Maksim Kunitski, Xiang Li, Tommaso Mazza, Severin Meister, Niklas Melzer, Jacobo Montano, Valerija Music, Giammarco Nalin, Yevheniy Ovcharenko, Christopher Passow, Andreas Pier, Nils Rennhack, Jonas Rist, Daniel E. Rivas, Daniel Rolles, Ilme Schlichting, Lothar Ph. H. Schmidt, Philipp Schmidt, Juliane Siebert, Nico Strenger, Daniel Trabert, Florian Trinter, Isabel Vela-Perez, Rene Wagner, Peter Walter, Miriam Weller, Pawel Ziolkowski, Sang-Kil Son, Artem Rudenko, Michael Meyer, Robin Santra, and Till Jahnke. X-ray multiphoton-induced Coulomb explosion images complex single molecules. *Nat. Phys.*, 18:423–428, 2022. doi: 10.1038/s41567-022-01507-0. URL `http://xfel.tind.io/record/2701`.

[220] C. Pellegrini, A. Marinelli, and S. Reiche. The physics of x-ray free-electron lasers. *Rev. Mod. Phys.*, 88:015006, 2016. doi: 10.1103/RevModPhys.88.015006. URL `https://doi.org/10.1103/RevModPhys.88.015006`.

[221] Nanshun Huang, Haixiao Deng, Bo Liu, Dong Wang, and Zhentang Zhao. Features and futures of x-ray free-electron lasers. *Innovation*, 2(2):100097, 2021. doi: 10.1016/j.xinn.2021.100097. URL `https://www.sciencedirect.com/science/article/pii/S2666675821000229?via%3Dihub`.

[222] N Hartmann, G Hartmann, R Heider, M S Wagner, M Ilchen, J Buck, A O Lindahl, C Benko, J Grünert, J Krzywinski, J Liu, A A Lutman, A Marinelli, T Maxwell, A A Miahnahri, S P Moeller, M Planas, J Robinson, A K Kazansky, N M Kabachnik, J Viefhaus, T Feurer, R Kienberger, R N Coffee, and W Helml. Attosecond time–energy structure of x-ray free-electron laser pulses. *Nat. Photon.*, 12:215–220, 2018. doi: 10.1038/s41566-018-0107-6.

[223] W. Decking, S. Abeghyan, P. Abramian, A. Abramsky, A. Aguirre, C. Albrecht, P. Alou, M. Altarelli, P. Altmann, K. Amyan, V. Anashin, E. Apostolov, K. Appel,

D. Auguste, V. Ayvazyan, S. Baark, F. Babies, N. Baboi, P. Bak, V. Balandin, R. Baldinger, B. Baranasic, S. Barbanotti, O. Belikov, V. Belokurov, L. Belova, V. Belyakov, S. Berry, M. Bertucci, B. Beutner, A. Block, M. Blöcher, T. Böckmann, C. Bohm, M. Böhnert, V. Bondar, E. Bondarchuk, M. Bonezzi, P. Borowiec, C. Bösch, U. Bösenberg, A. Bosotti, R. Böspflug, M. Bousonville, E. Boyd, Y. Bozhko, A. Brand, J. Branlard, S. Briechle, F. Brinker, S. Brinker, R. Brinkmann, S. Brockhauser, O. Brovko, H. Brück, A. Brüdgam, L. Butkowski, T. Büttner, J. Calero, E. Castro-Carballo, G. Cattalanotto, J. Charrier, J. Chen, A. Cherepenko, V. Cheskidov, M. Chiodini, A. Chong, S. Choroba, M. Chorowski, D. Churanov, W. Cichalewski, M. Clausen, W. Clement, C. Cloué, J. A. Cobos, N. Coppola, S. Cunis, K. Czuba, M. Czwalinna, B. D'Almagne, J. Dammann, H. Danared, A. de Zubiaurre Wagner, A. Delfs, T. Delfs, F. Dietrich, T. Dietrich, M. Dohlus, M. Dommach, A. Donat, X. Dong, N. Doynikov, M. Dressel, M. Duda, P. Duda, H. Eckoldt, W. Ehsan, J. Eidam, F. Eints, C. Engling, U. Englisch, A. Ermakov, K. Escherich, J. Eschke, E. Saldin, M. Faesing, A. Fallou, M. Felber, M. Fenner, B. Fernandes, J. M. Fernández, S. Feuker, K. Filippakopoulos, K. Floettmann, V. Fogel, M. Fontaine, A. Francés, I. Freijo Martin, W. Freund, T. Freyermuth, M. Friedland, L. Fröhlich, M. Fusetti, J. Fydrych, A. Gallas, O. García, L. Garcia-Tabares, G. Geloni, N. Gerasimova, C. Gerth, P. Geßler, V. Gharibyan, M. Gloor, J. Głowinkowski, A. Goessel, Z. Gołębiewski, N. Golubeva, W. Grabowski, W. Graeff, A. Grebentsov, M. Grecki, T. Grevsmuehl, M. Gross, U. Grosse-Wortmann, J. Grünert, S. Grunewald, P. Grzegory, G. Feng, H. Guler, G. Gusev, J. L. Gutierrez, L. Hagge, M. Hamberg, R. Hanneken, E. Harms, I. Hartl, A. Hauberg, S. Hauf, J. Hauschildt, J. Hauser, J. Havlicek, A. Hedqvist, N. Heidbrook, F. Hellberg, D. Henning, O. Hensler, T. Hermann, A. Hidvégi, M. Hierholzer, H. Hintz, F. Hoffmann, Markus Hoffmann, Matthias Hoffmann, Y. Holler, M. Hüning, A. Ignatenko, M. Ilchen, A. Iluk, J. Iversen, J. Iversen, M. Izquierdo, L. Jachmann, N. Jardon, U. Jastrow, K. Jensch, J. Jensen, M. Jeżabek, M. Jidda, H. Jin, N. Johansson, R. Jonas, W. Kaabi, D. Kaefer, R. Kammering, H. Kapitza, S. Karabekyan, S. Karstensen, K. Kasprzak, V. Katalev, D. Keese, B. Keil, M. Kholopov, M. Killenberger, B. Kitaev, Y. Klimchenko, R. Klos, L. Knebel, A. Koch, M. Koepke, S. Köhler, W. Köhler, N. Kohlstrunk, Z. Konopkova, A. Konstantinov, W. Kook, W. Koprek, M. Körfer, O. Korth, A. Kosarev, K. Kosiński, D. Kostin, Y. Kot, A. Kotarba, T. Kozak, V. Kozak, R. Kramert, M. Krasilnikov, A. Krasnov, B. Krause, L. Kravchuk, O. Krebs, R. Kretschmer, J. Kreutzkamp, O. Kröplin, K. Krzysik, G. Kube, H. Kuehn, N. Kujala, V. Kulikov, V. Kuzminych, D. La Civita, M. Lacroix, T. Lamb, A. Lancetov, M. Larsson, D. Le Pinvidic, S. Lederer, T. Lensch, D. Lenz, A. Leuschner, F. Levenhagen, Y. Li, J. Liebing, L. Lilje, T. Limberg, D. Lipka, B. List, J. Liu, S. Liu, B. Lorbeer, J. Lorkiewicz, H. H. Lu, F. Ludwig, K. Machau, W. Maciocha, C. Madec, C. Magueur, C. Maiano, I. Maksimova, K. Malcher, T. Maltezopoulos, E. Mamoshkina, B. Manschwetus, F. Marcellini, G. Marinkovic, T. Martinez, H. Martirosyan, W. Maschmann, M. Maslov, A. Matheisen, U. Mavric, J. Meißner, K. Meissner, M. Messerschmidt, N. Meyners, G. Michalski, P. Michelato, N. Mildner, M. Moe, F. Moglia, C. Mohr, S. Mohr, W. Möller, M. Mommerz, L. Monaco, C. Montiel, M. Moretti, I. Morozov, P. Morozov, D. Mross, J. Mueller, C. Müller, J. Müller, K. Müller, J. Munilla, A. Münnich, V. Muratov, O. Napoly, B. Näser, N. Nefedov, Reinhard Neumann, Rudolf Neumann, N. Ngada, D. Noelle, F. Obier, I. Okunev, J. A. Oliver, M. Omet, A. Oppelt, A. Ottmar, M. Oublaid, C. Pagani,

R. Paparella, V. Paramonov, C. Peitzmann, J. Penning, A. Perus, F. Peters, B. Petersen, A. Petrov, I. Petrov, S. Pfeiffer, J. Pflüger, S. Philipp, Y. Pienaud, P. Pierini, S. Pivovarov, M. Planas, E. Pławski, M. Pohl, J. Polinski, V. Popov, S. Prat, J. Prenting, G. Priebe, H. Pryschelski, K. Przygoda, E. Pyata, B. Racky, A. Rathjen, W. Ratuschni, S. Regnaud-Campderros, K. Rehlich, D. Reschke, C. Robson, J. Roever, M. Roggli, J. Rothenburg, E. Rusiński, R. Rybaniec, H. Sahling, M. Salmani, L. Samoylova, D. Sanzone, F. Saretzki, O. Sawlanski, J. Schaffran, H. Schlarb, M. Schlösser, V. Schlott, C. Schmidt, F. Schmidt-Foehre, M. Schmitz, M. Schmökel, T. Schnautz, E. Schneidmiller, M. Scholz, B. Schöneburg, J. Schultze, C. Schulz, A. Schwarz, J. Sekutowicz, D. Sellmann, E. Semenov, S. Serkez, D. Sertore, N. Shehzad, P. Shemarykin, L. Shi, M. Sienkiewicz, D. Sikora, M. Sikorski, A. Silenzi, C. Simon, W. Singer, X. Singer, H. Sinn, K. Sinram, N. Skvorodnev, P. Smirnow, T. Sommer, A. Sorokin, M. Stadler, M. Steckel, B. Steffen, N. Steinhau-Kühl, F. Stephan, M. Stodulski, M. Stolper, A. Sulimov, R. Susen, J. Świerblewski, C. Sydlo, E. Syresin, V. Sytchev, J. Szuba, N. Tesch, J. Thie, A. Thiebault, K. Tiedtke, D. Tischhauser, J. Tolkiehn, S. Tomin, F. Tonisch, F. Toral, I. Torbin, A. Trapp, D. Treyer, G. Trowitzsch, T. Trublet, T. Tschentscher, F. Ullrich, M. Vannoni, P. Varela, G. Varghese, G. Vashchenko, M. Vasic, C. Vazquez-Velez, A. Verguet, S. Vilcins-Czvitkovits, R. Villanueva, B. Visentin, M. Viti, E. Vogel, E. Volobuev, R. Wagner, N. Walker, T. Wamsat, H. Weddig, G. Weichert, H. Weise, R. Wenndorf, M. Werner, R. Wichmann, C. Wiebers, M. Wiencek, T. Wilksen, I. Will, L. Winkelmann, M. Winkowski, K. Wittenburg, A. Witzig, P. Wlk, T. Wohlenberg, M. Wojciechowski, F. Wolff-Fabris, G. Wrochna, K. Wrona, M. Yakopov, B. Yang, F. Yang, M. Yurkov, I. Zagorodnov, P. Zalden, A. Zavadtsev, D. Zavadtsev, A. Zhirnov, A. Zhukov, V. Ziemann, A. Zolotov, N. Zolotukhina, F. Zummack, and D. Zybin. A MHz-repetition-rate hard x-ray free-electron laser driven by a superconducting linear accelerator. *Nat. Photon.*, 14(6):391–397, June 2020. ISSN 1749-4893. doi: 10.1038/s41566-020-0607-z. URL `https://doi.org/10.1038/s41566-020-0607-z`.

[224] W Ackermann, G Asova, V Ayvazyan, A Azima, N Baboi, J Bähr, V Balandin, B Beutner, A Brandt, A Bolzmann, R Brinkmann, O I Brovko, M Castellano, P Castro, L Catani, E Chiadroni, S Choroba, A Cianchi, J T Costello, D Cubaynes, J Dardis, W Decking, H Delsim-Hashemi, A Delserieys, G Di Pirro, M Dohlus, S Düsterer, A Eckhardt, H T Edwards, B Faatz, J Feldhaus, K Flöttmann, J Frisch, L Fröhlich, T Garvey, U Gensch, Ch Gerth, M Görler, N Golubeva, H J Grabosch, M Grecki, O Grimm, K Hacker, U Hahn, J H Han, K Honkavaara, T Hott, M Hüning, Y Ivanisenko, E Jaeschke, W Jalmuzna, T Jezynski, R Kammering, V Katalev, K Kavanagh, E T Kennedy, S Khodyachykh, K Klose, V Kocharyan, M Körfer, M Kollewe, W Koprek, S Korepanov, D Kostin, M Krassilnikov, G Kube, M Kuhlmann, C L S Lewis, L Lilje, T Limberg, D Lipka, F Löhl, H Luna, M Luong, M Martins, M Meyer, P Michelato, V Miltchev, W D Möller, L Monaco, W F O Müller, O Napieralski, O Napoly, P Nicolosi, D Nölle, T Nuñez, A Oppelt, C Pagani, R Paparella, N Pchalek, J Pedregosa-Gutierrez, B Petersen, B Petrosyan, G Petrosyan, L Petrosyan, J Pflüger, E Plönjes, L Poletto, K Pozniak, E Prat, D Proch, P Pucyk, P Radcliffe, H Redlin, K Rehlich, M Richter, M Roehrs, J Roensch, R Romaniuk, M Ross, J Rossbach, V Rybnikov, M Sachwitz, E L Saldin, W Sandner, H Schlarb, B Schmidt, M Schmitz, P Schmüser, J R Schneider, E A Schneidmiller, S Schnepp, S Schreiber, M Seidel, D Sertore, A V Shabunov, C Simon, S Simrock,

E Sombrowski, A A Sorokin, P Spanknebel, R Spesyvtsev, L Staykov, B Steffen, F Stephan, F Stulle, H Thom, K Tiedtke, M Tischer, S Toleikis, R Treusch, D Trines, I Tsakov, E Vogel, T Weiland, H Weise, M Wellhöfer, M Wendt, I Will, A Winter, K Wittenburg, W Wurth, P Yeates, M V Yurkov, I Zagorodnov, and K Zapfe. Operation of a free-electron laser from the extreme ultraviolet to the water window. *Nat. Photon.*, 1(6):336–342, June 2007. doi: 10.1038/nphoton.2007.76. URL `http://www.nature.com/doifinder/10.1038/nphoton.2007.76`.

[225] Thomas Tschentscher, Christian Bressler, Jan Grünert, Anders Madsen, Adrian P. Mancuso, Michael Meyer, Andreas Scherz, Harald Sinn, and Ulf Zastrau. Photon beam transport and scientific instruments at the European XFEL. *Appl. Sci.*, 7(6): 592, 2017. doi: 10.3390/app7060592.

[226] P Abbamonte, Frank Abild-Pedersen, P Adams, M Ahmed, F Albert, R Mori, P Anfinrud, A Aquila, M Armstrong, J Arthur, J Bargar, A Barty, U Bergmann, N Berrah, G Blaj, H Bluhm, C Bolme, C Bostedt, S Boutet, G Brown, P Bucksbaum, M Cargnello, G Carini, A Cavalleri, V Cherezov, W Chiu, Y Chuang, D Cocco, R Coffee, G Collins, A Cordones-Hahn, J Cryan, G Dakovski, M Dantus, H Demirci, P Denes, T Devereaux, Y Ding, S Doniach, R Dorner, M Dunne, H Durr, T Egami, D Eisenberg, P Emma, C Fadley, R Falcone, Y Feng, P Fischer, F Fiuza, L Fletcher, L Foucar, M Frank, J Fraser, H Frei, D Fritz, P Fromme, A Fry, M Fuchs, P Fuoss, K Gaffney, E Gamboa, O Gessner, S Ghimire, A Gleason, S Glenzer, T Gorkhover, A Gray, M Guehr, J Guo, J Hajdu, S Hansen, P Hart, M Hashimoto, J Hastings, D Haxton, P Heimann, T Heinz, A Hexemer, J Hill, F Himpsel, P Ho, B Hogue, Z Huang, M Hunter, G Hura, N Huse, Z Hussain, M Ilchen, C Jacobsen, C Kenney, J Kern, S Kevan, J Kim, H Kim, P Kirchmann, R Kirian, S Kivelson, C Kliewer, J Koralek, G Kovacsova, A Lanzara, J LaRue, H Lee, J Lee, W Lee, Y Lee, I Lindau, A Lindenberg, Z Liu, D Lu, U Lundstrom, A MacDowell, W Mao, J Marangos, G Marcus, T Martinez, W McCurdy, G McDermott, C McGuffey, M Minitti, S Miyabe, S Moeller, R Moore, S Mukamel, K Nass, A Natan, K Nelson, S Nemsak, D Neumark, R Neutze, A Nilsson, D Nordlund, J Norskov, S Nozawa, H Ogasawara, H Ohldag, A Orville, D Osborn, T Osipov, A Ourmazd, D Parkinson, C Pellegrini, G Phillips, T Rasing, T Raubenheimer, T Recigno, A Reid, D Reis, A Robert, J Robinson, D Rolles, J Rost, S Roy, A Rudenko, T Russell, R Sandberg, A Sandhu, N Sauter, I Schlichting, R Schlogl, W Schlotter, M Schmidt, J Schneider, R Schoenlein, M Schoeffler, A Scholl, Z Shen, O Shpyrko, T Silva, S Sinha, D Slaughter, J Sobota, D Sokaras, K Sokolowski-Tinten, S Southworth, J Spence, C Stan, J Stohr, R Stroud, V Sundstrom, C Taatjes, A Thomas, M Trigo, Y Tsui, J Turner, A van Buuren, S Vinko, S Wakatsuki, J Wark, P Weber, T Weber, M Wei, T Weiss, P Wernet, W White, P Willmott, K Wilson, W Wurth, V Yachandra, J Yano, D Yarotski, L Young, Y Zhu, D Zhu, and P Zwart. New science opportunities enabled by LCLS-II x-ray lasers. Technical Report SLAC-R-1053, SLAC National Accelerator Laboratory, Menlo Park, CA, USA, June 2015. URL `https://www.osti.gov/biblio/1630267`.

[227] Linda Young, Kiyoshi Ueda, Markus Gühr, Philip H Bucksbaum, Marc Simon, Shaul Mukamel, Nina Rohringer, Kevin C Prince, Claudio Masciovecchio, Michael Meyer, Artem Rudenko, Daniel Rolles, Christoph Bostedt, Matthias Fuchs, David A Reis, Robin Santra, Henry Kapteyn, Margaret Murnane, Heide Ibrahim, François Légaré, Marc J J Vrakking, Marcus Isinger, David Kroon, Mathieu Gisselbrecht, Anne L'Huillier, Hans Jakob Wörner, and Stephen R Leone. Roadmap of ultrafast

x-ray atomic and molecular physics. *J. Phys. B*, 51(3):032003, 2018. doi: 10.1088/1361-6455/aa9735. URL http://iopscience.iop.org/article/10.1088/1361-6455/aa9735.

[228] K Tiedtke, A Azima, N von Bargen, L Bittner, S Bonfigt, S Düsterer, B Faatz, U Frühling, M Gensch, Ch Gerth, N Guerassimova, U Hahn, T Hans, M Hesse, K Honkavaar, U Jastrow, P Juranic, S Kapitzki, B Keitel, T Kracht, M Kuhlmann, W B Li, M Martins, T Núñez, E Plönjes, H Redlin, E L Saldin, E A Schneidmiller, J R Schneider, S Schreiber, N Stojanovic, F Tavella, S Toleikis, R Treusch, H Weigelt, M Wellhöfer, H Wabnitz, M V Yurkov, and J Feldhaus. The soft x-ray free-electron laser FLASH at DESY: beamlines, diagnostics and end-stations. *New J. Phys.*, 11(2):023029, feb 2009. doi: 10.1088/1367-2630/11/2/023029. URL https://doi.org/10.1088/1367-2630/11/2/023029.

[229] P Emma, R Akre, J Arthur, R Bionta, C Bostedt, J Bozek, A Brachmann, P Bucksbaum, R Coffee, F J Decker, Y Ding, D Dowell, S Edstrom, A Fisher, J Frisch, S Gilevich, J Hastings, G Hays, Ph Hering, Z Huang, R Iverson, H Loos, M Messerschmidt, A Miahnahri, S Moeller, H D Nuhn, G Pile, D Ratner, J Rzepiela, D Schultz, T Smith, P Stefan, H Tompkins, J Turner, J Welch, W White, J Wu, G Yocky, and J Galayda. First lasing and operation of an ångstrom-wavelength free-electron laser. *Nat. Photon.*, 4:641–647, Jul 2010. doi: 10.1038/nphoton.2010.176. URL http://www.nature.com/nphoton/journal/vaop/ncurrent/abs/nphoton.2010.176.html.

[230] H. Franz, O. Leupold, R. Röhlsberger, S. V. Roth, O. H. Seeck, J. Spengler, J. Strempfer, M. Tischer, J. Viefhaus, E. Weckert, and T. Wroblewski. Technical report: PETRA III: DESY's new high brilliance third generation synchrotron radiation source. *Synchrotron Radiat. News*, 19(6):25–29, December 2006. ISSN 0894-0886. doi: 10.1080/08940880601064984. URL http://dx.doi.org/10.1080/08940880601064984.

[231] G. Cerullo and S. De Silvestri. Ultrafast optical parametric amplifiers. *Rev. Sci. Instrum.*, 74:1–18, 2003. doi: 10.1063/1.1523642. URL https://doi.org/10.1063/1.1523642.

[232] Mikayel Musheghyan, Prabhash Prasannan Geetha, Davide Faccial, Aditya Pusala, Gabriele Crippa, Andrea Campolo, Anna G. Ciriolo, Michele Devetta, Andreas Assion, Cristian Manzoni, Caterina Vozzi, and Salvatore Stagira. Tunable, few-cycle, CEP-stable mid-IR optical parametric amplifier for strong field applications. *J. Phys. B*, 53(18):185402, 2020. ISSN 13616455. doi: 10.1088/1361-6455/aba127. URL https://dx.doi.org/10.1088/1361-6455/aba127.

[233] Katalin Mecseki, Matthew K. R. Windeler, Alan Miahnahri, Joseph S. Robinson, James M. Fraser, Alan R. Fry, and Franz Tavella. High average power 88 W OPCPA system for high-repetition-rate experiments at the LCLS x-ray free-electron laser. *Opt. Lett.*, 44(5):1257–1260, March 2019. doi: 10.1364/OL.44.001257. URL http://ol.osa.org/abstract.cfm?URI=ol-44-5-1257.

[234] Benjamin Wolter, Michael G. Pullen, Matthias Baudisch, Michele Sclafani, Michaël Hemmer, Arne Senftleben, Claus Dieter Schröter, Joachim Ullrich, Robert Moshammer, and Jens Biegert. Strong-field physics with mid-IR fields. *Phys. Rev. X*, 5:021034, Jun 2015. doi: 10.1103/PhysRevX.5.021034. URL https://link.aps.org/doi/10.1103/PhysRevX.5.021034.

[235] F. Krausz and M. Ivanov. Attosecond physics. *Rev. Mod. Phys.*, 81(1):163, 2009. URL https://doi.org/10.1103/RevModPhys.81.163.

[236] Mauro Nisoli, Piero Decleva, Francesca Calegari, Alicia Palacios, and Fernando Martín. Attosecond electron dynamics in molecules. *Chem. Rev.*, 117(16):10760–10825, 2017. doi: 10.1021/acs.chemrev.6b00453. URL https://pubs.acs.org/doi/10.1021/acs.chemrev.6b00453.

[237] F Calegari, D Ayuso, A Trabattoni, L Belshaw, S De Camillis, S Anumula, F Frassetto, L Poletto, A Palacios, P Decleva, J B Greenwood, F Martín, and M Nisoli. Ultrafast electron dynamics in phenylalanine initiated by attosecond pulses. *Science*, 346(6207):336–339, October 2014. doi: 10.1126/science.1254061. URL http://science.sciencemag.org/content/346/6207/336.full.

[238] Henry N. Chapman. X-ray imaging beyond the limits. *Nature Mater.*, 8(4):299–301, 2009. doi: 10.1038/nmat2402. URL http://dx.doi.org/10.1038/nmat2402.

[239] Henry N Chapman, Petra Fromme, Anton Barty, Thomas A White, Richard A Kirian, Andrew Aquila, Mark S Hunter, Joachim Schulz, Daniel P Deponte, Uwe Weierstall, R Bruce Doak, Filipe R N C Maia, Andrew V Martin, Ilme Schlichting, Lukas Lomb, Nicola Coppola, Robert L Shoeman, Sascha W Epp, Robert Hartmann, Daniel Rolles, Artem Rudenko, Lutz Foucar, Nils Kimmel, Georg Weidenspointner, Peter Holl, Mengning Liang, Miriam Barthelmess, Carl Caleman, Sébastien Boutet, Michael J Bogan, Jacek Krzywinski, Christoph Bostedt, Saša Bajt, Lars Gumprecht, Benedikt Rudek, Benjamin Erk, Carlo Schmidt, André Hömke, Christian Reich, Daniel Pietschner, Lothar Strüder, Günter Hauser, Hubert Gorke, Joachim Ullrich, Sven Herrmann, Gerhard Schaller, Florian Schopper, Heike Soltau, Kai-Uwe Kühnel, Marc Messerschmidt, John D Bozek, Stefan P Hau-Riege, Matthias Frank, Christina Y Hampton, Raymond G Sierra, Dmitri Starodub, Garth J Williams, Janos Hajdu, Nicusor Timneanu, M Marvin Seibert, Jakob Andreasson, Andrea Rocker, Olof Jönsson, Martin Svenda, Stephan Stern, Karol Nass, Robert Andritschke, Claus-Dieter Schröter, Faton Krasniqi, Mario Bott, Kevin E Schmidt, Xiaoyu Wang, Ingo Grotjohann, James M Holton, Thomas R M Barends, Richard Neutze, Stefano Marchesini, Raimund Fromme, Sebastian Schorb, Daniela Rupp, Marcus Adolph, Tais Gorkhover, Inger Andersson, Helmut Hirsemann, Guillaume Potdevin, Heinz Graafsma, Björn Nilsson, and John C H Spence. Femtosecond x-ray protein nanocrystallography. *Nature*, 470(7332):73–77, Feb 2011. doi: 10.1038/nature09750. URL http://www.nature.com/nature/journal/v470/n7332/full/nature09750.html.

[240] Joyce Woodhouse, Gabriela Nass Kovacs, Nicolas Coquelle, Lucas M. Uriarte, Virgile Adam, Thomas R. M. Barends, Martin Byrdin, Eugenio de la Mora, R. Bruce Doak, Mikolaj Feliks, Martin Field, Franck Fieschi, Virginia Guillon, Stefan Jakobs, Yasumasa Joti, Pauline Macheboeuf, Koji Motomura, Karol Nass, Shigeki Owada, Christopher M. Roome, Cyril Ruckebusch, Giorgio Schirò, Robert L. Shoeman, Michel Thepaut, Tadashi Togashi, Kensuke Tono, Makina Yabashi, Marco Cammarata, Lutz Foucar, Dominique Bourgeois, Michel Sliwa, Jacques-Philippe Colletier, Ilme Schlichting, and Martin Weik. Photoswitching mechanism of a fluorescent protein revealed by time-resolved crystallography and transient absorption spectroscopy. *Nat. Commun.*, 11(1):741, 2020. doi: 10.1038/s41467-020-14537-0. URL https://www.nature.com/articles/s41467-020-14537-0.

[241] Anton Barty, Jochen Küpper, and Henry N. Chapman. Molecular imaging using x-ray free-electron lasers. *Annu. Rev. Phys. Chem.*, 64(1):415–435, April 2013. doi: 10.1146/annurev-physchem-032511-143708. URL http://dx.doi.org/10.1146/

annurev-physchem-032511-143708.

[242] L Young, E P Kanter, Bertold Kraessig, Y Li, A M March, S T Pratt, R Santra, S. H. Southworth, N Rohringer, L F DiMauro, Gilles Doumy, C A Roedig, N Berrah, L Fang, M Hoener, P H Bucksbaum, J P Cryan, S Ghimire, J M Glownia, D A Reis, J D Bozek, C Bostedt, and M Messerschmidt. Femtosecond electronic response of atoms to ultra-intense x-rays. *Nature*, 466(7302):56, 2010. doi: 10.1038/nature09177. URL http://dx.doi.org/10.1038/nature09177.

[243] Benedikt Rudek, Sang-Kil Son, Lutz Foucar, Sascha-W. Epp, Benjamin Erk, Robert Hartmann, Marcus Adolph, Robert Andritschke, Andrew Aquila, Nora Berrah, Christoph Bostedt, John Bozek, Nicola Coppola, Frank Filsinger, Hubert Gorke, Tais Gorkhover, Heinz Graafsma, Lars Gumprecht, Andreas Hartmann, Günter Hauser, Sven Herrmann, Helmut Hirsemann, Peter Holl, Andre Hömke, Loic Journel, Christian Kaiser, Nils Kimmel, Faton Krasniqi, Kai-Uwe Kühnel, Michael Matysek, Marc Messerschmidt, Danilo Miesner, Thomas Möller, Robert Moshammer, Kiyonobu Nagaya, Bjorn Nilsson, Guillaume Potdevin, Daniel Pietschner, Christian Reich, Daniela Rupp, Gerhard Schaller, Ilme Schlichting, Carlo Schmidt, Florian Schopper, Sebastian Schorb, Claus-Dieter Schröter, Joachim Schulz, Marc Simon, Heike Soltau, Lothar Strüder, Kiyoshi Ueda, Georg Weidenspointner, Robin Santra, Joachim Ullrich, Artem Rudenko, and Daniel Rolles. Ultra-efficient ionization of heavy atoms by intense x-ray free-electron laser pulses. *Nat. Photon.*, 6:858–865, Nov 2012. ISSN 1749-4893. doi: 10.1038/nphoton.2012.261. URL http://dx.doi.org/10.1038/nphoton.2012.261.

[244] U. Eichmann, H. Rottke, S. Meise, J.-E. Rubensson, J. Söderström, M. Agåker, C. Såthe, M. Meyer, T. M. Baumann, R. Boll, A. De Fanis, P. Grychtol, M. Ilchen, T. Mazza, J. Montano, V. Music, Y. Ovcharenko, D. E. Rivas, S. Serkez, R. Wagner, and S. Eisebitt. Photon-recoil imaging: Expanding the view of nonlinear x-ray physics. *Science*, 369(6511):1630–1633, 2020. doi: 10.1126/science.abc2622. URL https://www.science.org/doi/abs/10.1126/science.abc2622.

[245] X. Li, L. Inhester, S. J. Robatjazi, B. Erk, R. Boll, K. Hanasaki, K. Toyota, Y. Hao, C. Bomme, B. Rudek, L. Foucar, S. H. Southworth, C. S. Lehmann, B. Kraessig, T. Marchenko, M. Simon, K. Ueda, K. R. Ferguson, M. Bucher, T. Gorkhover, S. Carron, R. Alonso-Mori, J. E. Koglin, J. Correa, G. J. Williams, S. Boutet, L. Young, C. Bostedt, S.-K. Son, R. Santra, D. Rolles, and A. Rudenko. Pulse energy and pulse duration effects in the ionization and fragmentation of iodomethane by ultraintense hard x rays. *Phys. Rev. Lett.*, 127:093202, Aug 2021. doi: 10.1103/PhysRevLett.127.093202. URL https://link.aps.org/doi/10.1103/PhysRevLett.127.093202.

[246] K. Fehre, N. M. Novikovskiy, S. Grundmann, G. Kastirke, S. Eckart, F. Trinter, J. Rist, A. Hartung, D. Trabert, C. Janke, G. Nalin, M. Pitzer, S. Zeller, F. Wiegandt, M. Weller, M. Kircher, M. Hofmann, L. Ph. H. Schmidt, A. Knie, A. Hans, L. Ben Ltaief, A. Ehresmann, R. Berger, H. Fukuzawa, K. Ueda, H. Schmidt-Böcking, J. B. Williams, T. Jahnke, R. Dörner, M. S. Schöffler, and Ph. V. Demekhin. Fourfold differential photoelectron circular dichroism. *Phys. Rev. Lett.*, 127:103201, Sep 2021. doi: 10.1103/PhysRevLett.127.103201. URL https://link.aps.org/doi/10.1103/PhysRevLett.127.103201.

[247] Lincoln D Carr, David DeMille, Roman V Krems, and Jun Ye. Cold and ultracold molecules: science, technology and applications. *New J. Phys.*, 11(5):055049, may 2009. doi: 10.1088/1367-2630/11/5/055049. URL https://doi.org/10.1088%2F1367-2630%2F11%2F5%2F055049.

[248] Sebastiaan Y. T. van de Meerakker, Hendrick L. Bethlem, and Gerard Meijer. Taming molecular beams. *Nat. Phys.*, 4(8):595–620, Aug 2008. doi: 10.1038/nphys1031. URL http://dx.doi.org/10.1038/nphys1031.

[249] Michal Fárník. Bridging gaps between clusters in molecular-beam experiments and aerosol nanoclusters. *J. Phys. Chem. Lett.*, 14(1):287–294, 2023. doi: 10.1021/acs.jpclett.2c03417. URL https://doi.org/10.1021/acs.jpclett.2c03417.

[250] Alexander A. Milner, Jordan A. M. Fordyce, Ian MacPhail-Bartley, Walter Wasserman, Valery Milner, Ilia Tutunnikov, and Ilya Sh. Averbukh. Controlled enantioselective orientation of chiral molecules with an optical centrifuge. *Phys. Rev. Lett.*, 122(22):223201, June 2019. doi: 10.1103/physrevlett.122.223201. URL https://doi.org/10.1103/physrevlett.122.223201.

[251] Frank Filsinger, Undine Erlekam, Gert von Helden, Jochen Küpper, and Gerard Meijer. Selector for structural isomers of neutral molecules. *Phys. Rev. Lett.*, 100: 133003, 2008. doi: 10.1103/PhysRevLett.100.133003. URL http://dx.doi.org/10.1103/PhysRevLett.100.133003.

[252] J Ullrich, R Moshammer, A Dorn, R Dörner, L Ph H Schmidt, and H Schmidt-Böcking. Recoil-ion and electron momentum spectroscopy: Reaction-microscopes. *Rep. Prog. Phys.*, 66(9):1463–1545, 2003. doi: 10.1088/0034-4885/66/9/203. URL https://dx.doi.org/10.1088/0034-4885/66/9/203.

[253] L J Frasinski, K Codling, and P A Hatherly. Covariance mapping: a correlation method applied to multiphoton multiple ionization. *Science*, 246(4933):1029–1031, November 1989. doi: 10.1126/science.246.4933.1029. URL http://www.sciencemag.org/cgi/doi/10.1126/science.246.4933.1029.

[254] Andras Bodi, Patrick Hemberger, Thomas Gerber, and Bálint Sztáray. A new double imaging velocity focusing coincidence experiment: i^2PEPICO. *Rev. Sci. Instrum.*, 83(8):083105, 2012. doi: 10.1063/1.4742769. URL https://doi.org/10.1063/1.4742769.

[255] Daniel Wood, Robert J. Burleigh, Natasha Smith, Daniela Bortoletto, Mark Brouard, Michael Burt, Andrei Nomerotski, Richard Plackett, and Ian Shipsey. Ion microscope imaging mass spectrometry using a Timepix3-based optical camera. *J. Am. Soc. Mass Spectrom.*, 33(12):2328–2332, 2022. doi: 10.1021/jasms.2c00223. URL https://pubs.acs.org/doi/10.1021/jasms.2c00223.

[256] Jochen Küpper, Henrik Haak, Kirstin Wohlfart, and Gerard Meijer. Compact in-place gate valve for molecular-beam experiments. *Rev. Sci. Instrum.*, 77(1):016106, 2006. doi: 10.1063/1.2162456. URL http://dx.doi.org/10.1063/1.2162456.

[257] Sebastian Trippel, Terry G. Mullins, Nele L. M. Müller, Jens S. Kienitz, Karol Długołęcki, and Jochen Küpper. Strongly aligned and oriented molecular samples at a kHz repetition rate. *Mol. Phys.*, 111:1738, 2013. doi: 10.1080/00268976.2013.780334. URL http://dx.doi.org/10.1080/00268976.2013.780334.

[258] Sebastian Trippel, Melby Johny, Thomas Kierspel, Jolijn Onvlee, Helen Bieker, Hong Ye, Terry Mullins, Lars Gumprecht, Karol Długołęcki, and Jochen Küpper. Note: Knife edge skimming for improved separation of molecular species by the deflector. *Rev. Sci. Instrum.*, 89:096110, September 2018. doi: 10.1063/1.5026145. URL https://doi.org/10.1063/1.5026145.

[259] B. Winter, S. J. King, M. Brouard, and C. Vallance. A fast microchannel plate-scintillator detector for velocity map imaging and imaging mass spectrometry. *Rev. Sci. Instrum.*, 85(2):023306, 2014. ISSN 0034-6748. doi: 10.1063/1.4866647.

URL https://aip.scitation.org/doi/10.1063/1.4866647.

[260] M. Takahashi, J. P. Cave, and J. H. D. Eland. Velocity imaging photoionization coincidence apparatus for the study of angular correlations between electrons and fragment ions. *Rev. Sci. Instrum.*, 71(3):1337–1344, 2000. doi: 10.1063/1.1150460. URL https://doi.org/10.1063/1.1150460.

[261] CFEL Controlled Molecule Imaging. PymePix. Code repository, URL: https://gitlab.desy.de/CMI/CMI-public/pymepix, 2024. URL https://gitlab.desy.de/CMI/CMI-public/pymepix.

[262] Chuan Cheng, Gönenç Moğol, Thomas Weinacht, Andrei Nomerotski, and Carlos Trallero-Herrero. 3D velocity map imaging of electrons with TPX3CAM. *Rev. Sci. Instrum.*, 93(1):013003, 2022. doi: 10.1063/5.0071804. URL https://doi.org/10.1063/5.0071804.

[263] Hubertus Bromberger, David Pennicard, Rafael Ballabriga, Sebastian Trippel, and Jochen Küpper. Timepix3: single-pixel multi-hit energy-measurement behaviour. *J. Instrum.*, 19(11):P11008, nov 2024. doi: 10.1088/1748-0221/19/11/P11008. URL https://dx.doi.org/10.1088/1748-0221/19/11/P11008.

[264] Joss Wiese, Jean-François Olivieri, Andrea Trabattoni, Sebastian Trippel, and Jochen Küpper. Strong-field photoelectron momentum imaging of OCS at finely resolved incident intensities. *New J. Phys.*, 21:083011, August 2019. doi: 10.1088/1367-2630/ab34e8.

[265] S. Trippel, T. Mullins, N. L. M. Müller, J. S. Kienitz, R. González-Férez, and J. Küpper. Two-state wave packet for strong field-free molecular orientation. *Phys. Rev. Lett.*, 114:103003, 2015. doi: 10.1103/PhysRevLett.114.103003. URL https://dx.doi.org/10.1103/PhysRevLett.114.103003.

[266] S M Hankin, D M Villeneuve, P B Corkum, and D M Rayner. Intense-field laser ionization rates in atoms and molecules. *Phys. Rev. A*, 64(1):013405, 2001. doi: 10.1103/PhysRevA.64.013405. URL https://doi.org/10.1103/PhysRevA.64.013405.

[267] Mahdi Yousefi, Peter F Bernath, Chris D Boone, and Geoffrey C Toon. Global measurements of atmospheric carbonyl sulfide (OCS), $OC^{34}S$ and $O^{13}CS$. *J. Quant. Spectrosc. Radiat. Transf.*, 238:106554, 2019. doi: 10.1016/j.jqsrt.2019.06.033. URL https://www.sciencedirect.com/science/article/pii/S0022407319301402.

[268] Felix Allum, Valerija Music, Ludger Inhester, Rebecca Boll, Benjamin Erk, Philipp Schmidt, Thomas M. Baumann, Günter Brenner, Michael Burt, Philipp V. Demekhin, Simon Dörner, Arno Ehresmann, Andreas Galler, Patrik Grychtol, David Heathcote, Denis Kargin, Mats Larsson, Jason W. L. Lee, Zheng Li, Bastian Manschwetus, Lutz Marder, Robert Mason, Michael Meyer, Huda Otto, Christopher Passow, Rudolf Pietschnig, Daniel Ramm, Kaja Schubert, Lucas Schwob, Richard D. Thomas, Claire Vallance, Igor Vidanović, Clemens von Korff Schmising, René Wagner, Peter Walter, Vitali Zhaunerchyk, Daniel Rolles, Sadia Bari, Mark Brouard, and Markus Ilchen. A localized view on molecular dissociation via electron-ion partial covariance. *Commun. Chem.*, 5(1):42, 2022. doi: 10.1038/s42004-022-00656-w. URL https://www.nature.com/articles/s42004-022-00656-w.

[269] Mark Brouard and Claire Vallance, editors. *Tutorials in Molecular Reaction Dynamics*. The Royal Society of Chemistry, 2012. ISBN 978-1-84973-530-8. URL https:

//pubs.rsc.org/en/content/ebook/978-1-84973-530-8.

[270] C R Gebhardt, T P Rakitzis, P C Samartzis, V Ladopoulos, and T N Kitsopoulos. Slice imaging: A new approach to ion imaging and velocity mapping. *Rev. Sci. Instrum.*, 72(10):3848–3853, October 2001. doi: 10.1063/1.1403010.

[271] D. Townsend, S. K. Lee, and A. G. Suits. Dc slice imaging of ch3cl photolysis at 193.3 nm. *J. Phys. Chem. A*, 108:8106–8114, 2004.

[272] Eric W. Hansen and Phaih-Lan Law. Recursive methods for computing the abel transform and its inverse. *J. Opt. Soc. Am. A*, 2(4):510–520, Apr 1985. doi: 10.1364/JOSAA.2.000510. URL https://opg.optica.org/josaa/abstract.cfm?URI=josaa-2-4-510.

[273] Vladimir Dribinski, Alexei Ossadtchi, Vladimir A. Mandelshtam, and Hanna Reisler. Reconstruction of Abel-transformable images: The Gaussian basis-set expansion Abel transform method. *Rev. Sci. Instrum.*, 73(7):2634, 2002. ISSN 00346748. doi: 10.1063/1.1482156. URL http://scitation.aip.org/content/aip/journal/rsi/73/7/10.1063/1.1482156.

[274] Z. Amitay and D. Zajfman. A new type of multiparticle three-dimensional imaging detector with subnanosecond time resolution. *Rev. Sci. Instrum.*, 68 (3):1387–1392, 03 1997. ISSN 0034-6748. doi: 10.1063/1.1147950. URL https://doi.org/10.1063/1.1147950.

[275] I. Ali, R. Dörner, O. Jagutzki, S. Nüttgens, V. Mergel, L. Spielberger, Kh. Khayyat, T. Vogt, H. Bräuning, K. Ullmann, R. Moshammer, J. Ullrich, S. Hagmann, K.-O. Groeneveld, C.L. Cocke, and H. Schmidt-Böcking. Multi-hit detector system for complete momentum balance in spectroscopy in molecular fragmentation processes. *Nucl. Instrum. Methods Phys. Res. B*, 149(4):490–500, 1999. ISSN 0168-583X. doi: 10.1016/S0168-583X(98)00916-1. URL http://dx.doi.org/10.1016/S0168-583X(98)00916-1.

[276] J J John, M Brouard, A Clark, J Crooks, E Halford, L Hill, J W L Lee, A Nomerotski, R Pisarczyk, I Sedgwick, C S Slater, R Turchetta, C Vallance, E Wilman, B Winter, and W H Yuen. PImMS, a fast event-triggered monolithic pixel detector with storage of multiple timestamps. *J. Instrum.*, 7(8):C08001, August 2012. doi: 10.1088/1748-0221/7/08/C08001. URL https://doi.org/10.1088/1748-0221/7/08/C08001.

[277] Daofu Yuan, Wentao Chen, Chang Luo, Yuxin Tan, Shihao Li, Yin Huang, Zhigang Sun, Xueming Yang, and Xingan Wang. Imaging the state-to-state dynamics of the h + d2 $\rightarrow$ HD + d reaction at 1.42 eV. *J. Phys. Chem. Lett.*, 11(4):1222–1227, 2020. ISSN 1948-7185. doi: 10.1021/acs.jpclett.9b03820.

[278] Matthieu Besemer, Guoqiang Tang, Zhi Gao, Ad van der Avoird, Gerrit C. Groenenboom, Sebastiaan Y. T. van de Meerakker, and Tijs Karman. Glory scattering in deeply inelastic molecular collisions. *Nat. Chem.*, 14(6):664–669, 2022. ISSN 1755-4330. doi: 10.1038/s41557-022-00907-2.

[279] N G Kling, D Paul, A Gura, G Laurent, S De, H Li, Z Wang, B Ahn, C H Kim, T K Kim, I V Litvinyuk, C L Cocke, I Ben-Itzhak, D Kim, and M F Kling. Thick-lens velocity-map imaging spectrometer with high resolution for high-energy charged particles. *J. Instrum.*, 9(05):P05005, 2014. doi: 10.1088/1748-0221/9/05/p05005. URL https://doi.org/10.1088/1748-0221/9/05/P05005.

[280] Iker León, Zheng Yang, Hong-Tao Liu, and Lai-Sheng Wang. The design and construction of a high-resolution velocity-map imaging apparatus for

photoelectron spectroscopy studies of size-selected clusters. *Rev. Sci. Instrum.*, 85 (8):083106, 2014. ISSN 0034-6748. doi: 10.1063/1.4891701.

[281] Steven J. Kregel, Glen K. Thurston, Jia Zhou, and Etienne Garand. A multi-plate velocity-map imaging design for high-resolution photoelectron spectroscopy. *J. Chem. Phys.*, 147(9):094201, 2017. ISSN 0021-9606. doi: 10.1063/1.4996011.

[282] Daniel Rósch, Raybel Almeida, Bálint Sztáray, and David L. Osborn. High-resolution double velocity map imaging photoelectron photoion coincidence spectrometer for gas-phase reaction kinetics. *J. Phys. Chem. A*, 126(10):1761–1774, 2022. ISSN 1089-5639. doi: 10.1021/acs.jpca.1c10293.

[283] A I Chichinin, K H Gericke, S Kauczok, and C Maul. Imaging chemical reactions — 3D velocity mapping. *Int. Rev. Phys. Chem.*, 28(4):607–680, 2009. doi: 10.1080/01442350903235045. URL `http://www.tandfonline.com/doi/abs/10.1080/01442350903235045`.

[284] Peng Zhang, Zheng-Peng Feng, Si-Qiang Luo, and Zhe Wang. Influence of the interaction volume on the kinetic energy resolution of a velocity map imaging spectrometer. *Chin. Phys. B.*, 25(3):033202, 2016. ISSN 1674-1056. doi: 10.1088/1674-1056/25/3/033202.

[285] Scientific Instrument Services, Inc. SIMION ion optics simulation program. `https://simion.com`, 2025. Version 8.1 or later.

[286] D. A. Dahl, J. E. Delmore, and A. D. Appelhans. Simion pc/ps2 electrostatic lens design program. *Rev. Sci. Instrum.*, 61:607–609, 1990. doi: 10.1063/1.1141932.

[287] Edwin Kukk. Ion momentum mapping in photodissociation and coulomb explosion events using ion time-of-flight analyzers. *J. Phys. B*, 58(6):065101, 2025. doi: 10.1088/1361-6455/adaf87. URL `https://iopscience.iop.org/article/10.1088/1361-6455/adaf87`.

[288] A. H. Zewail. Femtochemistry: Atomic-scale dynamics of the chemical bond. *J. Phys. Chem. A*, 104(24):5660–5694, June 2000. doi: 10.1021/jp001460h. URL `https://dx.doi.org/10.1021/jp001460h`.

[289] Kanupriya Pande, Christopher D. M. Hutchison, Gerrit Groenhof, Andy Aquila, Josef S. Robinson, Jason Tenboer, Shibom Basu, Sébastien Boutet, Daniel P. DePonte, Mengning Liang, Thomas A. White, Nadia A. Zatsepin, Oleksandr Yefanov, Dmitry Morozov, Dominik Oberthuer, Cornelius Gati, Ganesh Subramanian, Daniel James, Yun Zhao, Jake Koralek, Jennifer Brayshaw, Christopher Kupitz, Chelsie Conrad, Shatabdi Roy-Chowdhury, Jesse D. Coe, Markus Metz, Paulraj Lourdu Xavier, Thomas D. Grant, Jason E. Koglin, Gihan Ketawala, Raimund Fromme, Vukica Šrajer, Robert Henning, John C. H. Spence, Abbas Ourmazd, Peter Schwander, Uwe Weierstall, Matthias Frank, Petra Fromme, Anton Barty, Henry N. Chapman, Keith Moffat, Jasper J. van Thor, and Marius Schmidt. Femtosecond structural dynamics drives the trans/cis isomerization in photoactive yellow protein. *Science*, 352(6286):725–729, 2016. ISSN 0036-8075. doi: 10.1126/science.aad5081. URL `http://science.sciencemag.org/content/352/6286/725`.

[290] Ahmed H. Zewail. 4D ultrafast electron diffraction, crystallography, and microscopy. *Annu. Rev. Phys. Chem.*, 57:65–103, 2006.

[291] Anatoly A Ischenko, Peter M Weber, and R J Dwayne Miller. Capturing chemistry in action with electrons: Realization of atomically resolved reaction dynamics. *Chem. Rev.*, 117(16):11066–11124, June 2017. doi: 10.1021/acs.chemrev.6b00770. URL `https://dx.doi.org/10.1021/acs.chemrev.6b00770`.

[292] Cosmin I Blaga, Junliang Xu, Anthony D DiChiara, Emily Sistrunk, Kaikai Zhang, Pierre Agostini, Terry A Miller, Louis F DiMauro, and C D Lin. Imaging ultrafast molecular dynamics with laser-induced electron diffraction. *Nature*, 483(7388): 194–197, March 2012. doi: 10.1038/nature10820. URL https://www.nature.com/articles/nature10820.

[293] Evangelos T Karamatskos, Gildas Goldsztejn, Sebastian Raabe, Philipp Stammer, Terry Mullins, Andrea Trabattoni, Rasmus R Johansen, Henrik Stapelfeldt, Sebastian Trippel, Marc J J Vrakking, Jochen Küpper, and Arnaud Rouzée. Atomic-resolution imaging of carbonyl sulfide by laser-induced electron diffraction. *J. Chem. Phys.*, 150(24):244301, June 2019. doi: 10.1063/1.5093959. URL https://doi.org/10.1063/1.5093959.

[294] Andrea Trabattoni, Joss Wiese, Umberto De Giovannini, Jean-Franćois Olivieri, Terry Mullins, Jolijn Onvlee, Sang-Kil Son, Biagio Frusteri, Angel Rubio, Sebastian Trippel, and Jochen Küpper. Setting the photoelectron clock through molecular alignment. *Nat. Commun.*, 11:2546, May 2020. doi: 10.1038/s41467-020-16270-0. URL https://doi.org/10.1038/s41467-020-16270-0.

[295] J. Itatani, J. Levesque, D. Zeidler, H. Niikura, H. Pépin, J. C. Kieffer, P. B. Corkum, and D. M. Villeneuve. Tomographic imaging of molecular orbitals. *Nature*, 432: 867–871, 2004. doi: 10.1038/nature03183. URL https://dx.doi.org/10.1038/nature03183.

[296] C. Vozzi, M. Negro, F. Calegari, G. Sansone, M. Nisoli, S. De Silvestri, and S. Stagira. Generalized molecular orbital tomography. *Nat. Phys.*, 7:822–826, June 2011. doi: 10.1038/nphys2029.

[297] Hans Jakob Wörner, J B Bertrand, D V Kartashov, P B Corkum, and D M Villeneuve. Following a chemical reaction using high-harmonic interferometry. *Nature*, 466 (7306):604–607, 2010. doi: 10.1038/nature09185.

[298] Qiaoli Hao, Jinyou Long, Xulan Deng, Ying Tang, Bumaliya Abulimiti, and Bing Zhang. Superexcited state dynamics of ocs: An experimental identification of three competing decay channels among autoionization, internal conversion, and neutral predissociation. *J. Phys. Chem. A*, 121(20):3858–3863, 2017. ISSN 1089-5639. doi: 10.1021/acs.jpca.7b01895. URL https://pubs.acs.org/doi/full/10.1021/acs.jpca.7b01895.

[299] Narayan Kundu and Dhananjay Nandi. Observation of renner–teller and predissociation coupled vibronic intensity borrowing in dissociative electron attachment to ocs. *J. Chem. Phys.*, 160(11):114315, 2024. ISSN 0021-9606. doi: 10.1063/5.0188833. URL https://pubs.aip.org/aip/jcp/article/160/11/114315/3277921/Observation-of-Renner-Teller-and-predissociation.

[300] T. Baumert, B. Bühler, R. Thalweiser, and G. Gerber. Femtosecond spectroscopy of molecular autoionization and fragmentation. *Phys. Rev. Lett.*, 64(7):733–736, 1990. ISSN 0031-9007. doi: 10.1103/physrevlett.64.733. URL https://link.aps.org/doi/10.1103/PhysRevLett.64.733.

[301] Albert Stolow and Jonathan G. Underwood. Time-resolved photoelectron spectroscopy of nonadiabatic dynamics in polyatomic molecules. *Adv. Chem. Phys.*, 139:497–584, Apr 2008. ISSN 1934-4791. doi: 10.1002/9780470259498.ch6. URL http://dx.doi.org/10.1002/9780470259498.ch6.

[302] Rebecca Boll, Arnaud Rouzée, Marcus Adolph, Denis Anielski, Andrew Aquila, Sadia Bari, Cédric Bomme, Christoph Bostedt, John D Bozek, Henry N Chapman,

Lauge Christensen, Ryan Coffee, Niccola Coppola, Sankar De, Piero Decleva, Sascha W Epp, Benjamin Erk, Frank Filsinger, Lutz Foucar, Tais Gorkhover, Lars Gumprecht, André Hömke, Lotte Holmegaard, Per Johnsson, Jens S Kienitz, Thomas Kierspel, Faton Krasniqi, Kai-Uwe Kühnel, Jochen Maurer, Marc Messerschmidt, Robert Moshammer, Nele L M Müller, Benedikt Rudek, Evgeny Savelyev, Ilme Schlichting, Carlo Schmidt, Frank Scholz, Sebastian Schorb, Joachim Schulz, Jörn Seltmann, Mauro Stener, Stephan Stern, Simone Techert, Jan Thøgersen, Sebastian Trippel, Jens Viefhaus, Marc Vrakking, Henrik Stapelfeldt, Jochen Küpper, Joachim Ullrich, Artem Rudenko, and Daniel Rolles. Imaging molecular structure through femtosecond photoelectron diffraction on aligned and oriented gas-phase molecules. *Faraday Disc.*, 171:57–80, 2014. doi: 10.1039/c4fd00037d.

[303] M. Nisoli, S. De Silveshi, and O. Svelto. Generation of high-energy 10-fs pulses by a new pulse compression technique. *Appl. Phys. Lett.*, 68(20):189–190, 1996. ISSN 0003-6951. doi: 10.1063/1.116609. URL https://pubs.aip.org/aip/apl/article/68/20/2793/521166/Generation-of-high-energy-10-fs-pulses-by-a-new.

[304] M Nisoli, S De Silvestri, O Svelto, R Szipöcs, K Ferencz, Ch Spielmann, S Sartania, and F Krausz. Compression of high-energy laser pulses below 5 fs. *Opt. Lett.*, 22 (8):522, 1997. ISSN 0146-9592. doi: 10.1364/OL.22.000522. URL https://opg.optica.org/ol/fulltext.cfm?uri=ol-22-8-522&id=36058.

[305] Shohei Hattori, Kazuki Kamezaki, and Naohiro Yoshida. Constraining the atmospheric OCS budget from sulfur isotopes. *Proc. Natl. Acad. Sci. U.S.A.*, 117 (34):20447–20452, 2020. doi: 10.1073/pnas.2007260117.

[306] J. E. Campbell, J. A. Berry, U. Seibt, S. J. Smith, S. A. Montzka, T. Launois, S. Belviso, L. Bopp, and M. Laine. Large historical growth in global terrestrial gross primary production. *Nature*, 544(7648):84–87, 2017. ISSN 0028-0836. doi: 10.1038/nature22030. URL https://www.nature.com/articles/nature22030.

[307] David Asaf, Eyal Rotenberg, Fyodor Tatarinov, Uri Dicken, Stephen A. Montzka, and Dan Yakir. Ecosystem photosynthesis inferred from measurements of carbonyl sulphide flux. *Nat. Geosci.*, 6(3):186–190, 2013. ISSN 1752-0894. doi: 10.1038/ngeo1730. URL https://www.nature.com/articles/ngeo1730.

[308] Paris D. N. Svoronos and Thomas J. Bruno. Carbonyl sulfide: A review of its chemistry and properties. *Ind. Eng. Chem.*, 41(22):5321–5336, 2002. ISSN 0888-5885. doi: 10.1021/ie020365n.

[309] J. W. Rabalais, J. M. McDonald, V. Scherr, and S. P. McGlynn. Electronic spectroscopy of isoelectronic molecules. II. Linear triatomic groupings containing sixteen valence electrons. *Chem. Rev.*, 71:73–108, 1971. doi: 10.1021/cr60269a004. URL https://pubs.acs.org/doi/abs/10.1021/cr60269a004.

[310] Yoshihiro Sato, Yutaka Matsumi, Masahiro Kawasaki, Koichi Tsukiyama, and Richard Bersohn. Ion imaging of the photodissociation of OCS near 217 and 230 nm. *J. Phys. Chem.*, 99:16307–16314, 1995. doi: 10.1021/j100044a017. URL https://doi.org/10.1021/j100044a017.

[311] Toshinori Suzuki, Hideki Katayanagi, Shinkoh Nanbu, and Mutsumi Aoyagi. Nonadiabatic bending dissociation in 16 valence electron system OCS. *J. Chem. Phys.*, 109(14):5778–5794, 1998. doi: 10.1063/1.477200. URL https://doi.org/10.1063/1.477200.

[312] W. H. Breckenridge and Henry Taube. Ultraviolet absorption spectrum of carbonyl sulfide. *J. Chem. Phys.*, 52(4):1713–1715, 1970. doi: 10.1063/1.1673209. URL https://doi.org/10.1063/1.1673209.

[313] Hideki Katayanagi, Yuxiang Mo, and Toshinori Suzuki. 223 nm photodissociation of OCS. Two components in S($^1D_2$) and S($^3P_2$) channels. *Chem. Phys. Lett.*, 247 (4):571–576, 1995. ISSN 0009-2614. doi: 10.1016/S0009-2614(95)01253-2. URL http://www.sciencedirect.com/science/article/pii/S0009261495012532.

[314] Zee Hwan Kim, Andrew J. Alexander, and Richard N. Zare. Speed-dependent photofragment orientation in the photodissociation of OCS at 223 nm. *J. Phys. Chem. A*, 103:10144–10148, 1999. doi: 10.1021/jp991988q. URL https://doi.org/10.1021/jp991988q.

[315] Akihiro Sugita, Michio Mashino, Masahiro Kawasaki, Yutaka Matsumi, Richard Bersohn, Gundula Trott-Kriegeskorte, and K arl-Heinz Gericke. Effect of molecular bending on the photodissociation of OCS. *J. Chem. Phys.*, 112(16):7095–7101, 2000. doi: 10.1063/1.481324. URL https://doi.org/10.1063/1.481324.

[316] Hideki Katayanagi and Toshinori Suzuki. Non-adiabatic bending dissociation of OCS: the effect of bending excitation on the transition probability. *Chem. Phys. Lett.*, 360(1):104–110, 2002. ISSN 0009-2614. doi: 10.1016/S0009-2614(02)00788-1. URL http://www.sciencedirect.com/science/article/pii/S0009261402007881.

[317] Wei Wei, Colin J. Wallace, George C. McBane, and Simon W. North. Photodissociation dynamics of OCS near 214 nm using ion imaging. *J. Chem. Phys.*, 145(2):024310, 2016. doi: 10.1063/1.4955189. URL https://doi.org/10.1063/1.4955189.

[318] M. Brouard, A. V. Green, F. Quadrini, and C. Vallance. Photodissociation dynamics of OCS at 248 nm: The S($^1D_2$) atomic angular momentum polarization. *J. Chem. Phys.*, 127(8):084304, 2007. doi: 10.1063/1.2757618. URL https://doi.org/10.1063/1.2757618.

[319] Alrik J. van den Brom, T. Peter Rakitzis, and Maurice H. M. Janssen. State-to-state photodissociation of carbonyl sulfide ($v_2 = 0, 1|JIM$). II. The effect of initial bending on coherence of S($^1D_2$) polarization. *J. Chem. Phys.*, 123(16):164313, 2005. doi: 10.1063/1.2076647. URL https://doi.org/10.1063/1.2076647.

[320] T. P. Rakitzis, A. J. van den Brom, and M. H. M. Janssen. Directional dynamics in the photodissociation of oriented molecules. *Science*, 303:1852–1854, 2004. doi: 10.1126/science.1094186. URL http://dx.doi.org/10.1126/science.1094186.

[321] Dimitris Sofikitis, Jaime Suarez, Johan A. Schmidt, T. Peter Rakitzis, Stavros C. Farantos, and Maurice H. M. Janssen. Recoil inversion in the photodissociation of carbonyl sulfide near 234 nm. *Phys. Rev. Lett.*, 118:253001, June 2017. doi: 10.1103/PhysRevLett.118.253001. URL https://link.aps.org/doi/10.1103/PhysRevLett.118.253001.

[322] J. A. Schmidt, M. S. Johnson, G. C. McBane, and R. Schinke. The ultraviolet spectrum of OCS from first principles: Electronic transitions, vibrational structure and temperature dependence. *J. Chem. Phys.*, 137(5):054313, 2012. doi: 10.1063/1.4739756. URL https://doi.org/10.1063/1.4739756.

[323] J. A. Schmidt, M. S. Johnson, S. Hattori, N. Yoshida, S. Nanbu, and R. Schinke. OCS photolytic isotope effects from first principles: sulfur and carbon isotopes, temperature dependence and implications for the stratosphere. *Atmos. Chem. Phys.*, 13(3):1511–1520, 2013. doi: 10.5194/acp-13-1511-2013. URL https://acp.

copernicus.org/articles/13/1511/2013/.

[324] J. A. Schmidt, M. S. Johnson, G. C. McBane, and R. Schinke. Multi-state analysis of the OCS ultraviolet absorption including vibrational structure. *J. Chem. Phys.*, 136(13):131101, 2012. doi: 10.1063/1.3701699. URL https://doi.org/10.1063/1.3701699.

[325] G. C. McBane, J. A. Schmidt, M. S. Johnson, and R. Schinke. Ultraviolet photodissociation of OCS: Product energy and angular distributions. *J. Chem. Phys.*, 138(9):094314, 2013. doi: 10.1063/1.4793275. URL https://doi.org/10.1063/1.4793275.

[326] Sebastian O. Danielache, Shinkoh Nanbu, Carsten Eskebjerg, Matthew S. Johnson, and Naohiro Yoshida. Carbonyl sulfide isotopologues: Ultraviolet absorption cross sections and stratospheric photolysis. *J. Chem. Phys.*, 131(2):024307, 2009. doi: 10.1063/1.3156314. URL https://doi.org/10.1063/1.3156314.

[327] M. Laura Lipciuc and Maurice H. M. Janssen. Slice imaging of the quantum state-to-state cross section for photodissociation of state-selected rovibrational bending states of OCS ($v_2 = 0, 1, 2|JlM$) + $h\nu \rightarrow$ CO(J) + S($^1D_2$). *J. Chem. Phys.*, 126(19):194318, 2007. doi: 10.1063/1.2737450. URL https://doi.org/10.1063/1.2737450.

[328] Benjamin W. Toulson and Craig Murray. Decomposing the first absorption band of OCS using photofragment excitation spectroscopy. *J. Phys. Chem. A*, 120:6745–6752, 2016. doi: 10.1021/acs.jpca.6b06060. URL https://doi.org/10.1021/acs.jpca.6b06060.

[329] N. Sivakumar, I. Burak, W. Y. Cheung, P. L. Houston, and J. W. Hepburn. State-resolved photofragmentation of carbonyl sulfide (OCS) monomers and clusters. *J. Phys. Chem.*, 89(17):3609–3611, 1985. doi: 10.1021/j100263a008. URL https://doi.org/10.1021/j100263a008.

[330] G. Nan, I. Burak, and P.L. Houston. Photodissociation of OCS at 222 nm. The triplet channel. *Chem. Phys. Lett.*, 209(4):383–389, 1993. ISSN 0009-2614. doi: 10.1016/0009-2614(93)80035-N. URL http://www.sciencedirect.com/science/article/pii/000926149380035N.

[331] Anouk M. Rijs, Ellen H. G. Backus, Cornelis A. de Lange, Maurice H. M. Janssen, Nicholas P. C. Westwood, Kwanghsi Wang, and Vincent McKoy. Rotationally resolved photoionization dynamics of hot CO fragmented from OCS. *J. Chem. Phys.*, 116(7):2776–2782, 2002. doi: 10.1063/1.1434993. URL https://doi.org/10.1063/1.1434993.

[332] Alrik J. van den Brom, T. Peter Rakitzis, and Maurice H. M. Janssen. Photodissociation of laboratory oriented molecules: Revealing molecular frame properties of nonaxial recoil. *J. Chem. Phys.*, 121(23):11645–11652, 2004. doi: 10.1063/1.1812756. URL https://doi.org/10.1063/1.1812756.

[333] M. Laura Lipciuc, T. Peter Rakitzis, W. Leo Meerts, Gerrit C. Groenenboom, and Maurice H. M. Janssen. Towards the complete experiment: measurement of S($^1D_2$) polarization in correlation with single rotational states of CO(J) from the photodissociation of oriented OCS($v_2 = 1|JlM = 111$). *Phys. Chem. Chem. Phys.*, 13:8549–8559, 2011. doi: 10.1039/C0CP02671A. URL http://dx.doi.org/10.1039/C0CP02671A.

[334] Dimitris Sofikitis, Jaime Suarez, Johan A. Schmidt, T. Peter Rakitzis, Stavros C. Farantos, and Maurice H. M. Janssen. Exit-channel recoil resonances by imaging

the photodissociation of single quantum-state-selected OCS molecules. *Phys. Rev. A*, 98:033417, September 2018. doi: 10.1103/PhysRevA.98.033417. URL https://link.aps.org/doi/10.1103/PhysRevA.98.033417.

[335] Yuxiang Mo, Hideki Katayanagi, Michael C. Heaven, and Toshinori Suzuki. Simultaneous measurement of recoil velocity and alignment of $S(^1D_2)$ atoms in photodissociation of OCS. *Phys. Rev. Lett.*, 77:830–833, Jul 1996. doi: 10.1103/PhysRevLett.77.830. URL https://link.aps.org/doi/10.1103/PhysRevLett.77.830.

[336] T. Peter Rakitzis, Peter C. Samartzis, and Theofanis N. Kitsopoulos. Complete measurement of $S(^1D_2)$ photofragment alignment from Abel-invertible ion images. *Phys. Rev. Lett.*, 87:123001, Aug 2001. doi: 10.1103/PhysRevLett.87.123001. URL https://link.aps.org/doi/10.1103/PhysRevLett.87.123001.

[337] Suk Kyoung Lee, Ruchira Silva, Shakera Thamanna, Oleg S. Vasyutinskii, and Arthur G. Suits. $S(^1D_2)$ atomic orbital polarization in the photodissociation of OCS at 193 nm: Construction of the complete density matrix. *J. Chem. Phys.*, 125 (14):144318, 2006. doi: 10.1063/1.2357948. URL https://doi.org/10.1063/1.2357948.

[338] J. A. Schmidt and J. M. H. Olsen. Photodissociation of OCS: Deviations between theory and experiment, and the importance of higher order correlation effects. *J. Chem. Phys.*, 141(18):184310, 2014. doi: 10.1063/1.4901426. URL https://doi.org/10.1063/1.4901426.

[339] H. Stapelfeldt, H. Sakai, E. Constant, and P. B. Corkum. Deflection of neutral molecules using the nonresonant dipole force. *Phys. Rev. Lett.*, 79:2787–2790, 1997. doi: 10.1103/PhysRevLett.79.2787. URL http://dx.doi.org/10.1103/PhysRevLett.79.2787.

[340] C. Chin, T. Kraemer, M. Mark, J. Herbig, P. Waldburger, H. C. Nägerl, and R. Grimm. Observation of feshbach-like resonances in collisions between ultracold molecules. *Phys. Rev. Lett.*, 94:123201, 2005.

[341] Christer Z. Bisgaard, Owen J. Clarkin, Guorong Wu, Anthony M. D. Lee, Oliver Geßner, Carl C. Hayden, and Albert Stolow. Time-resolved molecular frame dynamics of fixed-in-space CS_2 molecules. *Science*, 323(5920):1464–1468, 2009. doi: 10.1126/science.1169183. URL http://science.sciencemag.org/content/323/5920/1464.

[342] Evangelos T. Karamatskos, Sebastian Raabe, Terry Mullins, Andrea Trabattoni, Philipp Stammer, Gildas Goldsztejn, Rasmus R. Johansen, Karol Długołęcki, Henrik Stapelfeldt, Marc. J. J. Vrakking, Sebastian Trippel, Arnaud Rouzée, and Jochen Küpper. Molecular movie of ultrafast coherent rotational dynamics of OCS. *Nat. Commun.*, 10:3364, 2019. doi: 10.1038/s41467-019-11122-y. URL https://dx.doi.org/10.1038/s41467-019-11122-y.

[343] M. Nisoli, S. De Silveshi, and O. Svelto. Generation of high-energy 10-fs pulses by a new pulse compression technique. *Appl. Phys. Lett.*, 68:2793–2795, 1996. doi: 10.1063/1.116609. URL https://pubs.aip.org/aip/apl/article/68/20/2793/521166/Generation-of-high-energy-10-fs-pulses-by-a-new.

[344] I. J. Sola, E. Mével, L. Elouga, E. Constant, V. Strelkov, L. Poletto, P. Villoresi, E. Benedetti, J.-P. Caumes, S. Stagira, C. Vozzi, G. Sansone, and M. Nisoli. Controlling attosecond electron dynamics by phase-stabilized polarization gating. *Nat. Phys.*, 2(5):319–322, 2006. doi: 10.1038/nphys281. URL https://www.nature.

com/articles/nphys281.

[345] G. Sansone, E. Benedetti, F. Calegari, C. Vozzi, L. Avaldi, R. Flammini, L. Poletto, P. Villoresi, C. Altucci, R. Velotta, S. Stagira, S. De Silvestri, and M. Nisoli. Isolated single-cycle attosecond pulses. *Science*, 314(5798):443–446, 2006. ISSN 0036-8075. doi: 10.1126/science.1132838. URL https://www.science.org/doi/10.1126/science.1132838.

[346] M. Lewenstein, P. Balcou, M. Y. Ivanov, A. L'Huillier, and P. B. Corkum. Theory of high-harmonic generation by low-frequency laser fields. *Phys. Rev. A*, 49: 2117–2132, 1994. doi: 10.1103/PhysRevA.49.2117. URL https://journals.aps.org/pra/abstract/10.1103/PhysRevA.49.2117.

[347] Rodrigo López-Martens, Katalin Varjú, Per Johnsson, Johan Mauritsson, Yann Mairesse, Pascal Salières, Mette B. Gaarde, Kenneth J. Schafer, Anders Persson, Sune Svanberg, Claes-Göran Wahlström, and Anne L'Huillier. Amplitude and phase control of attosecond light pulses. *Phys. Rev. Lett.*, 94:033001, 2004. doi: 10.1103/physrevlett.94.033001. URL https://journals.aps.org/prl/abstract/10.1103/PhysRevLett.94.033001.

[348] Song-Feng Zhao, Junliang Xu, Cheng Jin, Anh-Thu Le, and C D Lin. Effect of orbital symmetry on the orientation dependence of strong field tunnelling ionization of nonlinear polyatomic molecules. *J. Phys. B: At. Mol. Opt. Phys.*, 44(3):035601, 2011. ISSN 0953-4075. doi: 10.1088/0953-4075/44/3/035601.

[349] Wanjie Song, Yubin He, Muhammad A Shehzad, Xiaolin Ge, Liang Ge, Xian Liang, Chengpeng Wei, Zijuan Ge, Kaiyu Zhang, Geng Li, et al. Exploring h-bonding interaction to enhance proton permeability of an acid-selective membrane. *Journal of Membrane Science*, 637:119650, 2021.

[350] Subhrakant Jena, Juhi Dutta, Kiran Devi Tulsiyan, Akshay Kumar Sahu, Shubhranshu Shekhar Choudhury, and Himansu S Biswal. Noncovalent interactions in proteins and nucleic acids: beyond hydrogen bonding and π-stacking. *Chem. Soc. Rev.*, 51:4261–4286, 2022. doi: 10.1039/D2CS00133K. URL https://pubs.rsc.org/en/content/articlelanding/2022/cs/d2cs00133k/unauth.

[351] Igor A Yaroshevich, Eugene G Maksimov, Nikolai N Sluchanko, Dmitry V Zlenko, Alexey V Stepanov, Ekaterina A Slutskaya, Yury B Slonimskiy, Viacheslav S Botnarevskii, Alina Remeeva, Ivan Gushchin, Kirill Kovalev, Valentin I. Gordeliy, Ivan V. Shelaev, Fedor E. Gostev, Dmitry Khakhulin, Vladimir V. Poddubnyy, Timofey G. Gostev, Dmitry A. Cherepanov, Tomáš Polívka, Miroslav Kloz, Thomas Friedrich, Vladimir Z. Paschenko, Victor A. Nadtochenko, Andrew B. Rubin, and Mikhail P. Kirpichnikov. Role of hydrogen bond alternation and charge transfer states in photoactivation of the orange carotenoid protein. *Nature*, 4: 539, 2021. doi: 10.1038/s42003-021-02022-3. URL https://www.nature.com/articles/s42003-021-02022-3.

[352] Raúl Montero, Virginia Ovejas, Marta Fernández-Fernández, Álvaro Peralta Conde, and Asier Longarte. Revisiting the relaxation dynamics of isolated pyrrole. *J. Chem. Phys.*, 141:014303, 2014. doi: 10.1063/1.4885722. URL https://pubs.aip.org/aip/jcp/article/141/1/014303/352730.

[353] Andreas Hans, Philipp Schmidt, Catmarna Küstner-Wetekam, Florian Trinter, Sascha Deinert, Dana Bloß, Johannes H. Viehmann, Rebecca Schaf, Miriam Gerstel, Clara M. Saak, Jens Buck, Stephan Klumpp, Gregor Hartmann, Lorenz S. Cederbaum, Nikolai V. Kryzhevoi, and André Knie. Suppression of x-ray-

induced radiation damage to biomolecules in aqueous environments by immediate intermolecular decay of inner-shell vacancies. *J. Phys. Chem. Lett.*, 12(30):7146–7150, 2021. doi: 10.1021/acs.jpclett.1c01879. URL https://doi.org/10.1021/acs.jpclett.1c01879. PMID: 34297572.

[354] Geethanjali Gopakumar, I Unger, P Slavíček, Uwe Hergenhahn, G Öhrwall, Sebastian Malerz, D Céolin, Florian Trinter, Bernd Winter, I Wilkinson, I Caleman, E Muchová, and O Björneholm. Radiation damage by extensive local water ionization from two-step electron-transfer-mediated decay of solvated ions. *Nat. Chem.*, 15(10):1408–1414, 2023. doi: 10.1038/s41557-023-01302-1. URL https://www.nature.com/articles/s41557-023-01302-1.

[355] F Tarantelli, A Sgamellotti, L S Cederbaum, and J Schirmer. Theoretical investigation of many dicationic states and the auger spectrum of benzene. *J. Chem. Phys.*, 86(4):2201–2206, 1987. doi: 10.1063/1.452118. URL http://scitation.aip.org/content/aip/journal/jcp/86/4/10.1063/1.452118.

[356] U. Hergenhahn. Interatomic and intermolecular coulombic decay: The early years. *J. Electron. Spectrosc. Relat. Phenom.*, 184(3):78–90, 2011. ISSN 0368-2048. doi: 10.1016/j.elspec.2010.12.020. URL http://www.sciencedirect.com/science/article/pii/S0368204810002914. Advances in Vacuum Ultraviolet and X-ray Physics.

[357] Stephan Thürmer, Milan Ončák, Niklas Ottosson, Robert Seidel, Uwe Hergenhahn, Stephen E. Bradforth, Petr Slavíček, and Bernd Winter. On the nature and origin of dicationic, charge-separated species formed in liquid water on X-ray irradiation. *Nat. Chem.*, 5:590–596, 2013. doi: 10.1038/nchem.1680. URL https://doi.org/10.1038/nchem.1680.

[358] Rebecca Boll, Benjamin Erk, Ryan Coffee, Sebastian Trippel, Thomas Kierspel, Cédric Bomme, John D. Bozek, Mitchell Burkett, Sebastian Carron, Ken R. Ferguson, Lutz Foucar, Jochen Küpper, Tatiana Marchenko, Catalin Miron, Minna Patanen, Timur Osipov, Sebastian Schorb, Marc Simon, Michelle Swiggers, Simone Techert, Kiyoshi Ueda, Christoph Bostedt, Daniel Rolles, and Artem Rudenko. Charge transfer in dissociating iodomethane and fluoromethane molecules ionized by intense femtosecond x-ray pulses. *Struct. Dyn.*, 3:043207, 2016. doi: 10.1063/1.4944344. URL https://doi.org/10.1063/1.4944344.

[359] K. Grygoryeva, J. Rakovský, Ivo Vinklárek, O. Votava, M. Fárník, , and Viktoriya Poterya. Vibrationally mediated photodissociation dynamics of pyrrole. *AIP Adv.*, 9:0351511–0351517, 2019. doi: 10.1063/1.5091974. URL https://aip.scitation.org/doi/pdf/10.1063/1.5091974?class=pdf.

[360] Dashjargal Arildii, Yoshiteru Matsumoto, and Otto Dopfer. Microhydration of the pyrrole cation (Py^+) revealed by IR spectroscopy: Ionization-induced rearrangement of the hydrogen-bonded network of $Py^+(H_2O)_2$. *J. Phys. Chem. A*, 127(11):2523–2535, 2023. doi: 10.1021/acs.jpca.3c00363. URL https://doi.org/10.1021/acs.jpca.3c00363.

[361] Irmgard Frank and Konstantina Damianos. Excited state dynamics in pyrrole–water clusters: First-principles simulation. *Chem. Phys.*, 343(2):347–352, 2008. ISSN 0301-0104. doi: 10.1016/j.chemphys.2007.08.029. URL https://www.sciencedirect.com/science/article/pii/S0301010407003850.

[362] B Erk, D Rolles, L Foucar, B Rudek, S W Epp, M Cryle, C Bostedt, S Schorb, J Bozek, A Rouzee, A Hundertmark, T Marchenko, M Simon, F Filsinger, L Christensen, S De, S Trippel, Jochen Küpper, Henrik Stapelfeldt, S Wada, K Ueda, M Swiggers,

M Messerschmidt, C D Schroter, R Moshammer, I Schlichting, J Ullrich, and A Rudenko. Ultrafast charge rearrangement and nuclear dynamics upon inner-shell multiple ionization of small polyatomic molecules. *Phys. Rev. Lett.*, 110 (5):053003, January 2013. doi: 10.1103/PhysRevLett.110.053003. URL `http://prl.aps.org/abstract/PRL/v110/i5/e053003`.

[363] Eugene Hecht. *Optics*. Addison-Wesley, 4 edition, 2001.

[364] J J Yeh and I Lindau. Atomic subshell photoionization cross sections and asymmetry parameters: 1 ≤Z ≤ 103. *Atomic data and nuclear data table*, 32(1):1–155, 1985. doi: 10.1016/0092-640X(85)90016-6. URL `https://www.sciencedirect.com/science/article/pii/0092640X85900166`.

[365] Sebastian Schorb, Daniela Rupp, Michelle L Swiggers, Ryan N Coffee, Marc Messerschmidt, Garth Williams, John D Bozek, Shin-ichi Wada, Oleg Kornilov, Thomas Möller, and Christoph Bostedt. Size-Dependent Ultrafast Ionization Dynamics of Nanoscale Samples in Intense Femtosecond X-Ray Free-Electron-Laser Pulses. *Phys. Rev. Lett.*, 108(23):233401, June 2012. doi: 10.1103/PhysRevLett.108.233401. URL `http://link.aps.org/doi/10.1103/PhysRevLett.108.233401`.

Acknowledgments

Over the time of nearly five years of my doctoral journey, I have received an immense amount of help, companionship, and encouragement. Although this is my doctoral dissertation, behind every page lies the support and contributions of many people, to whom I owe my deepest gratitude.

First and foremost, I would like to express my heartfelt thanks to my supervisor, Prof. Jochen Küpper, for giving me the invaluable opportunity to join the Controlled Molecule Imaging group at the Center for Free-Electron Laser Science (CFEL-DESY) and to explore such exciting science. I am truly grateful for the excellent platform you have provided, which allowed me to learn, exchange ideas, and grow as a researcher. Your insightful guidance has been essential to the success of my project and has profoundly shaped my scientific training. Moreover, your rigorous approach to research are qualities that will always inspire me in my future endeavors.

Next, I would also like to express my sincere gratitude to my supervisor, Dr. Sebastian Trippel, for his continuous guidance and support throughout my project. Under your supervision, I gradually became proficient in experimental work, academic discussions, and scientific writing, and eventually gained the confidence and ability to conduct research independently. At the same time, your personal charisma and leadership created a lively and inspiring atmosphere within the Imaging Chemical Dynamics team, making my time there both fulfilling and enjoyable.

I would also like to extend my heartfelt thanks to all my team members for your support and kindness, both in my research and in my daily life. First, I want to thank Ivo Vinklárek, whose deep involvement in my project was truly invaluable. You provided crucial assistance with experiments, data analyzing, and manuscript preparation. I have learned so much from your work and from our many discussions, which have greatly enriched my understanding and broadened my perspective. I would also like to thank the other members of our team: Atilay Ayasli, Hubertus Bromberger, Matthew Robinson, Mukhtar Singh, Nidin Vadassery, Ilya Maksimov, and Aditi Pradhan, for your generous help in experiments, discussions, and everyday life. It has been my greatest honor and pleasure to work with you all.

I would also like to thank members of the other teams for their generous support. Andrey Yachmenev, Álvaro Fernández, and Emil Vogt provided valuable help with the theoretical aspects and simulations of my work. I am also deeply grateful to Karol Długołecki for his engineering expertise and experimental support, and to Barbora Vagovič for her kind assistance with administrative support, paperwork, and communication matters. My sincere thanks also go to all group members for their continuous help and companionship throughout my studies and daily life.

Furthermore, I would like to express my sincere gratitude to the Helmholtz–Lund International Graduate School (HELIOS) project for providing funding and continuous support throughout my PhD studies. I am very thankful for the valuable training opportunities and the collaborative platform that the program offered, as well as for the guidance and support from Dr. Mathieu Gisselbrecht as my project supervisor.

Next, I would like to thank the members of FS-ATTO and FEL's SQS teams for their generous assistance and strong support during my beamtime experiments. Your expertise and collaboration were essential for the success of my work.

Finally, I would like to express my deepest gratitude and respect to my Chinese friends and family. The following paragraph is written in Chinese to convey my heartfelt appreciation in my native language.

我想首先感谢吉林大学原子与分子物理研究所和丁大军教授提供给我宝贵的联合培养的机会，丁大军教授对我工作给予很多建议和支持，尤其是新冠疫情期间的大力帮助和斡旋，让我得以有机会来DESY进行合作交流并最终促成该博士项目的顺利开启和圆满结束，其中赫兰海师兄在我博士工作初期的帮助和培训对我适应新环境，工作交接和项目推进提供了极大帮助，并在工作过程中提供了非常多的建议。我还想特别感谢我在德国的亲朋好友们，陶成诚博士，杨光博士，孙文浩博士，李楚峰博士，谢帆博士，顾易坤博士，廖川博士，程雪梅博士，王佳博士，我的姐姐张睿导及其家人，以及所有在欧洲陪伴和支持我的朋友们，感谢你们在我学习和生活中的陪伴、鼓励，支持和帮助，让我在异国他乡依然感受到家的温暖。最后，我要感谢我远在国内的父母和亲友们，感谢你们无条件的理解和支持，跨越了将近五年和数万公里的时空距离，你们的信任与鼓励是我不断前行的力量源泉。没有你们，就没有今天的我。衷心地感谢你们！